

Integrated Energy Storage for Next-Generation Wind Turbines

A dissertation presented to the faculty of the School of Engineering and Applied Science, University of Virginia

In partial fulfillment of the requirements for the degree
Doctor of Philosophy

Juliet G. Simpson
December 2022

APPROVAL SHEET

This
Dissertation
is submitted in partial fulfillment of the requirements
for the degree of
Doctor of Philosophy

Author: Juliet G. Simpson

This Dissertation has been read and approved by the examining committee:

Advisor: Eric Loth

Advisor:

Committee Member: Chloe Dedic

Committee Member: Gary Koenig


Committee Member: Chao (Chris) Qin

Committee Member: Daniel Quinn

Committee Member:

Committee Member:

Accepted for the School of Engineering and Applied Science:



Jennifer L. West, School of Engineering and Applied Science

December 2022

Abstract

To reduce the impacts of climate change, the US must shift to a carbon-free electrical grid, requiring increasing renewable energy generation. The implementation of a carbon-free electrical grid is investigated from multiple different aspects within this work, including wind turbine modeling, energy storage modeling, and techno-economic analysis of renewable energy and energy storage systems.

To meet increasing wind energy generation goals, wind turbines may shift to downwind turbines, where the wind first hits the tower and then the rotor plane. The downwind turbine “tower shadow” effect, whereby blades experience a change in loading when they pass behind the tower, has not previously been studied with experimental field test data. Herein, a method was developed for simulating turbulent wind field conditions and used to compare wind turbine simulations to field test data. The tower shadow effect was simulated using the conventional Powles model and a new Eames model (developed herein).

With increasing generation of variable renewable energy, the ability to provide energy when demanded by the grid is critical. The standard design metric for renewable energy systems, Levelized Cost of Energy, does not consider the value of energy when it is produced. Herein, a new metric is proposed, the Cost of Valued Energy (COVE), to better account for the time-varying value of energy generation. Energy storage can also be used to meet electrical demand, but further analysis is needed on how to pair energy storage with renewable energy. A techno-economic analysis of Liquid Metal Battery storage located with an offshore wind turbine was completed and found that adding storage can increase the relative value of the combined system.

A low-cost, long-duration energy storage option, such as compressed air energy storage (CAES), is needed to provide sufficient energy stability for a fully renewable electrical grid. Increasing heat transfer during the compression and expansion processes through a method like droplet spray injection can increase the overall system efficiency of CAES. The key nondimensional parameters which control isothermal efficiency of CAES with spray injection are characterized herein, and paired compression and expansion 1-D numerical simulations are used to investigate roundtrip efficiency. A theory-based equation for polytropic index was derived using a new nondimensional number, the Crowe number. High-efficiency direct spray injection designs were identified, and pre-mixed cases were also considered with 1-D and 2-D simulations. Future work is suggested to further improve spray injection CAES modeling and test high-efficiency cases with experiments.

Acknowledgements

First, I want to thank my advisor, Dr. Eric Loth, for his tireless support through the last few years. I know I have challenged you at times, but I really appreciate your willingness to debate and not always agree. I always knew that you would have my back and advocate for my best interests. You really set a high bar for what work I should put out into the world with my name on it. In addition, Dr. Chris Qin gave me enormous support and advising, particularly on the last few chapters, and Dr. Dan Quinn mentored me through an amazing semester of co-teaching Fluid Mechanics. Furthermore, I would like to acknowledge those who supported me through my undergrad at NC State and encouraged my research interests including Dr. Allison Medlin of the Goodnight Scholars program and Dr. Stephen Terry of the Industrial Assessment Center.

I would also like to thank my labmates in FRIL, many of whom do totally different work than I do but have still been supportive. In particular, I would like to thank Meghan Kaminski and Carlos Noyes, who both answered so many questions my first year. All of the graduate students in MEC 116 have also been such a great community, along with the rest of my graduate student friends in the department, particularly those who served on the Graduate Student Board with me. Additionally, I'd like to acknowledge all of the ARPA-E Segmented Ultra-light Morphing Rotor (SUMR) and Segmented Outboard Articulating Rotor (SOAR) teams, who I started graduate school working with, and who taught me so much about research and team work.

Finally, I cannot say thank you enough to my friends and family who have supported me throughout my graduate school journey. My friends and community in Charlottesville (especially those at Rocky Top and the Hill Folk) have truly made this home for me. I also appreciate the continued support of friends outside of Charlottesville, including my best friend Megan. And of course my wonderful family (Mom, Dad, Garrett, Eva, and the Bamji's), always my best cheerleaders.

Table of Contents

Abstract.....	1
Acknowledgements.....	3
Table of Contents.....	4
1. Introduction.....	7
1.1. Motivation and background.....	7
1.2. Objectives.....	10
2. Simulating field test conditions of a downwind turbine for tower shadow analysis.....	12
Abstract.....	12
Nomenclature.....	13
2.1. Introduction.....	13
2.2. Experimental Methods.....	15
2.3. Computational Methods.....	19
2.4. Results and Discussion.....	25
2.5. Conclusions.....	27
3. Influence of tower shadow on downwind flexible rotors: field tests and simulations.....	29
Abstract.....	29
Nomenclature.....	30
3.1. Introduction.....	30
3.2. Experimental Methods.....	33
3.3. Computational Methods.....	35
3.4. Results and discussion.....	44
3.5. Conclusions.....	51
4. Cost of Valued Energy for design of renewable energy systems.....	52
Abstract.....	52
Nomenclature.....	53

4.1.	Introduction.....	53
4.2.	Proposed Model for Price	57
4.3.	Results.....	62
4.4.	Wind turbine design case study	71
4.5.	Conclusions and Future Outlook.....	74
4.6.	Data references.....	75
5.	Techno-economic analysis of Liquid Metal Battery storage in an offshore wind turbine	76
	Abstract.....	76
	Nomenclature.....	77
5.1.	Introduction.....	78
5.2.	Concept Design.....	82
5.3.	Economic Analysis	95
5.4.	Summary.....	104
	Appendix.....	106
6.	Spray-cooled compression: theory and simulation	109
	Abstract.....	109
	Nomenclature.....	110
6.1.	Introduction.....	112
6.2.	Methodology	115
6.3.	Validation against experimental data.....	128
6.4.	Results.....	129
6.5.	Conclusions.....	136
7.	Direct spray injection for Compressed Air Energy Storage compression and expansion.....	138
	Abstract.....	138
	Nomenclature.....	139
7.1.	Introduction.....	141
7.2.	Methodology	143

7.3.	Results and discussion	154
7.4.	Conclusions.....	163
8.	Pre-mixed droplet injection for efficient air compression and expansion: 1-D and 2-D simulations	165
	Abstract.....	165
	Nomenclature.....	166
8.1.	Introduction.....	168
8.2.	Methodology	169
8.3.	Parametric analysis with 1-D model	176
8.4.	1-D vs 2-D simulation comparisons.....	180
8.5.	Conclusions.....	186
9.	Conclusions.....	188
9.1.	Key results	188
9.2.	Contributions to the field	189
9.3.	Future studies and recommendations	190
	References.....	191

Chapter

1. Introduction

1.1. Motivation and background

It is critical that the US and the world shift to a carbon-free electrical grid to reduce the impacts of climate change. The US is working towards that goal, and the US Energy Information Administration's Annual Energy Outlook predicting rising renewable energy generation in the future energy mix.

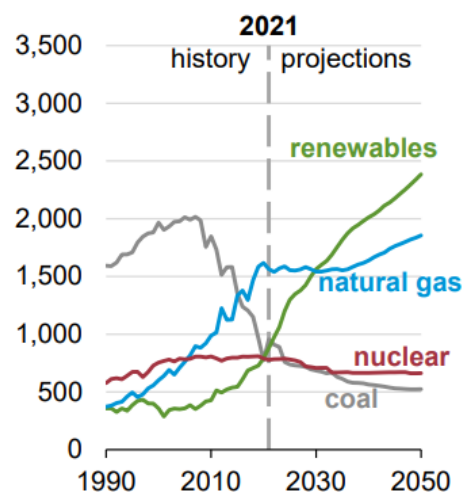


Figure 1-1. US electricity generation by source (in billion kWh) with future projections, from EIA [1].

Continuing to increase renewable generation at the necessary rate shown will require new, innovative renewable generation technology, with a focus herein on wind energy. Globally, wind energy already provides more than a quarter of the electricity consumption in three countries [2] and has already been deployed in many of the best wind resource areas. Potential areas for improvement of wind turbines to access new resource areas include increasing the size of the wind turbines, to increase the energy generation while taking advantage of economies of scale, and tapping into the offshore wind energy resource.

One solution to increasing the size and reducing the cost of wind turbines may be to shift to downwind turbines, where the wind first hits the tower and then the rotor plane (illustrated in Figure 1-2); a number of downwind turbines have been designed recently [3–9]. However, downwind turbines must contend with the “tower shadow” effect, whereby blades experience a change in loading when they pass through the velocity deficit behind the tower. The current tower shadow model in use today has not been

evaluated with experimental field test data, and thus uncertainty remains about the impact of the tower shadow effect on downwind turbines.



Figure 1-2. Downwind turbine schematic with wind direction shown for the SUMR-D rotor on CART-2 at the NREL Flatirons Campus outside Boulder, Co. (base webcam photo courtesy of Lee Jay Fingersh, NREL).

With increasing generation of variable renewable energy, the ability to provide energy when demanded by the grid is critical. Constant power sources, or those that can provide power on demand, therefore are more valuable. Yet it is still standard to design renewable energy systems based on the Levelized Cost of the Energy (LCOE) of the system [10–17], which is the ratio of the annualized total costs of the system and the expected annual energy production. This approach does not take into account the value of the energy produced. To quantify the effect of spot market price variations and the increasing value of meeting grid demand, new metrics have been introduced in the literature, but none have become standard for energy system design. Choosing a metric that can capture both the cost and value of a system is critical to designing an optimal renewable generation system.

While valuing renewable energy sources that better align with grid demand is important, energy storage will also be a vital part of meeting electrical demand as the US transitions to a carbon-free electrical grid. The hourly US electrical generation in different reference cases are shown in Figure 1-3 from the US EIA [1]. Both future reference cases utilize battery and pumped hydro storage for load shifting during the day.

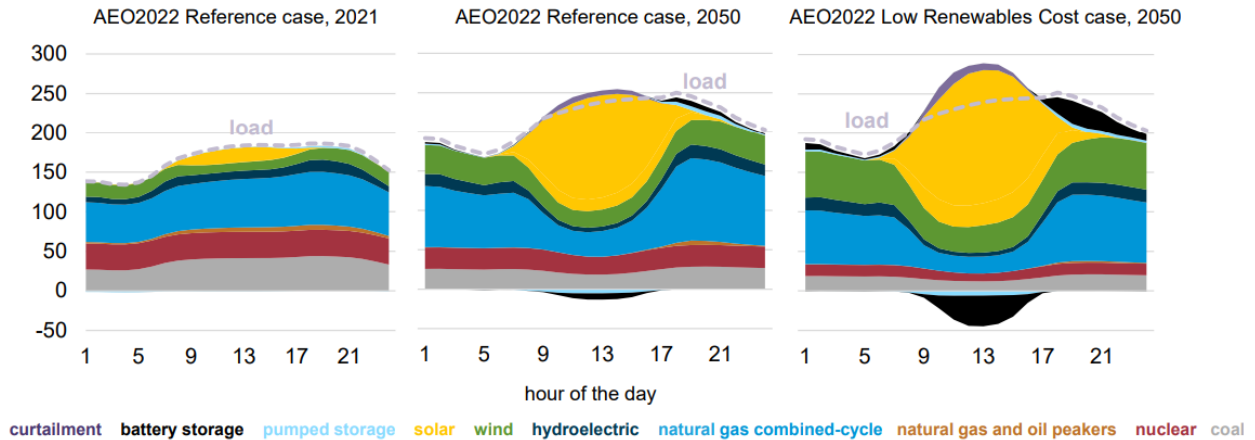


Figure 1-3. Hourly US electricity generation and grid load by fuel source (in billion kWh), from EIA [1].

Analysis will be needed on how to pair energy storage technologies with renewable energy generation to meet grid demand in an economical way. Renewable energy does not always align well with times of electricity demand, and overproduction of renewable energy may even reduce spot market prices. For example, the relative value of wind energy has been found to decrease when it becomes a larger fraction of the grid generation [18,19]. To combat this reduced value, long-duration energy storage can be used to shift generation to times when demand is high [20], but this will require a low-cost energy storage solution which can provide storage for hours or even days. In this future, renewable energy could increase its value significantly by pairing with storage systems, allowing it to participate in capacity markets, energy arbitrage, and auxiliary services.

There are limited options for energy storage, however, and most energy storage options are only able to handle peak loads or inter-day load shifting, as illustrated in Figure 1-3. A sample of energy storage options are shown in Figure 1-4, where it can be seen that battery storage and pumped hydro storage are able to handle short durations at low cost, but compressed air energy storage (CAES) is one of the few energy storage options available for low-cost, long-duration energy storage.

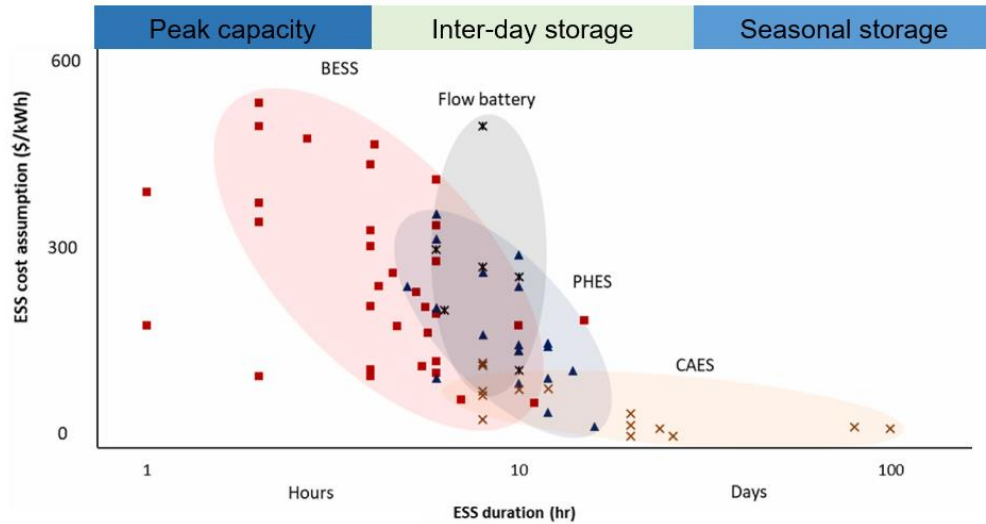


Figure 1-4. Energy storage system (ESS) cost and discharge duration, adapted from [21].

CAES generally suffers from low efficiency relative to batteries and other forms of storage [21], so additional research is needed to increase the efficiency of CAES systems. Increasing the heat transfer during the compression and expansion processes through a method like spray injection can approach isothermal CAES and increase the overall system efficiency without requiring fossil fuels or thermal storage systems. No studies have as of yet considered a fundamental characterization of the key nondimensional parameters which control isothermal efficiency with droplet spray injection. Additionally, the impact of spray work and paired compression and expansion systems for roundtrip efficiency are critical for high-efficiency CAES designs.

1.2. Objectives

The objectives of this dissertation can be broken down into three main thrusts:

1. Downwind turbine modeling (Ch. 2-3)
2. Techno-economic analysis of wind energy and storage (Ch. 4-5)
3. Spray injection for isothermal CAES (Ch. 6-9)

Cumulatively, this dissertation attempts to move the literature one step closer to a carbon-free electrical grid, both in terms of generation technologies (by way of wind turbine modeling) and in terms of energy storage deployment (by way of CAES modeling and techno-economic analysis). The major aims of the research chapters are as follows:

- **Chapters 2-3:** develop a method for modeling field test conditions and quantifying the tower shadow effect, and then compare a newly proposed tower shadow model to the traditional model,
- **Chapter 4:** examine the importance of time-dependent generation value and propose a new metric, COVE, for renewable system design,
- **Chapter 5:** complete a techno-economic analysis of a wind turbine combined with a new form of energy storage, Liquid Metal Batteries,
- **Chapters 6-8:** investigate spray injection for high-efficiency CAES by way of nondimensional compression analysis, roundtrip efficiency, spray work, and direct injection vs. pre-mixed compression.

The main body chapters are written as self-contained research articles, and each contains a brief literature review relevant to that chapter's topic. Finally, Chapter 9 includes a summary, conclusions, and key contributions of this dissertation, as well as recommendations for future work.

Chapter

2. Simulating field test conditions of a downwind turbine for tower shadow analysis

Abstract

Downwind wind turbines may be the future direction of large wind turbines, given their ability to have flexible, lightweight blades with much lower risk of tower strike. However, downwind turbines must deal with the “tower shadow” effect, whereby blades experience a velocity deficit as they pass through the tower wake, resulting in additional bending moments. The tower shadow effect is studied herein using field test data from a novel demonstrator turbine as well as simulations in OpenFAST using the Powles wake model. A method for simulating the turbulent wind field conditions using meteorological tower data is developed and applied to the turbine in operational conditions. The results show that the tower shadow effect is reasonably captured by OpenFAST, and that the strongest tower shadow effects on flapwise operational loads generally occur at wind speeds above the turbine rated wind speed.

Nomenclature

β	=	crosswind angle
ϕ	=	pitch angle
τ	=	shaft tilt
θ_T	=	twist angle
C_D	=	drag coefficient
d	=	distance (m)
I_t	=	turbulence intensity
M	=	bending moment (kN-m)
r	=	tower radius (m)
u_{wake}	=	nondimensional wind speed deficit
u	=	nondimensional wind speed, x-direction
U	=	wind speed, x-direction (m/s)
V	=	wind speed, y-direction (m/s)
W	=	wind speed, z-direction (m/s)
x	=	nondimensional distance, x-direction
X	=	distance, x-direction (m)
y	=	nondimensional distance, y-direction
Y	=	distance, y-direction (m)
$(\bar{\quad})$	=	average

Subscripts

∞	=	undisturbed flow
B	=	blade
EW	=	edgewise
FAST	=	OpenFAST
FW	=	flapwise
L	=	local airfoil
local	=	local wind
IP	=	in plane
met	=	meteorological tower
OoP	=	out of plane
X	=	X-direction
Y	=	Y-direction

2.1. Introduction

Wind energy produced 8.3% of U.S. electrical energy in 2020, and the average wind turbine capacity, rotor diameter, and hub height all continue to grow each year [22]. While larger wind turbines are often economically attractive, as they tend to have a reduced levelized cost of energy, they also have a greater risk of tower strike, where high loads force the blades to bend backwards until they strike the tower. The structural requirements to prevent these deflections lead to an increase in blade mass and cost, an issue that is exacerbated as turbines get larger and blades get more flexible. One solution to reduce blade mass (which reduces overall turbine cost) is to employ downwind turbines, where the wind first hits the tower

and then the rotor plane, deflecting the blades away from the tower and reducing tower strike risk. While not currently commercially produced, a number of downwind turbines have been designed recently, with increasingly large rotors [3–9]. Because of their potential benefits, especially as turbine sizes get larger, downwind turbines may be more commonplace in the future due to their ability to produce lighter rotors and thus less costly designs [23–25]. A new generation of large downwind turbine designs would likely include highly flexible blades [26]. When designing these flexible wind turbine rotors, it is important to include a high-temporal- and high-spatial-resolution 3-D turbulent wind field with shear since the field has a significant effect on the turbine response and loads [27].

However, a key question regarding downwind turbines is the influence of the “tower shadow” effect on transient blade loads. The effect occurs when the blades pass through the wake of the tower and experience a velocity deficit leading to a sudden change (typically a drop) in lift and therefore flapwise loads, shown in Figure 2-1. If this load unsteadiness is severe, it can cause increased blade fatigue. The degree of influence of tower shadow on blade loads is a strong function of blade flexibility [28]. Therefore, it is important to understand this effect for flexible blades on large turbines so that they can be optimally designed. To decrease the effect of tower shadow, previous studies have investigated the use of tower fairings as compared to a standard cylindrical tower, but only at lab scale [29]. Models for tower shadow effect have been developed, but these are generally based on a steady-state wind velocity deficit for the tower wake, so it is difficult to determine their fidelity for field operation. To date, there have been no published experimental field test data results for downwind flexible blades that evaluate the performance of tower shadow models and demonstrate the tower shadow effect. Previous work studying the tower shadow effect has focused on wind tunnel data from the Unsteady Aerodynamics Experiment (UAE) Phase VI downwind turbine with stiff blades [30], which did not include field testing, flexible blades, or a large cone angle.

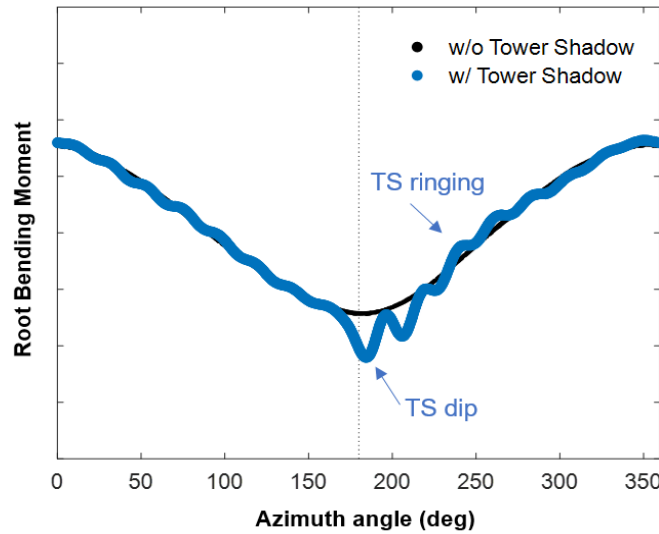


Figure 2-1. General effect of tower shadow (TS) on wind turbine blade root bending moment in steady wind, plotted versus azimuth angle. The tower shadow effect tends to significantly reduce root bending moments after passing the tower at 180° and then results in residual ringing in the blade.

The objectives of this study are threefold: 1) post-process field test measurements of a downwind turbine with flexible blades consistent with that of large turbines [31,32], 2) develop a method for replicating the field test conditions for computational simulation comparison, and 3) compare field test data to simulation predictions of blade bending moments. To the author’s knowledge, this is the first reported turbine field test with a downwind rotor that has flexible blades consistent with large-scale turbines (e.g., a rated power greater than 10 MW) to consider the impact of tower shadow on blade root bending moments. It is also the first to establish a numerical approach that converts the measured inflow wind field into an unsteady 3-D numerical field for simulated aeroelastic response. The field test data, the wind field simulation method, and the resulting tower shadow model assessment can all be important in helping design future generations of extreme-scale downwind turbines.

2.2. Experimental Methods

A novel two-bladed downwind rotor concept was developed known as the Segmented Ultralight Morphing Rotor (SUMR-13) with a 13 MW rated power design [3,7,33]. The SUMR-13 concept has two lightweight, flexible blades in a coned downwind configuration. A demonstrator rotor at one-fifth scale designated as the SUMR-Demonstrator turbine (SUMR-D) was designed and built with gravo-aeroelastic scaling methods [5,32,34,35] to replicate the full-scale 13 MW SUMR blade aeroelastic effects, with details in Table 2-1. In particular, the SUMR-D blade was specifically designed to have nondimensional blade flexibility, nondimensional flapwise deflections, and nondimensional dynamics (tip speed ratio, ratio of flapwise frequency to rated rotational frequency, etc.) that are consistent with the SUMR-13 design

[31,32,36]. The SUMR-D rotor was installed on the Controls Advanced Research Turbine (CART2) at the National Renewable Energy Laboratory's (NREL) Flatirons Campus near Boulder, Colorado. The blade design and fabrication was required to account for the NREL wind turbine testing guidelines and site conditions (where wind can reach up to 45 m/s). The high wind conditions were accommodated by increasing the blade stiffness while ensuring the mean and root mean square (rms) of the nondimensional blade deflection (normalized by blade length) were generally maintained for winds between 50% and 200% of the rated wind speed. The design and test setup of the SUMR-D turbine are detailed in [35].

Table 2-1 SUMR-D Parameters

Metric	Value
Blades	2
Rotor radius	22.25 m
Tower diameter	2.2 m
Hub height	36.6 m
Blade mass	990 kg
Flapwise frequency	1.13 Hz
Tip speed ratio	9.5
Coning angle	12.5°
Tilt angle	3.77°
Cut-in wind speed	3 m/s
Rated wind speed	5 m/s
Cut-out wind speed	11 m/s

The NREL Flatirons Campus wind conditions wind rose is shown in Figure 2-2, sampled from 2014 to 2017 at the CART2 meteorological (met) tower. The strong prevailing wind direction at 292° (based on wind flow through a nearby canyon) allowed for an upwind met tower (along the same direction) to capture incoming wind characteristics.

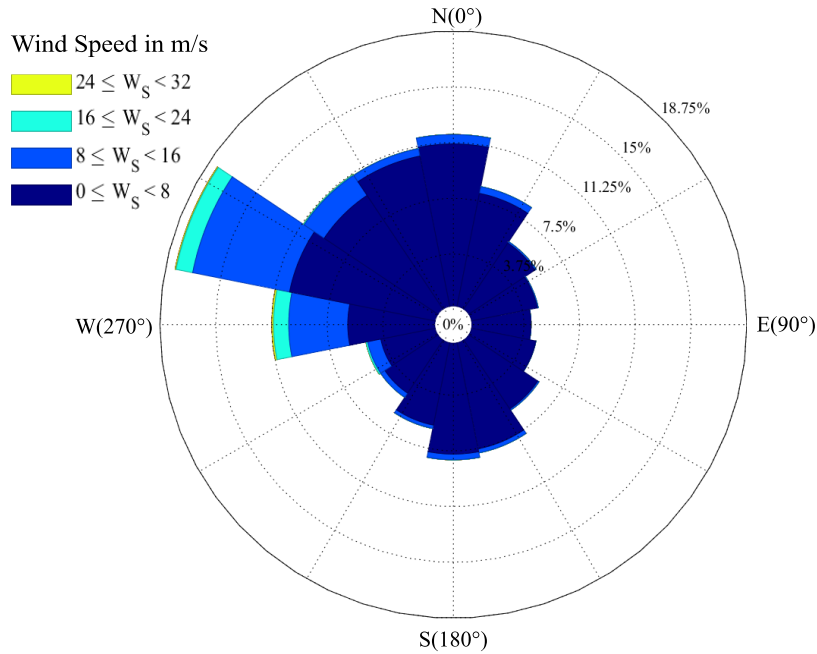


Figure 2-2. Wind rose with 1-minute average wind speed (m/s) and direction at 50 m from 2013 to 2017 for December to June at National Renewable Energy Laboratory Flatirons Campus [37]

NREL engineers collected turbine field test data during fall 2019 and spring 2020. Wind speed and direction are most consistent during these seasons and therefore allow for full test matrix capture. The CART2 data collection system outputs continuous 5-minute data files, sampling data at 400 Hz, which includes but is not limited to rotor speed, rotor azimuth angle, nacelle yaw, and blade pitch. The SUMR-D rotor, mounted on the CART2, was outfitted with strain gauges in both the flap and edge directions near the root (at 48 cm outboard of the root) and approximately mid-span (at 13.2 m outboard of the root). The hub height of the CART2 is 36.6 m. A meteorological tower is located 86 m upwind of the turbine and recorded key inflow conditions. Cup anemometers at multiple heights (15 m, 36 m, 58 m) on the tower measure wind speed for wind shear estimates and a sonic anemometer at hub height measures wind velocity in three directions. The ability to accurately model vertical wind shear in simulations is important since wind shear is known to have multiple effects on turbines, including increasing bending moments of upwind turbines [27] and decreasing the tower shadow effect on blade loads of downwind turbines [38]. Using the inflow wind direction, the nacelle yaw error (turbine direction relative to that of the incoming wind) was also recorded at the CART2 turbine. The horizontal turbulence intensity (I_t) of the horizontal wind speed time-series (U_{horiz}) at the CART2 test site was calculated based on the following equations, using x-direction (U_{met}) and y-direction (V_{met}) data from a three-directional sonic anemometer.

$$U_{horiz} = \sqrt{U_{met}^2 + V_{met}^2} \quad (2-1a)$$

$$\sigma_{U,horiz} = \sqrt{\frac{1}{N} \sum_{i=1}^N (U_{horiz,i} - \overline{U_{horiz}})^2} \quad (2-1b)$$

$$I_t = \frac{\sigma_{U,horiz}}{\overline{U_{horiz}}} \quad (2-1c)$$

The turbulence intensity is calculated as the ratio of the standard deviation about the mean of instantaneous horizontal wind speed ($\sigma_{U,horiz}$) to the mean horizontal wind speed ($\overline{U_{horiz}}$). The turbulence intensity for the wind input files seen by the demonstrator turbine is representative of common field turbulence, as seen in Fig. 2-3 with representative lines for International Electrotechnical Commission (IEC) Class A, B, and C wind fields.

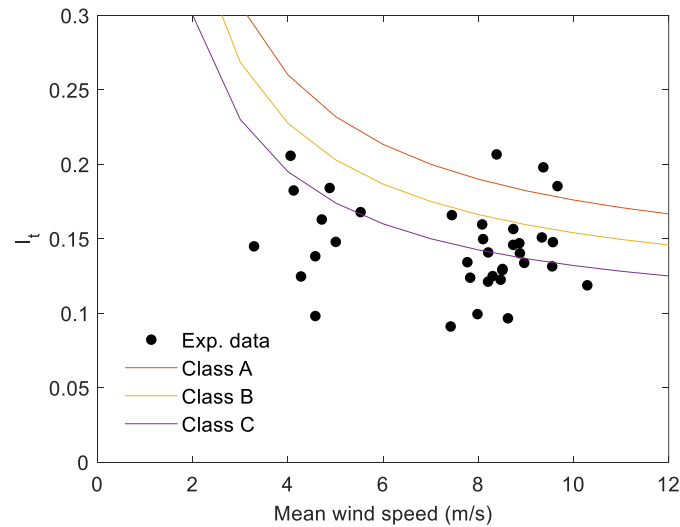


Fig. 2-3 Turbulence intensity of each 5-minute field test data set versus mean wind speed. IEC wind turbulence classes provided for reference [39]. Adapted from Simpson et al. [40].

2.3. Computational Methods

A. Tower Shadow Models

One of the most prevalent tower shadow models used for wind turbines is the Powles velocity deficit model, which was developed based on wind tunnel tests for an isolated tower [38]. The Powles model is the primary option used in OpenFAST, a commonly employed simulation tool developed by NREL for the modeling and design of wind turbines [41]. The original Powles model allowed shadow width and depth to be independent variables in order to predict the wake characteristics. In the current aerodynamic module of OpenFAST, AeroDyn15 [42], the shadow width and depth are determined in combination based on an input tower drag coefficient (C_D) prescribed by the user [43]. The relationship for the local wind velocity behind the tower (U_{local}) is reduced by a nondimensional fraction (u_{wake}) relative to the undisturbed velocity at the tower plane that excludes the tower disturbance (U_∞). The nondimensional wake deficit is related to the dimensionless wake distance (d), which is measured from a location in the wake to the tower center and is defined using the dimensionless x and y positions. These x and y positions are based on the dimensional streamwise and spanwise directions (X and Y) referenced to the tower center and normalized by tower radius (r) as

$$U_{local} = (1 - u_{wake}) U_\infty \quad (2-2a)$$

$$u_{wake} = \frac{C_D}{\sqrt{d}} \cos^2 \left(\frac{\pi}{2} \frac{y}{\sqrt{d}} \right) \quad (2-1b)$$

$$d = \sqrt{(x^2 + y^2)} \quad (2-1c)$$

$$x = X/r \quad (2-1d)$$

$$y = Y/r \quad (2-1e)$$

In these expressions, the X coordinate is downwind (in the direction of the local undisturbed velocity (U_∞)) and the Y coordinate is perpendicular in the cross-sectional plane as shown in Figure 2-4. The wake unsteadiness effects due to turbulent shedding are not included in this model.

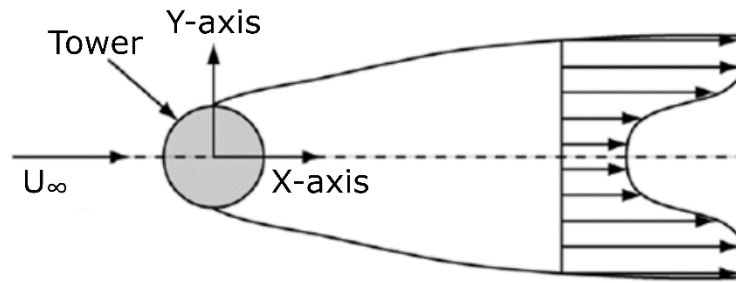


Figure 2-4. Diagram of tower shadow parameters from AeroDyn theory manual [43]

B. OpenFAST Model for SUMR-D

Simulations of the SUMR-D wind turbine were completed in the current version of OpenFAST [41]. A “Digital Twin” model of the SUMR-D rotor was used in the simulations and is further documented in Chetan et al. [44]. The SUMR-D model uses the as-designed airfoils, which likely results in some small deviations from the as-built airfoils flown on the CART2 during the experiment. Aerodynamics simulations in OpenFAST were completed using the AeroDyn15 module with the tower shadow velocity deficit using the Powles model (Eq. 2-2) turned on. The tower drag coefficient was set to 0.7 at all stations along the tower length based on supercritical cylinder drag [45]. To compare OpenFAST simulations to the root bending moment data available from the CART2, OpenFAST blade bending moments were output at a node located at approximately 48 cm, the location of the strain gauges on the experimental setup.

C. Generating Turbulent Wind Field Files

TurbSim v2 was developed by NREL [46] and used herein to simulate 3-D turbulent wind field files to represent the field testing conditions as closely as possible. TurbSim v2 allows for time-series wind speed input in three directions, along with other wind field parameters. For each field test turbine data file, the wind field conditions were used to build a comparable TurbSim file for use in OpenFAST simulations. The three-directional sonic anemometer data from the met tower at 36 m was used as the time-series wind speed input to build the wind field files.

The time series of the horizontal wind components measured by the sonic anemometer are defined as U_{met} and V_{met} wind speeds, which are in the X_{met} and Y_{met} directions, where X_{met} is the coordinate that is along the direction of the met tower toward the turbine (seen in Figure 2-5). For consistent simulations over a range of inflow angles, it is important to rotate these velocities into a coordinate system that is aligned with the mean flow. Therefore, the horizontal wind components were rotated so that the computational inflow direction for OpenFAST aligned with observed mean wind flow direction (eliminating mean

crosswind in the wind field file). The OpenFAST input wind field has a mean inflow angle that aligns with U-direction flow, and crosswinds are accounted for by setting a yaw error that corresponds to the field test inflow conditions. To accomplish this, the mean crossflow angle relative to the met tower direction (β) was obtained and used to define rotated time-series wind speeds (U and V) in the OpenFAST coordinate system (X and Y). Figure 5 shows the original and rotated coordinate systems.

$$\beta = \text{mean} \left[\tan^{-1} \left(\frac{V_{met}}{U_{met}} \right) \right] \quad (2-3)$$

$$U = \cos(-\beta) U_{met} - \sin(-\beta) V_{met} \quad (2-4a)$$

$$V = \sin(-\beta) U_{met} + \cos(-\beta) V_{met} \quad (2-4b)$$

$$W = W_{met} \quad (2-4c)$$

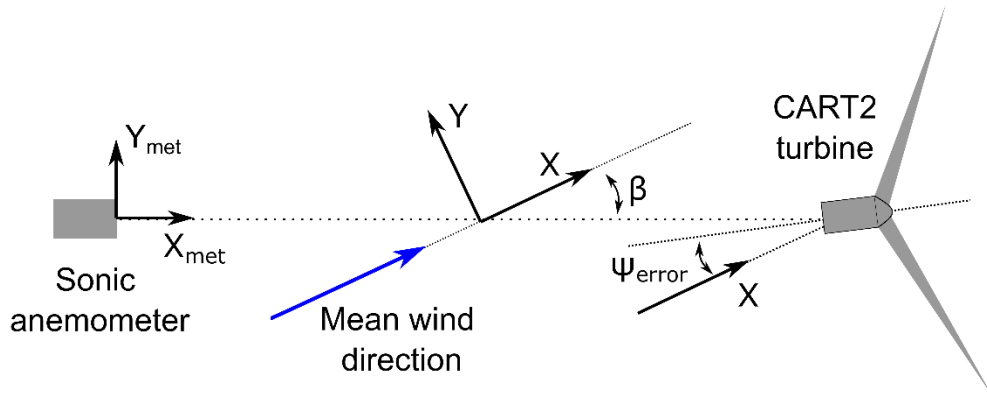


Figure 2-5. Wind field coordinate systems for a hub-height horizontal plane at the wind site showing the velocity components at the sonic anemometer and those used for OpenFAST, which are rotated to be consistent with the mean wind speed, while the yaw error is based on the difference between the instantaneous wind velocity direction and the turbine hub axis.

The nacelle yaw error (ψ_{error}) is based on the difference between the instantaneous wind direction and the hub axis of the turbine. Since the turbine yaw angle was often influenced by the wind field conditions before the start of each data set, and only data sets with less than 10° of yaw range were simulated, the simulated turbine yaw was fixed at the *average* measured nacelle yaw error of the CART2 turbine for a given simulation to ensure similar variations for the unsteady inflow wind angles. The rotated

3-D wind speed time series was also down-sampled from 400 Hz to 20 Hz to reduce computational time and memory.

An example 100 s of wind speed data are plotted in Figure 2-6, showing the meteorological tower velocity components (U_{met} and V_{met}) and those used in the OpenFAST simulation (U_{FAST} and V_{FAST}). While the combined wind speed is held constant, the U and V wind directions for the OpenFAST simulations were both rotated such that V_{FAST} has an average speed of zero and U_{FAST} is the mean wind direction. As such, the rotated OpenFAST wind field captures both the mean wind speed and time-dependent variations of the CART2 wind field data.

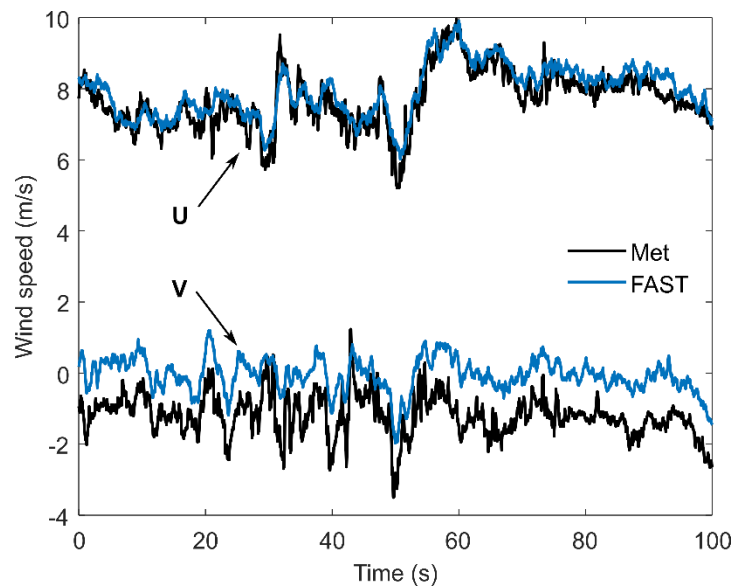


Figure 2-6. Wind speed time series from CART2 met tower (black) and used for OpenFAST (blue) where U and V directions are rotated so there is zero mean crosswind (V_{FAST} averages to zero).

Each time series data set from the CART2 was 300 s long. However, it is common to remove the first 100 s or so of an aeroelastic simulation to eliminate the influence of initial conditions and numerical transients. Therefore, an additional 100 s of “dummy” wind speed data were added to the beginning of the 300 s of true time series data. These dummy data are used to initialize the simulation and then are removed before data analysis. To ensure that these additional data have similar turbulence characteristics and do not have any discontinuities at the interface with the true 300 s data, the dummy data are reflected in time relative to the interface time (at $t_0=100$ s). For example, the U component used for OpenFAST as a function of time is given as

$$U_{FAST}(t) = U(t) \quad \text{for } 100 \text{ s} \leq t \leq 400 \text{ s} \quad (\text{true data}) \quad (2-5a)$$

$$U_{FAST}(t) = U(2t_0 - t) \quad \text{for } 0 \text{ s} \leq t \leq 100 \text{ s} \quad (\text{dummy initial data}) \quad (2-5b)$$

Similar time reversals were used for the V and W data sets. The FAST cases were then run starting at t=0 s but only the data for 100 s ≤ t ≤ 400 s was used to evaluate the tower shadow effect.

The mean wind shear was found by fitting a power law curve to the mean wind speeds from the 15 m, 36 m, and 58 m cup anemometers on the upstream met tower, which provides the gradient in the mean wind velocity as given in Figure 2-7a. The rotated wind time series, wind shear, average wind speed, and a random seed for each run were input to TurbSim v2 to provide the unsteady wind field files for each wind speed component as shown by Figure 2-7b.

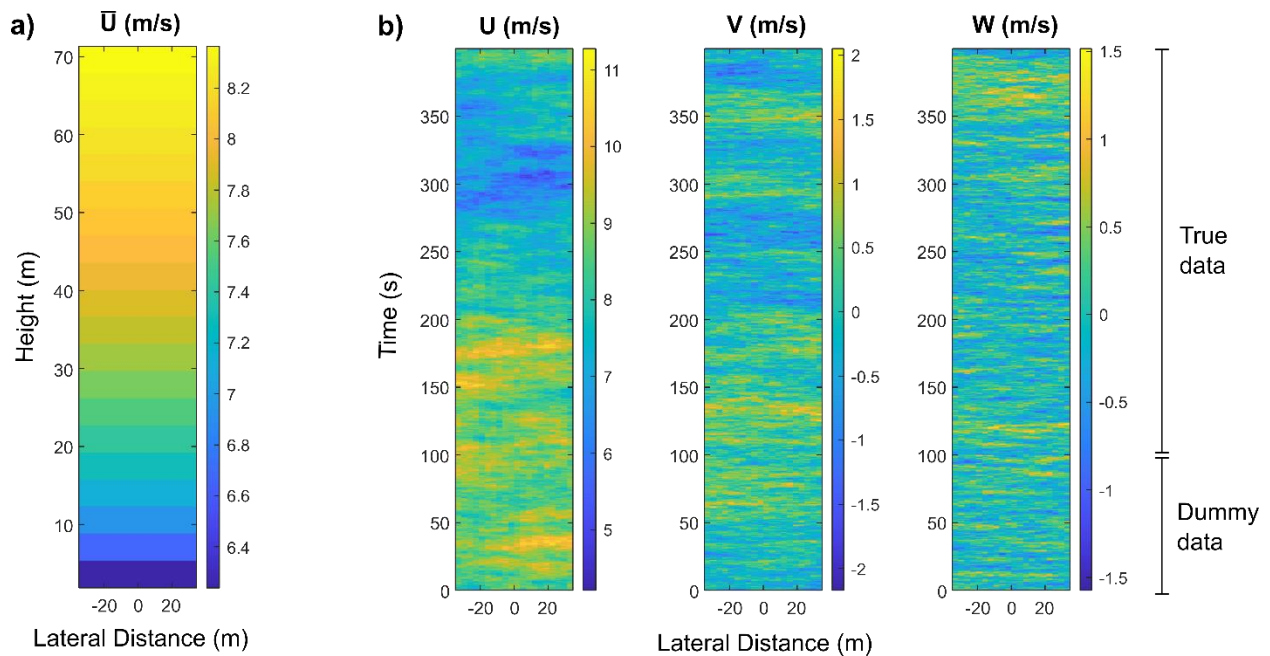


Figure 2-7. TurbSim generated wind field files derived from CART-2 sonic anemometer wind data from upstream met tower, where a) shows the mean wind speed (\bar{U}) at the rotor plane indicating vertical shear, and b) shows the U, V, and W components of wind speeds at the hub height as a function of time and lateral distance. The first 100 s of “dummy” data are used to initialize the simulation where there is reflected symmetry of the input data about 100 s, but the simulated data is otherwise random.

D. Blade Coordinate Transformations

The bending moment data from the experimental CART2 turbine and from OpenFAST simulations use different coordinate systems and must be transformed into a consistent coordinate system for comparison. Further documentation on the coordinate systems used herein can be found in the OpenFAST User Guide [47]. The CART2 blade strain gauges are oriented with the blade coordinate system, as in Figure 2-8a. Since the root of the blade is nearly circular in cross section, the root coordinate system is defined based on an outboard airfoil with zero twist. The output OpenFAST bending moment data at nodes along the blade (like at 48 cm) are based on the local airfoil coordinate system, which includes significant twist near the root of the blade, as in Figure 2-8b. In particular, the experimental and computational bending moments were both converted into in-plane and out-of-plane moments (M_{IP} and M_{OoP}), which are defined relative to the rotational plane defined by the rotor (perpendicular to the rotor hub axis). For the CART2 data, the root flapwise and edgewise bending moments of the blade coordinate system (M_{FW} and M_{EW}) are converted to M_{IP} and M_{OoP} via the blade pitch (ϕ , of Figure 2-8a) as

$$M_{OoP} = M_{FW} \cos(\phi) - M_{EW} \sin(\phi) \quad (2-6a)$$

$$M_{IP} = M_{EW} \cos(\phi) + M_{FW} \sin(\phi) \quad (2-6b)$$

When considering the moments at an outboard airfoil station, one must consider the local airfoil coordinates (X_L and Y_L) where Y_L is defined to be along the blade chord length which rotates with local twist (θ_T) as shown in Figure 2-8b. The local bending moments defined with these coordinates ($M_{X,L}$ and $M_{Y,L}$) can be transformed to In Plane (IP) and Out of Plane (OoP) moments based on the pitch and the local twist as

$$M_{OoP} = M_{Y,L} \cos(\theta_T + \phi) - M_{X,L} \sin(\theta_T + \phi) \quad (2-7a)$$

$$M_{IP} = M_{Y,L} \sin(\theta_T + \phi) + M_{X,L} \cos(\theta_T + \phi) \quad (2-7b)$$

The local twist at 48 cm outboard on the blade is 34.3°.

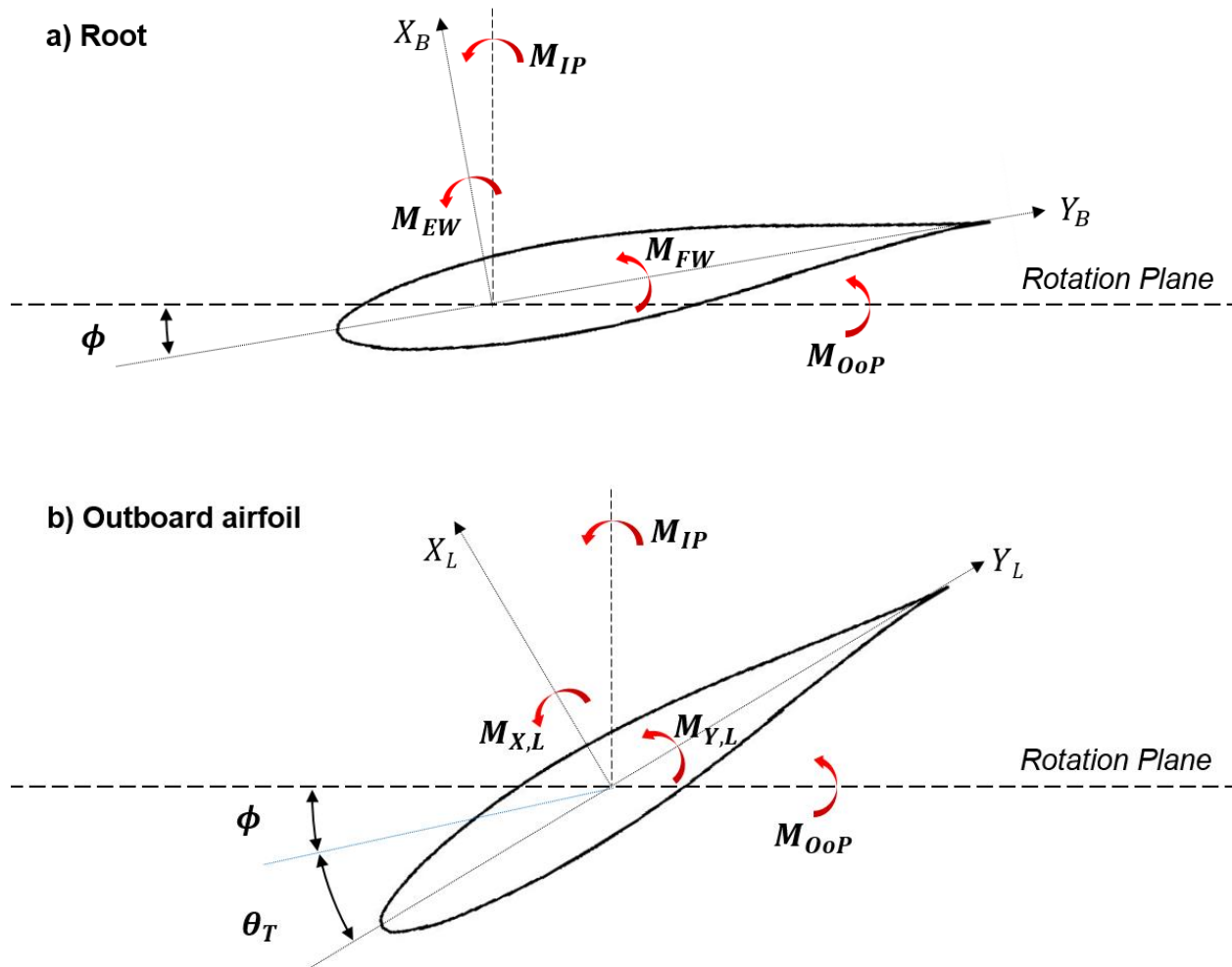


Figure 2-8. Diagram of different coordinate systems and axes for bending moments referenced a) at the root with the rotor blade coordinate system (X_B and Y_B) which depends on blade pitch (ϕ), and b) for an outboard airfoil along the span with local airfoil coordinate system (X_L and Y_L) which further varies due to local twist (θ_T).

2.4. Results and Discussion

Typical results comparing SUMR-D field test data from the CART2 to OpenFAST simulations are displayed in Figure 2-9 for a range of mean wind speeds. Since the rated wind speed for this scaled turbine is approximately 5 m/s (based on gravo-aeroelastic scaling), Figure 2-9a-b are below rated conditions (Region 2 operation) while Figure 2-9c-d are above rated conditions (Region 3 operation). Time-series bending moment data from the unsteady field test and simulation are plotted versus blade azimuth angle for each 5-minute interval. In addition, azimuthal averages (whereby all data at a given azimuthal angle are

averaged together) for the same interval are shown by the black solid line for CART2 data and by the blue dashed line for OpenFAST predictions.

Considering first the experimental data, the tower shadow effect is more apparent in Region 3 (Figure 2-9c-d) than in Region 2, as evidenced by the larger relative dip occurring at an azimuthal angle of 180°. This indicates that the design impact of tower shadow may need to focus on Region 3 conditions.

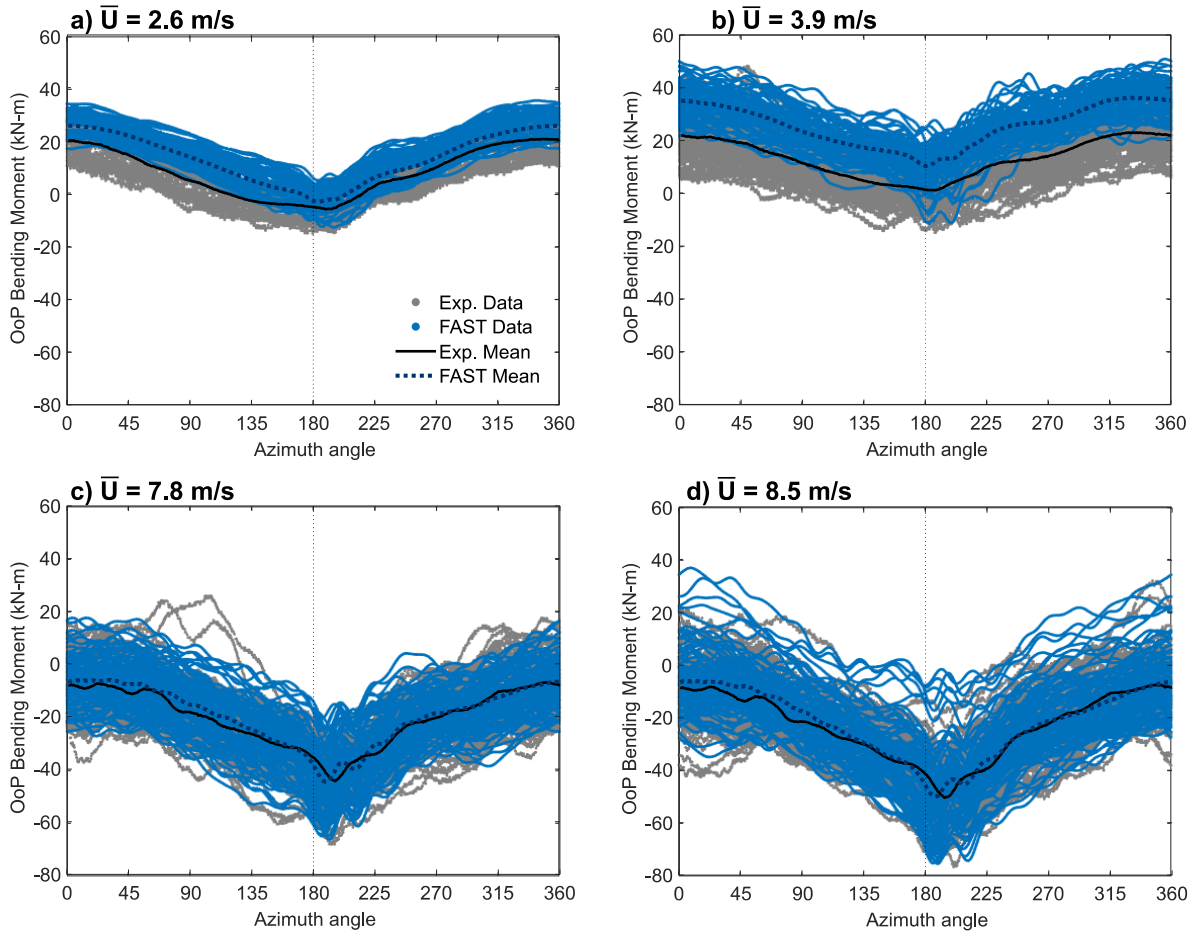


Figure 2-9. Blade 1 out-of-plane (OoP) bending moment data and azimuth-averaged mean for SUMR-D from experimental field test (blue, dashed) and OpenFAST simulations with comparable wind field (gray, solid). Each graph contains 5 minutes of data, with (a,b) below rated wind speed and (c,d) above rated wind speed. The location of the tower at 180° azimuth angle is denoted with a dotted vertical line.

The OpenFAST simulations generally capture the mean out-of-plane bending moments of the field test data in terms of the azimuthal averages as well as the general degree of variations about these azimuthal averages. In most cases, the mean bending moments are similar between simulations and experiments, indicating that the OpenFAST model for SUMR-D is a good representation of the real rotor. However, there are some significant differences between OpenFAST simulations and the experiments, in terms of both the

azimuthally averaged moments (e.g., the large offset in Figure 2-9b) and the fluctuations about those averages for instantaneous dynamics.

In Region 2, OpenFAST overpredicts the azimuthally averaged tower shadow dip compared to the experimental CART2 data. Limited wind field data, particularly in this turbulent setting, may be resulting in inaccurate wind field simulations. In addition, Simpson et al. [40] noted that OpenFAST tower shadow predictions should consider uncertainty associated with tower drag coefficients since the Reynolds numbers place this flow in the critical drag regime, which may be another cause for an overprediction of tower shadow dip in Region 2.

In Region 3, the magnitude of the azimuthally averaged tower shadow dip after passing the tower is reasonably captured by the OpenFAST simulations, but there are differences in the “ringing” of the blade (the oscillations of the black solid and black dashed lines in Figure 2-9c-d). In particular, the experimental data has a less-sharp moment return after the original dip, but continues to have significant oscillations to 360°, whereas the OpenFAST predicted oscillations are largely damped by 300°. Furthermore, the experimental ringing continues after passing 0° and is generally enhanced at that point (which is attributed to the time the opposite blade passes behind the tower). This indicates that the SUMR-D rotor may be less damped and more strongly coupled than predicted by OpenFAST. The differences indicate that the actual overall structural dynamics of the rotor are more complex and more coupled than modeled.

In terms of the fluctuations about the azimuthally averaged moments, the OpenFAST simulations generally predict similar data spreads as seen in the experiments. However, the predictions could be further improved by providing time-series wind speed data at more points in the wind field to better train the 3-D TurbSim wind field to match the test conditions.

2.5. Conclusions

Data from a field turbine test with a rotor that has flexible blades and a cone angle consistent with large-scale (>10 MW) downwind turbines were obtained to investigate the impact of tower shadow on blade root bending moments. In addition, a numerical method was developed herein to represent the turbulent wind conditions for field test operation within the OpenFAST framework as an unsteady 3-D numerical field for simulated aeroelastic response. This procedure could be used to create high-fidelity turbulent wind field files for other field test comparisons, though it is recommended that wind speed time series data are gathered at multiple locations to improve the fidelity of the wind field file. The tower shadow effect was assessed on a downwind demonstrator turbine by comparing OpenFAST simulations, using the Powles tower shadow model, to field test data in terms of out-of-plane bending moments. Though the effect of tower shadow can be difficult to see among inflow turbulence for the instantaneous data set, the model

appears to qualitatively capture the tower shadow effect in Regions 2 and 3 for the azimuthally averaged profile. These results indicate that the OpenFAST model can generally predict the effects of tower shadow, though further improvements to the wind field modeling and the structural model of the rotor (including blade and tower coupling) may increase the fidelity of the results.

Chapter

3. Influence of tower shadow on downwind flexible rotors: field tests and simulations

Abstract

As wind turbine rotors become larger, the blades become more flexible, requiring extra stiffness and cost to avoid the risk of tower strike. Wind turbines in a downwind configuration have a reduced risk of tower strike because the rotor thrust acts away from the tower. However, downwind blades pass through the wake of the tower and the resulting load variation may contribute to blade fatigue. To date, there have been no field tests to quantify this tower shadow effect on unsteady blade moments. The present study reports on the first field testing of a flexible, downwind, coned rotor and compares the experimental data against simulations run in OpenFAST. The tower shadow effect is simulated using the conventional Powles model and a new Eames model (developed herein), which includes the influence of upstream turbulence. Both models reasonably predict the blade root out-of-plane bending moment data and the tower shadow dip magnitude when compared to field test data in Region 3. Tower shadow was found to increase the short-term Damage Equivalent Loads (DEL) by less than 10% compared to other effects (gravity, shear, and turbulence), and the predictions were consistent with experiments. These results indicate that the tower shadow effect can be reasonably modeled with simpler Powles model and that the tower shadow effect can be small compared to the effect of turbulence. However, long-term fatigue due to tower shadow should be included in detailed structural analysis and design of the rotor and the tower.

Nomenclature

σ	=	standard deviation
μ	=	overall mean wind speed
C_D	=	drag coefficient
d	=	distance
I_t	=	turbulence intensity
r	=	tower radius
Re	=	Reynolds number
u_{wake}	=	wind speed deficit, non-dimensionalized by U_∞
u	=	x-direction wind speed, non-dimensionalized by U_∞
U	=	wind speed, x-direction
V	=	wind speed, y-direction
W	=	wind speed, z-direction
x	=	x-direction distance, non-dimensionalized by r
X	=	distance, x-direction
y	=	y-direction distance, non-dimensionalized by r
Y	=	distance, y-direction
$\overline{(\quad)}$	=	average
$\hat{(\quad)}$	=	predicted value
$(\quad)_\infty$	=	undisturbed wind flow (far upstream of the turbine)
$(\quad)_{local}$	=	local wind speed
$(\quad)_{up}$	=	wind speed just upwind of the tower

3.1. Introduction

Offshore wind turbines are becoming more common with global offshore wind installations growing each year [48]. While there are currently only 42 MW of commercial wind energy operating offshore in the US, the cumulative installed offshore wind capacity in the US is expected to be 11 GW or higher by 2030[48]. In general, offshore turbines are being designed with high turbine power (≥ 10 MW), such as the General Electric Haliade-X turbine which ranges from 12 MW to 14 MW rated power. These larger wind turbines are able to reduce the cost of energy by taking advantage of economies of scale. However, these large blades are inherently more flexible and thus upwind rotors run an increased risk of tower strike, where the blades may bend backwards during operation (due to aerodynamic thrust forces) and contact the tower. Downwind turbines can reduce the risk of tower strike because the thrust forces drive the blades away from the tower, and thus downwind turbines may provide an opportunity for increasing rotor diameter with lightweight blades [49–51].

While downwind turbines are advantageous to increasing the rotor diameter, there is an aerodynamic disadvantage which must be considered. As the blades pass behind the tower, they experience the tower shadow effect in the tower wake, as shown in Figure 3-1. The blades undergo a velocity deficit in the tower wake compared to the undisturbed incoming air velocity, and the resulting unsteady

aerodynamics can lead to blade fatigue and noise. Downwind turbine designers should generally consider three critical issues:

- 1) Aerodynamic performance and rotor mass: Downwind turbines (compared to upwind turbines) tend to have lower rotor masses due to flapwise load alignment but can have a reduction in annual energy production due to a decreased swept area caused by downwind aeroelastic deflections [52,53].
- 2) Low-frequency noise: Downwind turbines have been known to emit a low-frequency “thumping” noise that is louder than upwind turbines[54]; this can be an important issue for onshore wind farms (but may be less of an issue for offshore wind farms).
- 3) Fatigue: Increased structural fatigue for downwind turbines due to tower shadow has been identified as a potential issue that should be considered in structural design[52], but it is unclear if the current wake deficit models for tower shadow can capture the unsteady blade load impact for field conditions.

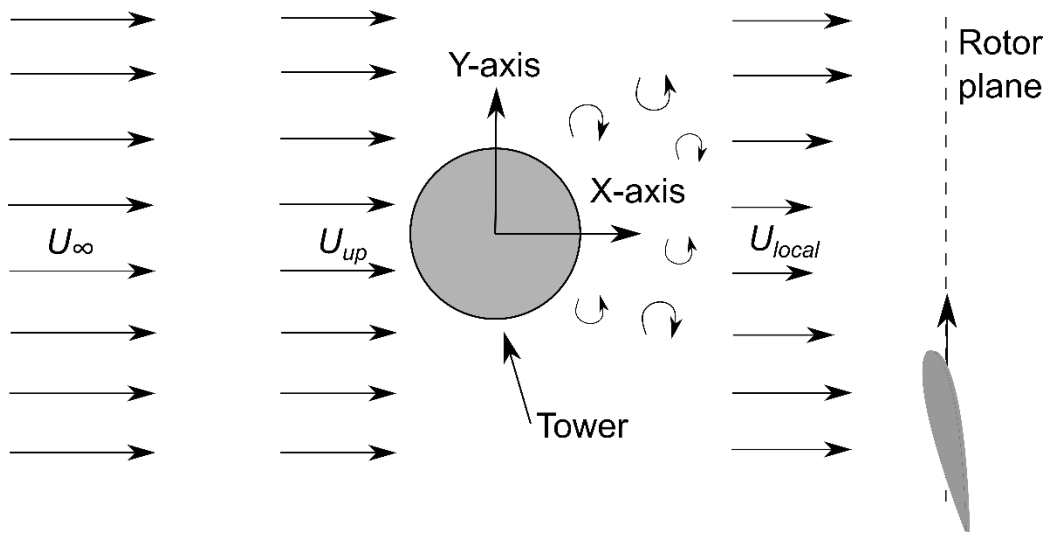


Figure 3-1. Downwind turbine tower shadow diagram, where freestream wind (U_{∞}) is reduced at the tower plane to (U_{up}) and then the rotor plane sees U_{local} with a velocity deficit behind the tower and a complex wind field.

There has been little experimental data to analyze the tower shadow effect on downwind turbines. Previously, the only publicly available dataset from a downwind turbine field test was from the Unsteady Aerodynamics Experiment (UAE) turbine developed and tested by the National Renewable Energy Laboratory (NREL). The UAE turbine Phase VI was a downwind turbine with stiff blades, tested at the NASA Ames Research Center wind tunnel [30]. Hitachi tested the SUBARU 80/2.0 2 MW downwind turbine [55,56], but have not published in full the field test data. Wind tunnel tests by Wang *et al.* visualized

the flow field behind a downwind turbine, but did not capture blade bending moment data [57]. No field test data exists for flexible downwind rotors, a current design direction of large wind turbines, which are expected to react differently to the tower shadow effect than stiff rotors. Without experimental data, tower shadow models are difficult to validate.

Since there have been no previous field experiments for flexible rotors, the influence of tower shadow for large downwind systems has been based on wind tunnel tests and simulations. In such simulations, tower shadow only appears to marginally increase blade fatigue[58], and the trends indicate that the effect is reduced for lighter and more flexible blades[59].

To provide experimental data to compare with numerical tower shadow models, a 1/5th-scale gravo-aeroelastic model was developed based on the Segmented Ultralight Morphing Rotor 13-MW (SUMR-13) turbine and is denoted as the SUMR Demonstrator (SUMR-D) [60–62]. The SUMR-13 turbine was designed as a flexible, downwind, load-aligned rotor [49,50,53,63]. This design showed that the rotor mass and the swept area are both reduced as is common for downwind turbines, but that the combination can reduce LCOE. The SUMR-D demonstrator turbine allows for the first field test data of a downwind flexible rotor. In terms of low frequency noise, NREL turbine operators standing outside reported minimal audible noise and no “thumping” from the SUMR-D rotor during testing (L. J. Fingersh, personal communication, 2019). As such, two of the three critical issues for downwind turbines (mentioned above) have been characterized but the effect of tower shadow has not been considered.

One common software for modeling wind turbines is OpenFAST[64], developed by the National Renewable Energy Laboratory (NREL). For tower shadow, OpenFAST uses a variation of the Powles model, a steady-state velocity deficit model based on wind tunnel tests (with negligible upstream turbulence) for an isolated tower [65]. Tower shadow is applied in OpenFAST’s aerodynamic subroutine, AeroDyn15 [66]. This variation of the Powles tower shadow model includes the tower drag coefficient (C_D) as the only input and gives a \cos^2 -shaped velocity deficit behind the tower.

Other tower shadow models and methods have been suggested over time, but none have gained as wide acceptance as the Powles model. Some studies suggest using computational fluid dynamic results to tune the parameters for the velocity deficit behind the tower[55,67], but this method requires time-consuming simulations for each design. Recently, Yoshida proposed improvements to tower shadow models by adding lifting line theory[68] and a dynamic stall model[69], and these models are worth further investigation for their fidelity once field test results are available. Most models require a known drag coefficient of the tower but this in itself is an issue of research since the influence of surface roughness and inflow turbulence can impact this drag coefficient[70].

As noted above, there have been no field tests of tower shadow with flexible blades (as would be expected for the next generation of large wind turbines) nor is there a tower shadow model that has been validated for field-level turbulence. This is problematic for downwind turbine design since it is critical to have experimental data that includes the effects of unsteady blade moments for a flexible rotor in turbulent wind conditions. Furthermore, it is critical to develop and assess tower shadow models that consider inflow turbulence and cylinder drag characteristics.

The present investigation is the first study to the author's knowledge to investigate tower shadow by obtaining field test data from a downwind, flexible rotor and comparing it to simulations. The present study also presents the first publicly available comparison to experimental results with a mid-scale prototype (more than 4x larger than the UAE rotor), and is the first to develop a tower shadow model that considers the influence of upstream turbulence. The corresponding objectives of this study are:

- to quantify the effect of tower shadow on flexible downwind turbines with field data,
- to propose a new tower shadow model that accounts for freestream turbulence intensity,
- to consider the ability of tower shadow models to accurately capture blade moments, and
- to consider the relative influence of tower shadow on blade Damage Equivalent Loads.

To achieve the latter two goals, simulations using different tower shadow models will be compared to experimental results in terms of tower shadow dip magnitude, dip location, and damage equivalent loads.

3.2. Experimental Methods

The SUMR Demonstrator (SUMR-D) rotor was flown on the CART-2 test turbine over fall 2019 and spring 2020 at the NREL Flatirons Campus. The rotor, shown in Figure 3-2, has two lightweight, flexible blades in a load-aligned (coned) downwind configuration. Specifications of the SUMR-D rotor are given in Table 3-1, and further details on the design and testing can be found in Yao *et al.* [60], Bay *et al.* [61], Kaminski *et al.* [62], and Simpson & Loth [71]. The blade chord and the blade clearance from the tower to the rotor are provided in Table 3-1 at 70% blade span.

Table 3-1. SUMR-D Parameters

Blades	2
Rotor radius	22.25 m
Tower diameter	2.2 m
Blade chord (at 70% span)	0.74 m
Clearance (at 70% span)	7.3 m
Blade mass	990 kg
Flapwise frequency	1.13 Hz
Edgewise frequency	2.17 Hz
Rated rotor speed	21.5 RPM
Optimal TSR	9.5
Rated Power	54 kW
Coning angle	12.5°
Tilt angle	3.77°
Cut-in wind speed	3 m/s
Rated wind speed	5 m/s
Cut-out wind speed	11 m/s



Figure 3-2. SUMR-D rotor being installed on CART-2 at the NREL Flatirons Campus outside Boulder, Co. (photo courtesy of Lee Jay Fingersh, NREL).

Notably, the SUMR-D rotor is extremely lightweight and flexible compared to a traditional rotor (the blades are half the weight of those typically used on the CART-2). The reduced mass is possible because of SUMR-D's downwind and coned configuration. Also, the SUMR-D rotor was designed to be gravo-aeroelastic scaled to replicate nondimensional blade flexibility, nondimensional flapwise deflections, and nondimensional dynamics consistent with the full-scale 13 MW SUMR design[60,62,72]. Because of this scaling, the rated wind speed of the SUMR-D is about 5 m/s.

Data streams from both the CART-2 turbine and an upwind meteorological tower are saved as 5-minute data files at 400 Hz. Strain gauges were placed near the root of the SUMR-D blades to read flap and edge bending moments. However, the Blade 2 root strain gauge was partially damaged during tested, so all data shown herein was gathered from Blade 1. Wind speed measurements were taken from the upwind meteorological tower with a sonic anemometer placed at CART-2 hub height, and wind shear was calculated from cup anemometers placed along the tower (further details available in Simpson & Loth [71]).

To ensure that simulations could replicate the wind field conditions, a subset of these field test data files were selected for analysis based on the following criteria:

- Normal operation (no parked, shutdown, startup, or cutout cases were included)
- Operation in a single control region (the entire 5-minute file in either Region 2 or Region 3 controller operation)
- Mean crosswind angle is low (less than 30°) relative to the direction of the upwind met tower
- Nacelle yaw error is low (less than 15°) relative to the direction of the incoming wind
- Yaw variation is low (less than 10° range) throughout the 5-minute file

The 5-minute files are used herein rather than standard 10-minute files to increase the number of files that meet the selection criteria. Based on these criteria, 40 files were identified for analysis, resulting in 200 minutes of field test data.

3.3. Computational Methods

Simulations of the SUMR-D turbine were conducted using OpenFAST[64] with a “Digital Twin” model of the SUMR-D rotor created by Chetan *et al.* [44] The model uses the as-designed airfoils, which likely results in some deviations from the as-built airfoils due to some manufacturing surface imperfections. Turbulent wind field files were built in TurbSim v2 to match meteorological tower data at the CART-2 field site [71]. Simulated wind field files include wind shear (calculated from cup anemometers on an upwind meteorological tower), 3-directional wind speed time series from a sonic anemometer upwind at hub height, and an extra 100 seconds of wind data inserted to initialize each simulation. Blade bending

moment data was gathered from simulations and converted to Out-of-Plane (OoP) bending moments (as documented by Simpson & Loth [71]) for comparison to experimental field test data.

A. Tower shadow models

A variation on the Powles tower shadow model is provided in OpenFAST as an option for modeling downwind turbines. The original Powles model allowed the shadow width and depth to be independently tuned to fit wake characteristics [65]. Note that the Powles model came from wind tunnel tests with low turbulence and used an octagonal-shaped tower.

In AeroDyn15 [42] (the current aerodynamic module of OpenFAST), the shadow width and depth for OpenFAST are determined based on the tower drag coefficient (C_D) prescribed by the user at stations along the tower height [43]. This is also known as the ‘‘Moriarty model’’ [69]. As defined by AeroDyn [43], the wind freestream velocity far upstream (U_∞) is used for determining the drag and to apply the tower shadow deficit, shown in Figure 3-1.

The effect of the tower drag is to cause a momentum deficit downstream, and the associated ‘‘local’’ wind velocity behind the tower (U_{local}) can be obtained in terms of a nondimensional deficit (u_{wake}) as in Eq. 3-1a. This nondimensional wake deficit is obtained via Eq. 3-1b, where it is a function of the drag coefficient, the nondimensional wake distance (d) given in Eq. 3-1c, as well the nondimensional distances of x and y . These nondimensional distances are based on the dimensional X and Y directions (relative to the incoming velocity field as shown in Figure 3-1) normalized by tower radius (r), as noted in Eqs. 3-1d and 3-1e.

$$U_{local} = (1 - u_{wake}) U_\infty \quad (3-1a)$$

$$u_{wake} = \frac{C_D}{\sqrt{d}} \cos^2\left(\frac{\pi}{2} \frac{y}{\sqrt{d}}\right) \quad (3-1b)$$

$$d = \sqrt{x^2 + y^2} \quad (3-1c)$$

$$x = X/r \quad (3-1d)$$

$$y = Y/r \quad (3-1e)$$

There are some limitations of this model. Notably, the flow just upstream of the tower (U_{up}) is slowed by the momentum extraction (due to axial induction) such that this approach velocity is lower than that of the far-field freestream velocity (depicted in Figure 3-1). As such, a more accurate description

would employ U_{up} instead of U_∞ in Eq. 3-1a, as noted by Yoshida *et al.*[73]. Defining a as the axial induction at the rotor disk downstream of the tower, $U_\infty < U_{up} < (1 - a) U_\infty$. This velocity error in Eq. 3-1a reduces as the tower distance from the rotor disk increases and as the induction factor reduces (as is the case for operation above the rated wind speed). Yoshida *et al.* also noted that there can be an additional effect on tower drag due to the axial pressure gradient; however, the pressure gradient effect is only 20% of the reported change in tower drag (reducing the drag coefficient by about 2%) and thus this effect is more reasonably ignored.

Another limitation of the AeroDyn model is that the wake description in the above relations assumes a steady deficit (neglecting unsteady turbulent shedding events). The impact of using a steady wake model is more difficult to quantify but the implementation of an unsteady wake model would also be quite difficult and complex, and thus is not pursued herein.

Two other model limitations (which are addressed herein) are wake shape and the impact of turbulence on the mean wake spread rate. The Powles model for this mean flow deficit employs a \cos^2 -shaped deficit (Eq. 3-1b) to model the cylinder wake. However, the more common approach is to use a Gaussian-shaped velocity deficit[74], since this profile better matches detailed experimental data, though the differences between \cos^2 -shaped and Gaussian-shaped velocity deficits are not large. Another issue with the Powles model is that it neglects freestream turbulence in terms of the wake spread, where such turbulence can hasten the diffusion of the tower wake velocity gradients.

To potentially improve upon these limitations, a new tower shadow model is proposed herein based on the work of Eames *et al.*[75]. The ‘‘Eames’’ model adjusts the tower shadow wake to include the additional effect of inflow wind turbulence intensity. This addition can account for the significant turbulence typically seen in field tests and atmospheric boundary layers. However, the Eames model still assumes a mean deficit, i.e., the effects of upstream turbulence are only included in a time-averaged sense by adjusting the spread of the steady-state velocity deficit based on the average turbulence intensity. In particular, with the Eames model, the nondimensional wake half-width (y_{wake}) and wake deficit (u_{wake}) depend on turbulence intensity (I_t) as follows

$$y_{wake} = I_t x \quad (3-2a)$$

$$u_{wake} = \frac{C_D}{y_{wake} \sqrt{2\pi}} \exp \left[-\frac{y^2}{2y_{wake}^2} \right] \quad (3-2b)$$

Notably, this model assumes that turbulence dominates the wake diffusion, which is appropriate for most atmospheric flows. However, it is not appropriate for low turbulence conditions (e.g. wind tunnel flows with turbulence levels of only a few percent or less).

To apply this model specifically to the SUMR-D, the average horizontal wind turbulence intensity from the 3-directional sonic anemometer wind speed data (U , V , W) was calculated for each data set as

$$U_{horiz} = \sqrt{U^2 + V^2} \quad (3-3a)$$

$$\sigma_{U,horiz} = \sqrt{\frac{1}{N} \sum_{i=1}^N (U_{horiz,i} - \overline{U_{horiz}})^2} \quad (3-3b)$$

$$I_t = \frac{\sigma_{U,horiz}}{\overline{U_{horiz}}} \quad (3-3c)$$

The turbulence intensity is based on the combined horizontal wind speed (U_{horiz}) and is the ratio of the standard deviation (σ) to the mean (denoted with an overbar, e.g., \overline{U}). The 40 field test files used in this study have a turbulence intensity (I_t) range of 9% to 21%, which is typical of the levels for most wind turbines, as shown in Figure 3-3.

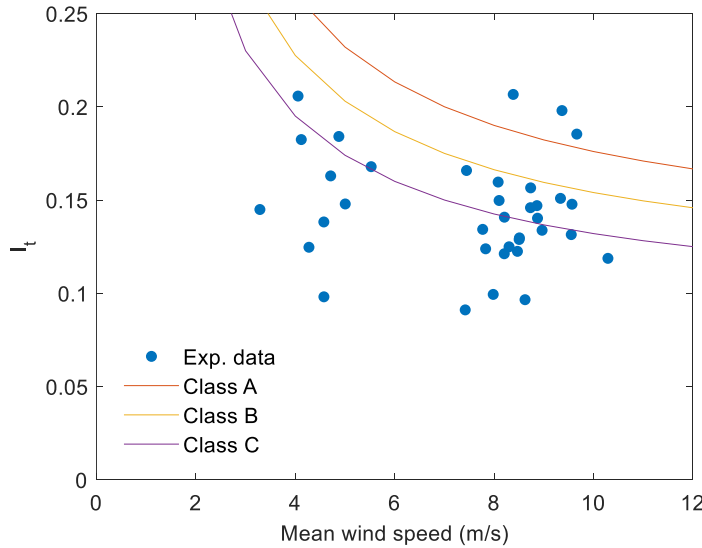


Figure 3-3. Experimental field test data turbulence intensity (I_t) for 5-minute data sets, plotted against mean wind speed. IEC wind turbulence classes provided for reference[39].

The wake deficits provided by the Powles and Eames models (using three different turbulence intensities for the Eames model) are compared in Figure 3-4, for one downwind location. Note that the wake shape will change based on downwind distance from the tower. In Figure 3-4, the deficit is shown for the CART-2 tower with a drag coefficient of $C_D = 0.7$ at a nondimensional distance away from the tower of $x = 6.6$ which corresponds to the approximate downwind distance from the tower at the 70% blade span on the SUMR-D rotor. For a turbulence intensity of 16% at this downwind distance, the Eames model and Powles model are nearly identical, but the Eames model provides a narrower and larger deficit for low turbulence and a wider and smaller deficit for high turbulence. This change based on turbulence matches the physical expectation that at high turbulence, the wake diffuses quicker so the velocity deficit behind the tower would be reduced and result in less impact on the blade loads.

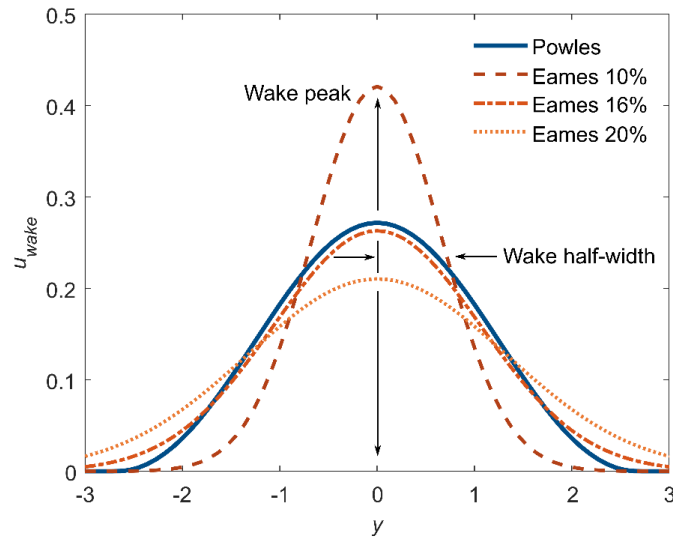


Figure 3-4. Comparison of Powles model and Eames model velocity deficit shapes for CART-2 tower with $C_D=0.7$ at $x = 6.6$ (approximate downwind location of 70% blade span). Eames model plotted with three different turbulence intensities (10%, 16%, 20%). Velocity deficit wake peak and half-width denoted for Eames $I_t = 10\%$ model where the wake peak is $u_{wake,max}$ and the wake half-width is the nondimensional width at $u_{wake,max} \times e^{-1/2}$.

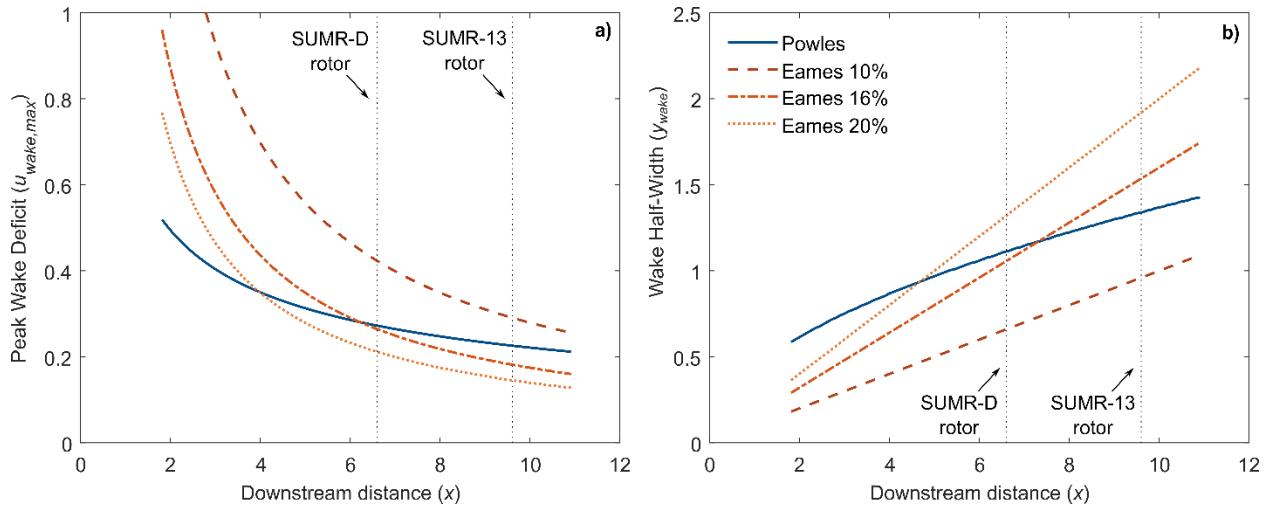


Figure 3-5. Tower wake peak velocity deficit in terms of u_{wake} (a) and velocity deficit wake half-width (y_{wake}) (b) over nondimensional downstream distance (x). Shown for $C_D=0.7$, with the downstream rotor distances for the SUMR-D and SUMR-13 rotors denoted.

The wake deficit peak height (or $u_{wake,max}$) and wake half-width (y_{wake} , which is located at $u_{wake,max} \times e^{-1/2}$) are also denoted in Figure 3-4. To see how they change when moving downstream from the tower, the wake peak and wake half-width are plotted against nondimensional downstream distance (x) in Figure 3-5. The approximate downstream distance for the SUMR-D rotor is denoted with a vertical dashed line, as is the approximate downstream distance for the SUMR-13 rotor [53,63], which may be more representative of a large-scale downwind turbine. In Figure 3-5a, the peak wake deficit is bounded from 0 to 1 because those are the physical limits based on Eq. 3-1a. However, it should be noted that close to the tower at low turbulence intensity the Eames model predicts a wake deficit greater than 1. This implies backflow (or a negative wind velocity), which is outside the physical scope of the Eames model derivation (though this backflow may occur physically). Users should therefore be cautious in applying the Eames tower shadow model close to the tower.

In terms of both wake peak and width, the Powles model is more moderate than the Eames, showing less change over downstream distance. For the Eames model, higher turbulence intensity relates to larger slopes and more change with downstream distance away from the tower. While it is anticipated that the Eames model is more accurate for flows with significant inflow turbulence, circular cross-sections, and when the blade is several diameters downstream of the tower, field test data at multiple downstream locations would be useful to assess the relative accuracy of the Powles vs Eames models for downstream wake shapes.

Through a collaboration with NREL, the Eames tower shadow model was added to OpenFAST (publicly available [64]) and used to run simulations of SUMR-D. All simulations also included the Bak tower influence model [43] which accounts for inviscid streamline deflections around the cylinder that can be important very near the tower. Simulations were run for all 40 wind field files three times: tower shadow off, the Powles model on, and the Eames model on.

B. Tower drag for field test conditions

The tower drag coefficient is critical to the proper modeling of the tower shadow effect in OpenFAST, and it can be approximated using the drag of a cylinder since the aspect ratios of wind turbine towers are much greater than unity. The cylindrical drag force is the product of the dynamic pressure, the frontal area, and the cylinder drag coefficient (C_D). This coefficient is generally estimated with an empirical relationship to the cylinder Reynolds number (Re), which is based on the freestream velocity, cylinder diameter, and kinematic viscosity. This relationship of C_D to Re depends significantly on whether the boundary layer that separates from the cylindrical surface is laminar (sub-critical regime) or is fully turbulent (super-critical regime). Between these two regimes (where the separating turbulent boundary layer is transitional), the drag coefficient can drop significantly, where this drop is often termed the “drag crisis”. The critical Reynolds number where this drop occurs can be influenced by the roughness of the cylinder surface and the inflow turbulence. In particular, turbulence intensity and integral length scales can influence drag, as reported by Bell [76]. In addition, cylinder aspect ratio and end conditions can also be influential, as described by Hoerner for sub-critical Reynolds numbers [70].

In Figure 3-6a, a common empirical model for drag coefficient versus Reynolds number for steady upstream flow past a cylinder is given with a solid black line (herein, from AeroDyn 14 [77]). A selection of experimental results for steady inflow (negligible freestream turbulence) [78–81] are shown, which corroborate the common empirical model for drag coefficient. Such a drag model is useful for wind tunnel tests of tower shadow (where freestream turbulence is negligible).

In Figure 3-6b, experimental results are shown for flows whose inflow turbulence and/or Reynolds numbers are high enough such that super-critical conditions are expected [78–80,82,83], i.e. the attached boundary layer becomes turbulent before the flow separates. Of particular interest is the data point ($C_D = 0.67$ at $Re = 3.9 \times 10^6$) from Dryden & Hill [83], taken from a power plant chimney in naturally turbulent field conditions. This is likely a good representation of the drag experienced by a large tall tower, e.g. for the tower of a full-scale wind turbine. Based on the data over a wide range of Reynolds numbers in Figure 3-6, a shaded region is shown for which the C_D may be expected for flows with high inflow turbulence, such as that experienced by a wind turbine in the field. It should be noted that there is no commonly available empirical relation between Re and C_D for cylinder drag coefficient with inflow turbulence.

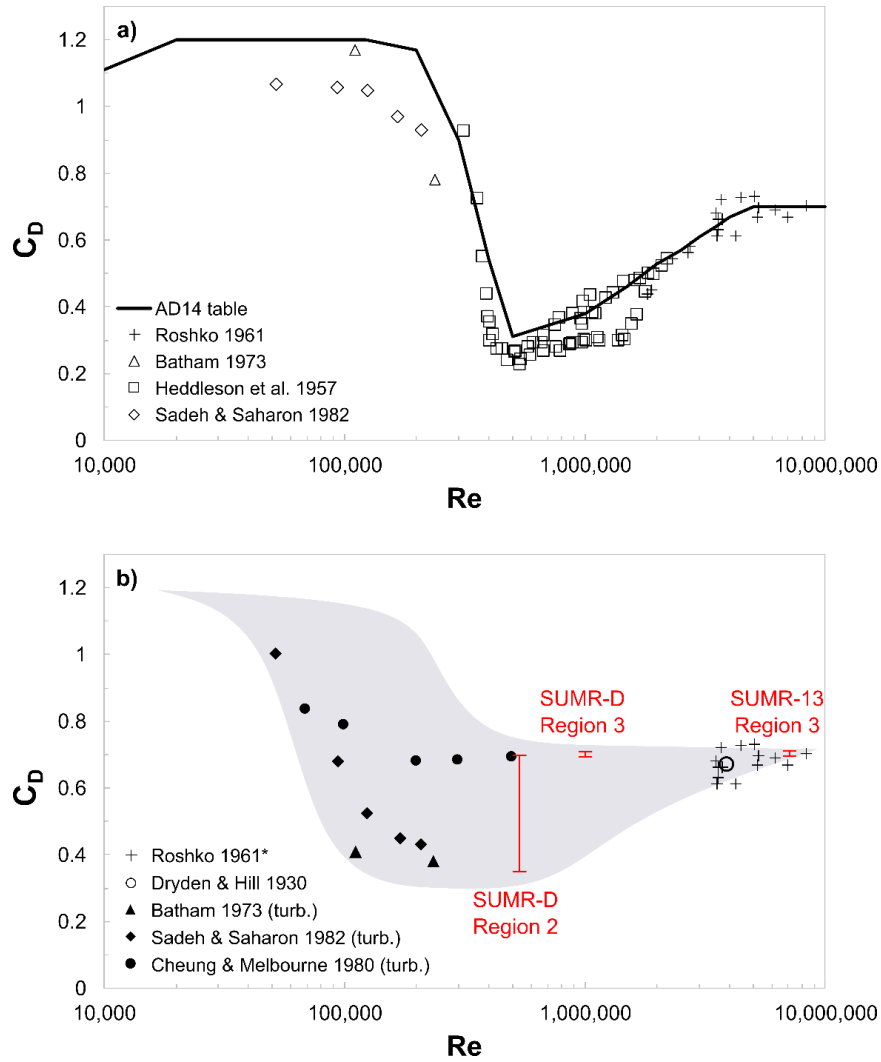


Figure 3-6. Drag coefficients (C_D) past circular cylinders as a function of Reynolds number (Re): a) for laminar inflow showing experimental results [78–81] along with an empirical fit, and b) for turbulent inflow (super-critical) experimental results [78–80,82,83] along with a shaded envelope indicating the range that may occur, where the ranges of drag coefficients used in simulation of SUMR-D as well as the expected range for the SUMR-13 turbine are labeled in red.

Fortunately, most large downwind turbine will have large Reynolds numbers in the super-critical range, as shown by that for the SUMR-13, so that $C_D = 0.7$ is a good approximation. However, the CART-2 tower diameter combined with the operational wind speeds for the SUMR-D rotor, places the cylinder Reynolds number in the critical drag region where the drag is more uncertain and the range of possible drag coefficients is quite large. With a rated wind speed of 5 m/s, the SUMR-D rotor has a rated Reynolds number of 620,000. The Reynolds number and simulated drag range for operation in Region 2 (< 5 m/s) and Region 3 (> 5 m/s) operation are denoted in Figure 3-6b. In particular, Region 2 simulations were run with $C_D = 0.7$ and $C_D = 0.35$, while Region 3 simulations were run only with $C_D = 0.7$.

C. Defining Tower Shadow Dip Magnitude and Location

Downwind turbine blades see a sudden reduction in load when they pass through the velocity deficit behind the tower. An example of azimuthally-averaged bending moment data from a 5-minute set of experiments and simulations are seen in Figure 3-7, which averages out the effects of turbulence to show the effect of tower shadow on the blade. To quantify this dip magnitude, a sine curve is fit to the azimuthally-averaged out-of-plane bending moment data for the azimuthal angle range of 0° - 150° and 270° - 360° (which avoids the angles where the tower shadow effect is significant). The sine curve acts as an estimation of the bending moment without the tower shadow effect, for both the CART-2 field test data and the FAST simulations. Shown in Figure 3-7, the dip location is the azimuth angle where the lowest bending moment occurs for the field data or simulation, while the dip magnitude is the difference between the field test data or simulation and the fitted sine curve at the dip location. Note that while gravity loads are nearly sinusoidal during operation (a prominent load on a highly coned rotor), wind shear can cause non-sinusoidal blade loads due to unequal thrust loading across the rotor. To account for this, wind shear estimates from field test data are included in OpenFAST simulations.

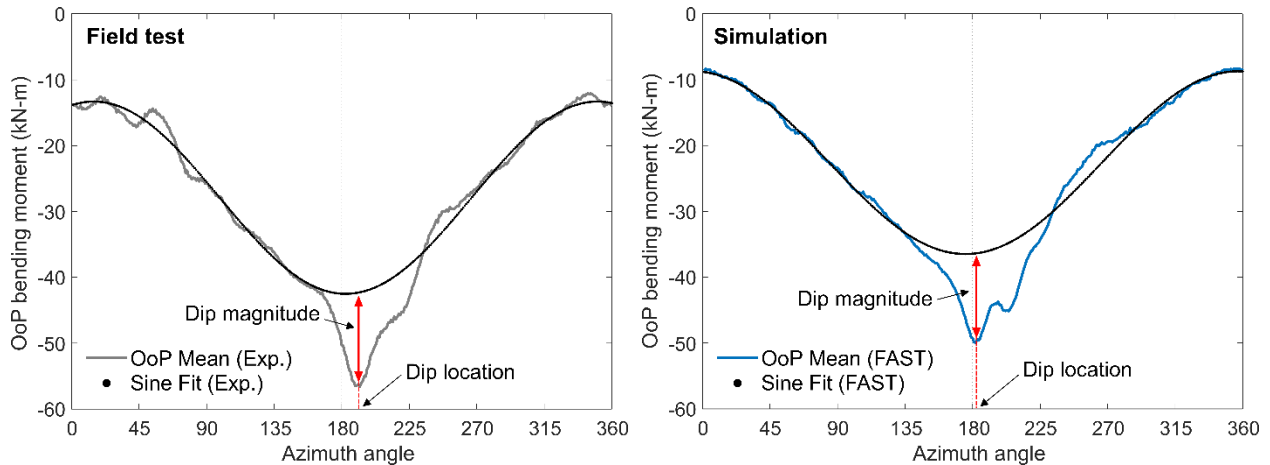


Figure 3-7. Sine-wave curves fitted to experimental field measurements and to FAST predictions of azimuthally-averaged Blade 1 Out-of-Plane (OoP) Bending Moments for a five-minute data set, along with measurements of tower shadow dip magnitude and dip location. FAST simulation uses the Powles tower shadow model.

The ability of a tower shadow model coupled with a tower drag coefficient to accurately predict dip magnitude for each 5-minute data set is quantified using the predicted Root Mean Square Error (RMSE).

$$RMSE = \left[\frac{1}{N} \sum_{i=1}^N (M_i - \bar{M}_i)^2 \right]^{\frac{1}{2}} \quad (3-4)$$

Where N is the number of data files, M is the dip magnitude measured from a single field test data set (5 minutes long), and \hat{M} is the predicted dip magnitude from the simulations for that same data set.

D. Fatigue calculations

Another important potential effect of tower shadow is its impact on blade fatigue life. MLife is a fatigue calculation software that uses a rainflow counting algorithm to find Damage Equivalent Loads (DELs) for an input signal [84]. MLife is used herein to calculate short-term zero-mean DELs from the root flap bending moment signal for both CART-2 field test data and FAST simulations. Flapwise bending moments are used here, rather than out-of-plane bending moments (where the two moments are related via a coordinate transformation), because dip locations do not need to align and since flapwise bending moments are more relevant for structural analysis. An inverse S-N slope of $m = 10$ was used for the blades. The 5-minute input files are binned by mean inflow wind speed and DELs are aggregated over the files in each bin.

Only short-term DELs are reported because of the limited data available for analyzing fatigue. As such, the results from the field test data may not be directly extrapolated to lifetime fatigue.

3.4. Results and discussion

A. Assessment of Out-of-Plane Bending Moments

For each of the 40 field data sets, comparable FAST simulations were run and the resulting data analyzed. An example of how the different tower shadow models performed is shown in Figure 3-8 for an example low wind speed case (8a and 8b) and for an example high wind speed case (8c and 8d). The experimental field test data and simulation instantaneous out-of-plane bending moments for the Eames and Powles models are shown in Figure 3-8a and Figure 3-8c. For a clearer look at trends over blade azimuth angle, the azimuthally-averaged moments and standard deviations are shown in Figure 3-8b and Figure 3-8d, with the experimental field test data shown in black. A vertical dashed line at 180° azimuth angle marks the location of the tower.

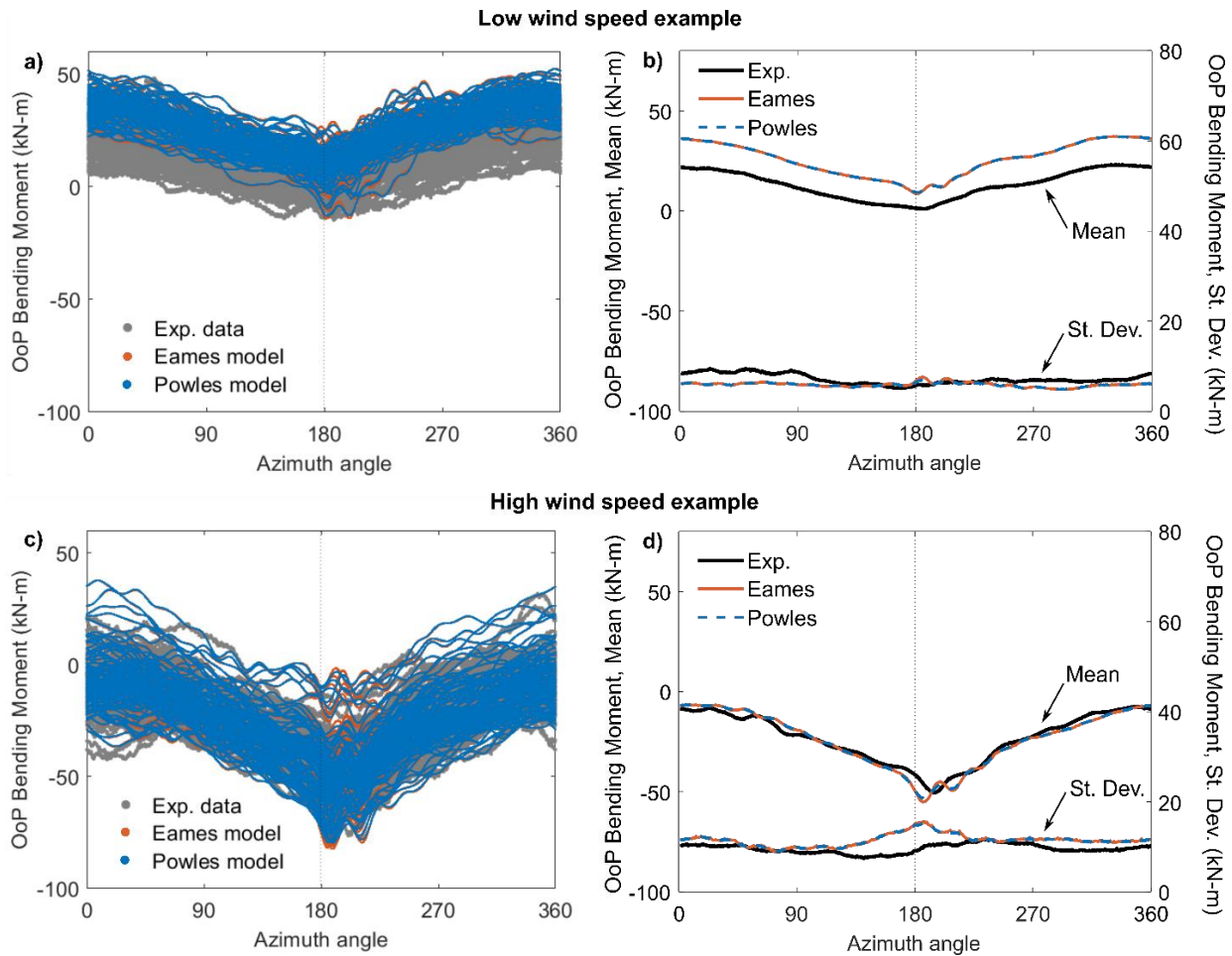


Figure 3-8. Blade 1 Out-of-Plane (OoP) bending moment data (a,c) and mean and standard deviation (b,d) for SUMR-D from experimental field test (grey/black) and FAST simulations using Eames (orange) and Powles (blue) models. Each graph contains an example of 5 minutes of data at a low wind speed (a,b) or high wind speed (c,d).

In some cases, the mean bending moment does not exactly align between the experimental data and the FAST simulations, e.g. as in Figure 3-8b. It is hypothesized that these discrepancies between experimental data and simulations are due to differences in the structural and aerodynamic properties between the designed and built blades. However, the simulations are generally able to capture the mean and variance of the bending moment data, as well as the qualitative tower shadow dip. The Eames model in the high wind speed example gives a narrower and stronger tower shadow dip than the Powles model. But generally, the Eames and Powles models give very similar results.

The compiled results of the mean out-of-plane bending moments are plotted versus mean wind speed in Figure 3-9. This rotor uses load alignment such that the mean bending moment is nearly zero at rated wind speeds (of 5 m/s), and it produces positive moments (away from the tower) at low speeds and

negative moments at high wind speeds (towards the tower)[50]. Here the predictions capture this trend in the experimental data with nearly equivalent accuracy for the Powles and Eames models. This indicates that the mean aerodynamic and gravitational loads for SUMR-D are reasonably captured by FAST using the inflow wind conditions.

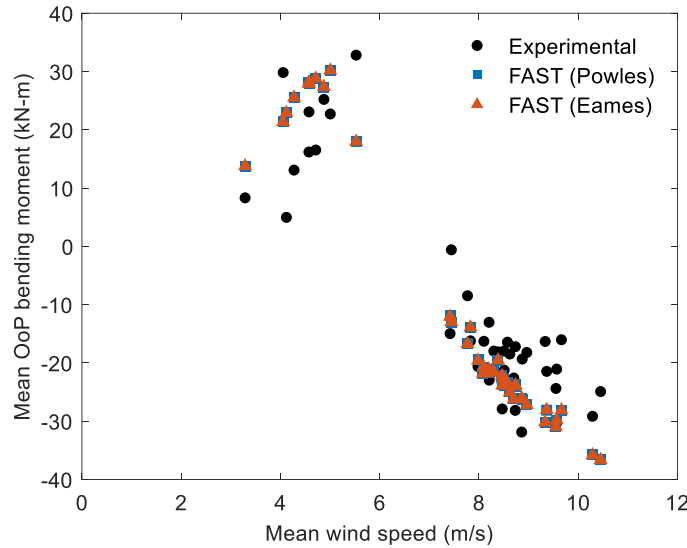


Figure 3-9. Mean Out-of-Plane (OoP) blade bending moment over 5-minute data files for experimental field test data, Powles model simulations, and Eames model simulations. Powles and Eames models result in equivalent mean bending moments.

B. Tower Shadow Dip Magnitude and Location

The dip magnitude based on the fitted sine curve is plotted versus mean wind speed in Figure 3-10 (using the process detailed in Figure 3-7). At higher wind speeds (in Region 3), simulations are able to capture the tower shadow dip magnitude on average with both the original (Powles) model and new (Eames) model. However, at lower wind speeds (in Region 2), simulations with $C_D = 0.7$ (solid symbols) overpredict the dip magnitude compared to field test data results. A second set of simulations at low wind speeds with $C_D = 0.35$ (hollow symbols) shows better correspondance with the experimental dip magnitude results. The reduced drag coefficient in Region 2 can be explained in part by the reduced wind velocity at the tower due to rotor axial induction (as discussed in Section 3.1), which is not captured in FAST. Additionally, the uncertainty of tower drag in this Reynolds number range, as discussed in Section 3.3, makes it difficult to know if the differences in dip magnitude are due to tower drag or another effect not captured by the model.

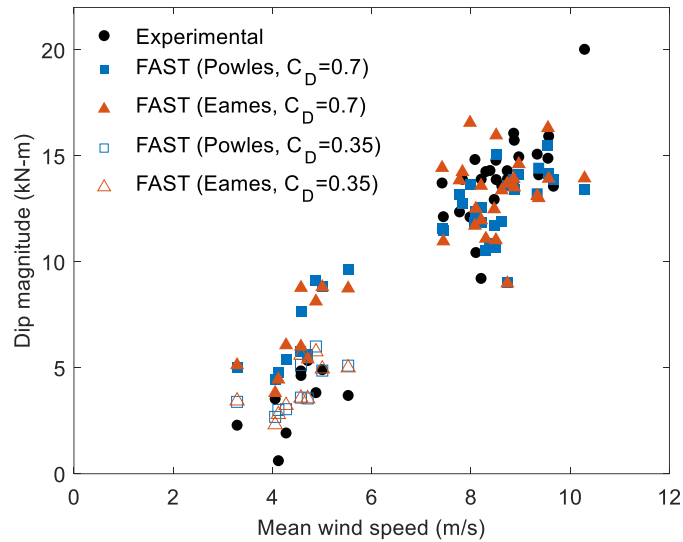


Figure 3-10. Azimuth-averaged out-of-plane bending moment dip magnitude (due to tower shadow, measured from fitted sine curve) for experimental field test data, Powles model simulations, and Eames model simulations. Each point represents 5-minute data file average.

The dip magnitude has a positive trend with wind speed, as expected. Higher wind speeds see a larger velocity deficit and thus impart a larger impulse on the blade as it passes through the tower wake. As such, Region 3 conditions are expected to contribute more to unsteady blade loads (which can contribute to fatigue).

Using the original tower drag coefficient ($C_D = 0.7$), the predicted Root Mean Square Error (RMSE) is 2.88 kN-m for the Powles model and 2.92 kN-m for the Eames model, compared to experimental results. Using the lower drag coefficient ($C_D = 0.35$) for low wind speeds and higher drag coefficient for high wind speeds, the predicted RMSE is 2.32 kN-m for the Powles model and 2.38 kN-m for the Eames model. Thus, there is a slight preference for the Powles model, but not a significant difference between the two models for predicting tower shadow dip magnitude, for the given inflow turbulence and field conditions.

The azimuth angle location of the tower shadow dip (defined in Figure 3-7) is plotted in Figure 3-11. The lower drag coefficient for Region 2 data points does not show a consistent change in the dip location. The experimental data shows the tower shadow dip occurring much later (approximately 6° - 8°) than predicted by either the Powles or Eames models in the OpenFAST simulations.

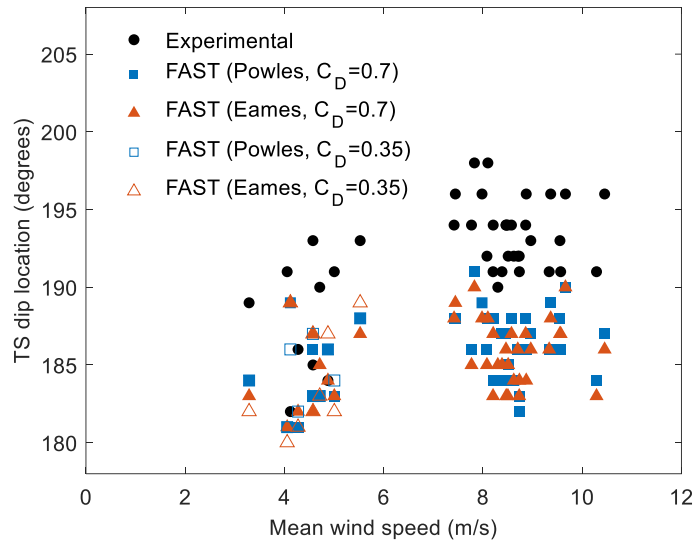


Figure 3-11. Azimuth-averaged out-of-plane bending moment tower shadow dip azimuth angle location vs mean wind speed for experimental field test data, Powles model simulations, and Eames model simulations. Each point represents 5-minute data file average.

It is proposed that the apparent delay in tower shadow dip may be caused by an aerodynamic or structural effect not captured by the model. One aerodynamic possibility is that the simulation code may not capture a delay in lift formation on the blade, which may result in a delay on the order of 1.8° based on the chord length at the 70% span. Other possible causes include a hysteresis effect or aeroelastic deflections not fully captured by OpenFAST.

Structurally, the as-built blades may be more or less stiff than designed in different sections, which may affect the timing and magnitude of deflection, as discussed in Section 4.4. Additionally, the SURM-D rotor geometry was modified by the use of an adapter plate on the CART-2 turbine to provide the coning angle needed for the SUMR-D rotor field test (as documented by Bay et al.[61]). The adapter can cause up to 3.5° azimuth angle delay when the blades are pitched in Region 3; however, this effect is not included in the FAST rotor geometry. Yet, these quantifiable effects, even combined, are not enough to account for the lag seen in the data.

Notably, such an azimuthal delay in the tower shadow dip has been seen in other studies. In particular, the flapwise bending moment dip for the UAE downwind rotor experiments occurred 16° later than predicted by FAST with the Powles model[85], while coefficient of lift data from a downwind turbine wind tunnel test indicated a tower shadow dip occurring between 186° - 191° depending on wind speed[69], which is more in line with the present simulation results.

C. Tower Shadow Impact on Damage Equivalent Loads

Finally, simulation and experimental damage equivalent loads are calculated using MLife with bending moment time series data as the input. The results are compared in terms of short term DELs for blade root flapwise bending moment in Figure 3-12 for different binned mean wind speeds. Only bins with more than 5 data sets were included. In all cases, adding one of the tower shadow models increases DELs. In Region 3 (greater than 5 m/s on average), simulations without tower shadow tended to under-predict DELs and simulations with tower shadow models predict DELs closer to the field test DELs. However, in Region 2 (below 5 m/s), all simulations over-predict DELs and both tower shadow models exacerbate this effect. With $C_D = 0.7$, the Powles and Eames models increase DELs over simulations without tower shadow by about 8% on average.

For Region 2 (4-5 m/s), simulations with $C_D = 0.35$ result in smaller increases in DELs when tower shadow models are added, but the simulations still all over-predict DELs. As seen in Figure 3-10 both the Powles and Eames tower shadow models over-predict the tower shadow dip magnitude in Region 2, which is consistent with over-estimating fatigue. The results indicate that the Eames and Powles models give nearly identical DEL results. However, this analysis does not consider enough data over a large enough range of wind speeds to conclude how the lifetime fatigue would be affected.

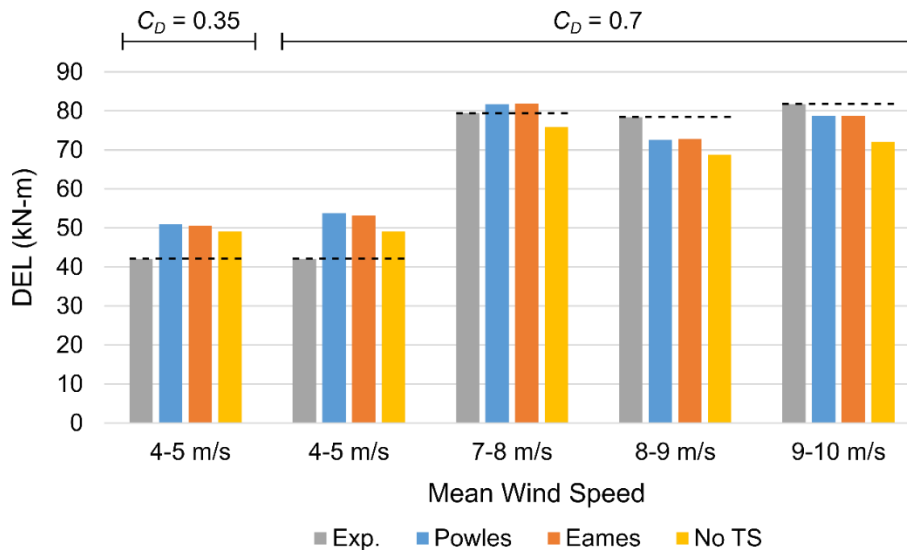


Figure 3-12. Short-term zero mean DELs for flap bending moment, aggregated over data files in each binned mean wind speed (4-5 m/s: 6 files, 7-8 m/s: 7 files, 8-9 m/s: 17 files, 9-10 m/s: 6 files). Experimental field test data (grey column and dashed black line for comparison) compared to FAST simulations with no Tower Shadow (TS), Powles model, and Eames model.

D. Effect of flexible rotor

One of the unique features of the SUMR-D rotor is the lightweight flexible blades. Simulations by Reiso & Muskulus showed that reducing the stiffness of a blade leads to a reduction in the blade root DEL[59]. Noyes *et al.* (2018) found the stiff blades of the UAE Phase VI resulted in a strong tower shadow effect, while Noyes *et al.* (2020) predicted that damping ratio of a blade may determine the magnitude of the tower shadow effect [58,85].

It was hypothesized that the flexible blades of the SUMR-D rotor would reduce the tower shadow effect compared to stiff blades. To test this theory, FAST simulations were run with fully stiff blades, where the first flapwise blade mode, second flapwise blade mode, and first edgewise blade mode degrees of freedom (DOFs) were all turned off. One comparison of the original blades and the fully stiff blades is shown in Figure 3-13. The stiff blade has a much larger dip magnitude, which occurs at nearly 180° azimuth angle. The dip location supports the theory that the delayed dip location in the experimental results may be due to the blade flexibility. The flexible SUMR-D rotor sees a much smaller tower shadow effect on the blade root bending moment.

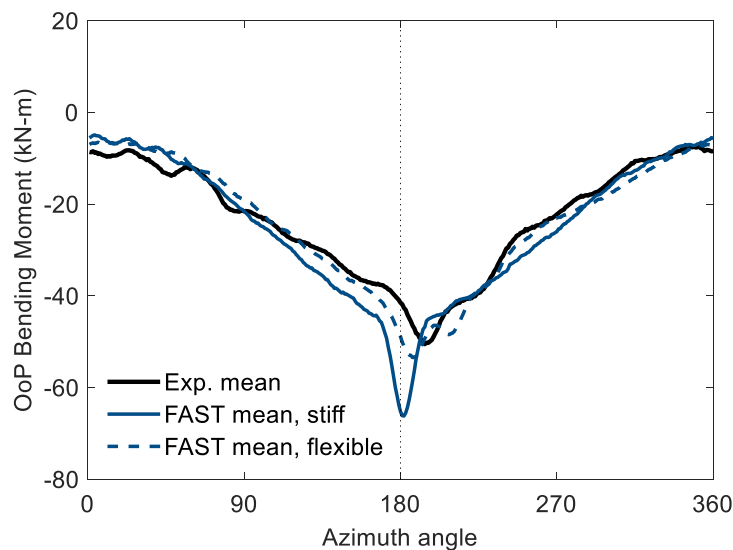


Figure 3-13. Comparison of tower shadow response on azimuth-averaged mean out-of-plane blade root bending moments between experimental data and FAST simulations using the Powles model with a “stiff” blade and with the SUMR-D flexible rotor. The stiff blade is modeled with the blade bending DOFs off, and shows a much stronger tower shadow dip.

3.5. Conclusions

The tower shadow effect on downwind turbines is investigated herein with field test data and simulations in OpenFAST. The field test data from the SUMR-D rotor is the first such data obtained and analyzed for a flexible downwind rotor. While the tower shadow effect can be clearly seen in the blade bending moment data, the effects are manageable compared to the effects of turbulence and cyclic gravity loads.

A new tower shadow model, the Eames model, was proposed which uses both tower drag and inflow turbulence as inputs. The Eames model was compared to the old Powles tower shadow model through simulations in OpenFAST. Both models produced simulations which generally captured the tower shadow dip magnitude in Region 3. The tower drag coefficient is difficult to estimate since the SUMR-D operating Reynolds numbers fall within the critical drag regime. Using a high drag coefficient tended to over-predict dip magnitude in Region 2, while using a low drag coefficient was better able to predict dip magnitude compared to experimental results. Fortunately, the tower for large downwind turbines (e.g., rated power in excess of 10 MW), will have high cylinder Reynolds numbers such that $C_D = 0.7$ is quite reasonable. Both models predicted the tower shadow dip to occur sooner than was seen in experimental data. Possible causes for that delay include aeroelastic deflections and hysteresis, but the exact cause is unknown. However, this delay does not significantly impact the bending moment mean values and peak deviations.

Both tower shadow models increased the DEL relative to simulations without tower shadow by about 8% and were reasonably consistent with the experimental DELs. Overall, the Eames model produced very similar results to the Powles model and both models appear to be good options for modeling tower shadow in field test conditions. The Eames model has the additional benefit of providing an opportunity to tune the inflow turbulence and see how that may affect the tower wake, but the simpler Powles model may be preferred as it does not require knowledge of the turbulence level.

The above results indicate that downwind turbines may be viable since tower shadow effects can be small compared to the effect of turbulence for flexible, coned rotors, where the rotor examined herein had the advantage of load-alignment and did not exhibit significant audible thumping. It is recommended that downwind turbine simulations include one of the present validated tower shadow models in order to quantify the net impact on DELs. In particular, long-term fatigue due to tower shadow should be included in detailed structural analysis and design of the rotor and tower.

Chapter

4. Cost of Valued Energy for design of renewable energy systems

Abstract

The design of renewable energy systems such as wind turbines or solar panels conventionally employs Levelized Cost of Energy (LCOE), but this metric fails to account for the time-varying value of energy. This is true both for a single turbine or an entire wind farm. To remedy this, two novel, relatively simple metrics are developed herein to value energy based on the time of generation and the grid demand: Levelized Avoided Cost of Energy simplified (LACEs) and Cost of Valued Energy (COVE). These two metrics can be obtained with: 1) a linear price-demand relationship, 2) an estimate of hourly demand, and 3) an estimate of predicted hourly generation data. The results show that value trends for both wind and solar energy were reasonably predicted with these simplified models for the PJM region (a mid-Atlantic region in the USA) with less than 6% error on average, despite significant stochastic variations in actual price and demand throughout the year. A case study with wind turbine machine design showed that increasing Capacity Factor can significantly reduce COVE and thus increase Return on Investment. As such, COVE and LACEs can be valuable tools (compared to LCOE) when designing and optimizing renewable energy systems.

Nomenclature

g	Hourly power generation (MW)
p	Hourly spot price / time-averaged spot price
D	Hourly demand / time-averaged demand
R	Hourly residual demand / time-averaged demand
W	Hourly wind generation / time-averaged demand
S	Hourly solar generation / time-averaged demand
Q	Hourly variable renewable generation / time-averaged demand
X	Extrinsic factors influencing price such as the economy or government regulations
CF	Capacity factor
m	Price-demand slope
$const.$	Arbitrary constant
VRE	Variable Renewable Energy (such as solar or wind)
$LCOE$	Levelized Cost of Energy
$LACE$	Levelized Avoided Cost of Energy
$sLCOE$	System Levelized Cost of Energy
$rsLCOE$	Revised System Levelized Cost of Energy
VF	Value Factor
$COVE$	Cost of Valued Energy
ROI	Return on Investment
$LACEs$	LACE simplified
$()_m$	Modeled value
$()_{avg}$	Time-averaged value over a year
$()'$	Temporal variation from the average, such that $() = ()_{avg} + ()'$

4.1. Introduction

Renewable energy production is increasing significantly, e.g. it reached 17% of the US production in 2017 [86]. Wind energy alone now contributes over 10% of electricity production in 8 countries [2], while cumulative solar capacity is expected to double between 2019 and 2022 [87]. A key driver for the

growth in deployment of wind and solar energy systems has been their rapidly declining costs in per unit energy production [88–90].

The common and current objective used when designing variable renewable energy (VRE) systems is the Levelized Cost of the Energy (LCOE) of the system [10–17]. The LCOE of a power generation system is the estimated cost per kilowatt-hour of produced electricity over the lifetime of the system based on the ratio between the annualized total costs of the system and the expected annual energy production. Herein, VRE system design is defined as the design of entire wind and solar power plants or design of individual units (wind turbines and photovoltaic panels). Designing by LCOE provides a straightforward metric that allows engineers and stakeholders to compare the cost of energy produced by different designs, while avoiding the complex relationship between renewable energy system performance and larger market dynamics. Historically, this LCOE-based design approach was reasonable as renewable power plants often received a fixed price for each kilowatt-hour produced and thus each kilowatt-hour of energy produced could be treated equally. In contrast, energy economists and system planners employ more sophisticated financial metrics (relative to LCOE) to accurately assess the value that different electricity generation assets will have within a particular system and market context.

As the renewable share in the electric grids increases, they are increasingly expected to participate in electricity markets for services, energy, and capacity, similar to conventional energy generation assets [19,91], and VRE generation may be well suited for some services [92]. Therefore, the industry is preparing for a paradigm shift where the objective is not simply to produce the cheapest possible electrons, but instead to create the highest possible value from a renewable power plant over the course of its lifetime [19].

As previously mentioned, LCOE does not take into account time-varying revenue streams for power plants. If power plants generate revenue from their ability to provide services and energy in markets with time-varying prices, then the overall profitability of the power plant depends on the correlation of the plant's output with the value of those revenue streams over time. Depending on the market, the price of electricity can rise to ten times the average price when demand is high and, in the other extreme, can even go negative when there is too much energy in the system. To quantify the effect of these price variations, other metrics have been introduced. One metric introduced to quantify the effect of price variations is the Value Factor (VF), defined by Hirth as the ratio of a VRE spot market price to the total average spot market price [18]. However, other scholars define Value Factor more generally as the levelized value of energy divided by the levelized value of a continuous baseload generation technology [93]. As the share of wind and solar energy increases, the relative Value Factor of the electricity they produce falls [18,93–95], since the amount of energy produced by sources with near zero marginal costs (such as wind and solar which have no fuel costs) drives down the market clearing price of electricity [18,96].

Determining the revenue from VRE production is further complicated by the nonlinear relationship between energy production and value. This dependence of energy price with VRE production highlights one of many deficiencies inherent in the LCOE metric [11,18,97–101]. Joskow [97] examined economic values of dispatchable (i.e. conventional) and intermittent (i.e. variable) power generation technologies and noted that a grid system that chooses technologies based on LCOE, without regard for the time of energy production, will be sub-optimal or even fail. Instead, Joskow proposed that *energy be valued based on the expected market value when the energy is produced*. Figure 4-1 illustrates the major components of LCOE as well as three of the most applicable current metrics that attempt to move beyond LCOE: Levelized Avoided Cost of Energy (LACE), System LCOE (sLCOE), and Revised System LCOE (rsLCOE).

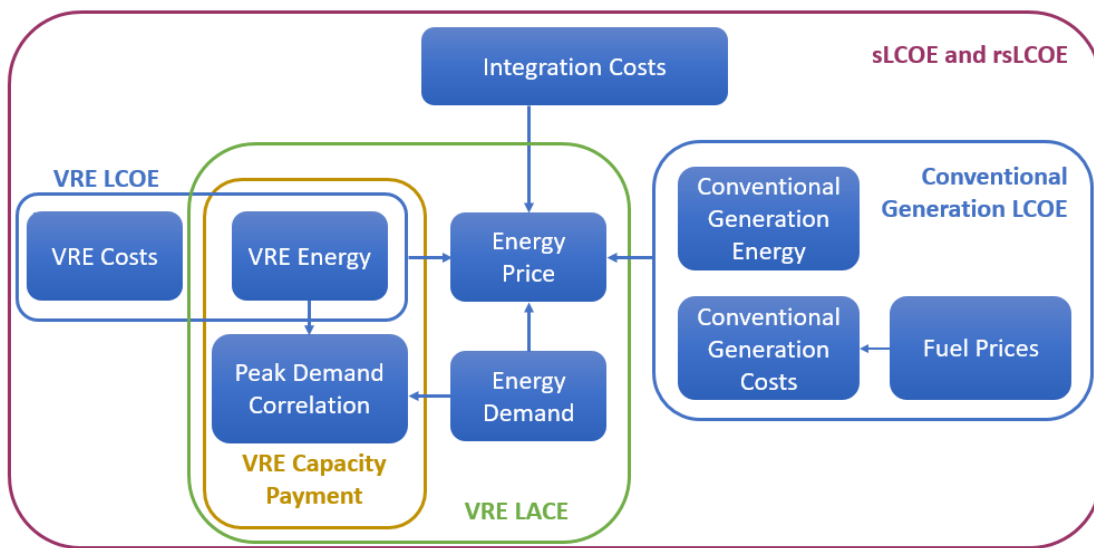


Figure 4-1. Factors influencing energy prices and current metrics used to quantify energy value including LCOE, LACE, sLCOE, and rsLCOE

The Department of Energy’s Energy Information Administration (EIA) has proposed the use of LACE and Net Value (NV) to better compare the benefits of proposed power generation options [99,102,103], similar to Mills and Wisser’s “marginal economic value” [104]. LACE adds up the revenue that can be gained from a new power generation system and levelizes it based on the expected annual energy production. For example, the EIA uses an extensive version of LACE in conjunction with the National Energy Modeling System (NEMS) to model the electricity grid and potential avoided costs when adding a new project to the grid [102]. The Net Value of a project is then simply the difference of LACE and LCOE. Using Net Value is a promising alternative as it takes both costs and revenues into account. However, calculating LACE usually requires complex, site-specific electricity price models, and thus Net Value is overly complex for use by power plant and machine designers.

Ueckerdt *et al.* propose a more complete cost metric than either LACE or LCOE defined as the System LCOE (sLCOE) [98]. As shown in Figure 4-1, sLCOE increases metric fidelity as it includes the many factors included in Integration Costs: additional costs felt by the electrical system when variable renewable energy generation is added. These integration costs are due to variability, uncertainty, and locational-constraints of the technologies [101,105], and are further detailed in [101]. Notably, the calculation of the sLCOE for a particular VRE system design would require extensive modeling and analysis and, furthermore, does not itself denote the economic viability of a project.

The National Renewable Energy Laboratory recently reviewed the benefits and drawbacks of a number of energy competitiveness metrics based on the perspective of a centralized planner [93]. They concluded that none of the previous metrics were able to take into account a comprehensive view of system-wide cost and value so as to determine economic viability with high fidelity. To address this, system profitability metrics were utilized to propose a Revised System LCOE (rsLCOE) based on the ratio of cost to value of the system and a benchmark price [93]. Using rsLCOE allows for a direct comparison to traditional LCOE values, while incorporating a system-level view of economic viability, but requires the choice of an accurate benchmark price.

Due to the complexity of the above metrics, as well as their historical irrelevance in energy markets with fixed prices, VRE designers have overwhelmingly employed LCOE for design optimization, even though LCOE does not have a method for valuing energy price at the time of generation of energy or potential capacity payments for the plant.

While valuable metrics to evaluate energy systems from the point of view of a centralized planner have been outlined above, there is a critical need for a practical metric that can be implemented by energy system designers. This is important for both individual machine design – i.e. solar panels and wind plants – as well as for the design of full power plants – which may contain solar panels, wind turbines, storage, or combinations thereof (i.e. hybrid power plants).

The purpose of this study is to develop a metric for VRE system design that values energy based on the time of generation, in a simple and easy-to-use manner. Two new metrics are proposed herein to accomplish this goal: LACE simplified (which is applied to calculate Net Value) and Cost of Valued Energy (COVE). As a case study for how this concept could be applied, the Return on Investment of a wind turbine is calculated for varying turbine parameters.

The contents of this study will be as follows: Section 2 will explain the proposed linear price-demand model, Section 3 will outline data sources and applying the linear model to calculate Value Factor, and Section 4 will include a case study applying COVE and Return on Investment.

4.2. Proposed Model for Price

LCOE is the standard metric used today by energy system designers to compare alternative technologies and optimize their systems.

$$LCOE \left(\frac{\$}{MWh} \right) = \frac{\text{Annualized Costs (Capital + O\&M)}}{\text{Annual Energy Production}} = \frac{\Sigma \text{costs}}{\int g dt} \quad (4-1)$$

In this expression, *Capital Costs* are the costs of designing, building, and installing the system while operating and maintenance costs (*O&M*) are the costs of operating and maintaining the system [99]. As shown, by the right-hand side of Eq. 4-1, LCOE is the sum of the costs over a period of time divided by the integral of hourly generation *g* over the same period of time.

Alternatively, the calculation of LACE is defined by the EIA in [99] as:

$$LACE = \frac{\sum_{i=1}^Y (p_{\text{marg},i} * \text{hours}_i) + (\text{capacity payment})}{\text{annual generation hours}} \quad (4-2)$$

$$\text{capacity payment} = \text{capacity value} * \text{capacity credit}$$

Where p_{marg} is the marginal generation price of energy in time period i , hours are the generation hours in time period i , capacity payment is the annual revenue an energy system can earn based on its ability to offset dispatchable resources used to meet peak demand, capacity value is the annualized cost of a dispatchable resource used to meet a reserve requirement, and capacity credit is the percentage of installed capacity that can offset reserve requirements [99]. Capacity credit takes into account the “peak demand correlation” shown in Figure 4-1, the likelihood that generation occurs at times of critically high demand. The revenue in LACE takes into account revenue from time of production and capacity credit; thus, LACE assumes that the power plant participates in both energy and capacity markets over its lifetime. Once the LACE and LCOE for a system have been calculated, the Net Value (NV) of the system can be calculated as

$$NV = LACE - LCOE \quad (4-3)$$

Note that a positive NV indicates a net profit and a negative NV indicates a net loss.

One of the main obstacles to renewable energy system designers moving beyond LCOE when optimizing a system is the need to model energy price. To simplify that process, a linear relationship between price and residual demand is proposed and combined with a simple demand profile to model price. A key assumption in this method is that the revenue from direct electricity production for VRE sources is much more significant than the revenue from capacity and other grid services. As described in the Introduction, energy markets currently dominate and while VRE generators qualify for varying capacity values by region, technology, and current regulations, their typical capacity value is only a fraction of total installed VRE capacity [106]. While this neglects a potentially important source of revenue for VREs, this assumption allows a simpler and more direct model to calculate value.

Residual demand (or residual load) is the demand that must be met by conventional energy sources once VRE production has been subtracted from the total energy demand.

$$\text{Residual Demand} = \text{Demand} - \text{VRE production} \quad (4-4)$$

The proposed linear relationship between spot market prices and residual demand has already been demonstrated by von Roon [107]. The study found a strong linear correlation between spot market prices of electricity and residual demand in Germany between 2007 and 2009 (e.g. Figure 4-2), with coefficients of determination between 0.54 and 0.77 [107]. Using residual demand as a key variable in models that predict price has become a recent topic of many papers as well [108–111].

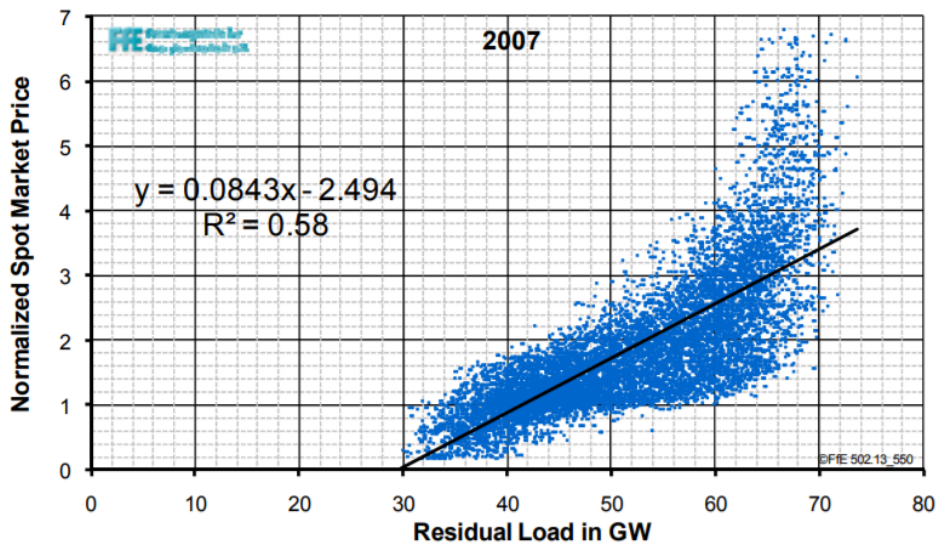


Figure 4-2. Spot Market Price from European Energy Exchange (normalized here by natural gas price) versus Residual Load [107]

Herein, we express this residual demand relationship in a normalized fashion that will be adapted to develop our models for LACEs and COVE.

$$p = mR + const. + X' \quad (4-5)$$

In this expression, m is the price-demand slope (a relationship which also depends on region and renewable energy shares), p is the hourly spot price divided by the time-averaged annual spot price, R is the hourly residual demand divided by the annual average demand, and X' reflects the variations due to extrinsic factors (such as those found in in Figure 4-1) which average to zero. As such, X' can be thought of as random fluctuations (as in a Markov chain) relative to the residual demand information.

Continuing with the model of Eq. 4-5, R can be replaced with D (hourly demand divided by the annual average demand) and Q (the hourly VRE generation divided by the annual average demand). Additionally, fluctuations in X' will be ignored herein as stochastic noise in the data set, simplifying the analysis but also introducing potential bias in the linear fit if X' is not normally distributed with a mean of zero.

$$p = m(D - Q) + const. \quad (4-6)$$

Note that an increase in demand or a decrease in VRE generation causes a price increase, a well-known trend in energy economics [18,108,112]. The constant in Eq. 4-6 can be determined by taking the annual time-average of Eq. 4-6 and noting $D_{avg} = p_{avg} = 1$, yielding

$$1 = m(1 - Q_{avg}) + const. \quad (4-7)$$

If one separates VRE production into average and variable components as $Q = Q_{avg} + Q'$, then Eqs. 4-6 and 7 can be combined and rearranged as

$$p = mD + (1 - m) - mQ' \quad (4-8)$$

When price, demand, and VRE data are all available for a location over a one-year period, an m -value can be fit to the data to predict price given a model for future demand and VRE generation data. However, when VRE generation data is not available, a simpler but less accurate correlation can still be found by neglecting Q' , whose average is zero (as was the case for X') given how it was defined. Modeling the price in this way yields

$$p = mD + (1 - m) \quad (4-9)$$

Note that the additional uncertainty that comes from ignoring mQ' in Eq. 4-9 is likely to increase with increasing VRE shares.

As an alternative for LCOE (Eq. 4-1), we define an original metric, the Cost of Valued Energy (COVE), by weighting the energy produced with the normalized market value at the time of production.

$$COVE = \frac{\text{Annualized Costs (Capital + O\&M)}}{\int p * g dt} = \frac{\Sigma \text{costs}}{\int [mD + (1 - m)] * g dt} \quad (4-10)$$

The last form of COVE in Eq. 4-10 employs the linear price relationship of Eq. 4-9 (which assumes $Q' = 0$), but could instead employ Eq. 4-8 if Q' is known. When $m = 0$, $LCOE = COVE$ indicating that energy has the same effective value no matter when it is produced. However, when $m > 0$, hourly generation is scaled up or down based on the modeled hourly spot price. As such, COVE can better incorporate the value of energy production, as well as the cost of the investment and operation, all in one metric. Thus, COVE improves upon LCOE to support a design process that better aligns with the expected profitability of the VRE asset. COVE is similar to rsLCOE when the benchmark price of rsLCOE is chosen to be the annual average spot price; however, COVE applies the linear price-demand assumption while rsLCOE has a broader definition of value and is thus more involved to calculate.

As an alternative for LACE (Eq. 4-2), we similarly define herein a simplified LACE (LACEs) which ignores capacity payments and estimates price with Eq. 4-9.

$$LACEs = \frac{\int [mD + (1 - m)] * g dt}{\int g dt} \quad (4-11)$$

This metric only requires the annual average spot price, the price-demand slope m , the time variation of energy demand, and the time variation of energy generation. It can be used in place of LACE to evaluate the relative potential economic performance of various engineering systems.

The two new metrics defined above are mapped out with relevant components in Figure 4-3. COVE starts with the components of LCOE then adds energy and demand data to estimate value. Furthermore, LACEs takes into account revenue from the energy market but excludes Capacity Credit, unlike standard LACE.

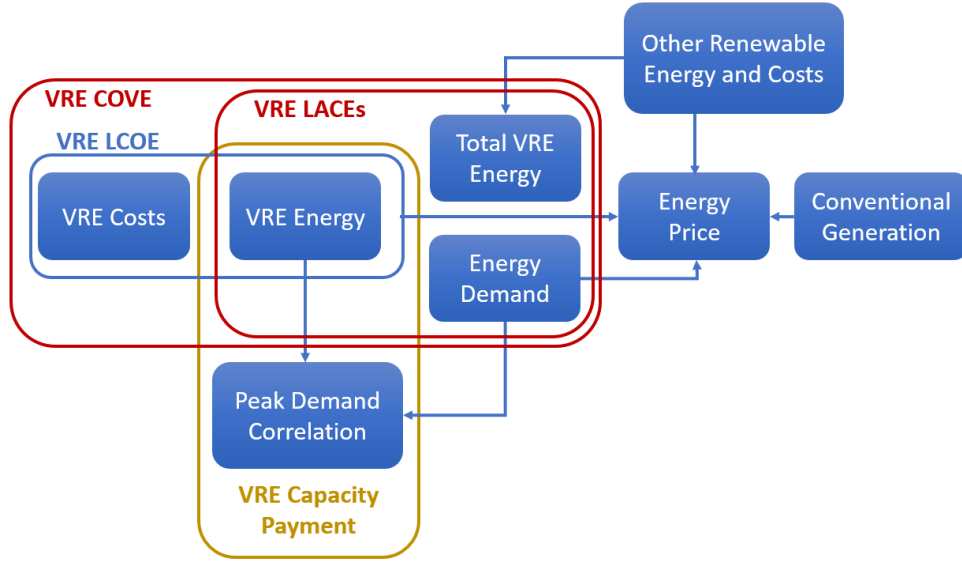


Figure 4-3. Energy components of newly proposed (COVE and LACEs) and conventional metrics

To aid in characterizing the economic performance for different VRE systems, the Value Factor (VF) is a useful measure that removes the relative costs of different technologies to focus on just energy value. To evaluate how well the linear relationship to modeled demand can predict spot prices, VF is computed in three different ways (in order of decreasing accuracy) as follows using: actual prices (conventional approach), demand-estimated prices, and modeled demand- estimated prices:

$$VF = \frac{\int p * g dt}{\int g dt} \quad (4-12)$$

$$VF = \frac{\int [mD + (1 - m)] * g dt}{\int g dt} \quad (4-13)$$

$$VF = \frac{\int [mD_m + (1 - m)] * g dt}{\int g dt} \quad (4-14)$$

Note that VF is dimensionless since it takes out the effect of the average annual spot price (given p is hourly spot price normalized by annual average spot price) and is related to the herein proposed cost metrics via

$$VF = \frac{LACEs}{p_{avg}} = \frac{LCOE}{COVE} \quad (4-15)$$

As such, the fidelity of VF using direct demand (Eq. 4-13) or modeled demand (Eq. 4-14) will represent the relative fidelity for COVE and LACEs.

4.3. Results

In the following, the linear relationship between price and demand will be investigated, followed by a model for the seasonal variations in energy demand. Finally, wind and solar data will be employed to estimate VF and determine the accuracy of the linear price-demand relationship.

A. Demand-Based Price Estimation

To test the demand-based value relationship of Eq. 4-9 (used by Eqs. 4-10 and 11), the price as a function of demand is shown for a one year period in Figure 4-4 for three different regions where data is publicly available to perform the analysis: PJM (a regional transmission organization in the Mid-Atlantic region of the US) [a,b]; Queensland, Australia [c]; and Ontario, Canada [d]. A linear regression for each location is shown as a straight line on all three plots, indicating the price-demand slope (represented by the m -value). For the PJM region, $m=1.5$, while larger values are found for the other two regions. Note that $m>1$ indicates that price will go negative as demand goes to zero, consistent with other recent studies [113,114]. As expected, the variation in actual price about this sloped line is large since it ignores factors associated with both extrinsic factors (X') and VRE variation (Q').

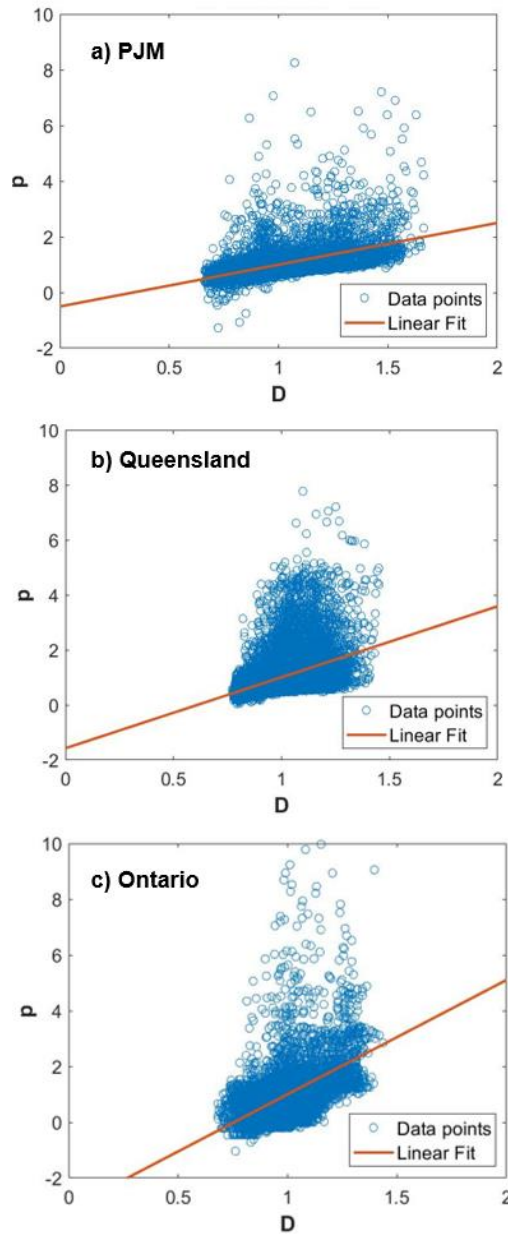


Figure 4-4. Hourly energy price (normalized by the average annual price) as a function of hourly demand (normalized by average annual demand) along with linear fit models for: a) PJM with $m = 1.5$, b) Queensland with $m = 2.53$, and c) Ontario with $m = 4.1$

It is interesting to consider how the price-demand slope correlates with generation mix, including the share of renewable energy, for each region. Queensland generates most of its electricity from coal power with a growing share of solar energy [e]; Ontario generates most of its power from nuclear and a large portion from hydropower and wind [f]; PJM generates power from coal, nuclear, and natural gas, with a

small portion of renewables [g]. Note that hydropower and biofuels are not considered in the renewable energy share due to their lower variability compared to the high intra-diurnal variability of wind and solar.

As shown in Figure 4-5, regions with higher VRE shares tend to have an increased price-demand slope. This is even true for PJM when comparing 2016 data to 2017 data – considering that the system generation mix is different from one year to the next. While the set of data is too small to draw a statistically relevant conclusion, one may infer from these cases that the share of VRE in the system is a key determinant of the price-demand slope. One exception is the von Roon data [107], which does not seem to follow this relationship. However, that data point was difficult to convert into the appropriate units using only the data provided in the paper, and thus may or may not be representative of the larger trend.

Based on Figure 4-5, an approximate relationship between price-demand slope and VRE is given as

$$m \sim 1 + 0.34 Q_{avg} \quad (4-16)$$

This relationship is consistent with the expectation that $m=1$ for a system with no VRE and that m increases as VRE penetration increases. However, this may only be reasonable for low VRE shares (under 10% in the cases studied), since the impact of variable generation for higher shares may become significantly non-linear. The calculation of m also does not address the variation in generation mix nor the impact of the interconnection and transmission connection on the relationship between energy prices and renewable shares.

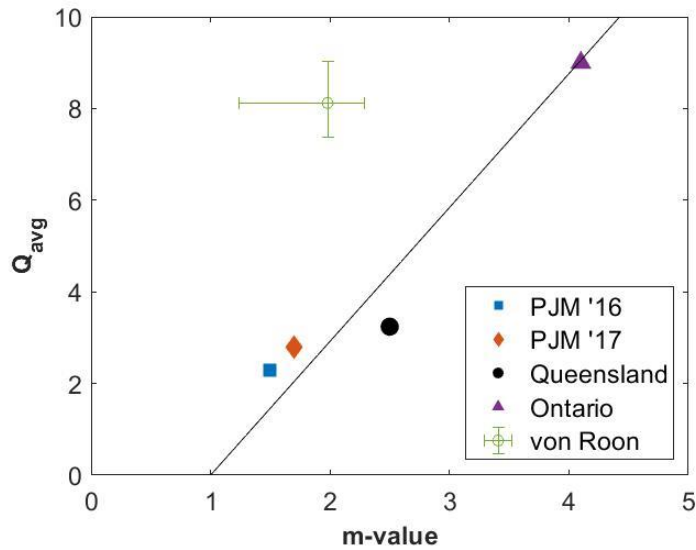


Figure 4-5. Price-demand m-values compared to renewable energy shares of total generation (Q_{avg}) for PJM (2016), PJM (2017), Queensland (2016), Ontario (2015), and estimated value from von Roon [107] for residual demand in Germany in 2008, as well as a linear fit given by $Q_{avg} = 2.92m - 2.92$

B. Proposed Model for Demand

In the following, the region of PJM (which has a large and publicly available set of self-consistent data on demand, generation, and prices) is used to construct a demand model and to assess COVE and other metrics. While real-time data is the most accurate to use for demand (as was used in Figure 4-4), a “standard demand” weekly profile is used to simplify modeling. Herein, three weekly standard profiles are developed based on seasons (summer, winter and spring/fall) by averaging weeks of Mid-Atlantic region demand data from PJM for 2016-2018 [b]. These are compared in Figure 4-6 to a randomly selected week of real demand for each season.

These standardized demand curves were used to create a “standard year” of modeled demand (D_m) by stringing together these seasonally-averaged weeks so that total demand is comparable to a year of actual demand data (Figure 4-7). For PJM, the season durations of winter, spring, summer, and fall were set as 16, 11, 17, and 8 week periods, to best match the real demand data for a year. While the length of each season may vary regionally, the general shape of the demand curves is typical of most regions in the USA [h]. This standard year of demand was created to smooth out single year irregularities which may occur due to weather, power plant or transmission downtime, regulation changes, etc. The differences between demand and modeled demand seen in Figure 4-7 are examples of these irregularities which will vary year to year.

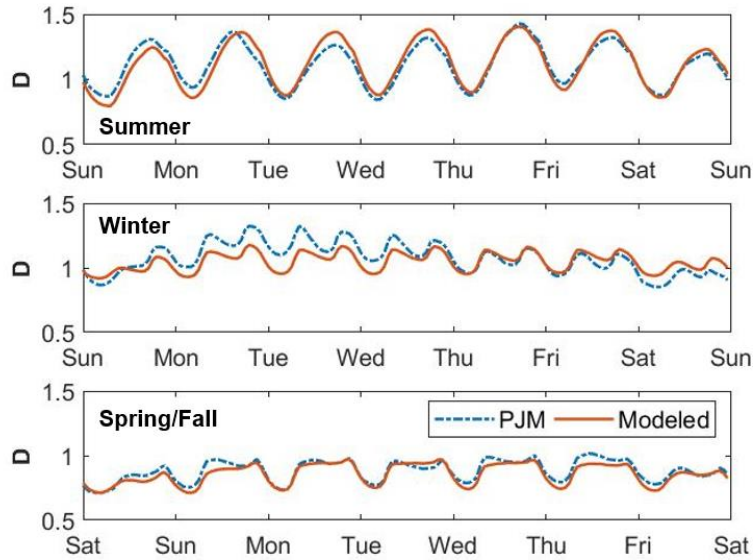


Figure 4-6. Seasonal demand profiles normalized by the annual average demand for a sample PJM week and for season-averaged (modeled) PJM week

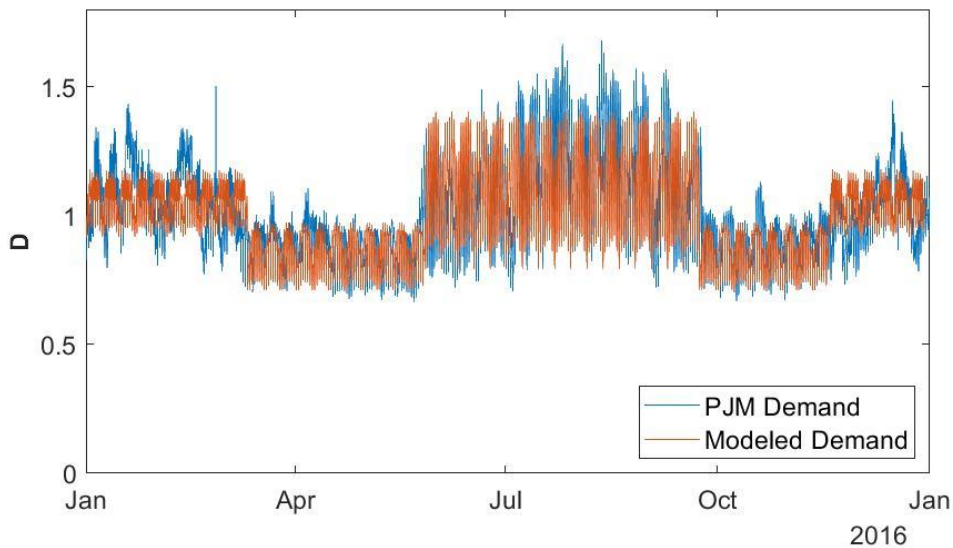


Figure 4-7. Normalized 2016 PJM demand data compared to standard year of demand created using season-averaged (modeled) PJM data

To assess the accuracy of the standard year of demand, the Root Mean Square Error (RMSE, Eq. 4-17) was used to evaluate how well real hourly demand was predicted. The modeled year of demand was compared to three years of real hourly demand; the three years of demand were also compared to each other. The results in Table 4-1 show that using the modeled year of demand results in differences on the

same order as real demand; in fact, the modeled demand predicted all three years of demand with lower RMS Errors than using real years of demand. Thus, in this case, the standard year of modeled demand is preferred over using a single year of demand data to predict other years of demand.

$$RMSE = \sqrt{\sum_{i=1}^N \frac{(x_{predicted,i} - x_{observed,i})^2}{N}} \quad (4-17)$$

Table 4-1. Annual RMS Error comparing the difference between years of demand

	Modeled Demand	2017 Demand	2018 Demand
2016 Demand	0.0256	0.0393	0.0340
2017 Demand	0.0319	-	0.0333
2018 Demand	0.026	-	-

C. VRE Generation Data

Hourly generation data is needed to evaluate COVE and LACEs (via Eqs. 4-10 and 11). While historical data is the most accurate to use (as was used in Figure 4-4), generation can also be estimated from wind resource data, solar radiation (insolation) data, and other plant output. To simulate future scenarios of solar and wind deployment in the region of Virginia (within the PJM region) hypothetical hourly generation distributions were obtained to represent generation from future installations of utility-scale VRE power plants. For solar energy generation, PV production data was gathered from a University of Virginia solar installation with a maximum output capacity of 126 kW for 2017-2018 [i]. Note that the size of the installation does not matter (for the assumption of small solar share) as it is nondimensional in the analysis below. For wind generation, offshore wind energy (expected to be a significant player in Virginia in the future) was employed by using one year of wind data at 90m from the DOE BUOY project off the Virginia coast [j] combined with the NREL 5 MW offshore wind turbine power curve [115] to calculate expected hourly wind power data. As with solar, the size of the wind turbine plant and the plant loss factor do not factor into this analysis. This simplification enables easier analysis of scaling the VRE generation up and down but does not account for the potential correlation (positive, neutral or negative) of VREs that are distributed geographically, which can mitigate against some of the impact to the price-demand relationship in a region [116–119].

The above example wind and solar data from locations within the Mid-Atlantic PJM region was used to investigate the potential correlation between generation and hourly demand before applying the linear price-demand model. Standard summer and winter demand curves are shown in Figure 4-8, along with a representative week of solar energy production and wind energy production for each season with hypothetical shares of 10%. In addition, the resulting residual demand for the summer only is shown in Figure 4-9 for both solar and wind. As can be seen in Figure 4-8a and Figure 4-8b, there is a general correlation of solar energy production with demand, but the evening rise in demand is not well correlated to solar energy, leading to a rise in residual demand during that portion of the day (seen in Figure 4-9a), a phenomena known as the “duck curve” [116,120]. In contrast, wind energy based on PJM offshore data as shown in Figure 4-8c and 8d is more stochastic with little correlation between production and demand and higher wind seen in the winter than summer. As such, the residual demand for wind is relatively stochastic about the standardized demand curve.

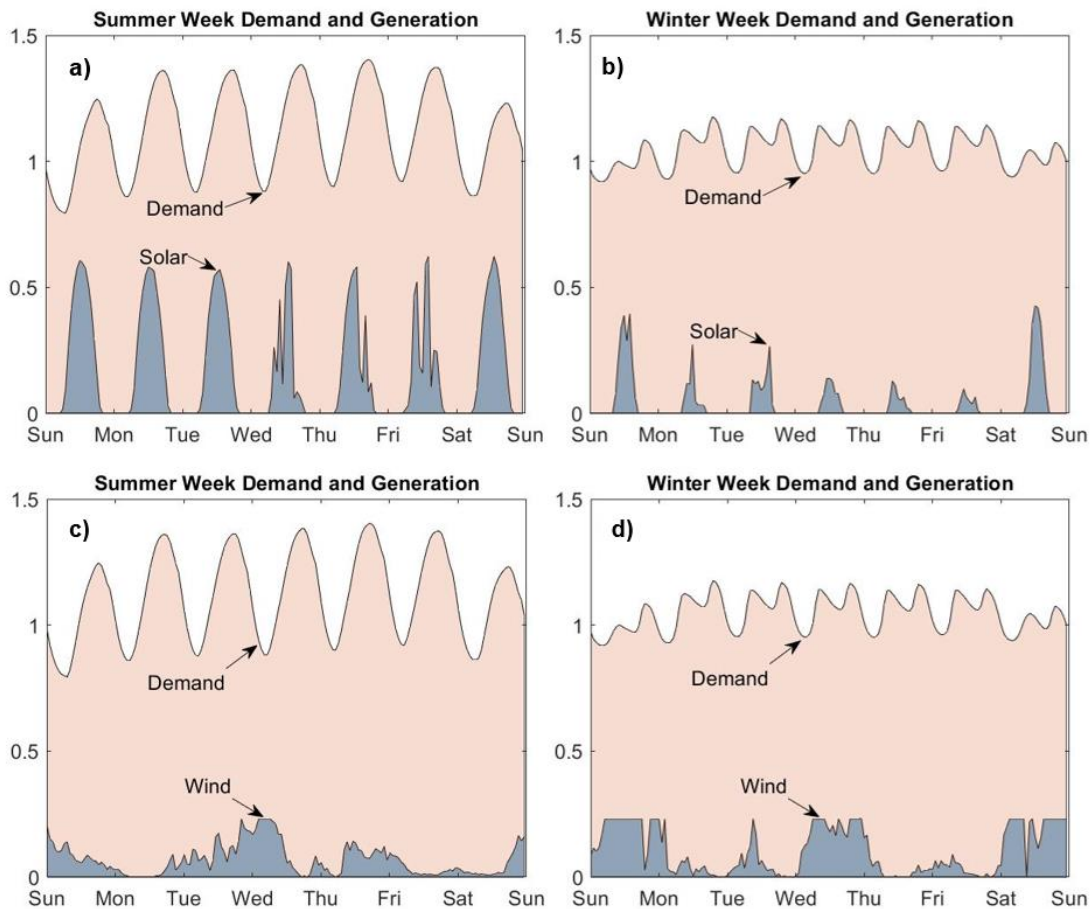


Figure 4-8. Electricity demand and generation for a hypothetical solar $S_{avg}=0.1$ (a,b) and a hypothetical wind $W_{avg}=0.1$ (c,d) for an example week in the summer and winter

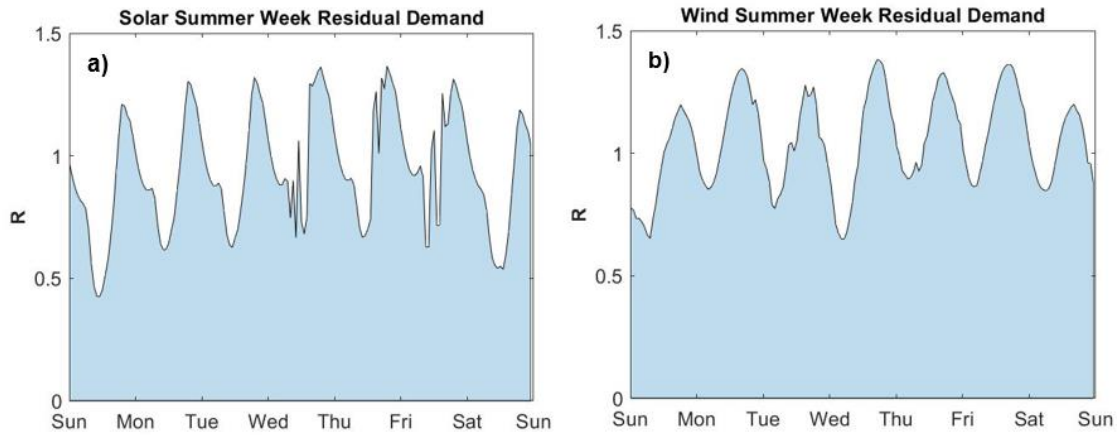


Figure 4-9. Residual Demand over summer week with hypothetical $S_{avg}=0.1$ solar generation (a) and $W_{avg}=0.1$ wind generation (b)

D. Value Factor Validation

Pulling together the price, demand, and generation data described above, VF was calculated by Eqs. 4-(12-14) for wind and solar. The results are shown in Table 4-2a, where Eq. 4-12 is applied to three years of real price data for PJM. The average and standard deviations of the error using the linear price model with demand and modeled demand (both relative to real-time price data) are given in Table 4-2b. While wind and solar VFs see similar errors when using the linear model with real-time demand, solar VF has a larger error than wind VF when using modeled demand. However, the VF errors are generally small, especially given the simplifications and assumptions associated with the linear-price model and the standardized demand curves.

Table 4-2a also gives important information about the relative values of wind and solar installations at low share of VRE penetration. Wind tends to have a VF close to 1 since its generation is largely stochastic and does not often correlate positively or negatively with demand. However, solar tends to have a higher VF that is above 1 since its generation often aligns with times of high demand, especially during the middle of the day.

Table 4-2. Value Factor for wind and solar examples: a) calculated with real price data (p) for PJM for 3 consecutive years, a linear relationship with a real demand (D), and a linear relationship with the modeled demand (D_m); and b) Percent error of real price data for the demand and modeled demand VF models.

a)

VF	Wind	Solar
using p (2016)	0.974	1.185
using p (2017)	1.012	1.133
using p (2018)	0.995	1.119
using D	0.972	1.114
using D_m	0.966	1.080

b)

VF	Wind		Solar	
	Avg. % Error	Error St. Dev.	Avg. % Error	Error St. Dev.
using D	2.20%	1.88%	2.68%	2.94%
using D_m	2.77%	1.86%	5.65%	2.85%

Figure 4-10 indicates the sensitivity of VF to price-demand slopes (associated with changes in VRE penetration per Figure 4-5) using the example wind and solar PJM data. The m -values for each of the three evaluated regions are denoted with vertical dashed lines, while the VF calculated with real spot prices (from Table 4-2a) are denoted with points. The spot price data (Eq. 4-12) falls close to the predicted trends for solar and wind (Eq. 4-14), but the modeled-demand values tend to under-predict VF. This may be attributed to over-smoothing of demand data, which reduces modeled price spikes and dips. It is recommended that further data should be collected from other regions with different VRE shares, generation mixes and demand profiles to better characterize the fidelity of modeled-demand VF.

For a given region, Figure 4-10 shows that solar and wind will have significantly different VFs, even for a moderate price-demand slope of $m=1.5$. This illustrates the relative benefit of solar's higher correlation of generation with demand, which only becomes more extreme with increasing m . For example, if PJM were to shift over time to $m=4.1$, solar would earn nearly a 50% higher VF than wind, using the linear price-demand relationship.

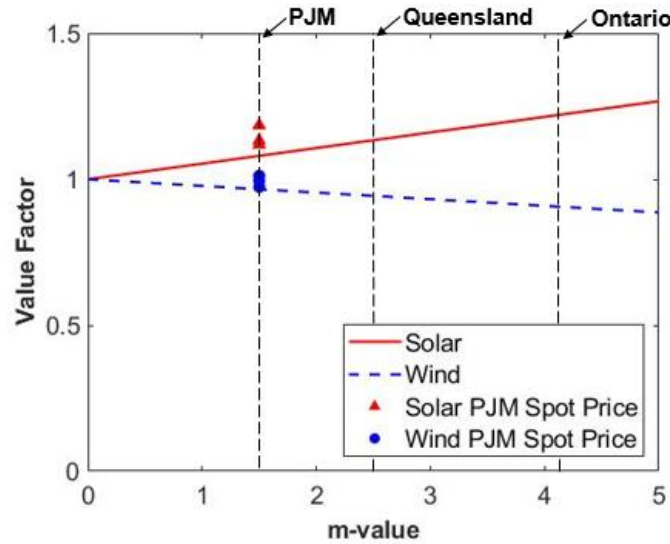


Figure 4-10. Value Factor as a function of changing m values based on actual price for 2016, 2017, and 2018 (symbols) and modeled price (lines)

4.4. Wind turbine design case study

To illustrate the trade-offs in design that can affect LCOE and COVE, a simplified example of the preliminary design of an individual wind turbine is considered. While this example focuses on wind turbine design, the approach could be similarly used for photovoltaic panel design, or even the design of entire wind and solar power plants. Conventionally, a designer optimizes the turbine design to produce as much energy as possible (within design load specifications) at the lowest possible cost for a given wind class and machine rating. Designing in this way to minimize LCOE may not be economically optimal. As an example of the separate influence of COVE beyond LCOE, we consider the influence of rotor size on the system design and value. From a pure LCOE perspective, “growing the rotor” for a fixed rating may have limitations, since the mass of the turbine can outpace the increase in power capture. However, increasing the rotor size relative to machine rating shifts the wind turbine power curve to allow for more energy capture at lower wind speeds and thus increases the Capacity Factor (CF) of the machine for a given site. With advances in technology, it may be possible for LCOE to not vary significantly with increasing rotor diameter [33,121].

The effect of CF variations is considered in an example case study using the offshore Virginia wind dataset. In particular, a set of turbine designs are considered for a fixed generator rating (5 MW) but with a range of rotor diameters (from 90 m to 180 m) and corresponding power curves. The result of the variation in rotor diameter on COVE (for a fixed LCOE) is shown in Figure 4-11, using Eq. 4-10 with two different

m -values: one based on the current PJM region ($m = 1.5$), and one based on Ontario ($m = 4.1$), representative of a region with higher VRE shares. Based on the results in Table 4-2, an estimated error of +/-2% is included in this plot as a shaded region to illustrate the potential uncertainty of the COVE trends. However, this uncertainty may be higher in regions with greater share of VRE, and there may be additional error from assuming that LCOE changes are negligible over the range of rotor sizes considered.

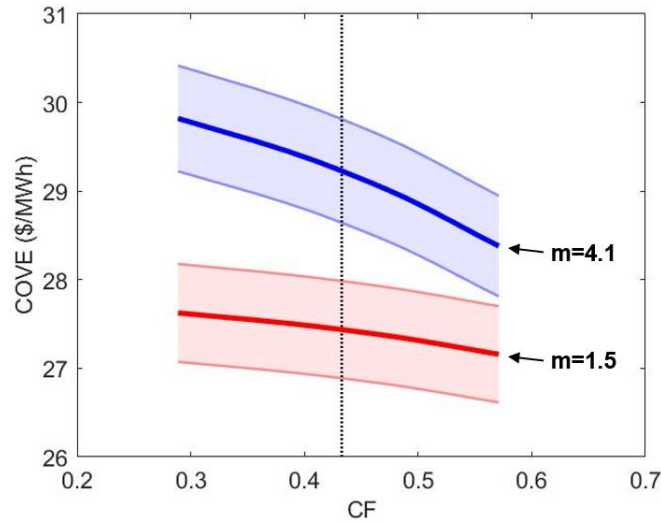


Figure 4-11. Influence of Capacity Factor (CF) on Cost of Valued Energy (COVE) where PJM $p_{avg} = 27.4 \text{ \$/MWh}$ and $LCOE = 26.5 \text{ \$/MWh}$ (for future plausible design) with two different m -values applied. The baseline CF of 0.43 is denoted with a vertical dotted line.

For this particular dataset, wind has a slight negative correlation with demand, and increasing Capacity Factor is shown to mitigate this effect, resulting in a favorable decrease in COVE (Figure 4-11). While the reduction in COVE is almost negligible for $m = 1.5$, a significant range of $\$1.5/\text{MWh}$ in COVE is seen with $m = 4.1$. This indicates that a region with a higher share of VRE will generally have a greater benefit when increasing the CF of a wind turbine.

The economic perspective that COVE provides for VRE system design can be shown more explicitly by considering the Return on Investment (ROI) for a particular wind turbine design. ROI is a common profitability metric used by investors to compare business options and economic performance of a system.

$$ROI = \frac{Revenue - Costs}{Costs} = \frac{p_{avg} * \int pg dt}{\Sigma costs} - 1 \quad (4-18)$$

Maximizing ROI is a useful overall objective from a system design and investment perspective. ROI can be approximately related to the herein proposed cost metrics as

$$ROI = \frac{NV}{LCOE} = \frac{p_{avg}}{COVE} - 1 = \frac{p_{avg} * VF}{LCOE} - 1 \quad (4-19)$$

However, the actual ROI depends on a variety of factors including the economic components in Figure 4-1. As such, the above is only a first-order approximation of ROI with respect to the influence of COVE (or VF or LACE). For the sake of this analysis, the potential *change* in ROI as a function of the cost metrics is used:

$$\Delta ROI = \Delta \left(\frac{p_{avg}}{COVE} - 1 \right) = \Delta \left(\frac{p_{avg} * VF}{LCOE} - 1 \right) \quad (4-20)$$

While many other factors outside of energy spot price influence ROI, Eq. 4-20 can be used to directly relate the influence of COVE on ROI. This relationship also shows that minimizing COVE (or equivalently maximizing VF while minimizing LCOE), may result in different design decisions than only minimizing LCOE, since LCOE does not take into account design trade-offs between producing higher value energy and producing energy for the least cost. In the present wind turbine case example, the result of the variation in capacity factor (through rotor diameter) on the change in ROI (for a fixed LCOE) is shown in Figure 4-12 using Eqs. 4-10 and 20 with two different *m*-values. While there are significant uncertainties that are not accounted for in this simple model, the results show that increases in CF (assuming a fixed LCOE) can lead to significant improvement in ROI.

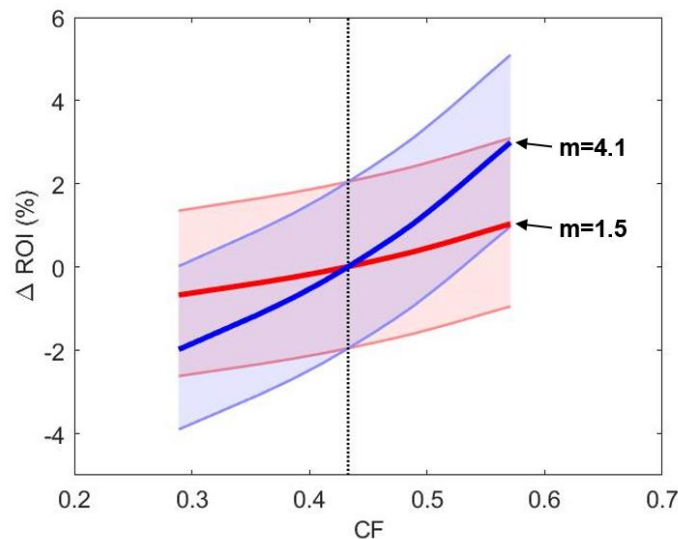


Figure 4-12. Influence of Capacity Factor (CF) on change in Return on Investment (Δ ROI) with two different *m*-values applied. The baseline CF of 0.43 is denoted with a vertical dotted line.

Limitations of this method include that COVE and ROI values calculated with Eq. 4-9 neglect variations in Residual Demand that will arise if VRE penetration increases. If Residual Demand data were available, Eq. 4-8 could be used to predict price, which does not neglect the variations described by Q' . Including this additional information is likely to increase the model accuracy, a hypothesis which is recommended for future investigation. This information may also increase the sensitivity of COVE to CF when designing a wind turbine for use in a region with high wind shares; an increased capacity factor would reduce the negative impact of producing energy at times of low price (i.e. at low residual demand due to high wind production), creating an enhanced levelization advantage.

4.5. Conclusions and Future Outlook

To improve upon the conventional use of LCOE for design of wind turbines and solar panels, as well as full wind and solar power plants, two relatively simple metrics, COVE and LACEs, are developed herein to take into account the changes in energy value and the time of generation. Using the proposed linear price-demand relationship combined with the LCOE value, LACEs and COVE can be obtained using: 1) season-based standardized weekly demand curves (D_m), 2) a price-demand slope (m) that is related to VRE penetration, and 3) predicted hourly VRE generation data. Both metrics are more straightforward to employ as compared to utility-based metrics, such as sLCOE or rsLCOE, which are more suited to grid-level decisions. As such, these simplified models can be helpful to VRE system designers during the initial stages of the design process.

The wind turbine design example showed that the ROI for a particular wind turbine design could be improved by increasing the CF through increasing the rotor diameter for the given machine rating (assuming LCOE remains unchanged). It also showed that for a region with low m (such as PJM), ROI is relatively insensitive to changes in rotor diameter, but a higher m region sees more significant effect on ROI with changes to rotor diameter. As a single, simple metric, COVE is able to directly relate to ROI for design decisions such as this one.

Future recommendations include additional data surveys for this design metric using a range of price and demand datasets in different regions, with varying levels of VRE shares, profiles of the overall generation mix, levels of transmission build-out, and demand profiles. The potential future work may also investigate extending COVE or LACEs to include aspects related to the technology capacity value and capacity payments and also for VRE power plants that include storage technologies. Finally, the impact of using COVE or LACEs on the design of renewable energy systems should be investigated to understand how the objectives influence the designs compared to traditional LCOE objectives.

4.6. Data references

- [a] [dataset] PJM Interconnect LLC. Data Miner 2. Real-Time Hourly LMPs. Historical Pricing Data 2016-2017, Mid-Atlantic Region. 9/7/18. https://dataminer2.pjm.com/feed/rt_hrl_lmpps/definition
- [b] [dataset] US Energy Information Administration. Demand for PJM Interconnection, LLC (PJM), Hourly data 2016-2017. 8/28/2018. <https://www.eia.gov/opendata/qb.php?category=2122628&sdid=EBA.PJM-ALL.D.H>
- [c] [dataset] Australian Energy Market Operator. Data Dashboard. Aggregated Price and Demand Data 2016. Queensland. <https://aemo.com.au/Electricity/National-Electricity-Market-NEM/Data-dashboard#aggregated-data>
- [d] [dataset] Independent Electricity System Operator. Power Data 2015. Data Directory. Ontario. <http://www.ieso.ca/en/power-data/data-directory>
- [e] [report] Department of the Environment and Energy, Australian Energy Statistics, Table O4 – Electricity generation in Queensland, by fuel type, physical units. April 2018. https://www.energy.gov.au/sites/default/files/aes-table-o-2016-17_2017.pdf
- [f] [report] Ontario Planning Outlook. *A technical report on the electricity system prepared by the IESO*. Sept. 1, 2016.
- [g] [report] Monitor Analytics. 2017 State of the Market Report for PJM. Table 3-10 PJM Generation. https://www.monitoringanalytics.com/reports/PJM_State_of_the_Market/2017.shtml
- [h] [website] US Energy Information Administration. US Electric System Operating Data, Balancing authority electricity demand. 4/12/2019 https://www.eia.gov/realtime_grid/#/status?end=20190412T12
- [i] [dataset] University of Virginia Facilities Management. Clemons Library Solar Array. 10/9/2018. <https://renewableenergy.fm.virginia.edu/>
- [j] [dataset] US Department of Energy. Buoy. Offshore Wind Energy – Buoy Lidar Project. Virginia Deployment. 8/27/2018 <https://a2e.energy.gov/projects/buoy>.

Chapter

5. Techno-economic analysis of Liquid Metal Battery storage in an offshore wind turbine

Abstract

As wind energy increases its global share of the electrical grid, the intermittency of wind becomes more problematic. To address the resulting mismatch between wind generation and grid demand, long-duration (day-long) low-cost energy storage is offered as a potential solution. Lithium-ion (Li-ion) storage is an obvious, well-developed candidate, but it is currently too expensive for such long-duration applications. Liquid metal battery (LMB) storage offers large cost reductions and recent technology developments indicate it may be viable for MW-scale storage. Accordingly, we investigate co-locating and integrating LMB and Li-ion storage within the substructure of an offshore wind turbine. Integration allows the substructure to cost-effectively double as a storage container and allows for costly electrical farm-to-shore connections to be reduced to near the average power size (by reducing peak power). These benefits are compared to the costs for battery integration. Simulations show that line size can be reduced by 20% with 4 hours of storage or by 40% with 12 hours of storage, with negligible capacity factor losses. However, with 24 hours of average power storage using LMB, no line size reduction provided the best overall net value of the turbine-storage system due to the ability to capture all available wind energy and profit from energy arbitrage and full capacity credit. In general, LMB integrated storage results in an increased relative value with current system costs. Projected technology trends indicate that these benefits will significantly improve and that integrated Li-ion storage will also become cost-effective.

Nomenclature

Symbols

C	Battery C rate [1/hrs]
G	Energy generated [MW]
k	Heat transfer coefficient [W/m-k]
P	Power [MW]
q	Heat rate [kW]
r	Radius [m]
t	Thickness [cm]
T	Temperature [°C]
V	Battery volume [m ³]
W	Wind speed [m/s]
η	Charge or discharge efficiency [%]

Subscripts

avg	Average power
b	Battery
$heater$	Heater
i	Insulation
$Joule$	Joule heating
$loss$	Heat loss
$rated$	Rated power
$storage$	Storage system
$total$	Combined system
$turbine$	Wind turbine system
w	Water
$wall$	Substructure wall

Abbreviations

AEP	Annual energy production [MWh/yr]
BOS	Balance of station
CapEx	Capital expenses [\$]
CC	Capacity credit [%]
CF	Capacity factor [%]
CP	Capacity payment [\$/yr]
CV	Capacity value [\$/MW-day]
FCR	Fixed charge rate [1/yr]
LACE	Levelized avoided cost of energy [\$/MWh]
LCOE	Levelized cost of energy [\$/MWh]
Li-Bi	Li LiCl-LiBr-LiI Bi battery chemistry
Li-ion	Lithium-ion
LMB	Liquid metal battery
MGP	Marginal generation price [\$/MWh]
NV	Net value [\$/MWh]
OpEx	Operating expenses [\$/yr]
SCAPP	Storage capacity at average plant power [hrs]
SCRPP	Storage capacity at rated plant power [hrs]
VSD	Variable speed drive

5.1. Introduction

Wind energy already provides more than a quarter of the electricity consumption in three countries around the world [2], and its share of the energy grid is expected to grow as offshore wind technology matures. The wind speeds on offshore projects are much steadier and faster than wind speeds on land, and offshore wind provides a location that is close to high demand coastal areas and avoids space constraints [122].

However, as grid penetration from variable (inconstant) renewable sources increases worldwide, their intermittency becomes more problematic [123]. As seen in Figure 5-1, wind generation does not align well with times of electricity demand. Furthermore, the relative value of wind energy decreases when it

becomes a larger fraction of the grid generation [18,19]. When in demand, renewable energy sources may have a high value compared to baseload generation, e.g., such as when solar produces power during the day at times of relatively high demand. However, the value of these resources falls when a glut of renewable energy with no marginal cost enters the market and depresses prices or forces curtailment of renewable resources [18,96]. This issue is expected to intensify since the electrical market structure is moving away from a purely energy-based market and towards a structure with greater focus on capacity and grid services [91]. While some have suggested improving forecasting methods to better handle renewable energy on the grid [124], another potential way to deal with these issues is to install high-capacity energy storage that can shift the time of generation to times when demand is stronger [20]. This will require a low-cost energy storage solution that can provide storage for hours or even days. In this future, renewable energy could increase its value significantly by pairing with storage systems, allowing it to participate in capacity markets, energy arbitrage, and auxiliary services.

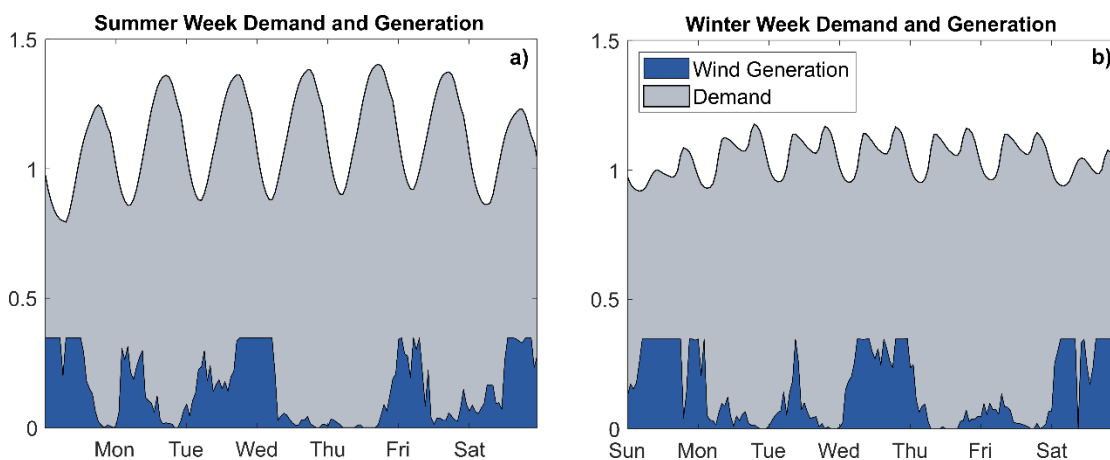


Figure 5-1. Offshore wind energy generated at 15% penetration compared to electrical grid demand (both normalized by annual average) over a representative week for a) summer, and b) winter.

Multiple strategies have been pursued to optimize the operation of battery storage with variable renewable energy. These include reducing the error between the forecasted wind power and the actual wind power [125,126], using a combination of energy storage and demand-side management [127], introducing incentives [128], and using large-scale transmission systems [129] to integrate high shares of wind energy.

One potential advantage to storage with wind energy is the ability to employ time-shifting for energy arbitrage. Previous work and modeling in energy arbitrage suggests that batteries are too expensive to breakeven in most arbitrage markets [130–133]. Salles [132] simulated energy storage systems in PJM (a mid-Atlantic electrical transmission organization) over 2008 to 2014 and found the best possible scenario

yielded enough revenue to breakeven with battery installed costs at \$200/kWh; however, other locations, during other years, required installation costs of half that value to break even [132]. As such, the more likely potential advantages to storage with wind energy are to time-shift the energy generated, balance the grid, and provide additional peak reserves [20,123].

Battery storage system capacity is typically quantified based on nameplate duration of discharge, or how many hours the battery can discharge at full rated battery power generation. Battery storage capacity is thus specified as, short-duration: less than 0.5 hours of rated capacity, medium-duration: 0.5-2 hours of rated capacity, or long-duration: more than 2 hours of rated capacity [134]. For grid applications, 4 hours of rated capacity may be more representative of “long-duration” storage [111,135]. This is an appropriate and critical quantification of the battery; however, for a storage system co-located and integrated with a plant, it is important to also consider the battery storage capacity relative to the plant power.

Thus far, battery storage systems co-located with wind turbines are small relative to turbine power generation. GE installed a wind farm consisting of 13 turbines, with total rated generation of 37 MW for their Tullahennel project in north-western Ireland, where each turbine is accompanied by a Li-ion battery to provide a total of 897 kWh of storage [136]. Deepwater Wind recently won a bid from the state of Rhode Island to build a 144 MW wind farm co-located with a 10 MW/40 MWh Tesla battery, with a goal of shifting energy production to meet peak demand [137]. The largest battery storage system in the world is the Hornsdale Power Reserve installed in South Australia in 2017; the system consists of 315 MW of wind power combined with a 100 MW/129MWh battery used primarily for the purposes of grid stabilization [138].

If one considers the battery capacity relative to the plant power (not the rated battery power limit), these installations would all store an hour or less of average wind power. While such energy storage capacity has not been commonly defined nor reported (to the author’s knowledge), this characterization can value the integrated performance of a system composed of an energy source and its associated energy storage. This is important as wind energy can have periods of little or no generation that exceed 12 hours as shown in Figure 5-1. A power spectral density analysis in [139], found that using energy storage to help smooth out the most common frequencies of wind power oscillation (12-hour and 24-hour) will likely require long-duration storage. As such, substantial levelization and/or demand-shaping requires storage in the range of 10-24 hours of average wind plant power [140]. Thus, if battery storage is going to be used to significantly levelize and control wind energy generation for day-to-day operation, then new storage options will be needed that are operable over much longer durations in the context of storage capacity relative to the plant average or rated power. In particular, none of the current or planned wind energy storage projects are able to address the majority of wind energy generation intermittency.

Therefore, there is significant interest in the potential benefits for energy storage systems that have the capacity to store a fraction of a day up to a full day or more of average power [141]. The solution would seem to indicate that more storage capacity is needed for a given wind farm. However, utility-scale energy storage for even day-long duration is currently prohibitively expensive with conventional battery technologies. Limited options for low-cost, high-performance energy storage are even inspiring hybrid energy storage systems instead [142].

As noted above, a key to employing long-duration energy storage for wind is to ensure that the capacity comes at low enough cost with respect to the benefits it can provide. The cost for electrical energy storage is often driven by materials, packaging, and level of development. Currently, the most commonly installed and well-developed electrical energy storage option is Li-ion batteries. Li-ion battery costs have dropped 85% from 2010-2018 [143], and battery pack prices have been projected to reach between \$62/kWh and \$76/kWh by 2030 [144]. Despite the declining prices, Li-ion batteries come with certain disadvantages, especially at MW-scale. They have a tendency to overheat, sometimes leading to thermal runaway and combustion [145,146]. Li-ion batteries also operate within a narrow temperature region and have significantly reduced performance outside that temperature region necessitating active thermal management systems [146]. Li-ion batteries can have a lifetime of more than 3500 cycles or 10 years operation with a wind farm, over which their capacity declines (since cycle life is nominally defined by 20% capacity loss) [147]. As such, integrated Li-ion batteries would need to be significantly oversized or replaced at least once during the 20-30 year life of a wind turbine to continue providing adequate storage capacity.

An alternative electrical storage option that has been developed in recent years and may be approaching commercial production is the liquid metal battery (LMB) [148–153]. These batteries feature low raw-material cost, high thermal resilience, and long lifespan, and thus are judged to be a good fit for large-scale energy storage [151]. Additionally, their chemistries are neither volatile nor flammable. The liquid metal electrodes and molten salt electrolyte must be operated at elevated temperature so as not to solidify. With proper insulation, LMB can maintain operating temperature by generating adequate heat while cycling (charging and discharging) without the need for auxiliary heaters [153]. This feature favors LMB for large-scale storage applications (MWh) rather than small-scale storage applications (kWh). This paper will focus on the working composition “Li | LiCl-LiF | Bi” as specified in [149] and herein referred to as “Li-Bi”, where the anode is Lithium, the electrolyte is LiCl-LiF, and the cathode is Bismuth. This composition will be used because it has operational metrics reported in the literature. However, Ambri, a company working to commercialize the LMB technology, has recently announced a new Ca-Sb battery

composition which is expected to exceed the high performance of Li-Bi while reducing the cost of storage even further to well below the projected price of Li-ion [153].

The significant benefits of long-duration storage for wind energy combined with recent developments in LMB technology suggest that this combination may have strong potential to address intermittency, especially offshore where storage can reduce farm-to-shore electrical connection costs. In order to investigate this hypothesis in a system-based cost-effective manner, the objectives of this work are: i) to develop a technical concept design for integrating LMB into a monopile offshore wind turbine to examine influence of storage capacity and electrical connection line size on overall capacity factor (Section 2), and ii) to determine the expected cost and value of such a wind-integrated battery system and compare these to those of a wind turbine with no energy storage and one with Li-ion battery storage (Section 3).

This is the first study, to the author's knowledge, that investigates integration of wind turbines with LMB storage and the first to consider offshore energy storage capacity factors and economics for long-duration storage. This study is also the first to parameterize the battery capacity relative to the average plant power generation (not just the battery rated generation power). This capacity parameter represents a change in perspective which characterizes the energy storage and the energy source as an integrated system. As the LMB concept combined with a wind turbine has not been explored before in terms of an engineering nor a cost basis, the present work is based on a first-order analysis to evaluate the leading factors that govern performance and cost.

5.2. Concept Design

A. Capacity at Average Plant Power

As discussed above, energy storage capacity is typically measured based on the discharge time at rated power. This gives hours of storage capacity in terms of rated battery power, i.e. the time it takes to drain the battery at the maximum discharge rate. However, when thinking about integrating an energy storage system with a power plant (such as a wind farm), we can also measure the storage capacity in relation to the output power from the plant. This approach means that as the generation scales up or down, the associated storage hours can stay constant while the actual capacity (in MWh) varies. Quantifying the integrated storage capacity can either be defined relative to the rated (maximum) power of the plant or the average power produced by the plant, where the plant may be a solar farm, wind turbine, nuclear generator, etc. For these definitions, the rated and average power are proposed to be defined as that without storage to ensure a consistent baseline reference. In particular, for the rated version, we define storage capacity at rated plant power (SCRPP) in hours as the ratio of total storage capacity (MWh) to rated plant power (MW)

$$SCRPP = \frac{\text{Total Storage Capacity (MWh)}}{P_{rated}(MW)} \quad (5-1)$$

However, since the typical goal of co-located storage is to smooth or level the output from a variable renewable power plant, the average power production is more germane. For this, we define the storage capacity at average plant power (SCAPP) as the ratio of total storage capacity (MWh) to the mean (or average) wind power (MW) in hours and relate this to the plant capacity factor (CF)

$$SCAPP = \frac{\text{Total Storage Capacity (MWh)}}{P_{avg}(MW)} = \frac{\text{Total Storage Capacity (MWh)}}{P_{rated}(MW) \times CF} \quad (5-2a)$$

$$CF = \frac{P_{avg}}{P_{rated}} \quad (5-2b)$$

The latter expression uses the conventional definition of plant capacity factor as the average power (P_{avg}) normalized by the rated plant power (P_{rated}). A typical photovoltaic solar system will have a CF of about 15% to 25% with predictable daily cycles while a typical wind turbine will have a CF of 30% to 50% with more irregular day-to-day, week-to-week and even season-to-season variations. Thus, storing one or more days of energy at average power (e.g. SCAPP > 24 hours) is needed to achieve nearly leveled wind energy generation. However, there are significant benefits for partial levelization and as such a range of SCAPP durations will be considered to provide the best net economic value for the integrated system.

B. Overview of Turbine for Storage Integration

We propose placing a battery storage system within the tower of an offshore wind turbine, as depicted in Figure 5-2a. The integrated battery storage would allow the wind turbine system to regulate when and how much power it is producing and control what power travels along the electrical lines to shore. The battery would interact with the variable speed drive (VSD) as depicted in Figure 5-2b, thereby removing the need for additional power electronics in the system [154,155]. Thus, DC power would travel along the turbine tower to and from the battery, while AC power would travel out of the VSD and through lines to shore.

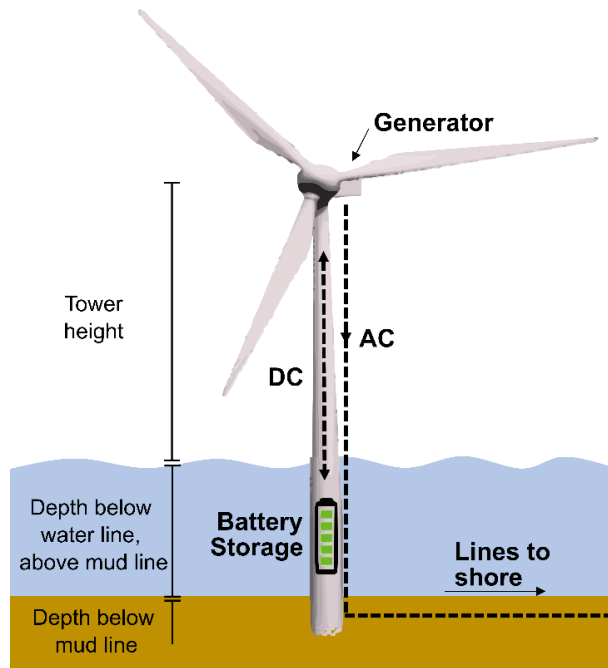


Figure 5-2a. Battery storage integrated into offshore wind turbine tower. Tower and substructure heights are denoted on the left and are specified for the NREL 5 MW turbine in Table 5-1.

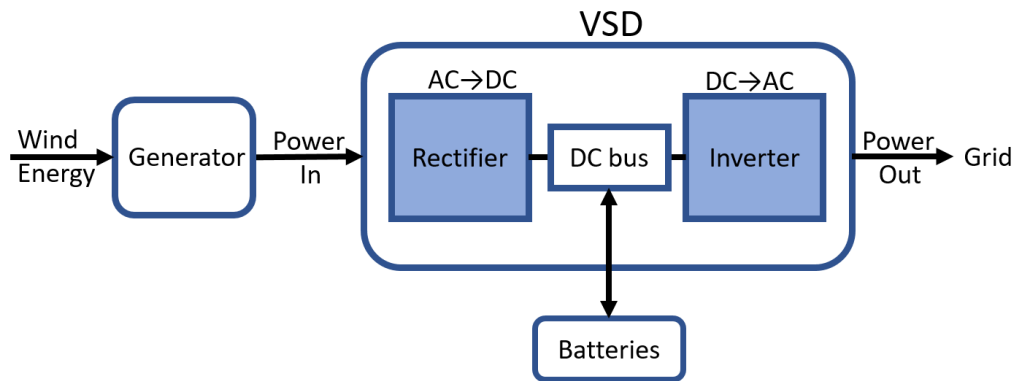


Figure 5-2b. Battery connection to wind turbine electrical system via variable speed drive (VSD) [155]

One benefit of the proposed system is the possibility of reducing the size of the electrical lines to shore and the corresponding infrastructure. An example of how this storage system would function with reduced electrical line size is shown in Figure 5-3 for a 5 MW turbine with a 2.5 MW line size and 6 hours of storage at average turbine power, i.e. 6 hours of SCAPP. When more wind power is generated than the maximum power that the transmission line can handle, the excess power charges the battery until it is full, and then the excess power is curtailed. When less wind power is produced than the line size, the battery discharges to provide additional power. This scheme attempts to provide power at a constant level as often

as possible, but other storage schemes could seek to maximize energy revenue or to smooth the hour-to-hour output of wind energy, all of which will have different costs and values.

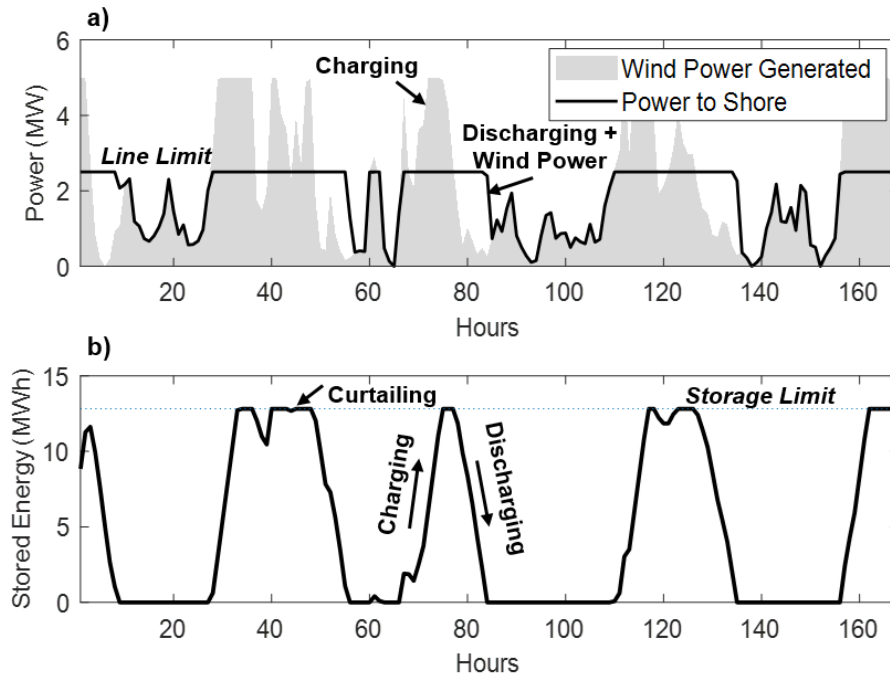


Figure 5-3. Energy storage example for a 5 MW turbine over one week with a 2.5 MW electrical line size and 6 hours of SCAPP, where times of charging, discharging, and curtailing are highlighted for a) power generated from the rotor and power sent to shore, as well as b) energy stored in the battery.

Wind speed data were gathered from the DOE BUOY project during its deployment off the coast of Virginia at a height of 90 m [156]. A representative week of hourly wind speed data was pulled from the DOE BUOY data (a week with typical periods of high and low wind speeds and no missing data points) and was used throughout this paper. The probability distribution of the one week of data used herein and the entire year of data are shown in Figure 5-4, with a Weibull distribution fitted to the year of wind speed data described by $Scale = 9.5$ and $Shape = 2.1$. Using one week of data reduced computational time while still capturing the important time scales on which the proposed storage system would be operating.

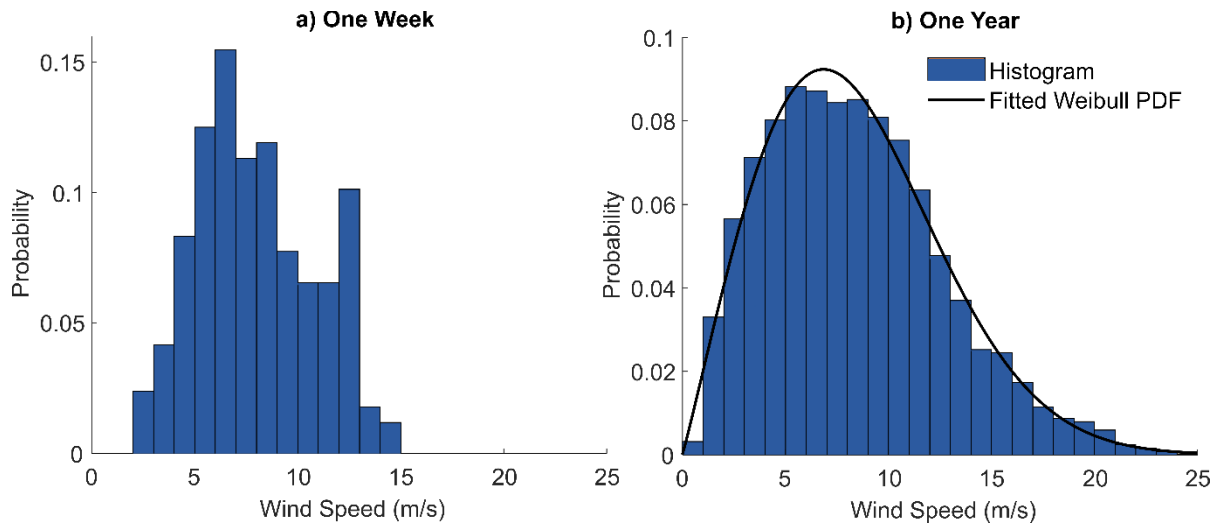


Figure 5-4. Probability distribution of one week of wind speed data (a) and one year of wind speed data (b) off the coast of Virginia at 90 m above sea level from DOE BUOY project [156]. The week (a) has a mean wind speed of 8 m/s while the year (b) has a mean wind speed of 8.4 m/s.

Table 5-1. NREL 5 MW monopile turbine specifications, with site specific information [12,115,157]

Specification	Value
Rotor diameter	126 m
Blade clearance	24.6 m
Tower height	87.6 m
Depth below water line, above mud	20 m
Depth below mudline	36 m
Diameter, thickness at and below waterline	6 m, 0.027 m
Diameter, thickness at top	3.87, 0.019 m
Rated Power	5 MW
Capacity Factor (site-specific)	0.427
Average Power (site-specific)	2.135 MW

The energy production of the wind turbine is based on values from the NREL 2017 Cost of Wind Energy Review [12] to allow for direct comparison with the LCOE breakdown provided in that report. The week of wind speed data was converted to wind power data using Eq. 5-3 by applying the NREL 5 MW reference turbine power coefficient curve [115] and scaling the wind speeds such that the average wind power yielded a capacity factor of 0.427 to be consistent with the 2017 Cost of Wind Energy Review [12]. For the baseline conventional 5 MW turbine (without storage and with the original electrical connection line size of 5 MW), resulting wind power generated (G) as a function of wind speed (W) is then given by

$$W < 3 \text{ m/s or } W > 25 \text{ m/s} \quad G = 0 \text{ MW} \quad (5-3a)$$

$$3 \text{ m/s} \leq W < 11.4 \text{ m/s} \quad G = 0.00343 \times W^3 \text{ MW} \quad (5-3b)$$

$$11.4 \text{ m/s} \leq W \leq 25 \text{ m/s} \quad G = 5 \text{ MW} \quad (5-3c)$$

For simplicity, wind farm wake losses and dynamic effects of turbulence are ignored when converting wind speed data into wind power results, as is typical in initial designs.

For this conceptual design of integrated storage, the baseline wind turbine was the monopile offshore NREL 5 MW reference turbine [115], whose details are given in Table 5-1. The turbine tower and substructure heights are denoted in Figure 5-2a. The battery system can be integrated into the monopile substructure of the turbine, either above water or below water, to create an integrated wind-storage system. The batteries will be considered with long-duration options of 6, 12, and 24 hours of SCAPP, where the average turbine power is 2.135 MW based on the above capacity factor.

C. Battery Storage Options

Potential battery storage options within the wind turbine are compared in Table 5-2 for LMB, Li-ion, and Lead-acid batteries. The values for the more conventional energy storage battery options of Li-ion and Lead-acid in Table 5-2 are from [158] and [159], and both technologies have been implemented in large-scale storage installations [138,158]. Comparing these two options, Lead-acid is less expensive, but Li-ion has superior performance characteristics, in particular, a much longer cycle life. Space, mass, and life-cycle constraints tend to dominate for long-term installations, which is consistent with Li-ion being the dominant battery option in current large-scale energy storage installations, as of the time of this writing [134].

The LMB storage options include both a published Li-Bi system [149] and an announced Ca-Sb system [153]. The performance specifications for these two systems configured for a large-scale application are listed in Table 5-2 and discussed below. However, in the absence of a full-scale deployment, LMB performance metrics contain a high degree of uncertainty. The Li-Bi LMB system was tested at lab scale in cells as high as 200 Ah capacity. Note that the Li-Bi system reported in [149] was not optimized and would be less expensive in a large-scale format. For example, in a large cell the ratio of the thickness to volume of the electrolyte would be significantly reduced. Furthermore, for the large battery comprising hundreds of large-format cells, the metals of the electrodes and the salts of the electrolyte materials would be purchased at bulk market cost, with lower metallurgical-grade purity. In order to estimate cost for a large-scale system composed of Li-Bi LMB, an “optimized” version of the Li-Bi system is used in Table 5-2 based on estimated manufactured pack cost (with more details on the assumptions in the Appendix).

For the projected Ca-Sb LMB, the cycle life is from [150] while the rest of the battery specifications are based on published Ambri estimates [153]. The Ca-Sb system has not yet been commercially installed, but the production cell size is reported to be 800 Ah, which will be aggregated into a 1000 kWh battery.

A comparison of the conventional battery options to the LMB options shows that both Li-ion and Lead-acid have higher roundtrip efficiencies than either LMB option. However, both LMB options have much lower cost than the traditional battery options as well as much higher cycle-life numbers. For integration into a wind turbine that is slated to have 20+ years of operation, low cost and high cycle-life are the driving factors for performance. Additionally, the high energy density of LMB is an advantage when integrating into a structure with finite available space. As such, LMB is a strong candidate for integrated wind energy storage though it requires additional technology development. Details on the how the LMB concept could be integrated are given in the next section.

Table 5-2. Current and predicted LMB performance compared to other battery types

Battery type	Specific Energy (Wh/kg)	Energy Density (Wh/L)	Cost (\$/kWh)	Cycle Life	Roundtrip Efficiency	Operational Temperature (°C)	Size Built/Tested
Li-ion	150-180	300-350	600-800 (installed)	1,500-5,000	90%	Ambient (-20° – 50°)	129 MWh, Hornsdale Power Reserve, Australia
Lead-acid	35-40	80-90	150-200 (installed)	500-1,200	85%	Ambient (-30° – 40°)	40 MWh, Chino, California
LMB Li-Bi	113	592	89 (predicted pack cost)	~10,000	70%	~550°	200 Ah (~79 Wh) Li-Bi battery, Cambridge, MA
LMB Ca-Sb (Ambri projections)	-	-	~21 (projected)	~10,000 (projected)	>80% (projected)	~500°	800 Ah (~760 Wh) battery, Marlborough, MA

D. Liquid Metal Battery Integration

The proposed integration of LMB into the substructure is shown in Figure 5-5 along with a generic cross-sectional design of the LMB. The LMB system would comprise custom-made cells with form factor of either disk (hockey puck-shaped) or prismatic (cereal box-shaped) configuration. Some hundreds of these cells are stacked in the tower substructure so as in aggregate to provide the desired storage capacity, i.e., required voltage and current. However, there is ample space available in the tower substructure since there

is approximately 550 m³ of volume between the waterline and the mudline (Table 5-1), which is a factor of five more than volume needed for the LMB (details on the battery sizing within the turbine structure are given in the Appendix).

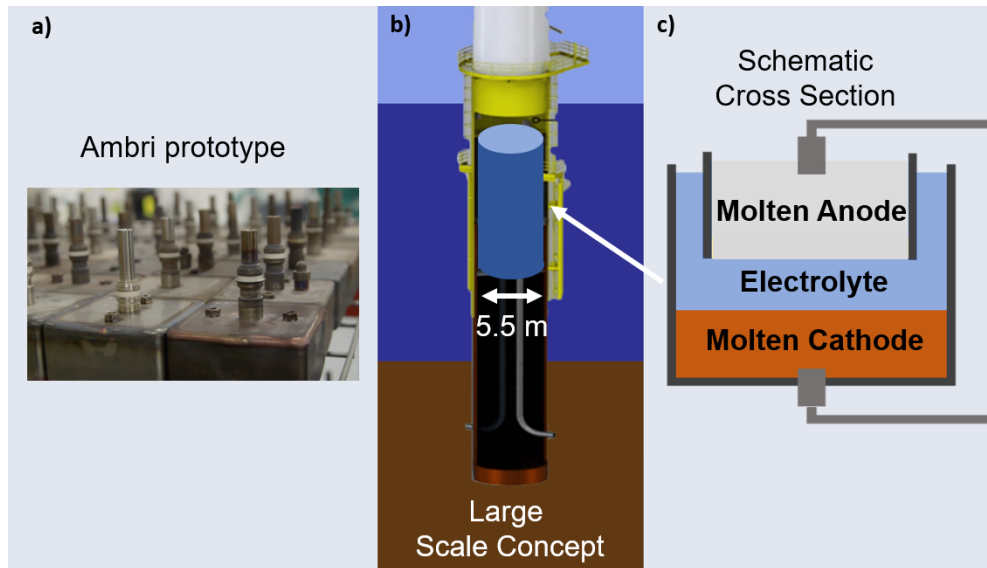


Figure 5-5. Liquid metal batteries: a) photo of prototype, b) integrated into offshore wind turbine tower, and c) schematic of active materials.

Safe operation of the batteries will be critical to their integration into offshore turbine structures. Using properly designed packaging, the LMB system has been demonstrated by Ambri to maintain safe exterior temperature and to keep its core molten by cycling every two days [153]. Joule heating within the battery (the energy loss associated with reductions in round-trip efficiency in Table 5-2) combined with device insulation and packaging has been found to generate enough heat to maintain the requisite high internal working temperature while ensuring the external temperatures are low [153]. Additional insulation will be added between casing and tower to maintain lower external surface temperatures for the storage system.

The battery stores energy during periods of excess wind power (generation exceeds demand or line size) and then discharges it during periods of low wind power. In particular, a battery management system (BMS) will decide when to store and when to deliver power. The BMS will need its own power electronics, which may be housed in the tower substructure. The space and power requirements of the BMS are expected to very small (relative to that of the turbine) such that they can be neglected with respect to power generation results in the present first-order concept design. However, round-trip efficiency of energy storage and regeneration can be significant and should be considered.

The energy efficiency for a large-scale storage system can be sensitive to the rates of charge and discharge relative to the capacity of the storage system. Given the very large size of the battery relative to the maximum charge or discharge power, the resultant low charge and discharge rates should result in high electrochemical energy efficiency. For the LMB system considered herein, current experimental data suggests there is negligible change in capacity utilization or coulombic efficiency for C rates relevant to the grid LMB in this study, and that the voltage efficiency has a linear dependence on C rate over the same charge/discharge rates considered [149]. A linear model (Eq. 5-4) relating battery charge/discharge efficiency (η) to the battery charge/discharge rate (C) was calculated based on the LMB data provided in [149], as follows:

$$C = \frac{\text{Rate of charge/discharge}}{\text{Capacity}} = \frac{\text{Power}}{\text{Energy}} \quad (5-4a)$$

$$\eta = 0.98 - 0.020(\text{hrs}) \times C(1/\text{hrs}) \quad (5-4b)$$

In general, the grid-connected LMB system considered in this study will operate at a much lower C rate ($<1C$) than those previously experimentally evaluated, such that the linear regime is very reasonable approximation. As such, this efficiency model is used for the present study. The energy lost to charge/discharge efficiency for a given power is assumed to all be in the form of Joule heating in the battery (q_{Joule}).

Heat transfer from the battery to the environment must also be considered. Ideally, the heat transfer rates (based on thermal insulation) match the Joule heating rates so that the battery can remain at a nearly constant temperature and there is no additional loss of energy from the system. One may size the thermal insulation to balance this heat generation on average. However, the charge rates (and thus the Joule heating) will vary depending on wind power availability so the heat transfer variations must be considered with respect to both the duty cycle and the operational temperature range associated with a particular LMB chemistry and design. When the Joule heating is high or the battery temperature is close to the peak operating range, active cooling from the much cooler external water may be used. When Joule heating is low or the battery temperature is close to the minimum operating range, heat addition (q_{heater}) can be employed to maintain the operational temperature of the system. Such heat addition is an additional energy loss to the system, so one may define the general energy loss via steady-state heat transfer at any given time as

$$q_{\text{loss}} = q_{\text{Joule}} + q_{\text{heater}} \quad (5-5)$$

For a 24-hour SCAPP system, the average Joule heating of the battery from efficiency losses is 53 kW. This can be used to make a first-order estimate of the thermal insulation system such that average heat loss matches the average Joule heating and minimizes time the heater is needed.

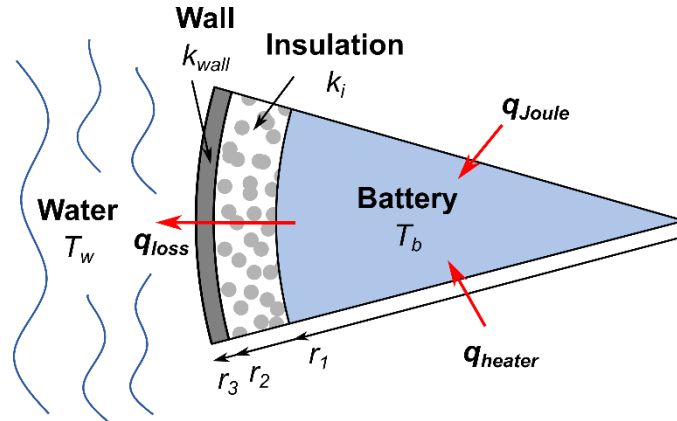


Figure 5-6. Cross-sectional schematic of storage system components in thermal circuit

To consider these thermal effects, the key components in the thermal system with a cross-sectional view of the battery within the turbine substructure is shown in Figure 5-6. Based on this axisymmetric geometry, the heat lost to the water can be approximated as

$$q_{loss} = \frac{T_b - T_w}{\frac{\ln\left(\frac{r_2}{r_1}\right)}{2\pi L k_i} + \frac{\ln\left(\frac{r_3}{r_2}\right)}{2\pi L k_{wall}}} \quad (5-6a)$$

$$L = \frac{V}{\pi r_1^2} \quad (5-6b)$$

$$t_i = r_2 - r_1 \quad (5-6c)$$

where T_b is the LMB operating temperature, T_w is the water temperature, r_3 is the outer substructure radius, r_2 is the inner substructure radius, r_1 is the battery radius, L is the vertical length of the battery within the underwater substructure, k_i is the insulation thermal conductivity, t_{insul} is the insulation thickness, and k_{wall} is the steel wall thermal conductivity. The battery length (L) stems from the volume (V) which is based on the total energy capacity and the LMB energy density. The heat transfer was found to be relatively insensitive to the water free convection, so it was assumed that the outer temperature of the substructure is the same as the water temperature. This temperature was taken as the average water temperature off the coast of Virginia. The design specifications, thermal material characteristics, and system temperatures are given in Table 5-3 and indicate that an average thermal insulation of 7.6 cm is needed for this system. Given

these specifications and assumptions, 53 kW of heat loss is expected, which must be made up by either Joule heating or heat addition to maintain operating temperature of the battery. For a 24 hour SCAPP battery system discharging average turbine power (2.14 MW), there is sufficient Joule heating to keep the system warm, but discharging at 0.5 MW requires use of heaters and reduces the one-way efficiency of the battery from 97.6% to 89.4%.

Table 5-3. Heat transfer analysis properties and dimensions for 24-hour SCAPP system

Variable	Value
T_b	550°C (based on Li-Bi, Table 5-2)
T_w	18°C [160]
V	86.6 m ³ (based on Li-Bi density, Table 5-2)
L	3.3 m
r_1, r_2, r_3	2.897 m, 2.973 m, 3.000 m
t_i	7.6 cm
k_{wall}	39.2 W/m-K [161] (Steel at 800 K)
k_i	0.125 W/m-K [161] (alumina-silica blanket at 750 K)

E. Levelization and Capacity Factor Results

The levelization and capacity factor are next considered in terms of two independent variables: the maximum electrical connection line size and the storage capacity in terms of hours of average power (SCAPP). Note that the resulting capacity factor is based on power produced to shore. The SCAPP is considered up to 24 hours which is enough to ensure significant smoothing and peak reduction. The optimum storage capacity will vary based on turbine size, wind conditions in the chosen location, and the grid valuation of energy as a function of time. Herein, we will employ the baseline 5 MW NREL offshore turbine described in Section 2.2 such that the maximum power delivered is 5 MW when the full 5 MW farm-to-shore electrical connection line is employed.

For the simulations, the charge and discharge strategy is to levelize power production for a given line size. Alternative regeneration strategies could be used based on the system’s goal such as minimizing energy loss, reducing hour-to-hour variations in power output [162], or maximizing spot market profit [163]. For the levelization strategy chosen herein, the battery charges when power is produced above the line size limit (until the battery storage is full), and discharges when wind power is below the line size limit (until the battery storage is empty). To reduce the influence of the starting storage level, simulations were

run iteratively with the final storage amount carrying over to the starting storage amount until an equilibrium point was reached.

For each timestep in the simulation, any charging or discharging from the battery has an efficiency loss as calculated by Eq. 5-4. If there is not sufficient Joule heating (q_{Joule}) from the efficiency loss to balance the mean thermal heat loss (q_{loss}), additional energy is used from the battery or reduced from the turbine generation until the necessary 53 kW is met.

The impact of different amounts of battery storage and line sizes on levelization is illustrated in the two examples shown in Figure 5-7 for a sample of one week of wind data (sampled from the BUOY wind data as described in Section 2.2). In these figures, the generated wind power shown in grey is bounded by the maximum power output of the turbine of 5 MW, while the delivered power (black line) is bounded by the electrical connection line size. Both are quantified by the left-hand-side vertical axis. In addition, these plots include the battery storage level in orange-dashed line which is quantified by the right-hand-side vertical axis (ranging from 0 to maximum storage). Figure 5-7a based on a small reduction in line size (to 4 MW) and 6 hours of average wind energy storage capacity. It can be seen that the peak power production is shaved by 1 MW and that the energy storage is often emptied soon after the wind power drops below the rating of the line size. Figure 5-7b has a larger reduction in line size (to 2.5 MW) and a larger amount of storage (18 hours SCAPP) which results in more frequent storage utilization and a smoother output power profile.

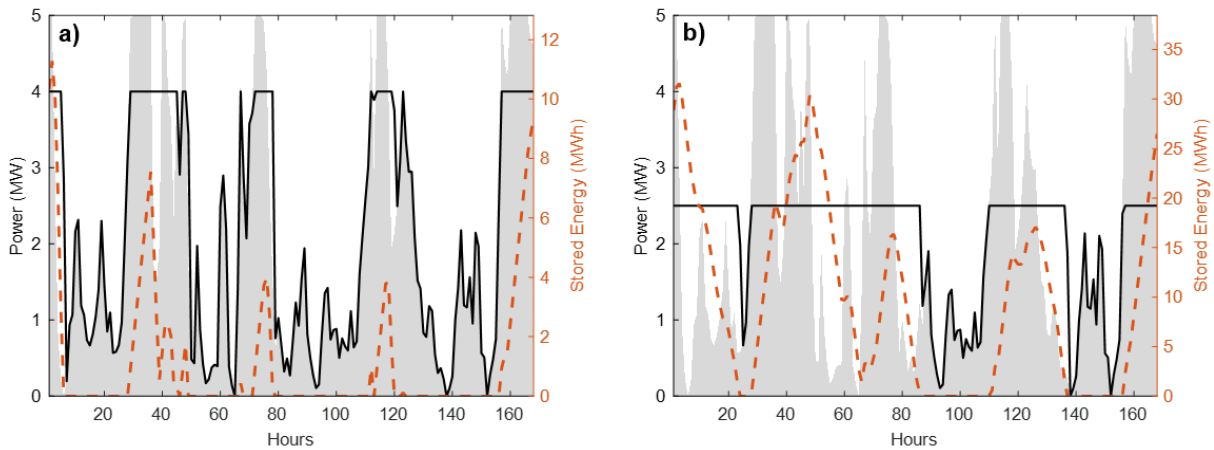


Figure 5-7. Two options of line sizes and storage capacities illustrated with zero curtailment for a week of real wind data: a) 4 MW line size and 6 hours SCAPP, b) 2.5 MW line size and 18 hours SCAPP

The influence of storage on capacity factor (Eq. 5-3b) is considered in Figure 5-8 for a range of battery capacities that can provide 0 to 24 hours of SCAPP and for a range of line sized from 2 MW to 5

MW. The capacity factor reflects losses due to curtailment, storage inefficiency (using Eq. 5-4b), and heating (q_{heater}). It can be seen that for a fixed amount of storage, reducing the line size, which reduces farm-to-shore connection costs, results in an expected loss in capacity factor. The black line in Figure 5-8 denotes 98% of the original wind farm capacity factor, and thus shows how much the line size can be reduced for a given storage capacity without significantly reducing the capacity factor. For example, 98% of the original capacity factor is maintained with a line size of 4 MW and 4 or more hours of storage, or a line size of 3 MW and 12 or more hours of storage. Reducing line size further requires significantly more storage to retain this capacity factor; thus, one must consider whether the savings associated with reducing line connection outweigh the loss in capacity factor. This compromise will be discussed in the next section. Using battery storage to reduce variations in the wind power output (“smoothing”) results in two additional benefits, not quantified here: reduction in penalties for balancing error when wind power output does not meet expected output, and ability to participate in day-ahead market auction [123,139,162].

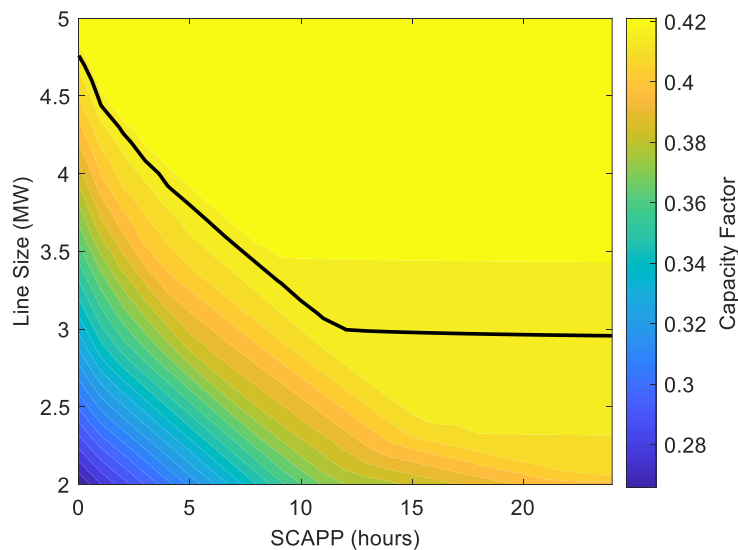


Figure 5-8. System capacity factor based on line size and storage time, accounting for losses due to curtailment, inefficiency, and heating. Black line represents 98% of original wind capacity factor.

The average “production efficiency” for each simulated week was calculated as the total energy generated to the grid, divided by the total energy produced by the wind turbine. This is not the storage efficiency, as most energy does not go through the storage system. Instead, this efficiency reflects average losses due to curtailment, storage efficiency, and heating losses, as the system tries to levelized the output power generation. The production efficiency for the 24 hours SCAPP system is 96.7%, averaged across all line sizes considered herein, which will be used to simplify the simulations in the Section 5.3C case study.

5.3. Economic Analysis

A. LCOE and Net Value of Energy

The value of energy produced by a wind turbine can be considered in terms of costs and revenues, and these are generally normalized by the annual energy production in the wind turbine literature as levelized cost of energy (LCOE) and levelized avoided cost of energy (LACE) [99,103]. The baseline LCOE, divided into categories, is pulled from the 2017 Cost of Wind Energy Review for Fixed Bottom Offshore wind turbines [12]. This LCOE includes the annualized costs of a system divided by the annual energy production.

$$LCOE = \frac{(CapEx \times FCR) + OpEx}{AEP} \quad (5-7)$$

In this expression, CapEx is the total capital expenditures for the system lifetime, FCR is the fixed charge rate which annualizes the capital expenses based on financial considerations, OpEx is the annual operating expenditures, and AEP is the total annual energy production [12].

To value the revenue, LACE annualizes the revenue sources divided by annual energy generation.

$$LACE = \frac{\sum_{i=1}^Y (MGP_i \times G_i) + CP}{AEP} \quad (5-8)$$

$$CP = CV \times CC \times \left(\frac{days}{yr} \text{available} \right)$$

In this expression, MGP is marginal generation price (price of energy) in time period i , G is the energy generated in time period i , CP is the capacity payment (the revenue an energy system can earn based on its ability to offset dispatchable resources used to meet peak demand), CV is the capacity value (the annualized cost of a dispatchable resource used to meet peak demand), and CC is the capacity credit (the percentage of installed capacity that can offset reserve requirements during peak demand) [99].

Based on the cost and revenue, the resultant net value (NV) from the system is then the difference

$$NV = LACE - LCOE \quad (5-9)$$

A system can thus be designed to maximize net value. While the addition of storage will generally increase LCOE, storage may increase LACE such that there is a net improvement in NV.

Information from the 2017 NREL Cost of Wind Energy Review [12] and 2018 Energy Information Administration (EIA) Annual Energy Outlook [103] is used herein for the economic evaluation of turbines with and without storage. For offshore wind turbines in the US, the predicted LCOE is \$124.6/MWh

(\$106.2/MWh with tax credits) and LACE is \$47.6/MWh [103]. Even though these estimates result in a net loss ($NV < 0$), offshore wind farms continue to be built in Europe and are beginning to break ground in the US as well [164]. This can be attributed to additional financial aspects not directly related to engineering design—such as renewable energy credits, different financial assumptions, and government-based and corporate-based decisions to invest in renewable infrastructure. While these factors are important and should be considered in future studies, herein these additional factors are ignored in favor of a focus on engineering design aspects, and only LCOE and LACE will be considered.

Note that LCOE and LACE are used herein due to the current comparable data in the wind turbine literature, but other cost metrics such as COVE [165] and sLCOE [98] may be equally able to consider the potential costs and benefits of adding storage to wind energy.

B. Cost and Value of Energy Storage

Quantifying cost of storage depends on the technical specifics of the storage format. The configurations of large-scale LMB and Li-ion storage systems would likely be different when integrated with a wind turbine. Li-ion is typically manufactured in small cells that are then added together in a specific configuration to make modular battery packs [159], while the large-scale configuration of LMB storage is still unknown. Given the unknowns in these potential configurations, LMB and Li-ion storage systems are assumed to be comparable on a kWh basis and costs for both are estimated at the battery pack level.

To determine net cost changes due to the addition of energy storage, BatPaC, a battery cost estimation tool from Argonne National Labs [166,167], was used to estimate the manufactured battery pack costs for a standard Li-ion composition (NMC/Graphite), as well as an LMB composition. The details of this cost analysis and the assumptions used are further specified in the Appendix. The BatPaC results give an average cost of energy capacity for Li-ion NMC/Graphite manufactured battery packs to be \$137/kWh_{storage}, where kWh_{storage} is the energy capacity of the battery. The lab-scale Li-Bi system in [149] was optimized herein for large-scale production and projected to have a manufactured battery pack capacity cost of \$89/kWh_{storage}. These costs include estimates for materials, battery management system, and manufacturing cost. These price differences are primarily driven by differences in raw material input prices per kWh_{storage}.

To convert battery costs ($CapEx_{battery}$) into total storage costs ($CapEx_{storage}$) into storage system LCOE ($LCOE_{storage}$) comparable to turbine LCOE, we use the following equations.

$$CapEx_{storage} (\$) = CapEx_{battery} \left(\frac{\$}{kWh_{storage}} \right) \times SCAPP(hours) \times P_{avg} (kW) \quad (5-10a)$$

$$LCOE_{storage} \left(\frac{\$}{MWh_{turbine}} \right) = CapEx_{storage} (\$) \times \frac{FCR (1/yr)}{AEP (MWh_{turbine}/yr)} \quad (5-10b)$$

where the AEP is 18,703 MWh/yr for the turbine, P_{avg} is the average plant power (2.135 MW if no storage), and FCR (real fixed charge rate) is 7% which annualizes the investment over 20 years. This FCR is taken from the 2017 Cost of Wind Energy Review [12] and assumes the storage system would be financed with the wind farm on the same timeframe. This likely underestimates Li-ion costs because of their shorter expected cycle life compared to the lifetime of a wind turbine. Applying Eq. 5-10 to the three storage capacities considered herein gives the transformed battery costs listed in Table 5-4.

Table 5-4. LMB Li-Bi and Li-ion battery costs per annual turbine energy generation ($LCOE_{storage}$) for 6, 12, and 24 hours of SCAPP

Battery size (hrs)	Li-Bi (\$88.9/kWh _{storage})		Li-ion (\$137/kWh _{storage})	
	$CapEx_{storage}$	$LCOE_{storage}$	$CapEx_{storage}$	$LCOE_{storage}$
6	\$1,140,000	\$4.26	\$1,750,000	\$6.57
12	\$2,280,000	\$8.52	\$3,510,000	\$13.10
24	\$4,560,000	\$17.00	\$7,020,000	\$26.30

In general, the batteries will not require additional grid connections or inverters since the battery storage system will be integrated into the wind turbine power generation system (as indicated in Figure 5-2). However, there will be other cost changes in the system's total LCOE associated with the integration of storage. Storage can be used to levelize power and reduce the electrical connection cost and size from farm-to-shore as shown in Figure 5-7. To evaluate the economic impacts of such changes, electrical connection costs are assumed to be proportional to maximum power plus a baseline cost for distance offshore (held fixed at 40 miles) [168], while installation costs are assumed to scale with the cost of the installed parts (turbine, battery storage, electrical, substructure). As such, the battery system increases the turbine installation CapEx costs (due to incorporation of storage) but any associated transmission line reduction decreases the connection installation CapEx costs (due a reduction in connection power rating). Financial costs are assumed to scale with total CapEx (turbine, electrical connection, substructure, BOS, installation, battery storage, installation) and thus can have similar increases and decreases. Herein, OpEx is assumed to remain constant for simplicity, but should be further investigated in later work. The resulting total system LCOE is thus defined by Eq. 5-11.

$$LCOE_{total} = LCOE_{turbine} + LCOE_{storage} \quad (5-11)$$

While the above identifies changes in costs due to battery storage, the following considers potential revenue increases due to battery storage. In this economic analysis, the case of 24 hours of storage is examined in detail due to its ease of calculation for energy and capacity revenues. The change in value due to the addition of the battery storage is assumed to come primarily from energy arbitrage revenue and capacity credit; the sum of these revenue streams is analyzed via LACE. The baseline energy revenue for the 5 MW wind turbine without storage is calculated by applying the week of wind power utilized in Figure 5-7 to each week of 2018 PJM spot market prices (a Mid-Atlantic regional transmission organization) [169]. Utilizing storage, a simple energy arbitrage scheme was implemented using hourly spot price data to estimate revenue. One day (24 hours) of SCAPP storage was used to shift average daily wind power output to the times with the highest energy spot market price, with maximum output constrained by line size, as illustrated in Figure 5-9. Note that this uses a different storage strategy than that used in Figs. 6-7. Additionally, the system was not allowed to charge from the grid, only from generated wind power. An average production efficiency of 96.7% (based on the 24-hour SCAPP simulations in Section 2.4) was used (rather than calculating losses due to curtailment, heater loss, and battery efficiency at each time step). This arbitrage scheme was applied for varying line sizes between 2.5 MW and 5 MW to constrain the amount of power that could be produced at once during peak hours. For example, with a 2.5 MW line size, power is produced to the grid at maximum output (2.5 MW) for 19.5 hours each day, while a 4 MW line size produced 4 MW of power for 12.25 hours.

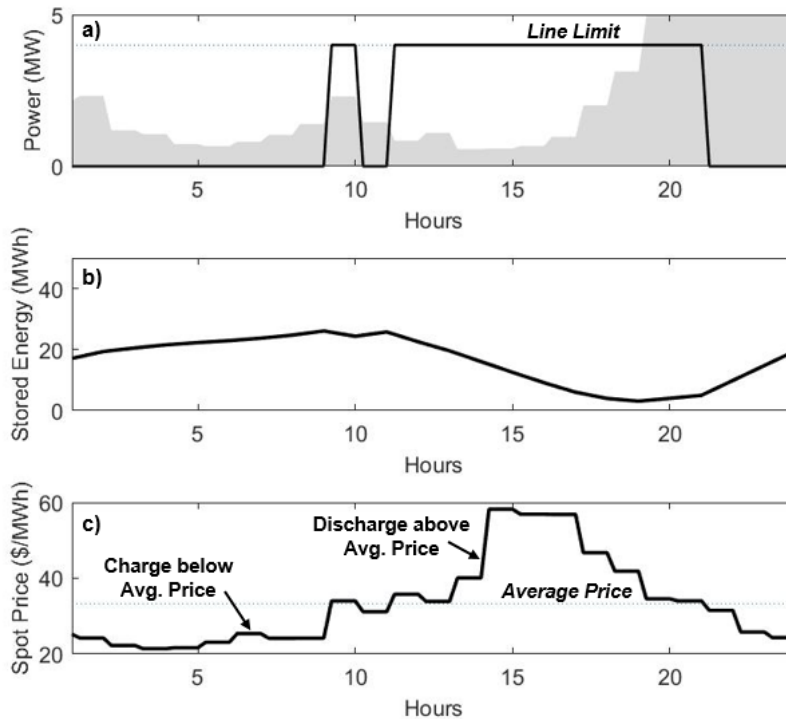


Figure 5-9. Energy arbitrage scheme with 24 hours of SCAPP and a 4 MW electrical line size depicting a) the wind power generated (grey area) and the electricity generated to shore (black line), b) stored energy over time, and c) spot market price sampled from PJM region.

The next revenue source comes from the capacity payment that wind energy can receive based on its location and which electrical transmission system it feeds into. For example, PJM onshore wind can receive a range of 14.7% -17.6% capacity credit [170], but offshore wind is likely to receive a much higher capacity credit. In this analysis, it is assumed that an offshore wind turbine would receive 33% capacity credit based on how the US EIA calculates LACE for offshore wind turbines [171]. This case study utilizes a capacity price from PJM for the 2021/2022 auction of \$140/MW-day [172], which is consistent with past PJM capacity prices in the last 10 years [170]. Storage could be optimized to provide maximum capacity payment, limited by line size. Based on results from [173], 10 hours of storage is predicted to earn a capacity credit of over 90%; thus as a first-order estimate, 24 hours of storage is assumed to provide sufficient capacity for full credit, limited by line size. A capacity credit of 100% is assumed for all 365 days of the year to determine capacity payment.

In order to compute the changes in LACE with storage, a method is needed that is consistent with the baseline offshore turbine LACE (no storage). If one only combines energy revenue and capacity payments for the baseline wind turbine using Eq. 5-8 with PJM values for energy and capacity payment, the result computed herein is \$37.5/MWh, which is less than the EIA value of offshore LACE of

\$47.6/MWh [103]. This difference can be attributed to additional factors (not included in Eq. 5-8) such as the expected increase in natural gas price (and therefore all energy prices) over time and location-dependent price variations. In order to employ current PJM energy and capacity credit prices in this study when evaluating various storage options while still matching LACE values from literature, these additional factors are accounted for by the addition of a PJM scaling factor (f_{site}) for LACE as

$$LACE = \frac{f_{site} \times (Energy\ Revenue + Capacity\ Payment)}{AEP} \quad (5-12)$$

To match the EIA value for LACE, $f_{site} = 1.27$ is used herein. The introduction of this site factor adds significant uncertainty into the analysis and thus the following results should be considered only as first-order economic estimates to estimate potential economic impact of various design choices. Also, note that other revenue streams associated with storage may also be possible such as forecasted energy balancing, frequency regulation, and other auxiliary services. Currently, such revenue is small and is therefore neglected herein. However, these revenue streams may become increasingly important as renewable energy penetration increases.

C. Case Study Results of Economic Impact of Storage

Based on the above assumptions and methods, the economic impact of storage is considered relative to a baseline offshore wind turbine. This case study assumes a fixed amount of storage capacity of 24 hours of SCAPP (equivalent to 51,240 kWh for the 5 MW rated wind turbine) and varies the line size. Lesser amounts of storage will have economic impacts between that of the baseline turbine (with no storage) and the turbine with 24 hours of energy storage.

Figure 10 compares the total LCOE of the original system with a 5 MW electrical connection line to one with 24 hours of storage and a 2.5 MW electrical connection line size. While the battery storage does increase the overall system cost, it also allows for reductions in cost in some areas such that the net cost increase is less than the total cost of the batteries.

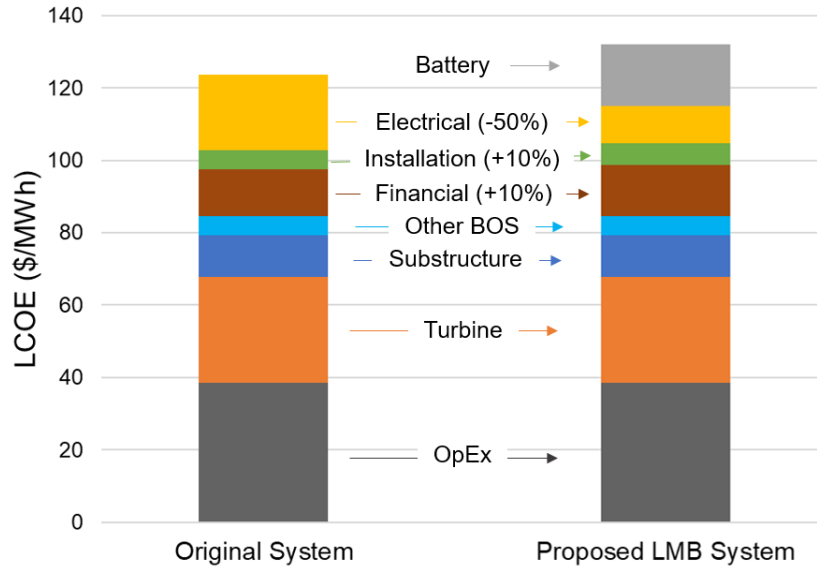


Figure 5-10. LCOE effect of switching from Original System with 5MW line size to Proposed LMB System with 2.5 MW line size and 24 hours of SCAPP

Next, we consider the revenue aspects for a range of line sizes using PJM 2018 data. As shown in Table 5-5, there is net savings in the electrical infrastructure associated with reducing the line size (which partially offsets the cost of the battery as noted in Figure 5-10). The table also shows that the baseline wind turbine generates \$32.88/MWh in energy revenue (using units as in Eq. 5-7), while applying energy arbitrage (with 24 hours of storage) resulted in a maximum annual increase in average spot price revenue of 31% over the baseline wind turbine profile. The baseline wind turbine without storage generates \$4.51/MWh (using units as in Eq. 5-8) in capacity payment revenue. The breakeven cost is the maximum battery cost at which the economic benefits associated with storage (due to the combination of energy revenue and capacity payment revenue) outweigh the costs. In Table 5-5, the breakeven manufactured battery pack cost in $\$/\text{kWh}_{\text{storage}}$ was found by iteratively seeking a battery cost such that the change in LACE and change in LCOE were equal. Thus any battery cost lower than the breakeven cost would reflect a net addition of value to the system, whereas battery costs higher than the breakeven indicate a net reduction of value for integration in this 5 MW offshore wind turbine.

Table 5-5. Changes with different potential line sizes for a turbine with 24 hours of SCAPP (irrespective of storage technology as battery costs are not included)

Line Size	5	5	4.5	4	3.5	3	2.5
SCAPP (hours)	0 hrs	24 hrs	24 hrs	24 hrs	24 hrs	24 hrs	24 hrs
Electrical Infrastructure Cost Reduction	N/A	0%	9%	18%	27%	35%	44%
Energy Revenue (\$/MWh)	\$32.88	\$43.18	\$41.65	\$40.56	\$38.91	\$36.8	\$34.58
Capacity Revenue (\$/MWh)	\$4.51	\$13.70	\$12.30	\$10.90	\$9.56	\$8.20	\$6.83
Breakeven Cost (\$/kWh_{storage})	N/A	\$100.73	\$96.57	\$94.70	\$89.96	\$83.22	\$75.11

If one now considers a specific battery technology with identified cost per capacity, the likelihood of meeting the breakeven requirements of Table 5-5 can be determined. The change in net value was calculated (compared to a baseline no storage wind turbine) as shown in Figure 5-11 for Li-Bi storage and in Figure 5-12 for a variety of storage options. Recall that the integrated storage system is based on a fixed capacity of 24 hours of SCAPP. In Figure 5-11, the change in LACE and LCOE for the current estimates of LMB storage start as a net loss for the smallest line size since the increase in revenue from storage does not outweigh the battery costs. However, as the line size increases, the increased value becomes greater than the increased cost, resulting in a positive change in net value (the difference between the blue and yellow lines, which is also indicated by the orange line). This indicates that adding 24 hours of battery storage, with a line size of 3.5 MW or greater, would result in increased profit for the system. Furthermore, it is found that the 5 MW line case gives the maximum increase in NV, indicating that the concept of net cost benefits associated with a reduced line size are never realized for this amount of storage and the given revenue assumptions.

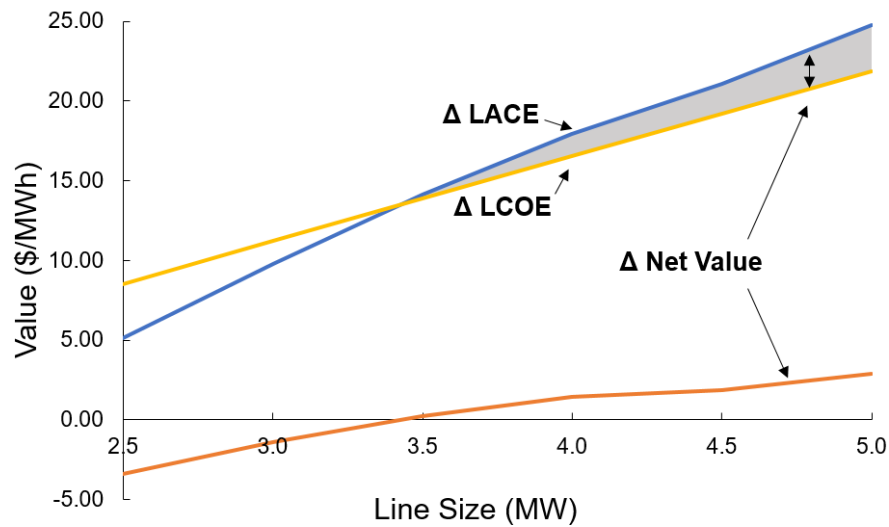


Figure 5-11. Change in LACE, LCOE, and Net Value for wind turbine with 24 hours integrated Li-Bi storage compared to wind turbine system alone

In Figure 5-12, the change in net value is plotted for current and future storage costs for both Li-ion and LMB. Costs for storage capacity are based on current predicted LMB (Li-Bi), \$89/kWh_{storage}; predicted LMB by 2030, \$21/ kWh_{storage}; current Li-ion (NMC/Graphite), \$137/kWh_{storage}; predicted Li-ion by 2030, \$67/ kWh_{storage} [144]. All storage types show the same trend of increased value with increased line size, again indicating that the concept of net cost benefits associated with a reduced line size are never realized for this amount of storage for the current case study. In addition, it can be seen that the projected cost decreases in Li-ion and LMB will serve to make energy storage have positive net value in the considered grid application. In particular, the falling cost of Li-ion technology may reach the breakeven cost in the next 10 years. In contrast, the estimated cost of LMB technology is already at the break-even cost and is projected to drop even further in the future, but the LMB technology requires additional development before it will be ready for large-scale commercial applications.

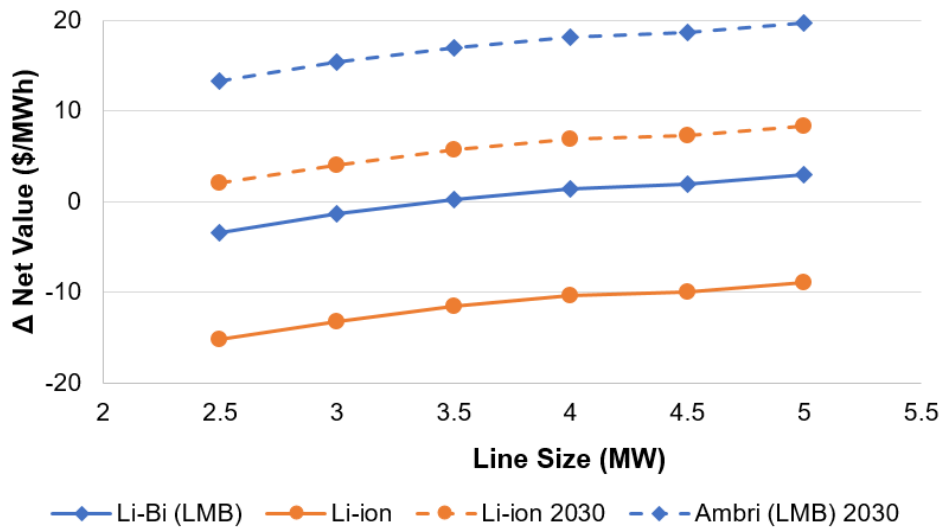


Figure 5-12. Change in net value of a turbine with 24 hours of storage (compared to baseline wind turbine system with no storage) for current and future Li-ion and LMB predicted costs

It should be again noted that the present case study results are specific to current PJM data whereas other locations and times would require different scaling factors (Eq. 5-12) and so the quantitative results provided herein are for specific conditions and cannot be broadly employed for other locations and future times. However, one may expect that the net value will rise as renewable energy penetration rises since power fluctuations will be stronger and there will be increased value placed on smoothing power output. Additionally, markets with higher capacity prices or more variable energy spot pricing may see additional benefits than demonstrated herein.

5.4. Summary

To address the resulting mismatches between generation and grid demand and to increase the value of wind energy, long-duration low-cost energy storage is needed as renewables increase shares on the electrical grid. LMB has a potentially very low energy cost and good performance (high efficiency, high cycle life, etc.) and thus may be a good fit for use with wind energy. To investigate a co-located system, the battery capacity is quantified relative to the average plant power rather than the battery rated power. Such a change in perspective is important for an integrated system with energy storage and generation.

A concept is proposed to place the battery within the substructure of offshore wind turbines. By co-locating, simulations indicate that the line size can be reduced to 4 MW with about 4 hours of storage, and reduced to 3 MW with about 12 hours of storage. Smoothing the wind power output provides additional

benefits which could include increased participation in day-ahead market auctions (recommended for future study).

As a case study, 24 hours of storage with variable electrical line sizes to shore was analyzed. Reductions in cost due to decreased line sizes, combined with synergistic benefits of co-locating storage and wind energy, results in the total LCOE for a turbine + storage system to be less than the sum of both individual system costs. However, while reducing the line size helps offset the cost of adding batteries, greater value is added to the system in the form of energy and capacity revenue from maintaining high line size, as seen in Figure 5-11. Applying energy arbitrage (with 24 hours of storage) resulted in a maximum increase in energy revenue of 31% over baseline wind generation. Adding Li-Bi batteries (one optimized form of LMB) to the offshore wind turbine system is predicted to result in a net increase in net value. Breakeven costs are high enough that current LMB technology (Li-Bi) is expected to be profitable and future Li-ion technology is expected to be profitable by 2030, if not sooner.

The present engineering analysis is limited based on current knowledge of liquid metal batteries. The LMB technology is still being developed and changes to the cost and performance estimates are expected in the near future. This simple analysis did not model full battery operation (as in [133]), consider battery lifetime with a wind-based duty cycle, or investigate the potential increased maintenance for battery integration, and these are recommended for future investigation.

There are also limitations with respect to the economic analysis. The potential cost savings from reducing electrical line size should be further investigated with a more complete electrical system model with a large-scale wind farm. Along these lines, integration and installation aspects for LMB storage with a *floating* wind turbine should be considered, since the weight of the battery may positively help offset cost of ballast weight and the line cost savings are expected to be even larger (as compared to the present fixed-bottom turbine). Furthermore, the economic analysis would also benefit from the application of a detailed energy arbitrage scheme with the policy and temporal constraints of practical energy markets. In addition, the economic analysis is based on the current electrical market, but this market is expected to significantly change with increased renewable penetration in the near future. Based on the above, LMB integration into a wind turbine is highly promising but more work, including an experimental prototype demonstration, is needed to assess its quantitative impact on its net value.

Finally, the environmental impact of integrating a battery storage system into an offshore wind turbine is also of importance. While the footprint of the wind turbines are not expected to change, there may be an increased surface temperature from the LMB system or reduced electrical line sizes, which may

affect the local environment. Most importantly, the reduction in carbon emissions from integrating wind turbines with battery storage into the grid could also be quantified and valued.

Appendix

Specifications of the proposed LMB system based on the optimized Li-Bi chemistry are given in Table A.1. The storage time is based on hours of storage at average power, 2.135 MW. The dimensions are based on the expected interior diameter of the monopile tower substructure (using specifications given in Table 3) and demonstrate that the battery system would take up a small fraction of that space. The battery cost is based on the total manufactured battery pack cost estimated in Table A.2.

Table A.1 LMB Specifications for use in monopile wind turbine, running at average power output, based on reported numbers from [149] (assuming optimized battery costs) and assumed space available in monopile.

Storage Time (h)	Energy Stored (MWh_{storage})	Mass (Mg)	Volume (m³)	Height (m)	Battery Cost (\$)
6	12.81	113.4	21.64	0.82	\$1,139,321
12	25.62	226.7	43.28	1.64	\$2,278,643
24	51.24	453.5	86.55	3.28	\$4,557,286

Table A.2 Battery costs (\$/kWh_{storage}) based on Li-ion costs from BatPaC and corresponding costs for LMB from Ning et al. [149], optimized Li-Bi, and Ambri

Battery Type	Li-Ion	LMB (Ning)	LMB (opt)	LMB (Ambri)
Chemistry	NMC/Graphite	Li-Bi	Li-Bi	Ca-Sb
Status	<i>Realized</i>	<i>Realized</i>	<i>Projected</i>	<i>Projected</i>
Electrode	\$42.28	\$154.00	\$19.41	\$17.00
Carbon and Binders	\$2.27	\$0.00	NA	TBD
Positive Current Collector	\$2.08	\$2.08	\$2.08	TBD
Negative Current Collector	\$8.70	\$4.35	\$4.35	TBD
Separators	\$13.56	\$0.00	NA	TBD
Electrolyte	\$9.45	\$66.00	\$15.63	\$4.00
Cell Hardware	\$3.92	\$3.92	\$3.92	TBD
Module Hardware	\$14.07	\$14.07	\$14.07	TBD
Battery Jacket	\$9.87	\$4.94	\$4.94	TBD
Battery Management System	\$11.33	\$11.33	\$11.33	TBD
Thermal Management System	\$0.70	\$1.00	\$1.00	TBD
Battery Pack Total	\$118.24	\$261.69	\$76.73	TBD
Battery Pack Manufactured Total	\$137.06	\$303.35	\$88.94	TBD

The battery modeling tool BatPaC, developed by Argonne National Lab [166,167], was used extensively to estimate battery costs in this work. The Cost Breakdown Analysis from this tool provided the Li-ion costs for nickel-manganese-cobalt (NMC)/Graphite type batteries in Table A.2 (column 1). Then manufactured battery pack cost for variations on LMB storage were then calculated based on known specifications for different systems, as well as assumptions based on the original BatPaC numbers. The LMB (Ning) column is based on battery specifications found in [149] for a lab-scale battery; thus, the material costs and quantities are not optimized for full-scale production. The LMB (opt) column attempts to optimize the values from [149] to reflect the costs of full-scale production by reducing the amount of electrolyte used and switching to market pricing for materials [174,175]. Finally, LMB (Ambri) is based on the material costs provided by LMB manufacturer, Ambri, and thus reflects the expected future costs of LMB. The assumptions used for each battery component are given in Table A.3 where many components are directly based on the Li-ion costs and the final manufactured cost is based on a scale factor of 1.16 up from the battery pack total (based on the same scaling with Li-ion).

Table A.3 Assumptions used for battery cost components costs for LMB from Ning et al. [149], optimized Li-Bi, and Ambri based on Li-ion BatPaC reference

Battery Type	LMB (Ning)	LMB (opt)	LMB (Ambri)
Electrode	Given	Market prices (\$10.78/kg and \$100/kg)	Given
Carbon and Binders	N/a	N/a	
Positive Current Collector	=	=	
Negative Current Collector	50% reduction	50% reduction	
Separators	N/a	N/a	
Electrolyte	Given	25% reduction, \$5/kg	Given
Cell Hardware	=	=	
Module Hardware	=	=	
Battery Jacket	50% reduction	50% reduction	
Battery Management System	=	=	
Thermal Management System	\$1/kWh	\$1/kWh	
Battery Pack Total	(summation)	(summation)	
Battery Pack Manufactured Total	(Scale factor)	(Scale factor)	

Chapter

6. Spray-cooled compression: theory and simulation

Abstract

Compressed air energy storage (CAES) is a low-cost, long-duration, and reliable storage option, but the conventional adiabatic approach leads to heat build-up that is lost during storage, rendering poor roundtrip efficiency. The efficiency of CAES can be significantly improved with isothermal compression; this can be accomplished with spray cooling during the compression process, where interphase heat transfer reduces the unwanted gas temperature rise. However, the theoretical limits and the key nondimensional parameters which control the spray-cooling efficiency have not been previously identified to guide the system design and optimization. These are addressed in the present study and favorably compared with results from a computational model validated against recently published experimental results for spray-cooled air compression. Using this computational model, a parametric analysis of the design space was performed using a new nondimensional number for droplet heat transfer speeds, the Crowe number, which was theoretically related to the effective polytropic index of the compression process. The results indicated that a high isothermal efficiency can be achieved with droplet mass loadings of 3 or more coupled with a Crowe number of 0.1 or less. Future work is recommended to consider multi-dimensional effects, expansion conditions, and losses due to spray work.

Nomenclature

ρ	density ($\frac{\text{kg}}{\text{m}^3}$)
γ	ratio of specific heats of air
η	efficiency
μ	dynamic viscosity ($\frac{\text{kg}}{\text{m-s}}$)
θ	Temperature ratio constant
τ	time constant (s)
c_p	air specific heat capacity at constant pressure ($\frac{\text{J}}{\text{kg-K}}$)
c_s	water specific heat capacity at constant pressure ($\frac{\text{J}}{\text{kg-K}}$)
c_v	air specific heat capacity at constant volume ($\frac{\text{J}}{\text{kg-K}}$)
$C_{d,\text{term}}$	droplet terminal velocity drag coefficient
Cr	Crowe number
d	droplet diameter (m)
D	cylinder diameter (m)
dt	time step (s)
g	gravity ($\frac{\text{m}}{\text{s}^2}$)
k	air thermal conductivity ($\frac{\text{W}}{\text{m-K}}$)
L	vertical length from cylinder head (m)
m	mass (kg)
ML	mass loading
N_d	number of droplets
n	polytropic index
Nu	Nusselt number
P	pressure (Pa)
ΔP	overspray pressure (Pa)
Pr	Prandtl number
PR	pressure ratio
Q	heat transfer rate (W)
q_{spray}	spray flow rate ($\frac{\text{L}}{\text{s}}$)
R	gas constant ($\frac{\text{J}}{\text{kg-K}}$)

Re	Reynolds number
T	temperature (K)
t	time
U_{piston}	piston speed ($\frac{\text{m}}{\text{s}}$)
u	air velocity ($\frac{\text{m}}{\text{s}}$)
V	volume (m^3)
v	droplet velocity ($\frac{\text{m}}{\text{s}}$)
W	work (W)
w_{term}	droplet terminal relative velocity ($\frac{\text{m}}{\text{s}}$)
z	position (m)
Subscripts	
1	beginning of process
2	end of process
a	air
atm	atmospheric
avg	average
C	compression
CR	critical
cyl	air cylinder total length
d	droplet
D	domain
env	environment
eq	equilibrium
fall	fall
i	time index
init	initial
iso	isothermal
j	droplet index
m	mixture
P	momentum
th	theoretical
T	thermal

6.1. Introduction

A. Motivation and Compression Efficiency

The need for long-duration, low-cost energy storage continues to grow as an increasing amount of electricity comes from variable renewable sources. Energy storage allows for variable generation sources to meet electrical demand and increases the stability and security of the electrical grid. To avoid overbuilding renewable energy to meet energy demand, a cheap and abundant energy storage technology is needed that is less costly than current battery prices [176] and can operate on the timescale of days, weeks, or even months [177].

Many storage options exist, but compressed air energy storage (CAES) provides a unique combination of low-cost and long-duration storage. CAES can be combined with renewable energy directly to provide more leveled power to the electrical grid or increase the value of the power sold to the grid [178,179]. However, it generally suffers from low efficiency relative to batteries and other forms of storage [21]. A key approach to improve its efficiency without requiring fossil fuels or thermal storage systems is Isothermal CAES (ICAES) [180], which relies on increased heat transfer during the compression process to reduce or eliminate the temperature rise of the compressed air.

The advantage of isothermal compared to adiabatic CAES can be seen by considering the process thermodynamics, as shown in Figure 6-1. The adiabatic process (shown as $1 \rightarrow 2 \rightarrow 3 \rightarrow 4 \rightarrow 1$) causes some of the compression work to go into heating the gas. Generally, this heat is lost in storage, thereby reducing the round-trip efficiency of the process. For the isothermal process (shown as $1 \rightarrow 2' \rightarrow 3 \rightarrow 4 \rightarrow 1$), the air is compressed at a constant temperature, so all of the work input goes into compression and no energy is lost to heat generation. As such, isothermal compression requires less work to compress to the same pressure ratio and push the air out into a storage tank than the adiabatic process.

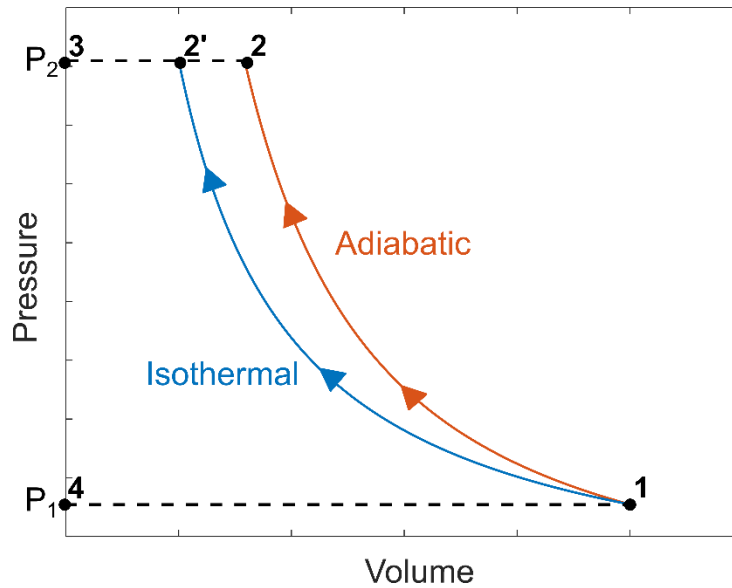


Figure 6-1. Isothermal compression requires less work than adiabatic compression to reach the same final pressure via (1-2) and push out the remaining volume via (2-3).

In reality, it is challenging to achieve isothermal compression, so most processes are near-isothermal and can be characterized by the polytropic index for the process. For an ideal gas, the polytropic index in the limit of an adiabatic process is the specific heat ratio (γ) and in the limit of an isothermal process is unity. Therefore, the index for a near-isothermal process will ideally tend to unity. The polytropic index of air and most diatomic gases is $\gamma = 1.4$, but other gases have higher or lower polytropic indices. Additionally, the isothermal efficiency of a compression process can be defined as the ratio of work for an isothermal process to the work for the given process, when working between the same overall pressure ratio. This definition is used throughout and is further defined in Section 2.

B. Previous work

Isothermal efficiency depends on many factors, including pressure ratio, speed of compression, and temperature abatement techniques, and the ranges found in the literature depend on many of these factors. Previous work on ICAES to help achieve a near-isothermal process has focused on three leading technologies (and their combinations): liquid piston, porous media, and spray injection.

Liquid piston compression uses a column of water pumped into a cylinder that acts as a piston to compress air [181]. The water acts as a heat transfer medium and also allows for more variation in the compression topology and technique [182–185]. Multiple experiments have confirmed that slower compression with a liquid piston reduces temperature rise (and approaches isothermal compression) [184–186]. There is an inherent trade-off between high efficiency and high power density for compression speed since faster compression reduces the time for heat transfer and reduces efficiency, but faster speeds provide

higher power per system mass [184]. Liquid piston compression alone (without porous media or sprays) has a reported isothermal efficiency of 63-94% from experiments [184] and 80-90% from simulations [181].

Liquid piston compression has also been investigated in combination with different forms of porous media, including metal foam and interrupted plate ABS structures [184,185]. Yan *et al.* found that adding inserts allows for higher efficiency or high power density and that surface area is the most critical factor for increasing efficiency and power density [185]. With the addition of inserts or porous media, liquid piston compression efficiency has been reported in the range of 80-95% from experimental results [184,185,187].

Spray-cooling can also increase efficiency by injecting small water droplets during the compression process to increase heat transfer. For a low compression ratio of two, experimental results show that spray cooling can increase compression efficiency into the range of 88-97% [188], while one-dimensional simulation results show that efficiencies as high as 70-98% can be achieved a compression ratio of 10 [189,190]. Water droplets are an effective form of heat transfer due to the high heat capacity of water and the high surface area of a spray of droplets. Experimental work with spray cooling includes solid piston compression with water spray cooling [188], liquid piston compression with spray cooling [186], and liquid piston compression with spray cooling and porous media [191]. Previous simulations of spray cooling for a solid reciprocating piston moving in a sinusoidal motion, with or without a layer of liquid on the piston, have generally employed 1-D idealizations [190,192,193].

The 1-D spray-cooled compression code developed by Qin & Loth [190] was validated against horizontal HVAC spray cooling experiments, since spray-cooled liquid piston experiments had not yet been published in the literature, but was compared favorably against 2-D computational fluid dynamics models in Ref. [189]. These results also showed that the polytropic index tended to reduce as the droplet size decreased and droplet mass loading increased but did not reach the lower-bound theoretical limit derived by Kersey *et al.* [194].

The Stokes number relates the droplet momentum response time (τ_p) to the fluid domain time scale (τ_D) and is helpful in determining whether a spray droplet has time to reach velocity equilibrium with a fluid [195]. However, a similar nondimensional number does not exist for the droplet thermal response time.

While the above studies have considered many aspects and conditions of spray-based cooling, they lack a fundamental characterization of the key nondimensional parameters which control isothermal efficiency, which has prevented clear guidelines for optimization. There is also a lack of theoretical

understanding of the effect of droplet size (and thermal inertia) on the polytropic index. In addition, no numerical studies have been quantitatively validated with the spray-based compression.

C. Objectives

This study aims to characterize the theoretical behavior and the key nondimensional parameters that control the spray-cooling efficiency and to understand their parametric influence using a validated numerical model, with a focus on the heat transfer aspects.

This is the first paper, to the author's knowledge, to validate a spray-cooled compression model against comparable spray-cooled liquid piston experimental results. It is also the first to derive an equation for the polytropic index of a spray-cooled compression process which accounts for thermal response time.

In Section 2, the methodology for the flow physics, proposed Crowe number, predictive polytropic index equation, and parametric sweeps are described. Section 3 contains the experimental validation, and Section 4 provides the results of the parametric analysis and theoretical polytropic index equation.

6.2. Methodology

A. Physics and geometry of the numerical model

An idealized depiction of the spray-cooled compression process is shown in Figure 6-2, including cylinder length (L), piston speed (U_{piston}), droplet diameter (d), and spray volumetric flow rate (q_{spray}). While illustrated in 2-D, the present numerical model only accounts for 1-D droplet motion along the z -axis, which starts at the top center of the cylinder. The simulations do not specify the piston material, which could either be water (liquid piston) or a solid piston. Air in the cylinder is assumed to have uniform pressure, temperature, and density, obeying the ideal gas law, which is a common assumption for modeling air compression [188,190]. Thus, the model is 0-D for air temperature and pressure, assuming it is spatially uniform. The maximum length of air in the cylinder (which equals the cylinder length if one neglects the piston length) is defined as L_{cyl} . For each compression process, $L_1 = L_{\text{cyl}}$.

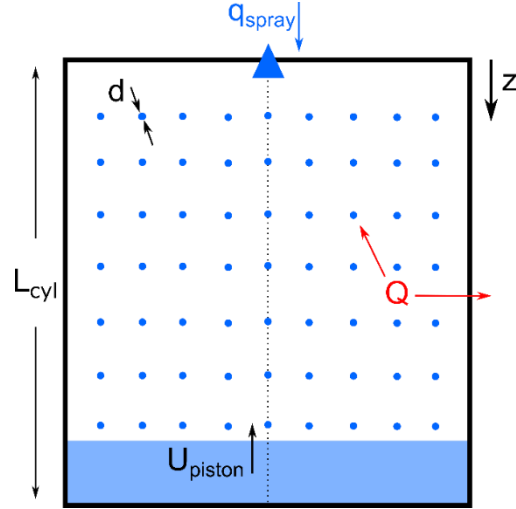


Figure 6-2. Idealized liquid piston compression with spray cooling.

The droplet size would likely be polydisperse (e.g., following a Rosin-Rammler distribution as in Ref. [196]) with a mean size and spread that varies with nozzle pressure. However, herein the spray is assumed to be monodisperse (constant size) for a given nozzle pressure using the Sauter mean diameter (as was done in Ref. [189]). The droplet Reynolds number, relative terminal velocity (w_{term}), and drag coefficient ($C_{D,\text{term}}$) are found iteratively using Eqs. 6-1a-c, based on White's drag coefficient for intermediate range Reynolds number [197].

$$w_{\text{term}} = (\rho_d - \rho_a)g \sqrt{\frac{4d}{3\rho_a g C_{d,\text{term}} |\rho_d - \rho_a|}} \quad (6-1a)$$

$$Re_{\text{term}} = \frac{\rho_a w_{\text{term}} d}{\mu_a} \quad (6-1b)$$

$$C_{d,\text{term}} = \frac{24}{Re_{\text{term}}} + \frac{6}{1 + \sqrt{Re_{\text{term}}}} + 0.4 \quad (6-1c)$$

Where μ is the dynamic viscosity, calculated using Sutherland's law.

The droplet velocity (v) can be calculated by the sum of the relative velocity and the local air velocity (u). For these 1-D simulations, droplets are only allowed to move in the z -direction (positive towards the piston).

$$u = U_{\text{piston}} * \frac{z_d}{L} \quad (6-2a)$$

$$v = w_{\text{term}} + u \quad (6-2b)$$

$$\frac{dz_d}{dt} = v \quad (6-2c)$$

Where ρ_d is the density of the droplet, ρ_a is the density of the air, L is the instantaneous height of the air column in the chamber, and z_d is the droplet position.

The heat transfer rate between the air and each droplet (Q_j) and the change in droplet temperature ($T_{d,j}$) are given by Eqs. 6-3a-b. The convective Nusselt number (Nu) is calculated based on the Prandtl number (Pr) and Reynolds number (Re) from the Ranz-Marshall relation [198]. The heat transfer to all the droplets is summed, and any additional heat transfer to the environment (Q_{env}) is added to calculate the total heat transfer (Q_{tot}) to the air, and the change in air temperature is given by Eq. 6-3d.

$$Q_j = \pi d k_a Nu (T_a - T_{d,j}) \quad (6-3a)$$

$$\frac{dT_{d,j}}{dt} = \frac{Q_j}{m_d c_s} \quad (6-3b)$$

$$Q_{\text{tot}} = \Sigma Q_j + Q_{\text{env}} \quad (6-3c)$$

$$\frac{dT_a}{dt} = - \frac{Q_{\text{tot}}}{m_a c_v} \quad (6-3d)$$

Where k_a is the air thermal conductivity, m_d is the mass of the droplets, m_a is the mass of the air, c_s is the droplet specific heat capacity, and c_v is the air specific heat capacity at constant volume.

The process of the numerical method is as follows, where the model tracks a single line of droplets in one-dimension falling along the centerline of the cylinder over time (i -index), modeling their position, velocity, and temperature. The numerical model uses a first-order, forward, explicit time-marching Lagrangian scheme.

The droplet momentum response time (τ_p) and thermal response time (τ_T) are defined as

$$\tau_p = \frac{24\rho_d d^2}{18\mu_a Re_{\text{term}} C_{d,\text{term}}} \quad (6-4)$$

$$\tau_T = \frac{\rho_d c_s d^2}{6k_a Nu} \quad (6-5)$$

The response times quantify how responsive a droplet is to changes in the fluid temperature or velocity [197]. The droplet thermal response time and momentum response time are used to set the time step (dt) for the simulation. Simulations are run at either 1% or 0.1% of the smaller droplet response time (thermal or momentum), based on the stability needed to minimize the effect of the 2-step compression process and ensure that only small changes to the droplet temperature occur in each time step.

The air is compressed in a two-step process, where first the air is compressed adiabatically, and then heat transfer is allowed between the air and the droplets. During adiabatic compression of the air, the temperature increases as a function of cylinder volume and the specific heat ratio of air. A temporary temperature is calculated (T').

$$T_a'^{i+1} = \left(\frac{V^i}{V^{i+1}} \right)^{\gamma-1} T_a^i \quad (6-6)$$

Then air and water properties are recalculated: air density, air viscosity, droplet terminal velocity, Reynolds number, air thermal conductivity, and Nusselt number. The air velocity is assumed to be a linear distribution from the moving piston surface to the stationary top of the chamber. Next, new droplets are injected at the top of the chamber (except for floating droplet simulations). The number of droplets (N_d) injected in each time step depends on the spray flow rate, droplet diameter, and number of time steps. The new droplet positions (z) are calculated based on the previous droplet location, droplet terminal velocity, local air velocity, and time step. Drops are removed from the simulations when they hit the piston surface.

The heat transfer between the air and each droplet (j) is calculated, and the droplet temperatures are updated. Lastly, the final air temperature is calculated, based on the temporary air temperature and total heat transfer to droplets, and the air pressure is updated based on the ideal gas law, using the final air temperature.

$$T_a^{i+1} = T_a'^{i+1} - \frac{Q_{\text{tot}} dt}{m_a c_v} \quad (6-7)$$

$$P^{i+1} = \frac{m_a R T_a^{i+1}}{V^{i+1}} \quad (6-8)$$

The resulting heat transfer coefficient for heat transfer to the droplets can be calculated based on the temperature difference between the droplet temperature and air temperature, and the droplet surface area. Average heat transfer coefficients from the simulations ranged from $2,000 \frac{W}{m^2-K}$ for 25 μm droplets to $60 \frac{W}{m^2-K}$ for 400 μm droplets. Note that the heat transfer in a real system would be higher than predicted by the parametric sweeps because those simulations neglect heat transfer to the piston and walls. However, this effect would be small if the surface area of the wall and piston is a small fraction of that for the droplets (as is typically the case for conditions where the isothermal efficiency is high).

B. Performance metrics for parametric studies

The following nondimensional values and mean quantities are used to capture the important aspects of each simulation within a single quantity, for studying the parametric sweeps of simulations in aggregate.

The compression work is divided into two periods, both of which are included for efficiency calculations: i) compression occurs from the initial atmospheric pressure (P_{atm}) and volume (V_1) and to the final pressure (P_{CR}) and volume (V_2), and then ii) the air is pushed out of the cylinder while maintaining the final pressure. For the parametric studies, the final pressure is set, and the final volume and final time are dependent on the compression process and correspond to when the final pressure is reached. The total work is thus calculated as

$$W = \int_{V_1}^0 (P - P_{\text{atm}}) dV = \int_{V_1}^{V_2} (P - P_{\text{atm}}) dV - (P_{\text{CR}} - P_{\text{atm}}) V_2 \quad (6-9)$$

The isothermal efficiency of the compression process is measured by the ratio of work for an isothermal process to the work for the given process, where the initial pressure, initial temperature, and final pressure are all fixed. The isothermal efficiency can thus be written as

$$\eta_{\text{iso}} = \frac{\left[\int_{V_1}^{V_2, \text{iso}} (P - P_{\text{atm}}) dV \right]_{\text{iso}} - (P_{\text{CR}} - P_{\text{atm}}) V_{2, \text{iso}}}{\int_{V_1}^{V_2} (P - P_{\text{atm}}) dV - (P_{\text{CR}} - P_{\text{atm}}) V_2} \quad (6-10)$$

For a fully isothermal process $\eta_{\text{iso}} = 1$. Note that Eq. 6-10 only considers how efficient the compression process is in comparison to the isothermal process; it does not reflect other losses and round-trip efficiency.

For example, spray work is not included in the calculations herein because it is assumed to have a small effect for moderate mass loading, and because this study is focused on the heat transfer physics and dynamics. It is recommended that spray work be included in more applied design studies.

Another parameter to quantify the entire compression process is to treat it as a polytropic process with a single equivalent polytropic index (n). A polytropic process obeys the following relationship.

$$PV^n = \text{constant} \quad (6-11)$$

For an adiabatic process on a dry ideal gas, the polytropic index is the ratio of specific heats (γ); for a process with heat transfer, $1 < n < \gamma$. In this case, the overall polytropic index for a compression process can be computed by setting the total work (Eq. 6-9) equal to the equivalent average work (Eq. 6-12).

$$W_{\text{avg}} = \frac{n_{\text{avg}}}{n_{\text{avg}} - 1} P_{\text{atm}} V_1 \left(1 - PR^{\frac{n_{\text{avg}} - 1}{n_{\text{avg}}}} \right) \quad (6-12)$$

The average polytropic index thus reflects a process that would require the same work to reach a given pressure ratio (PR), starting from the same initial volume and pressure.

Many aspects of the spray-cooled compression process can be captured with nondimensional numbers. The amount of water sprayed into the chamber during compression is captured by the mass loading (ML). Specific definitions for mass loading include the average droplet mass aloft during compression time and the maximum mass of aloft droplets. For floating droplet simulations, the mass loading is fixed and prescribed for each simulation in lieu of spray flow rate; the initial droplets never fall out of the chamber, and no new droplets are sprayed in. Thus, the average, maximum, and injected mass loadings are all equivalent and the movement of droplets in and out of the domain does not complicate the compression model. Herein the total mass loading (ML_{tot}) is used, defined as the ratio of total injected droplet mass to the compressed air mass.

The mass loading that gave the most consistent efficiency results between the floating droplet (where mass loading is fixed) and the falling drop (where mass loading varies with time) simulations is the total mass loading.

$$ML_{\text{tot}} = \frac{m_d}{m_a} = \frac{(m_{d,1} + m_{d,1 \rightarrow 2})}{m_a} \quad (6-13)$$

This includes both the droplets already in the chamber when the compression process starts ($m_{d,1}$), and those sprayed in during the compression process ($m_{d,1\rightarrow 2}$).

C. Theoretical polytropic index equation and Crowe number

The mixture of droplets and air makes it difficult to predict the polytropic index of the compression process without a simulation. A mixture ratio of specific heats can be written as the mass-average of the specific heats. For a mixture with infinitely small droplets, thermal equilibrium between the droplets and air would be reached, and the thermal equilibrium mixture polytropic index can be written as follows [194].

$$n_{m,eq} = \frac{m_a c_p + m_d c_s}{m_a c_v + m_d c_s} = \frac{c_p + c_s ML_{tot}}{c_v + c_s ML_{tot}} \quad (6-14)$$

Herein, Eq. 6-14 will be called the “thermal equilibrium limit” as it is the lowest polytropic index expected for a given mixture of droplets and air, without heat transfer to the environment. For conciseness, it is also referred to as the “Kersey limit” stemming the original derivation. If the air and droplets are not in thermal equilibrium, the mixture polytropic index can be written with the air and droplet temperatures as constants.

$$n_m = \frac{m_a c_p T_a + m_d c_s T_d}{m_a c_v T_a + m_d c_s T_d} = \frac{c_p + c_s ML_{tot} \frac{T_d}{T_a}}{c_v + c_s ML_{tot} \frac{T_d}{T_a}} = \frac{c_p + c_s ML_{tot} \theta}{c_v + c_s ML_{tot} \theta} \quad (6-15)$$

Where the ratio of droplet temperature to air temperature can be rewritten as a temperature ratio, $\theta = \frac{T_d}{T_a}$.

In the thermal equilibrium limit, $\theta_{eq} = 1$.

The temperature ratio can be approximated with a theoretical value θ_{th} based on a time average of the droplet temperature over a characteristic droplet time (τ_d) from $t = 0$ to $t = \tau_d$, assuming the fluid temperature is constant during that time. The change in droplet temperature at time t , relative to a constant fluid temperature, can be calculated as defined in Ref. [197] and substituted into the temperature ratio approximation, assuming that τ_T and T_a are constant.

$$T_d(t) = (T_{d,0} - T_a) \exp\left(-\frac{t}{\tau_T}\right) + T_a \quad (6-16a)$$

$$\begin{aligned}\theta_{\text{th}} &= \frac{\int_0^{\tau_d} \frac{T_d(t)}{T_a} dt}{\tau_d} = \frac{1}{T_a \tau_d} \int_0^{\tau_d} \left[(T_{d,0} - T_a) \exp\left(-\frac{t}{\tau_T}\right) + T_a \right] dt \\ &= \frac{T_a - T_{d,0}}{T_a} \left(\frac{\tau_T}{\tau_d}\right) \exp\left(-\frac{\tau_d}{\tau_T}\right) - \frac{T_a - T_{d,0}}{T_a} \left(\frac{\tau_T}{\tau_d}\right) + 1\end{aligned}\quad (6-16b)$$

Noting that $\left(\frac{\tau_T}{\tau_d}\right)$ is a key parameter in the temperature ratio, we can define this as a new nondimensional number, called the Crowe number. The ratio of the droplet thermal response time (τ_T) to the fluid domain time scale (τ_D), once proposed by Crowe *et al.* [195], can be defined as the Crowe number (Cr) as follows.

$$Cr = \frac{\text{thermal response time}}{\text{domain time scale}} = \frac{\tau_T}{\tau_D} \quad (6-17)$$

Note that the characteristic droplet time (τ_d) is thus approximated with the domain time scale (τ_D). The Crowe number can thus be used to quantify responsiveness of a droplet (or other thermal mass) within the time of the fluid domain, accounting for finite droplet size and response time.

The domain time scale of the Crowe number should estimate the amount of time each droplet spends aloft in the cylinder, i.e., the residence time. A combination of droplet fall time and isothermal compression time estimates that could be calculated *a priori* was developed, where the isothermal compression time (t_{iso}) is the time for an isothermal process to reach the given pressure ratio, while the fall time (t_{fall}) is based on the terminal velocity and average isothermal cylinder length. Herein, for all compression processes, $L_1 = L_{\text{cyl}}$, and for an isothermal process, $L_{2,\text{iso}} = \frac{L_{\text{cyl}}}{PR}$.

$$t_{\text{fall}} = \frac{\frac{L_1 + L_{2,\text{iso}}}{2}}{w_{\text{term}}} = \frac{\left(1 + \frac{1}{PR}\right)L_{\text{cyl}}}{2 \times w_{\text{term}}} \quad (6-18a)$$

$$t_{\text{iso}} = \frac{L_1 - L_{2,\text{iso}}}{U_{\text{piston}}} = \frac{\left(1 - \frac{1}{PR}\right)L_{\text{cyl}}}{U_{\text{piston}}} \quad (6-18b)$$

For a floating drop, there is no terminal velocity time, so $\tau_D = t_{\text{iso}}$. However, a falling drop will have a smaller time aloft than either of the idealized times (Eqs. 6-18a-b), which can be estimated in advance as

$$\tau_D = \left(\frac{1}{t_{\text{fall}}} + \frac{1}{t_{\text{iso}}} \right)^{-1} \quad (6-19)$$

Combing Eq. 6-5 and 6-19 yields the Crowe number equation used herein.

$$Cr = \frac{\tau_T}{\tau_D} = \frac{\rho_d d^2 c_s}{6Nuk_a} \left(\frac{1}{t_{\text{fall}}} + \frac{1}{t_{\text{iso}}} \right) \quad (6-20)$$

The theoretical temperature ratio (Eq. 6-16b) is thus simplified as

$$\theta_{\text{th}} = Cr \times \exp\left(-\frac{1}{Cr}\right) - Cr + 1 \quad (6-21)$$

where the temperature ratio is now assumed to be a constant during the process. As the Crowe number approaches zero, θ_{th} approaches 1, and as the Crowe number approaches infinity, θ_{th} approaches zero. The assumption of constant thermal response time in this derivation (used for Eq. 6-16) requires that Nusselt number hold constant, which occurs when a droplet enters the creeping flow regime and Reynolds number approaches zero. Thus, the assumptions used to derive Eqs. 6-16b and 6-21 are best applied when Crowe number is small.

The theoretical temperature ratio approximation is applied to the polytropic index equation for a mixture to result in the proposed theoretical polytropic index equation as follows.

$$n_{\text{m,th}} = \frac{c_p + MLc_s(Cr \times \exp\left(-\frac{1}{Cr}\right) - Cr + 1)}{c_v + MLc_s(Cr \times \exp\left(-\frac{1}{Cr}\right) - Cr + 1)} \quad (6-22)$$

To the author's knowledge, Eq. 6-22 is the first theoretical derivation of the polytropic index that accounts for thermal response time. The influence of the newly proposed Crowe number and mass loading on the theoretical polytropic index equation will be investigated for parametric compression simulations.

D. Parametric sweep simulation conditions

Building off the numerical compression model detailed in Ref. [190], a process was developed for running a large number of compression simulations with spray cooling in a parametric sweep. For the parametric sweep simulations, the cylinder starts at a set volume and atmospheric pressure and then compresses until critical air pressure is reached, related to the pressure ratio as

$$P_{CR} = PR * P_{atm} \quad (6-23)$$

This simplified description does not consider the aerodynamic losses associated with the valves that would move air in and out of the cylinder and their potential losses (since this study focuses on the compression efficiency aspects). Instead, the work to push the air out at constant pressure is determined using boundary work theory. In reality, the air may be pushed out into the next stage or a storage vessel.

The piston speed profile can affect the temperature rise in the piston and the resulting efficiency. Sinusoidal and uniform piston motion were both considered for the parametric sweeps, but uniform speed was chosen to better align with previously reported experiments and reflect a liquid piston with a constant pump flow rate. The air velocity (u) is assumed to be a linear distribution from the moving piston surface to the stationary top of the chamber.

Heat transfer from the air to the droplets is assumed to be the dominant form of heat transfer during compression, and thus the piston and walls are considered adiabatic. In the parametric sweeps of simulations, the droplet heat transfer area is significantly larger than the piston area, often by a factor of 10 to 100 depending on mass loading, indicating the majority of heat transfer will occur to the droplets. Therefore, the heat transfer to the environment is set to zero, i.e., $Q_{env} = 0$.

For the droplets, two primary conditions were considered: floating and falling. In the “floating” droplet simulations, droplets are given no relative velocity and thus float in the cylinder during the simulation, with no droplets added or lost during each simulation. The droplet terminal velocity is thus set to zero. The droplets are all initialized within the cylinder before the compression process starts. In the “falling” droplet simulations, the droplets fall at terminal velocity, which is a commonly used assumption [190,199] and is valid for droplets with small Stokes numbers [197]. The water spray is assumed to be injected with a constant flow rate, constant temperature, and constant droplet size from the top of the cylinder. For falling droplet simulations, the initial droplet positions are set by assuming droplets are injected and allowed to fall at terminal velocity during the intake air stroke time, which is assumed to take the same time as the compression stroke and have the same spray flow rate. Depending on the size of the droplets and the compression time, the droplets may or may not fill the cylinder (reach the piston location) during the expected intake time.

Table 6-1 details the parameters that were varied for the floating and falling droplet simulations. The ranges attempt to capture the experimental validation parameters and a full range of application-based parameters. For example, droplet sizes much less than 100 μm are likely preferred in terms of surface area, but experiments have often used with droplet size distributions with diameters as large as 400 μm , so a

range is given. Other parameters were held constant, including piston diameter ($D = 11$ cm) and initial temperature ($T_0 = 300$ K).

Table 6-1. Parametric sweep variables

Floating:

Parameter	Units	Values	Count
d	μm	400, 325, 250, 175, 100, 25, 10	7
L_{cyl}	m	0.1, 0.2, 0.3	3
U_{piston}	m/s	0.03, 0.14, 0.25	3
ML_{tot}	-	[0.1,61] log spacing	14
PR	-	2, 4, 6, 8, 10	5
Total			4410

Falling:

Parameter	Units	Values	Count
d	μm	400, 325, 250, 175, 100, 25	6
L_{cyl}	m	0.1, 0.2, 0.3	3
U_{piston}	m/s	0.03, 0.14, 0.25	3
q_{spray}	L/s	[5e-4, 5e-2] linear spacing	5
PR	-	2, 6, 10	3
Total			810

A simulation result was removed from the dataset if any of the following occurred:

- Droplet momentum response time (τ_p) was greater than 10% of the total stroke time (terminal velocity assumption may not be valid),
- There were less than 100 steps in the simulation (potentially inadequate temporal discretization for accuracy),
- More water droplet volume was added each time step than piston volume (piston would need to move backwards),

- Mean droplet temperature was warmer than air temperature more than 2% of the time (sign of thermal instability in code, does not obey 2nd law principles).

E. Evaporation analysis

One issue that can be important in the spray cooling process is droplet evaporation, particularly for small droplets and low mass loadings. Previous studies have neglected droplet mass transfer (condensation and evaporation) effects [189,199], with Ref. [189] stating that the large mass of injected water droplets will cause the air to quickly reach a saturated condition and cause negligible change to droplet diameters. To verify these claims, a set of simulations was run, including evaporation effects, as a matched set to the floating droplet simulations to compare and quantify the potential error.

For the simulations that included evaporation, the following equations were added to the numerical method to account for mass transfer, heat transfer due to evaporation, and the resulting gas mixture.

The specific humidity of the air or vapor mass fraction (ω) varies greatly with temperature and can be calculated for water vapor in air as [200].

$$\omega = 0.622 \frac{p_v}{p - p_v} \quad (6-24)$$

The saturation pressure of water vapor (p_v) at a given temperature is found using CoolProp [201], while the total pressure accounts for the air and vapor mixture (p). In these simulations, the air was assumed to start at 50% relative humidity at room temperature ($\omega = 0.01$). The initial humidity affects both the compression polytropic index and the likelihood of the water droplets evaporating, and a range of relative humidities should be considered during the design process. The increasing water vapor during the simulation was calculated as

$$\omega_i = \omega_{i-1} + \frac{\rho_d (V_{d,i-1} - V_{d,i})}{m_a} = \omega_{i-1} + \frac{\rho_d \frac{\pi}{6} N_d (d_{i-1}^3 - d_i^3)}{m_a} \quad (6-25)$$

The Spalding mass transfer number (B) compares the vapor mass fraction in the far-field (ω_∞) to the vapor mass fraction at the surface (ω_{surf}) [197].

$$B = - \frac{\omega_\infty - \omega_{surf}}{1 - \omega_{surf}} \quad (6-26)$$

Herein, we assume that the vapor mass fraction at the surface is equal to the saturated vapor mass fraction at the particle temperature ($\omega_{surf} = \omega_{sat, T_p}$).

The Schmidt number is defined as follows, where Θ is the diffusion coefficient [197].

$$Sc = \frac{\text{momentum diffusivity}}{\text{mass diffusivity}} = \frac{\mu}{\rho\Theta} \quad (6-27)$$

The Nusselt number (Nu) and Sherwood number (Sh) are calculated using the Ranz-Marshall correlation [198].

$$Nu = \left[2 + 0.6Re_d^{1/2} Pr^{1/3} \right] \frac{\ln(1+B)}{B} \quad (6-28)$$

$$Sh = \left[2 + 0.6Re_d^{1/2} Sc^{1/3} \right] \frac{\ln(1+B)}{B} \quad (6-29)$$

The diffusion coefficient of water vapor in air is $\Theta = 0.26 \times 10^{-4} \frac{m^2}{s}$ at 298K and 1 atm (Ref. [161] Table A.8). The diffusion coefficient is proportional to $T^{3/2}$ and inversely proportional to pressure [161]. Thus, the current diffusion coefficient for water vapor in air can be calculated as

$$\Theta = 0.26 \times 10^{-4} \left(\frac{m^2}{s} \right) * \left(\frac{P}{101 \text{ kPa}} \right)^{-1} * \left(\frac{T}{298 \text{ K}} \right)^{3/2} \quad (6-30)$$

Droplet heat and mass transfer are calculated using the differential equations below, based on equations in [194,197], replacing equation A4b when evaporation is included in the simulation.

$$\frac{dd}{dt} = -\frac{2\rho_a\Theta}{\rho_d d} B Sh \quad (6-31)$$

$$\frac{dT_d}{dt} = \frac{3\lambda_v}{c_s d} \frac{dd}{dt} + \frac{6k_a Nu}{\rho_a c_s d^2} (T_a - T_d) \quad (6-32)$$

Where λ_v is the latent heat of vaporization for the droplets.

The ratio of specific heats used for adiabatic compression can be calculated as follows for humid air (a mixture of air and water vapor) assuming air and water vapor are ideal gases.

$$n_{\text{humid}} = \frac{c_{p,m}}{c_{v,m}} = \frac{m_a c_{p,a} + m_v c_{p,v}}{m_a c_{v,a} + m_v c_{v,a}} = \frac{c_p + \omega c_{p,v}}{c_v + \omega c_{v,a}} \quad (6-33)$$

The air and water vapor mixture tends to have a slightly lower ratio of specific heats (and thus polytropic index of the compression process) than that of dry air alone because water vapor has a lower ratio of specific heats than dry air.

6.3. Validation against experimental data

Experiments reported in Patil *et al.* [186] combined a liquid piston compressor with spray cooling. These experiments provide the first public data that combined a fully-liquid piston with spray cooling and will be used for validation of the model defined in Section 2.1.

The experiments involved a liquid piston system submerged in a water tank. The slow compression speed, along with the unique under-water setup, allowed for significant heat transfer to the environment in addition to heat transfer to the injected droplets. Unlike in the parametric sweeps, the walls are not considered adiabatic and the heat transfer to the environment was estimated based on the reported “No Spray” case. A model was fit based on an internal energy balance for the No Spray data to find an overall heat transfer coefficient (U) dependent on chamber volume.

The experimental chamber diameter and length are 11 cm and 12 cm, respectively, and the piston location over time is calculated based on volume-time plots. The liquid piston motion is nearly linear, with a piston velocity of approximately 0.03 m/s. Therefore, the validation simulations run from an initial to a final volume, rather than a final pressure limit.

For validating our model, we focused on replicating the “fast” compression (3 s), 90° spray angle, 10 psi and 70 psi spray cases. As the spray pressure was varied, the droplet sizes and spray flow rates changed. The BETE spray nozzle used provided a polydisperse droplet distribution with a Sauter mean diameter of 487 μm for 10 psi and 117 μm for 70 psi. Note that the polydisperse droplet distribution creates increased uncertainty when using the Sauter mean diameter in the simulations to represent a wider range of droplet sizes.

No spray, low spray (10 psi), and high spray (70 psi) simulations are compared to reported experimental data Figure 6-3. The simulations fall within the error bars for the 10 psi and 70 psi spray experimental cases, indicating that this model is able to capture the chamber pressure for a specified volume.

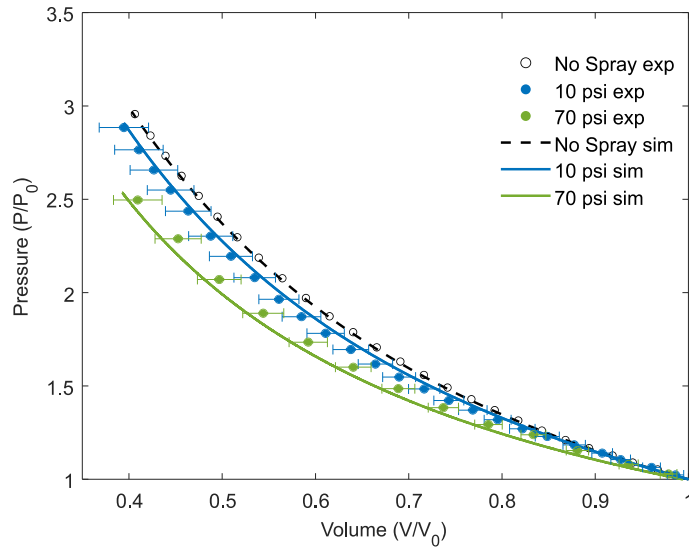


Figure 6-3. Pressure rise as a function of volume contraction for without spray cooling (“No Spray”) and with low and high spray injection (10 psi and 70 psi), comparing simulations with experimental data from Ref. [186].

Additionally, the average polytropic index was calculated based on Eq. 6-12 for the three cases based on experimental data and simulation results, as seen in Table 6-2. The calculated polytropic indices for the simulations are 5% or less away from the calculated polytropic indices for the experiments.

Table 6-2. Calculated polytropic index compared for experimental and simulation results of No Spray, 10 psi spray, and 70 psi spray cases. Experimental data from [186].

	Exp. data	Sim. results	% error
No Spray	1.27	1.26	-1%
10 psi	1.18	1.18	0.4%
70 psi	1.06	1.00	-5%

6.4. Results

A. Floating droplet simulations

The first sweep of simulations used floating droplets with no relative velocity. The mass loading was calculated based on the initial mass loading, which stayed constant throughout the simulation, and the Crowe number was calculated based on Eq. 6-20 with infinite droplet fall time and $Nu = 2$. The average polytropic indices are plotted in Figure 6-4, where each point represents one simulation result and the line

is the thermal equilibrium limit (Eq. 6-14). The thermal equilibrium limit approaches the isothermal limit of $n = 1$ for high mass loading, as the large water mass is able to absorb the heat of compression, in theory, with infinitely small droplets. Simulations with small Crowe numbers (corresponding to small, finite droplet sizes and large compression times) are closest to the equilibrium limit, while simulations with large Crowe numbers approach the adiabatic limit (for air) of $n = 1.4$. Thus, it can be seen in Figure 6-4 that the polytropic index depends on mass loading and Crowe number, as proposed earlier in Eq. 6-22.

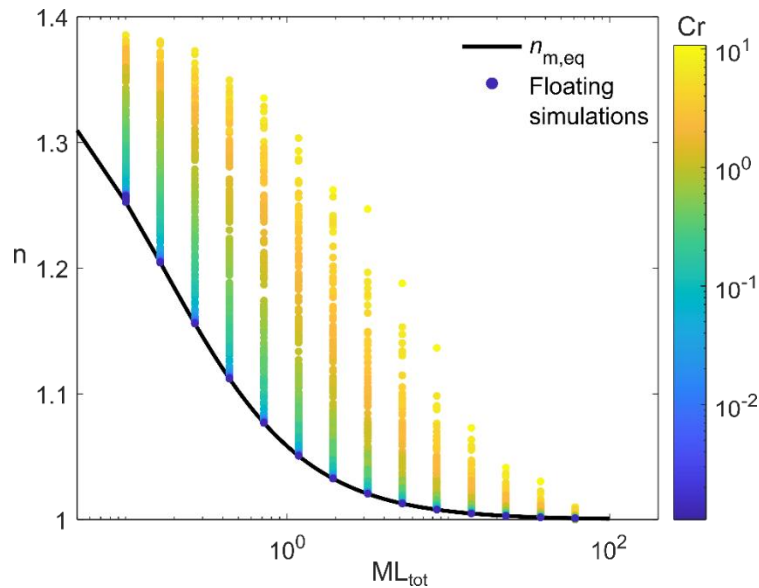


Figure 6-4. Parametric sweep of floating droplet simulations plotted by total droplet mass loading (ML_{tot}), polytropic index (n), and Crowe number (Cr), where the thermal equilibrium limit polytropic index curve ($n_{m,eq}$) is plotted in black.

The theoretical polytropic index equation of Eq. 6-22 is plotted in Figure 6-5 for select Crowe numbers (log-spaced throughout the domain) and compared to simulation results. Overall, the equation is able to closely predict the simulation results, though the predictions are more accurate for low Crowe number simulations as expected from the theoretical assumptions.

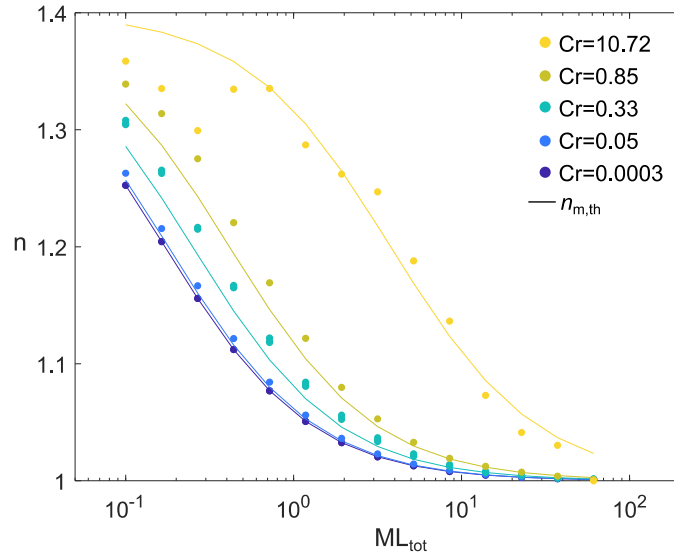


Figure 6-5. Theoretical polytropic index equation using theoretical temperature ratio approximation based on total mass loading and Crowe number (Cr) plotted for five different Crowe numbers and compared to floating droplet simulation results.

B. Falling droplet simulations

The second sweep of simulations used falling droplets that fell at their terminal velocity (Figure 6-6). For these simulations, the mass loading was calculated based on the total spray injected during the compression process (Eq. 6-13). Again, the simulations with small Crowe numbers approach the equilibrium limit, while simulations with large Crowe numbers approach the adiabatic limit, and increased mass loading results in lower polytropic index. The simulation polytropic index is within 2% of the equilibrium limit when $Cr < 0.1$. As compared to the floating droplet polytropic indices of Figure 6-4 (where mass loading is held fixed throughout the compression cycle), the falling drop results on Figure 6-6 are more scattered for a given mass loading and Crowe number, indicating the additional influence of the mass loading dynamics within the compression cycle. In particular, the total mass injected depends on the spray flow rate and the compression time, which varies based on the speed of compression, pressure ratio, length of the piston travel, and heat transfer. Additionally, droplets that hit the piston at the bottom and leave the air are no longer effective in terms of heat transfer. Based on differences between injection rate at the top and loss rate at the bottom, the instantaneous mass loading during the compression process can vary significantly, increasing or decreasing. These variations in instantaneous mass loading are more likely to occur at higher pressure and longer compression times and result in changes to the polytropic index of compression, beyond those given by Crowe number and total mass loading.

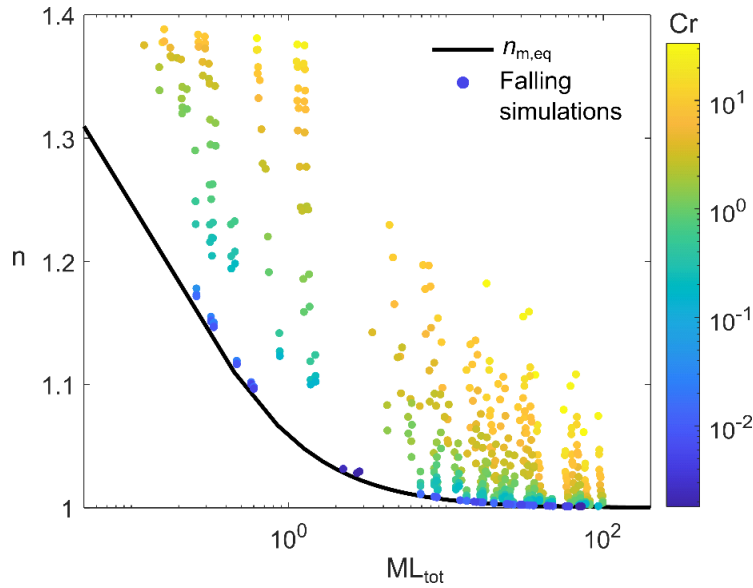


Figure 6-6. Polytropic index for falling drops as a function of total droplet mass loading (ML_{tot}), polytropic index (n), and Crowe number (Cr), for simulations compared against thermal equilibrium limit for infinitely small drops.

The isothermal efficiency for the floating droplet simulations is plotted in Figure 6-7, separated by pressure ratio. Increasing pressure ratio results in an increasing dependence of efficiency on mass loading. Thus, at $PR = 2$, the efficiency does not change significantly with mass loading, and the simulations are all clustered in the high-efficiency region. However, at $PR = 10$, efficiency varies greatly with mass loading, and a much larger spread is seen based on Crowe number. The shaded grey regions denote the areas where the floating droplet simulation results lie, which overlaps nicely with the falling droplet results. Small Crowe numbers and large mass loading simulations approach the ideal isothermal limit.

The relative increase in isothermal efficiency with increasing mass loading is small after a mass loading of 10; therefore, higher mass loadings may not be worth the additional cost of increasing the spray. Additionally, Crowe numbers less than 0.1 may be small enough to approach thermal equilibrium, while smaller Crowe numbers will only slightly increase isothermal efficiency.

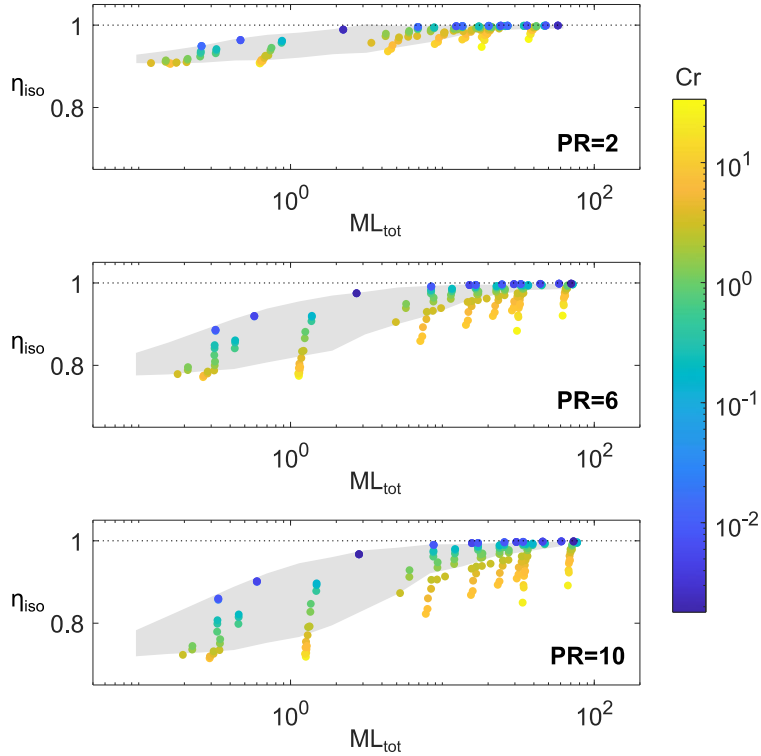


Figure 6-7. Isothermal efficiency (η_{iso}) for falling droplets for pressure ratios of 2, 6, and 10 as a function of total droplet mass loading and Crowe number, where shaded grey regions show the comparative results for floating droplets.

Using the same theoretical polytropic index equation (Eq. 6-22) as for the floating droplets, the polytropic index is predicted for each falling droplet simulation, and then the resulting isothermal efficiency is calculated. The difference ($\eta_{iso,diff}$) is thus calculated between the theoretical isothermal efficiency and the simulation isothermal efficiency.

$$\eta_{iso,diff} (\%) = \eta_{iso,th} (\%) - \eta_{iso,sim} (\%) \quad (6-34)$$

Using this definition, an over-prediction indicates that the theoretical process is more efficient than the simulated process. In Figure 6-8, isothermal efficiency difference is plotted in percentage points for all falling droplet simulations. The theoretical polytropic index equation predicts isothermal compression efficiency with less than 1.5% error for $Cr < 0.1$ or $PR = 2$. In general, the difference is positive indicating that the theoretical compression efficiency is greater than the actual efficiency, i.e., non-linear effects incorporated in the simulations tend to reduce the efficiency of the process. In particular, these differences are larger for large Crowe numbers (which can be qualitatively expected since Eq. 6-21 was derived for small Crowe numbers). In addition, higher pressure ratios push the results further from this equation, likely because these cases tend to be associated with larger variations in instantaneous mass loading and

temperature ratio between air and droplets, and thus the assumptions of constant mass loading and temperature ratio break down.

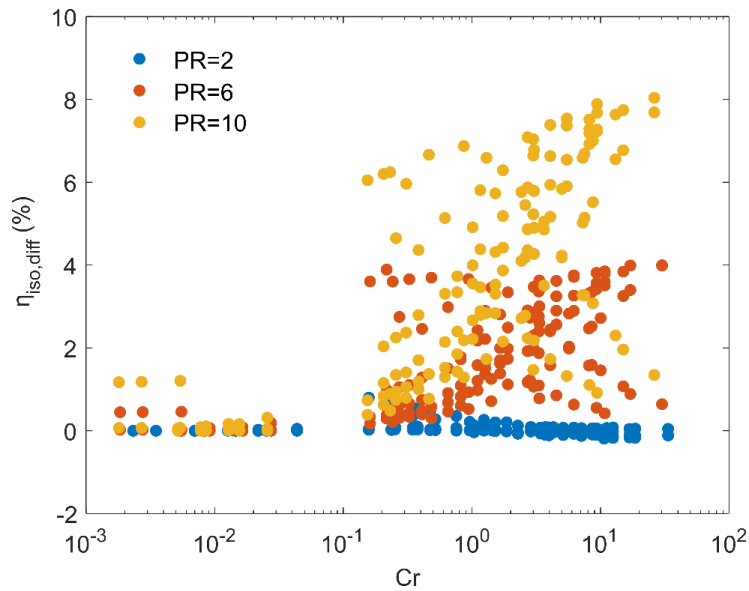


Figure 6-8. Difference in terms of percentage points between theory and simulation of isothermal efficiency for all falling droplet simulations, colored by pressure ratio.

C. Evaporation simulations

The simulations to investigate the effects of evaporation used floating droplets with no relative velocity. The results of the parametric sweep including evaporation (using the same parameters as the floating droplet sweep) are shown in Figure 6-9. It can be seen that at low Crowe numbers and small mass loadings, the polytropic indices are reduced relative to the original floating droplet simulations. However, at higher Crowe numbers and mass loadings, the results are relatively unchanged. The compression processes with the highest efficiency (which are the most likely to be implemented) are not significantly affected by the inclusion or exclusion of evaporation in the compression process.

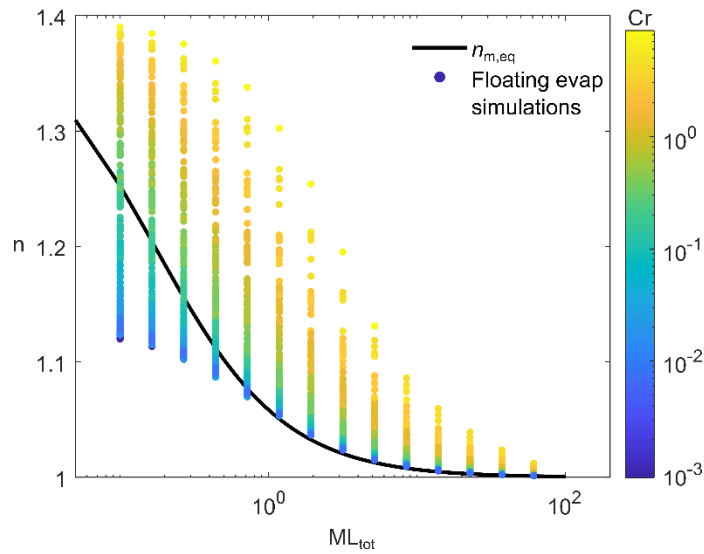


Figure 6-9. Parametric sweep of floating droplet simulations including evaporation effects plotted by total droplet mass loading (ML_{tot}), polytropic index (n), and Crowe number (Cr).

The average polytropic index of compression for the floating droplet simulations with and without evaporation are compared in Figure 6-10. The maximum error is near 14% for the smallest mass loading. However, the median polytropic index error from excluding evaporation effects is less than 1% when $ML_{tot} > 2$, and the median error remains below 3% for smaller mass loadings.

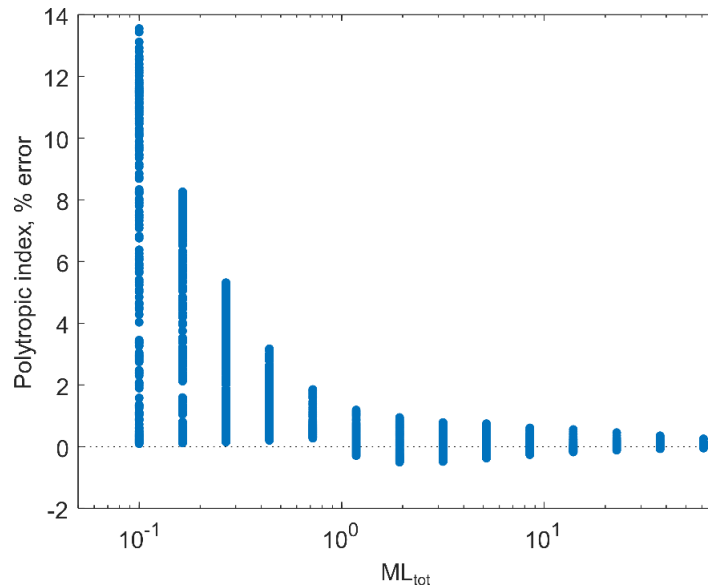


Figure 6-10. Polytropic index percent error comparing floating droplet simulations with and without evaporation effects.

Evaporation can be seen to be most significant for processes with small droplets and low mass loading. In these cases, evaporation is more likely to occur because of increased air and droplet temperature during the compression process. Moreover, that evaporation significantly increases the total heat transfer during the compression process. Thus, evaporation tends to lower the polytropic index for cases with small droplet diameters (herein found to be approximately $d < 50 \mu\text{m}$) and small mass loadings, but has little effect on the polytropic index for larger droplet sizes and/or mass loadings. While evaporation was neglected from the results in Sections 6.4A-B due to significantly increased computational time and a relatively small effect on heat transfer for high efficiency cases, it is recommended for future study for cases with $ML_{\text{tot}} < 2$ and $d < 50 \mu\text{m}$.

6.5. Conclusions

A novel theoretical polytropic index equation was derived using a newly proposed nondimensional parameter, the Crowe number (Cr). The Crowe number is the ratio of the droplet thermal response time to the domain time scale, and it was found to be an important predictor for polytropic index and compression efficiency. This theoretical work for spray-cooled compression was complimented with 1-D numerical simulations that are the first (to the author's knowledge) to be validated with liquid piston experiments. The numerical model was then used to complete a parametric analysis of spray-based simulations for floating and falling droplets and compared with the theoretical results. For the polytropic index, the thermal equilibrium limit (which is consistent with infinitely small droplets with negligible thermal response) was found to approach the isothermal limit ($n = 1$) for high mass loading while forming a lower bound for moderate to small mass loadings. For both floating and falling simulations, small Crowe number simulations (corresponding to small, finite droplet sizes and long compression times) were found to approach the thermal equilibrium limit, while large Crowe number simulations approach the adiabatic limit. When $Cr < 0.1$, for both floating and falling simulations, the simulation polytropic index is within 2% of the equilibrium limit indicating thermal inertia effects can be approximately neglected for these conditions. However, floating simulations show more consistent Crowe number trends than falling simulations. This is attributed to the constant mass loading for the floating cases (which eliminates the complexity of droplets entering and leaving the simulation over time that give rise to time-varying mass loading).

As expected from previous experimental results in the literature, isothermal efficiency was improved by increasing the spray mass and by decreasing drop size. The present results identify the nondimensional regime for high isothermal efficiency as a combination of mass loading above three and Crowe numbers below 0.1. As such, thermal response time relative to the compression time (in the form of the Crowe number) was found to be a critical parameter for predicting the polytropic index and thus

compression efficiency. Increasing pressure ratio reduced isothermal efficiency, for a given mass loading and Crowe number.

In general, the new theoretical polytropic index equation was able to well predict the simulation polytropic indices, with better results at smaller Crowe numbers (for which it was derived). In particular, the falling droplets cases with $Cr < 0.1$ typically had isothermal efficiency errors less than 1.5% while cases with $0.1 < Cr < 50$ had larger errors that approached a maximum of 8%. The larger errors were due to greater time variations in instantaneous mass loading and temperature ratio that tended to occur at higher pressure ratios. Based on this performance, the theoretical polytropic index model can be used in the future to predict the thermodynamics of a compression process without requiring simulation for small Crowe numbers (where efficiencies are highest). This can speed up the design modeling process when exploring new variables and configurations to be used for more detailed simulations and/or experiments.

The effect of evaporation in the code was considered but excluded from most simulations as the effect is small except in cases of low mass loading and small Crowe number. One set of simulations run with evaporation effects showed that evaporation may need to be included in more detailed models and designs that use with $ML < 2$ and $d < 50 \mu\text{m}$.

A numerical method combining previously studied liquid piston heat transfer with the droplet heat transfer considered herein would give a more complete view of a near-isothermal piston. In addition, future work is recommended to consider multi-dimensional effects, expansion conditions, and losses due to spray work.

Chapter

7. Direct spray injection for Compressed Air Energy Storage compression and expansion

Abstract

Compressed air energy storage (CAES) is a low-cost, long-duration storage option under development. Several studies indicate that near-isothermal compression may be achieved by injecting water droplets into the air during the process to increase the overall efficiency. However, little is known about the thermal-fluid mechanisms and controlling nondimensional parameters of the expansion process. Furthermore, the round-trip efficiency and the impact of spray-based CAES are even less understood. This study uses a validated 1-D model for compression and expansion with spray injection to complete a parametric analysis to analyze the thermal-fluid physics and roundtrip isothermal efficiency of a CAES system. For both compression and expansion, polytropic index tends to decrease and approach isothermal as nondimensional mass loading increases and as nondimensional Crowe number decreases. As such, the highest efficiency designs are those with slow compression speeds and high spray flow rates to achieve high mass loading and those with small droplets to achieve low Crowe numbers. Additionally, the work related to spray injection was modeled in a second set of compression and expansion simulations. When spray work is factored in for a pressure ratio of ten, roundtrip isothermal efficiency peaks around 95% at a mass loading of 15 and at Crowe numbers less than 0.1. The results indicate that high roundtrip efficiencies for CAES are possible with proper test conditions and that spray work should be included for significant mass loadings (e.g. greater than unity) due to the potential adverse effect on efficiency. In addition, further investigation is recommended to consider effects of multi-dimensionality, turbulence, wall-interactions, and droplet dynamics.

Nomenclature

ρ	density ($\frac{\text{kg}}{\text{m}^3}$)
γ	ratio of specific heats of air
η	efficiency
τ	time constant (s)
c_p	air specific heat capacity at constant pressure ($\frac{\text{J}}{\text{kg-K}}$)
c_s	water specific heat capacity at constant pressure ($\frac{\text{J}}{\text{kg-K}}$)
c_v	air specific heat capacity at constant volume ($\frac{\text{J}}{\text{kg-K}}$)
Cr	Crowe number
d	droplet diameter (m)
D	cylinder diameter (m)
k	air thermal conductivity ($\frac{\text{W}}{\text{m-K}}$)
L	vertical length from cylinder head (m)
m	mass (kg)
ML	mass loading
n	polytropic index
Nu	Nusselt number
P	pressure (Pa)
ΔP	overspray pressure (Pa)
PR	pressure ratio
q_{spray}	spray flow rate ($\frac{\text{L}}{\text{s}}$)
T	temperature (K)
t	time (s)
U_{piston}	piston speed ($\frac{\text{m}}{\text{s}}$)
V	volume (m^3)
W	work (W)
w_{term}	droplet terminal relative velocity ($\frac{\text{m}}{\text{s}}$)
z	position (m)

Subscripts

1	beginning of process
---	----------------------

2	end of process
a	air
atm	atmospheric
avg	average
C	compression
CR	critical
cyl	cylinder
d	droplet
D	domain
E	expansion
fall	fall
init	initial
iso	isothermal
RT	roundtrip
spray	spray
T	thermal
tot	total

7.1. Introduction

A. Motivation

Inexpensive, long-duration energy storage options are needed to meet electrical demand as an increasing share of electricity comes from renewable sources. Currently, dispatchable fossil fuel generation or overbuilding renewable generation are often more economical solutions than long-duration energy storage with Lithium-Ion batteries, so other energy storage options are needed [176]. Compressed air energy storage (CAES) has strong potential as a low-cost, long-duration storage option, but it has historically experienced low roundtrip efficiency [21].

Isothermal compressed air energy storage (ICAES) utilizes increased heat transfer during the compression and expansion processes to reduce temperature change in the compressed air and increase the overall efficiency of the process. If air can be compressed at a constant temperature, then all of the work input goes into compression rather than heat generation, and thus there is a potential to retrieve all of the input work during the expansion process. One option for achieving near-isothermal air compression and expansion is by injecting water droplets during the process. The spray injection has a large thermal mass and can absorb heat from the air during compression and transfer heat to the air during expansion.

For a CAES system, the physics of the thermal and fluid interaction as well as the overall roundtrip efficiency of the process are important to understand how much of the energy put into storage can be recovered for later use and to design a system for grid-scale energy storage.

B. Previous work

Both experimental and computational work has been previously completed to investigate near-isothermal CAES, with the primary emphasis on compression portion (rather than on the expansion portion or on the entire roundtrip process).

Experimental work by Wieberdink *et al.* [184] and Yan *et al.* [185] looked at liquid piston compression and expansion cases, both with and without porous media inserts. They found that piston speed had a large effect on efficiency, where slower piston speeds resulted in processes closer to isothermal for both compression and expansion. Notably, the temperature and pressure plots from these studies showed different trends for compression and expansion processes. While a fully-isothermal process would look the same for compression and expansion, the real processes showed more irregularities. Temperature and pressure plots for compression are relatively monotonic and follow a relatively constant curve. However, for expansion, the temperature plots are not monotonic and the pressure plots show a clear change in slope over time. As such, the expansion process was not as well understood.

Experiments on spray-cooled compression with a liquid piston were reported in Patil *et al.* [186] and the data was used to validate the present numerical method as discussed in Chapter 6. Previous work on modeling spray-cooled compression has included 1-D droplet heat transfer modeling by Qin & Loth [190] and Sapin *et al.* [202], both of which document an increase in compression efficiency with increasing spray mass loading.

While there has not been any published experimental data on expansion with spray injection (which remains an area of interest), some researchers have modeled the process. Yu *et al.* [203] modeled a generally complete expansion system including orifices, nozzles, and the motion of the piston while injecting high-temperature water mist during expansion. However, the model was only applied for one spray case. Zhang *et al.* [199] also simulated spray injection during expansion and varied the injected mass loading, finding that spray heat transfer increased the expansion work production by 16% over adiabatic expansion.

Experiments by Patil *et al.* [186] reported both compression work and spray work, separately, and they found that spray work could approach the magnitude of compression work thus offsetting the heat transfer benefits. Furthermore, while initial increases in spray pressure resulted in large temperature abatement, larger increases in spray pressure provided only marginal temperature reductions due to spray heat transfer [186]. In simulation studies, increasing the spray pressure (and thus increasing flow rate and decreasing droplet size) also reduced temperature rise during compression, but the increased spray pressure must be balanced against the increased spray work which can negatively affect efficiency [186,188,191,192]. Thus, it is important to consider the impact of spray work when using spray cooling for both compression and expansion.

CAES can use multiple types of compressors, but reciprocating compressors are common for isothermal CAES, either using a solid/mechanical piston or a liquid piston. One benefit of reciprocating compressors is the ability to use them both for compression and expansion, cutting the equipment costs in half. Roundtrip efficiency is critical to a CAES design, and if the same equipment is used for both compression and expansion, then it is important to consider roundtrip efficiency early in the design process. Liquid piston roundtrip efficiency varies and was found to be 78% for a pressure ratio of 39 by Hu *et al.* [204]. Some unique CAES designs that utilize spray cooling have found that adding water spray increased roundtrip efficiency [205,206].

However, few studies have considered the performance of a paired compression and expansion system for a standard compression system, where the system parameters are the same for both, and no experimental results have been reported. Compression and expansion are not identical processes, for a non-isothermal process, so the same system set up will have different efficiencies for compression and

expansion. Optimizing for a roundtrip system is critical when designing a near-isothermal CAES system for long-duration storage and may give different results than optimizing for either compression or expansion individually.

C. Objectives

The objective of this paper is to complete a parametric analysis of compression and expansion processes with spray injection using a validated 1-D model to analyze the thermal-fluid physics and roundtrip isothermal efficiency of a CAES system. This paper also seeks to identify high efficiency designs for spray-injection systems with different droplet sizes, both with and without spray work considerations.

This is the first paper to the author's knowledge to complete a parametric analysis of roundtrip performance by modeling matched pairs of compression and expansion cases. Additionally, it is the first to implement an equation for overspray pressure into simulations to account for varying spray work.

7.2. Methodology

A. Physics and geometry of numerical model

The system considered herein involves first-stage air compression or expansion in a cylinder with direct water spray injection. The simulations do not specify the piston material since heat transfer is only considered between the air and the droplets. As such the results can reflect the spray-based effects for either water (liquid piston) or solid piston systems. The model considers 1-D droplet motion along the z-axis, which starts at the top center of the cylinder, as seen in Figure 7-1. The 1-D model for compression is described in detail in Chapter 6 and builds upon work by Qin & Loth [190]. The numerical model assumes inert droplets within laminar air flow with one-way coupling between the air and droplets and no multi-dimensional or wall interactions. The 1-D model was expanded to simulate expansion processes herein.

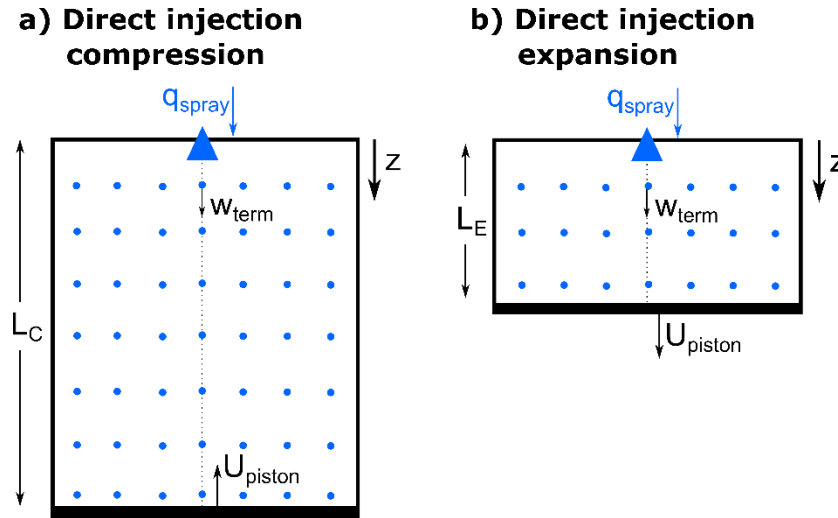


Figure 7-1. Notional schematics of direct injection spray at the beginning of each piston motion (after air has entered the chamber with initial spray injection): a) compression and b) expansion

The compression cylinders considered herein have a diameter of 10 cm and range from 10-50 cm in length. The diameter was chosen based on a reasonable diameter for one nozzle to fill with spray, and thus a system with a larger diameter may be approximated as a set of multiple 10 cm diameter cylinders each with one nozzle.

For all simulations, the piston speed (U_{piston}), total cylinder length (L_{cyl}), water volumetric spray flow rate (q_{spray}), droplet diameter (d), and maximum pressure ratio (PR) are prescribed. For simplicity, the piston speed is a constant within a given simulation, which is representative of a liquid piston compression process. Notably, this may give different results than sinusoidal piston speed profiles that are typical of solid, mechanical pistons.

In a complete compressed air energy storage system, the air would enter and leave the cylinder through valves and incur frictional losses in piping and storage losses. However, for simplicity in this assessment, only the compression and expansion process are considered; major and minor losses from valves, fittings, and piping are not included, and a constant pressure storage system is assumed.

For compression, the cylinder starting length (L_C) is prescribed as the total cylinder length, $L_1 = L_C = L_{\text{cyl}}$. Before the compression process, air at atmospheric pressure (P_{atm}) and room temperature is drawn into the cylinder during the “draw in” process. The cylinder starts at an initial volume and atmospheric pressure, and it compresses until the critical pressure is reached. The critical pressure (P_{CR}) can be defined as

$$P_{CR} = PR * P_{atm} \quad (7-1)$$

The process to push the air out at constant pressure is not simulated and is instead determined using boundary work theory. In reality, the air may be pushed out into the next stage or a storage vessel.

In expansion, the air starts at the critical pressure at cylinder length L_E and is expanded until it reaches the final atmospheric pressure. The initial expansion cylinder length is defined based on an isothermal process, where the starting cylinder length (L_E) can be related to the total cylinder length (L_{cyl}) and the pressure ratio as follows, given that the volume of an isothermal, ideal gas is inversely related to the pressure.

$$L_1 = L_E = \frac{L_{cyl}}{PR} \quad (7-2)$$

Thus, L_E is the length that the piston moves during the draw in process when high pressure air is drawn into the cylinder at constant temperature and pressure while droplets are sprayed into the cylinder, and L_{cyl} is the maximum expected length of the cylinder at the end of the expansion process (as an isothermal process is the longest possible process).

The water droplet spray would have a range of droplet sizes and would take time to disperse from the injection site and fill the chamber fully. Herein the droplets are modeled using a single size, the Sauter mean diameter, to simplify the simulations and focus on the fundamental effect of drop size on efficiency. In actual sprays, there would be a range of droplets (some smaller and some larger than the Sauter mean diameter) and a corresponding a range of terminal velocities and heat transfer rates. Only modeling the droplets in 1-D accounts for the time to disperse in the z-direction but does not account for radial dispersion of droplets within the chamber.

The water droplets are sprayed in at a constant flow rate from the top of the chamber during the draw in process and during the compression/expansion process until the desired pressure is reached. The droplets are sprayed in at the same volumetric flow rate during the draw in process for both compression and expansion. Note that at constant piston speed, the draw in process takes longer for compression due to the longer starting cylinder length ($L_C > L_E$), and thus more droplets are sprayed in initially for compression than expansion, as illustrated nominally in Figure 7-1 where the compression schematic has more droplets in the chamber at the beginning of the process than the expansion schematic.

The droplet Reynolds number, relative terminal velocity, and drag coefficient are found iteratively, based on White's drag coefficient, which is appropriate for particle Reynolds number up to 1,000 [197], as

described in Chapter 6. Droplet velocity is then the sum of the relative terminal velocity (w_{term}) of the droplet and the local air velocity. The air in the cylinder is assumed to have a linear velocity profile, from the moving piston surface to the stationary cylinder top.

The air in the cylinder is assumed to have uniform pressure, temperature, and density and is assumed to obey the ideal gas law. The starting air temperature for all simulations is room temperature (300 K), assuming there is sufficient time between cycles for the air to return to room temperature.

Heat transfer from the air to the droplets is assumed to be the dominant form of heat transfer during compression, and thus the piston and walls are considered adiabatic and heat transfer is only allowed to the droplets. Heat transfer between each droplet and the air is calculated and then summed to find total heat transfer with the air. Droplet evaporation, boiling, and freezing were not included in the simulations as droplet temperatures are intended to stay between the freezing and boiling points of water. Processes with high isothermal efficiency, as sought by this study, would not experience extreme droplet temperatures, so those effects were excluded for simplicity. Additionally, an anti-freeze compound could be added to lower the droplet freezing temperature if needed.

The numerical method employs a two-step process, where first the air is compressed or expanded adiabatically, and then heat transfer is allowed between the air and the droplets. Readers are referred to Chapter 6 and Chapter 6 Appendix for details on the numerical method.

A simulation result was removed from the dataset if any of the following occurred:

- Droplet momentum response time (τ_p) was greater than 10% of the total stroke time (terminal velocity assumption may not be valid),
- There were less than 100 steps in the simulation (potentially inadequate temporal discretization for accuracy),
- Piston speed exceeded $\frac{U_{\text{piston}}}{t_{\text{iso}}} < 0.1g$ (ensuring that if this system was implemented with a real piston, the speed and acceleration would be physically realistic),
- The added water droplet volume at a time step was more than 50% of the change in piston volume (the majority of the change in air volume should come from piston motion), or
- More than 10% of the initial volume of initial volume was droplets (the initial draw in spray should not significantly change the cylinder volume).

B. Outputs and nondimensional parameters

The compression and expansion processes can each be quantitatively characterized in terms of their work, isothermal efficiency, and polytropic index.

The compression work is divided into two periods: i) compression occurs from initial atmospheric pressure (P_{atm}), cylinder length (L_C), and initial volume (V_{1C}) to the final critical pressure (P_{CR}) and final volume (V_{2C}), and then ii) the air is pushed out of the cylinder while maintaining the final pressure. Note that $P_{1C} = P_{\text{atm}}$ and $P_{2C} = P_{\text{CR}}$ for compression, but the pressure terms are used herein since they are fixed for each simulation for both compression and expansion, while the volume terms vary. The final pressure is set as the critical pressure, and the final volume and final time are dependent on the compression process and correspond to when the critical pressure is reached. The total work is thus calculated as

$$W_C = \int_{V_{1C}}^0 (P - P_{\text{atm}})dV = \int_{V_{1C}}^{V_{2C}} (P - P_{\text{atm}})dV - (P_{\text{CR}} - P_{\text{atm}})V_{2C} \quad (7-3)$$

Note that compression work is negative because work is put into the system.

The efficiency of the compression process is measured by the ratio of work for an isothermal process to the work for the given process, where the initial (atmospheric) pressure, initial temperature, and critical pressure are all fixed. The isothermal efficiency can thus be written as

$$\eta_{\text{iso,C}} = \frac{\left[\int_{V_{1C}}^{V_{2C,\text{iso}}} (P - P_{\text{atm}})dV \right]_{\text{iso}} - (P_{\text{CR}} - P_{\text{atm}})V_{2C,\text{iso}}}{\int_{V_{1C}}^{V_{2C}} (P - P_{\text{atm}})dV - (P_{\text{CR}} - P_{\text{atm}})V_{2C}} \quad (7-4)$$

For a fully isothermal process $\eta_{\text{iso}} = 1$. To minimize work lost due to heat, it is desired that this isothermal efficiency be as close to unity as possible.

If the compression process is treated as a polytropic process, it can be quantified with a uniform polytropic index (n). A polytropic process obeys the following relationship.

$$PV^n = \text{constant} \quad (7-5)$$

For an adiabatic process on an ideal gas, the polytropic index is the ratio of specific heats, i.e. $n = \gamma$. For an isothermal process, $n = 1$. For a process with finite heat transfer, n may vary with time during the process due to variations in heat transfer, but the overall average polytropic index (n_{avg}) will lie between these bounds such that $1 < n_{\text{avg}} < \gamma$. In this case, the average polytropic index for a compression process can be computed by setting the total compression work (Eq. 7-3) equal to the equivalent average compression work which assumes a constant polytropic index.

$$W_{\text{avg,C}} = \frac{n_{\text{avg}}}{n_{\text{avg}} - 1} P_{\text{atm}} V_{1C} \left(1 - PR^{\frac{n_{\text{avg}}-1}{n_{\text{avg}}}} \right) \quad (7-6)$$

The average polytropic index thus reflects a process that would require the same work to reach a given pressure ratio (PR), starting from the same initial volume and pressure. For high isothermal efficiency, it is desired that n be as close to unity as possible.

The expansion work occurs in two periods: i) air is drawn into cylinder at constant pressure, and then ii) air is expanded from the critical pressure (P_{CR}), initial cylinder length (L_E), and initial volume (V_{1E}) to the final pressure (P_{atm}) and volume (V_{2E}). The final volume and time are dependent on the expansion process. The total expansion work can be calculated as

$$W_E = \int_0^{V_{2E}} (P - P_{\text{atm}}) dV = \int_{V_{1E}}^{V_{2E}} (P - P_{\text{atm}}) dV + (P_{\text{CR}} - P_{\text{atm}}) V_{1E} \quad (7-7)$$

Note that expansion work is positive because work is moving out of the system.

The efficiency of the expansion process is measured by the ratio of work for the given process to the work for an isothermal process, where the initial pressure, initial temperature, and final pressure are all fixed. The isothermal expansion efficiency can thus be written as

$$\eta_{\text{iso,E}} = \frac{\left[\int_{V_{1E}}^{V_{2E,\text{iso}}} (P - P_{\text{atm}}) dV \right]_{\text{iso}} + (P_{\text{CR}} - P_{\text{atm}}) V_{1E}}{\int_{V_{1E}}^{V_{2E}} (P - P_{\text{atm}}) dV + (P_{\text{CR}} - P_{\text{atm}}) V_{1E}} \quad (7-8)$$

The average polytropic index of the expansion process can be calculated by setting the total expansion work (Eq. 7-7) equal to the equivalent average expansion work (Eq. 7-9).

$$W_{\text{avg,E}} = \frac{n_{\text{avg}}}{n_{\text{avg}} - 1} V_{1E} P_{\text{CR}}^{\frac{1}{n_{\text{avg}}}} \left(P_{\text{CR}}^{\frac{n_{\text{avg}}-1}{n_{\text{avg}}}} - P_{\text{atm}}^{\frac{n_{\text{avg}}-1}{n_{\text{avg}}}} \right) \quad (7-9)$$

The average polytropic index can then be solved for.

The isothermal roundtrip efficiency (η_{RT}) for a paired set of compression and expansion processes can be calculated as

$$\eta_{RT} = -\eta_{iso,C} * \eta_{iso,E} = -\frac{\int_{V_{1E}}^{V_{2E}} (P - P_{atm}) dV + (P_{CR} - P_{atm}) V_{1E}}{\int_{V_{1C}}^{V_{2C}} (P - P_{atm}) dV - (P_{CR} - P_{atm}) V_{2C}} \quad (7-10)$$

This roundtrip efficiency only accounts for the losses in the compression and expansion processes and does not include valve losses, mechanical losses, or storage losses. It assumes constant pressure storage and the ability to keep the output pressure constant during the discharge process. Therefore, to get a full view of the overall roundtrip efficiency of a CAES system, this isothermal roundtrip efficiency should be combined with other roundtrip system losses.

Mass loading (ML) is the ratio of droplet mass (m_d) currently aloft in the chamber to air mass (m_a) in the chamber at any given time.

$$ML = \frac{m_d}{m_a} \quad (7-11)$$

Other forms of mass loading are useful to define since the instantaneous mass loading defined above will vary over the course of a process. The total mass loading (ML_{tot}) is defined herein as the total mass of droplets in contact with air during the process, divided by the air mass. This includes both the droplets already in the chamber when the compression or expansion process starts ($m_{d,1}$) from the draw in process, and those injected during the compression or expansion process ($m_{d,1 \rightarrow 2}$).

$$ML_{tot} = \frac{(m_{d,1} + m_{d,1 \rightarrow 2})}{m_a} \quad (7-12)$$

When considering a combined compression and expansion process, the roundtrip mass loading (ML_{RT}) is defined as the average of the two total mass loadings.

$$ML_{RT} = \frac{ML_{tot,C} + ML_{tot,E}}{2} \quad (7-13)$$

The Crowe number (Cr) was proposed in Chapter 6 to relate the droplet thermal response time (τ_T) to the fluid domain time scale (τ_D). It can be calculated before simulations as follows, where the isothermal process time is the same for either compression or expansion. For all compression processes, $L_1 = L_C = L_{cyl}$, and for an isothermal process, $L_{2,iso} = L_{cyl}/PR$; for all expansion processes, $L_1 = L_E = L_{cyl}/PR$, and for an isothermal expansion process, $L_{2,iso} = L_{cyl}$.

$$Cr = \frac{\text{thermal response time}}{\text{domain time scale}} = \frac{\tau_T}{\tau_D} \quad (7-14a)$$

$$Cr = \frac{\rho_d d^2 c_s}{6Nuk_a} \left(\frac{1}{t_{\text{fall}}} + \frac{1}{t_{\text{iso}}} \right) \quad (7-14b)$$

$$t_{\text{fall}} = \frac{\frac{L_1 + L_{2,\text{iso}}}{2}}{w_{\text{term}}} = \frac{(1 + \frac{1}{PR})L_{\text{cyl}}}{2 \times w_{\text{term}}} \quad (7-14c)$$

$$t_{\text{iso}} = \frac{|L_1 - L_{2,\text{iso}}|}{U_{\text{piston}}} = \frac{(1 - \frac{1}{PR})L_{\text{cyl}}}{U_{\text{piston}}} \quad (7-14d)$$

When evaluating how well the droplets are able to improve the compression or expansion processes, the thermal equilibrium limit (defined in Chapter 6, based on Ref. [194]) can be used as a lower limit on polytropic indices.

$$n_{\text{m,eq}} = \frac{m_a c_p + m_d c_s}{m_a c_v + m_d c_s} = \frac{c_p + c_s}{c_v + c_s} \frac{ML_{\text{tot}}}{ML_{\text{tot}}} \quad (7-15)$$

The thermal equilibrium limit is the polytropic index that would be reached if droplets and air were always in thermal equilibrium in the limit of infinitely fast heat transfer with infinitely small droplets. Therefore, this limit is the lowest polytropic index expected for a mixture of droplets and air without heat transfer to the environment. It is calculated herein using the total injected mass loading.

C. Parametric analysis

A sweep of compression simulations and a matching sweep of expansion simulations were run based on the parameters given in Table 7-1. The ranges of parameters attempt to capture a wide range of design options, while staying within the bounds of realistic processes and including the range of parameters used to validate the numerical method in Chapter 6. For example, $U_{\text{piston}} = 0.03$ m/s is the piston speed from the experiments used to validate the 1-D method, but it is likely too slow for an energy storage process. At the other extreme, $U_{\text{piston}} = 0.6$ m/s is estimated to the maximum speed for a partially or fully liquid piston. For cylinder lengths, the experiments used to validate to 1-D method used a length around 0.1 m, but longer pistons are predicted to increase the system efficiency, so the range was extended up to $L_{\text{cyl}} = 0.5$ m.

Table 7-1. Parametric sweep parameters for compression and expansion sweeps with direct injection spray.

Parameter	Units	Values	Count
d	μm	200, 150, 100, 50, 25	5
L_{cyl}	m	0.1, 0.3, 0.5	3
U_{piston}	m/s	[0.03, 0.6] linear spacing	4
q_{spray}	L/s	[5e-4, 2e-2] linear spacing	8
PR	-	2, 6, 10	3
Total			1440

D. Spray work validation

In general, spray work depends on the overspray pressure (ΔP) and the spray flow rate (q_{spray}) (based on Ref. [192]) as

$$W_{\text{spray}} = \int_0^{t_2} \Delta P q_{\text{spray}} dt \quad (7-16)$$

Spray is injected during the draw-in period and also during the compression or expansion process from time $t = 0$ to $t = t_2$. This spray work should be added to the compression work to find the total input work or subtracted from expansion work to find the net output work.

Experimental data reported in Patil *et al.* [186] provides information on compression work and spray work for a spray-cooled liquid piston compressor. These experiments were previously used to validate the 1-D compression model in Chapter 6, within the margin of experimental error. Using the same method detailed in Chapter 6, Section 6.3, the 10 psi and 70 psi spray cases were simulated using the Sauter mean diameter of the spray distributions. The BETE spray nozzle used provided a polydisperse droplet distribution with a Sauter mean diameter of 487 μm for 10 psi and 117 μm for 70 psi.

The compression work and spray work are compared between reported experimental results and calculated simulation results in Table 7-2. The overspray pressure was set based on the given spray pressures of 10 psi and 70 psi, respectively. The simulation results are able to predict experimental work with less than 8% error. Also note that the spray work only slightly increases the total work for the low spray case (10 psi), but the spray work nearly doubles the total work for the high spray case (70 psi).

Table 7-2. Comparison of compression and spray work reported from Patil *et al.* [186] with simulation results.

10 psi	Exp. data	Sim. results	% error
Comp. work	42.6 J	44.4 J	4%
Comp. + Spray work	43.7 J	45.6 J	4%
70 psi	Exp. data	Sim. results	% error
Comp. work	35.7 J	37.3 J	4%
Comp. + Spray work	63.9 J	68.5 J	7%

E. Spray work parametric analysis

A model was needed to incorporate spray work for water droplets into simulations where the droplet diameter is specified but the overspray pressure is not known. As such, a model for overspray pressure was developed based on experimental results from the literature to estimate the spray work in a sweep of simulations. The relationship between droplet size, flow rate, and overspray pressure is highly complex and depends on nozzle type, chamber pressure, etc. Many relationships can be found in the literature [207], but most either require specific nozzle information or use fluids other than water. Since pressure-swirl nozzles were found by Qin *et al.* [208] to provide high flow rates for small drop size (less than 100 μm) while avoiding spray-work losses due to aeration, the present study focused on these same type of nozzles.

Data published in Wang & Lefebvre [209] provides the good data for conditions relevant to these simulations (Figure 7-2). In that paper, water sprays were analyzed and the Sauter mean diameter, flow rate, and overspray pressure were all reported. Wang & Lefebvre proposed an equation to predict the Sauter mean diameter of a spray, but it uses many additional terms like the spray cone angle and film thickness. These terms allow consideration of multiple spray nozzles and conditions; however, the present study sought a simplified relationship for a single nozzle in terms of water spray Sauter mean diameter. A surface was fit to the data [209] based on the following relationship for diameter, which can be rewritten for overspray pressure as

$$d = A * q_{\text{spray}}^B * \Delta P^C \quad (7-17a)$$

$$\Delta P = \left(\frac{d}{A * q_{\text{spray}}^B} \right)^{\frac{1}{C}} \quad (7-17b)$$

The form of Eq. 7-17a is similar to those reported in Ref. [207]; where C is generally between -0.25 and -0.47. Based on the experimental data, the coefficient values were adjusted to minimize error resulting in

values of $A = 2.612 \times 10^4$, $B = 0.082$, and $C = -0.383$, with $R^2 = 0.97$. The results with these fitted coefficients are compared to the experimental data in Figure 7-2 for six different overspray conditions. Increasing flow rate slightly increases droplet diameter but increasing overspray pressure has a much stronger effect on droplet diameter.

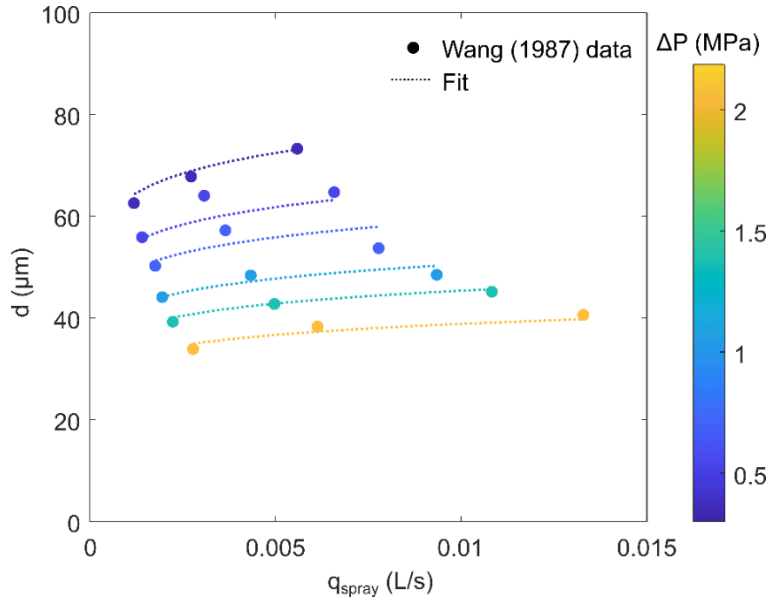


Figure 7-2. Present fitted relation compared to Wang & Lefebvre [209] water spray data in terms of flow rate and droplet diameter for a set of overspray pressures.

Using the spray pressure equation developed above, a sweep of simulations was run including spray work for conditions within or near the experimentally-based conditions of Figure 7-2. Thus, it is a more concentrated and physically realistic sweep (assuming use of pressure-swirl nozzles) than the first one outlined in Table 7-1. The parameters for the sweep with spray work are given in Table 7-3. Additionally, the length of the cylinder was extended, to seek higher roundtrip efficiencies, as discussed in Section 7.3C.

Table 7-3. Parametric sweep including spray work parameters, for compression and expansion simulations.

Parameter	Units	Values	Count
d_p	μm	80, 50, 30	3
L_{cyl}	m	[0.1, 1] linear spacing	4
U_{piston}	m/s	[0.05, 0.5] linear spacing	5
q_{spray}	L/s	[1e-3, 1.5e-2] linear spacing	4
PR	-	2, 6, 10	3
Total			720

7.3. Results and discussion

A. Time-series results

The compression and expansion simulations are assessed as time-series results and their differences are discussed to investigate the fluid physics. Figure 7-3 and Figure 7-4 show one example set of matching compression and expansion simulations with the following parameters: $D = 0.1 \text{ m}$, $L_{\text{cyl}} = 0.3 \text{ m}$, $PR = 10$, $U_{\text{piston}} = 0.2 \text{ m/s}$, $d = 100 \text{ }\mu\text{m}$, $q_{\text{spray}} = 5 \times 10^{-3} \text{ L/s}$, and $Cr = 0.23$.

In Figure 7-3, the log-log pressure-volume changes are shown for the spray-based simulation as well as for an isothermal and an adiabatic process for this pressure ratio. The shaded pink region denotes the time spent between $PR = 5$ and $PR = 10$. The work in or out of the process for the spray-based simulation is shaded in light blue. Ideally, the process would approach the isothermal curve for both the compression and expansion processes. Similar to results found in liquid piston experiments [184] and simulations [204], the compression simulation gives a relatively straight line (on a log-log plot) and is initially favorably close to isothermal limit, while the expansion simulation favorably curves towards the isothermal limit later in the simulation. These different phases that diverge from isothermal may be due to a combination of when the majority of the work is going into and coming out of the compression and expansion processes, respectively, and when the instantaneous mass loading is lowest.

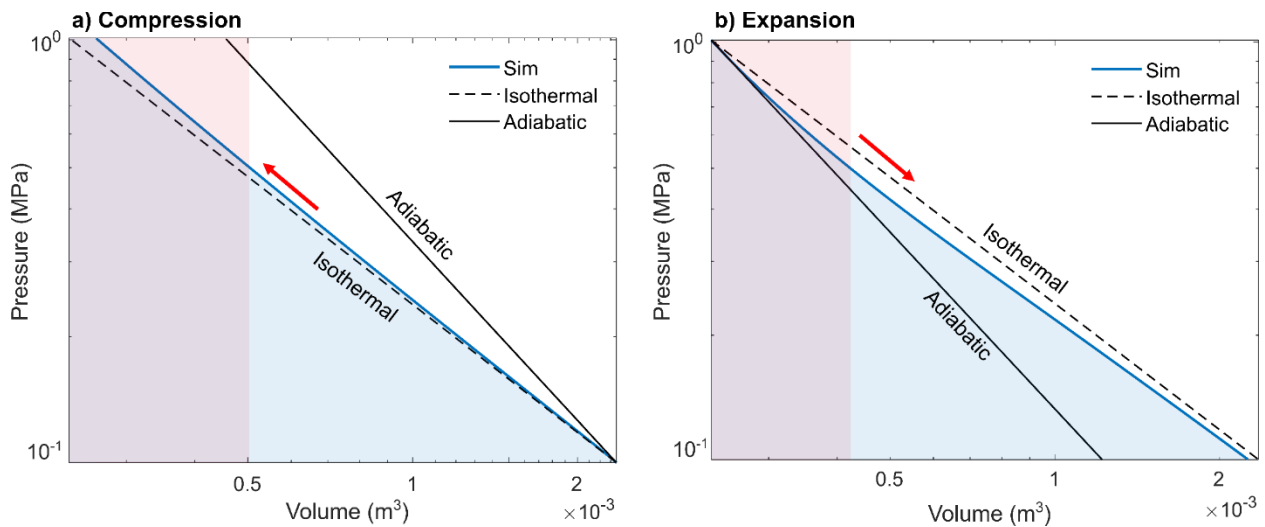


Figure 7-3(a-b). Pressure-volume curves for 1-D spray simulations of compression and expansion, compared to isothermal and adiabatic curves. The shaded blue region denotes the work in or out of the simulation process, while the shaded pink region denotes the first/last 50% of the expansion/compression process.

To further investigate the differences, the instantaneous mass loading, droplet and air temperatures, and polytropic index are plotted over time for the same example compression and expansion processes in Figure 7-4. Again, the first/last 50% of the expansion/compression process is shaded pink. This region is a

small fraction of the process in time but accounts for a large fraction of the total work and results in large changes in air and droplet temperature. Note that the mass loading does not start at zero because spray is injected during the draw in process when air is brought into the cylinder. The draw in process takes longer before the compression process because the piston moves further, and thus the starting mass loading is higher for the compression process than the expansion process (as seen in Figure 7-1).

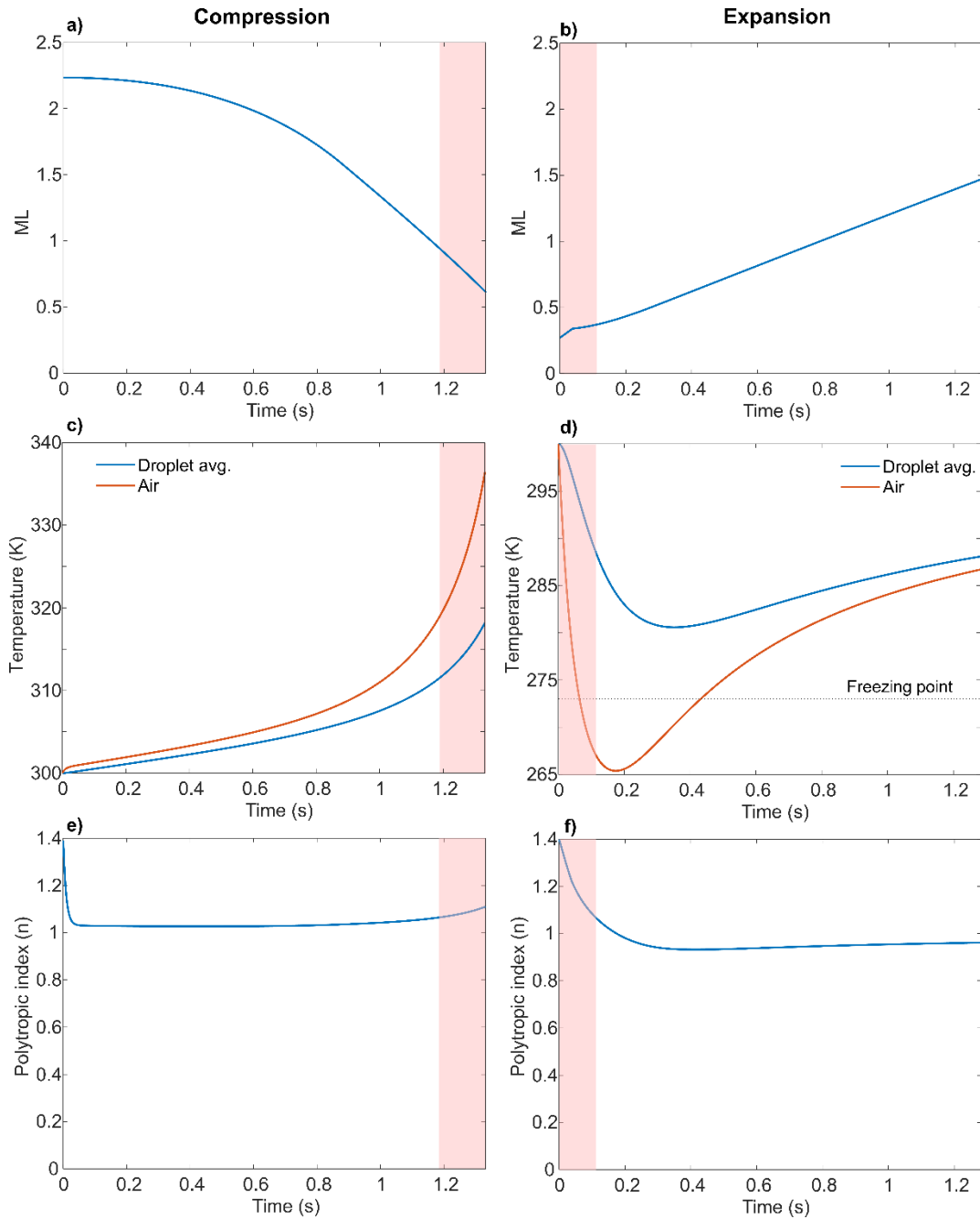


Figure 7-4(a-f). Time series results from 1-D model for an example pair of compression and expansion simulations at $PR = 10$, where the pink-shaded region denotes the last/first 50% of the compression/expansion process.

B. Compression, expansion, and roundtrip efficiency

The results of the parametric analysis defined by Table 7-1 are presented below, for compression and expansion without accounting for spray work. The polytropic index (n) is plotted against total mass loading (ML_{tot}) in Figure 7-5. In both cases, the polytropic index tends to decrease and approach the thermal equilibrium limit as mass loading increases and as the Crowe number decreases. As such, the spray-based performance cannot exceed the thermal equilibrium performance, which only tends to the isothermal limit for high mass loading (much greater than unity). Furthermore, both expansion and compression performance can only approach the equilibrium limit when the Crowe number is small (much less than unity).

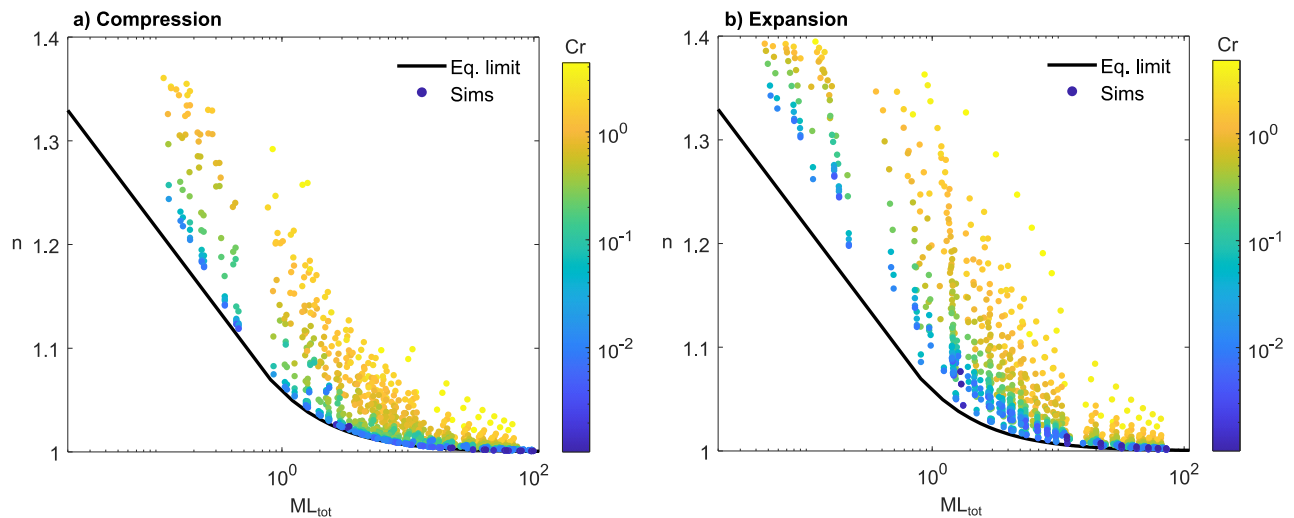


Figure 7-5: Polytropic index (n) versus total mass loading (ML_{tot}) colored by Crowe number (Cr) where the thermal equilibrium limit is plotted in black (while $n=1$ is isothermal limit and $n=1.4$ is adiabatic limit) for: a) compression and b) expansion.

In addition to the above commonalities, there are also differences between expansion and compression. Notably, the expansion simulation polytropic indices do not approach as close to the thermal equilibrium limit as the compression cases. The increased polytropic index for expansion is particularly true for mass loadings less than unity and for high pressure ratios. For a fixed piston speed, high pressure ratios lead to longer compression and expansion times, and thus lower Crowe numbers for a given droplet size, which is favorable. However, for a fixed amount water injected, these longer times lead to lower initial mass loading at the critical start of the expansion process. Thus, the difference in instantaneous mass loadings between compression and expansion simulations during times of large temperature changes is likely the cause of the difference in polytropic indices, which is exaggerated at low total mass loading and high pressure as those are the least efficient cases. This aspect suggests that performance can be increased if the water flow rates are varied in time such that higher mass loadings would occur during the interval when most of the work interaction occurs.

To further investigate the compression and expansion differences, the mass loading and polytropic index can be seen in Figure 7-6, where each circle represents one pair of compression and expansion simulations at the same pressure ratio, spray parameters, and piston parameters. The compression total mass loading is equal to or higher than the expansion mass loading for each pair of simulations, and the compression polytropic index is equal to or lower than the expansion polytropic index. Thus, expansion tends to have a lower mass loading (and higher polytropic index) than compression for the same set up; in addition, for the same mass loading, expansion still has a worse polytropic index than compression (as seen in Figure 7-5). Therefore, a change to the design would be needed to reach an equivalent polytropic index for both the compression and expansion processes, such as increasing the spray flow rate during the expansion draw in process.

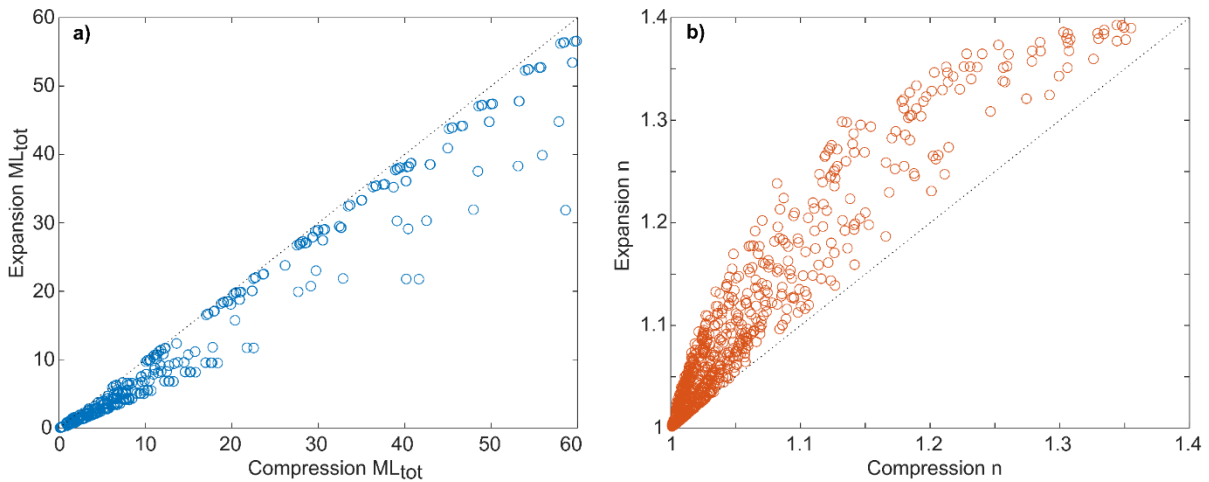


Figure 7-6: Comparing compression and expansion matched simulations a) total mass loading and b) polytropic index. Each circle represents a matched pair of compression and expansion simulations.

While the polytropic index tells us about the thermodynamics of the process, the isothermal efficiency is most useful to a CAES system designer. For conciseness, only the expansion isothermal efficiency results are plotted in Figure 7-7 as a function of total mass loading, divided by pressure ratio; a similar parametric sweep of compression simulation isothermal efficiencies is reported in Chapter 6. Expansion simulations approach isothermal compression with increased mass loading and reduced Crowe number. The effect of Crowe number becomes more pronounced at large pressure ratios. Again, it can be seen that the spray-based expansions at higher pressure ratios are not able to reach the thermal equilibrium limit, even with small Crowe numbers, and this is particularly true for the mass loadings around unity.

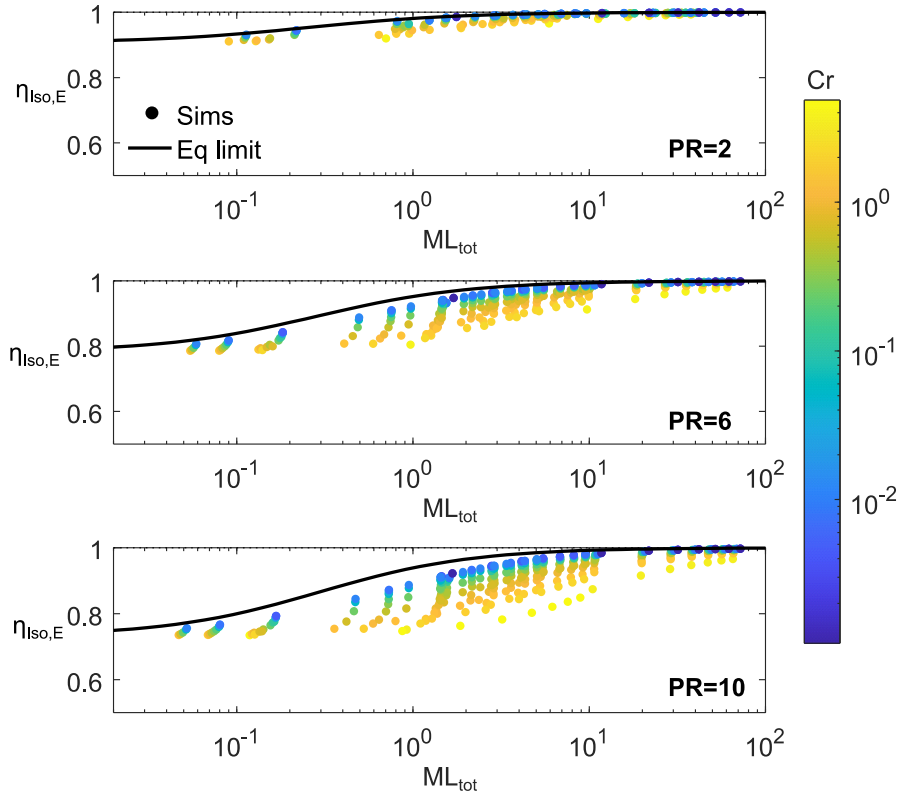


Figure 7-7. Expansion simulations isothermal efficiency vs mass loading, separated by pressure ratio and colored by Crowe number. Thermal equilibrium limit as black line upper limit.

The results from the compression and expansion simulations are combined to calculate isothermal roundtrip efficiencies, plotted in Figure 7-8. Every point in Figure 7-8 represents a pair of compression and expansion simulations with matching pressure ratio, droplet size, and piston parameters, with the isothermal roundtrip efficiency calculated with Eq. 7-12 and the roundtrip mass loading calculated with Eq. 7-11. For a pressure ratio of 2, the change in efficiency with mass loading and Crowe number is small. The efficiencies are all generally high, whereby isothermal roundtrip efficiency greater than 95% can be reached with $ML_{RT} > 1$ for $Cr < 0.06$, or with $ML_{RT} > 10$ for $Cr < 4$. For a pressure ratio of 10, the changes in efficiency with mass loading and Crowe number are more significant, consistent with Figure 7-7. To reach a roundtrip efficiency greater than 95%, the spray-based system must employ $ML_{RT} > 6$ for $Cr < 0.02$, or $ML_{RT} > 20$ for $Cr < 0.77$.

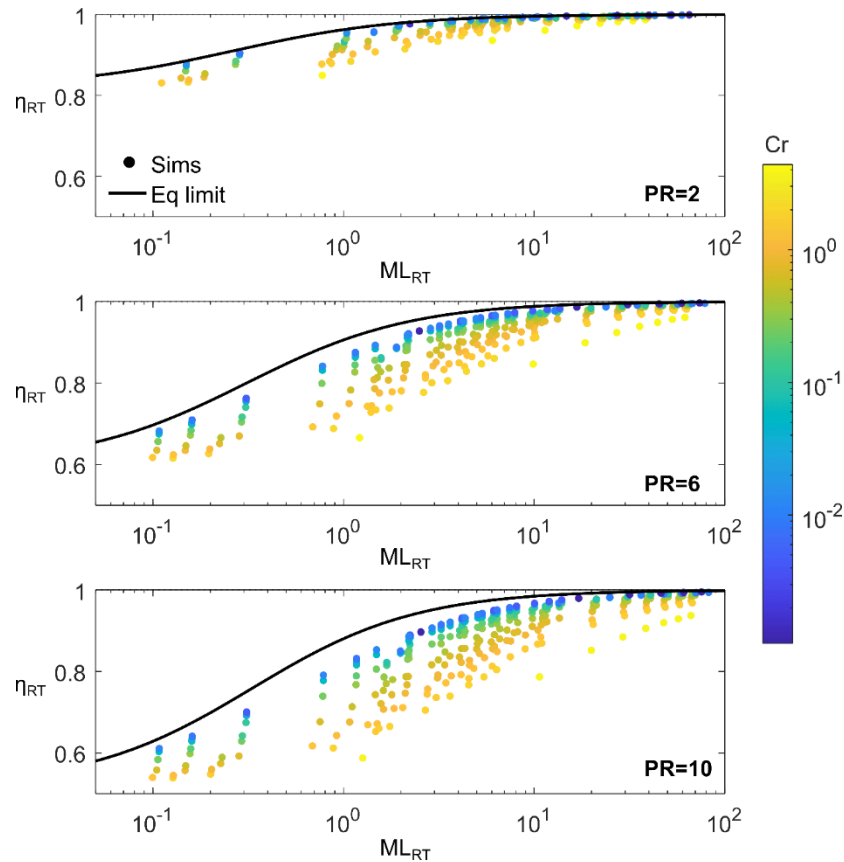


Figure 7-8. Isothermal roundtrip efficiency for matched compression and expansion direct injection simulations plotted against the roundtrip mass loading, colored by Crowe number (Cr) and with the ideal equilibrium limit for roundtrip efficiency plotted in black.

In future compressed air energy storage systems, it is expected that high pressure ratios will be used to increase the power to weight ratio of the system. To investigate, the highest isothermal roundtrip efficiency cases at a pressure ratio of 10 for each droplet diameter are given in Table 7-4. When spray work is not factored into the efficiency calculation, the highest efficiency cases are the highest mass loading cases, with slow compression speed and high spray flow rates. In addition, isothermal roundtrip efficiencies of more than 99% are readily obtained with droplet sizes below 100 μm , if spray-work is neglected.

Table 7-4. Highest isothermal roundtrip efficiency cases for pressure ratio of 10 for each droplet size without spray work.

d (μm)	q_{spray} (L/s)	L_{cyl} (m)	U_{piston} (m/s)	Cr	ML _{RT}	η_{RT}
25	1.44×10^{-2}	0.3	0.03	0.002	75.5	99.5%
50	2×10^{-2}	0.3	0.03	0.016	82.3	99.4%
100	2×10^{-2}	0.5	0.03	0.093	70.1	99.3%
150	2×10^{-2}	0.5	0.03	0.327	67.7	98.9%
200	2×10^{-2}	0.5	0.03	0.769	66.7	98.2%

C. Spray work

The second set of compression and expansion simulations includes spray work for the parameters given in Table 7-3. The resulting isothermal efficiencies for the compression and expansion simulations are shown in Figure 7-9, where pressure ratios are shown with colors and droplet diameters are shown with shapes. Unlike the efficiencies in Figure 7-7 and Figure 7-8, these curves have a parabola-like trend where the efficiency first increases with mass loading and then decreases at high mass loadings, with a peak at intermediate mass loadings. For a given droplet size and pressure ratio, the results indicate an optimal mass loading that creates the highest efficiency, though the optimal value varies based on pressure ratio and droplet size. Also note that at low mass loadings, the highest efficiency processes are those with a pressure ratio of 2 (blue symbols), while at high mass loadings, the highest efficiency processes have droplet diameters of 80 μm (triangular symbols).

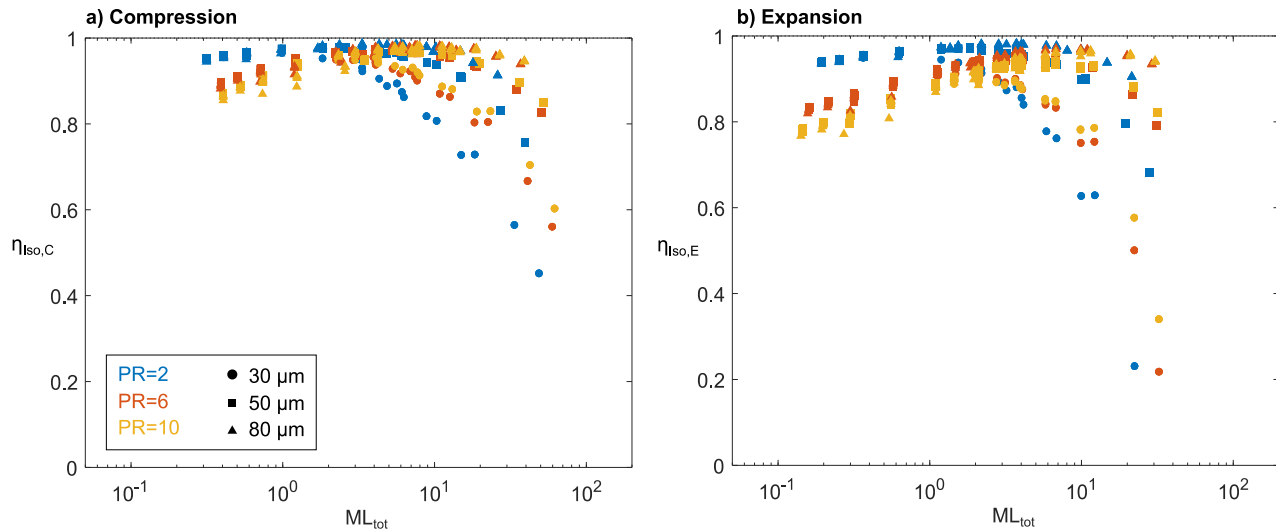


Figure 7-9(a-b). Isothermal efficiency for compression and expansion simulation sweeps including spray work. Pressure ratio (PR) shown in colors, droplet size shown in symbols.

Finally, the spray work compression and expansion simulations were paired to find the roundtrip efficiencies, plotted in Figure 7-10. The previous Crowe number trend, where low Crowe numbers approach the thermal equilibrium limit, can be seen for low mass loadings. However, at higher mass loading the Crowe number relation reverses as the inclusion of spray work lowers the isothermal roundtrip efficiency. Thus, Crowe number becomes less important as a design parameter at higher mass loadings. As a result, roundtrip efficiencies tend to peak around a mass loading of $5 < ML_{RT} < 15$, and then decline as the additional spray work outweighs the additional temperature benefits of the spray. This is particularly true at high mass loadings for the smaller drops, which give small Crowe numbers but require higher spray overpressures. Similar results are seen in the literature, where increasing spray pressure can decrease compression efficiency [186,188,192]. As such, spray work should be generally included in the evaluation of droplet heat transfer systems with significant mass loadings (greater than unity) due to the potential adverse effect on efficiency.

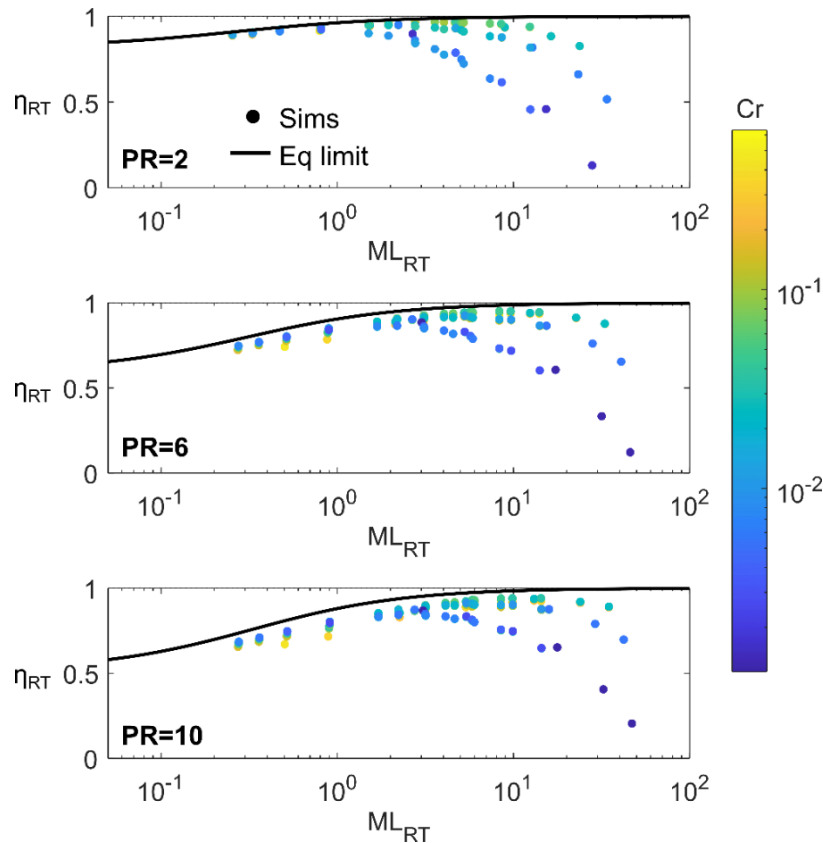


Figure 7-10. Isothermal roundtrip efficiency for combined direct injection compression and expansion simulations including spray work, plotted against the roundtrip mass loading. Simulation results divided by pressure ratio (PR) and colored by Crowe number (Cr), where black line shows ideal thermal equilibrium limit for roundtrip efficiency without spray work.

The highest isothermal roundtrip efficiencies including spray work for a pressure ratio of 10 for a given droplet size are listed in Table 7-5 for the parametric sweep of Figure 7-10. Contrary to the results shown in Table 7-4, here the highest efficiency cases are those with moderate mass loadings. This is because the highest isothermal roundtrip efficiencies represent balances between spray work losses and temperature abatement improvements from the spray heat transfer. Additionally, the highest efficiencies expected with spray work are noticeably lower than those expected without accounting for spray work, where the differences are especially acute at small drop sizes. The highest efficiency cases resulted from the largest droplets of 80 μm , due to their low injection work relative to the smaller droplets. For these droplets sizes, long cylinder lengths and medium-speed piston motion tend to result in the highest efficiency. This is attributed to conditions that allow a low Crowe number (which allows more time for heat transfer to occur) while avoiding large mass loading and small drops (which use too much spray work). The cylinder length was extended to see if an ideal length could be found, but the highest efficiency case continues to be the longest cylinder in the sweep. However, these longer lengths are likely to increase the influence of multi-

dimensional flow features, turbulence, and wall interactions, which are not included in the present study but which are expected to reduce the overall roundtrip efficiency.

Table 7-5. Highest isothermal roundtrip efficiency cases for pressure ratio of 10 for each droplet size, including spray work.

d (μm)	q_{spray} (L/s)	L_{cyl} (m)	U_{piston} (m/s)	Cr	ML_{RT}	η_{RT}
30	1×10^{-3}	1	0.05	0.001	3.1	86.9%
50	5.7×10^{-3}	1	0.1625	0.010	5.4	91.3%
80	1.5×10^{-2}	1	0.1625	0.035	14.3	94.2%

7.4. Conclusions

Using a previously validated 1-D model for compression and expansion with spray injection, a parametric analysis of compression and expansion simulations was completed to better understand the thermal-fluid physics and roundtrip isothermal efficiency of a CAES system. Time-series results from simulations show that compression and expansion processes are not identical and have different polytropic index and temperature trends.

For both compression and expansion, polytropic index of the process decreases and approaches isothermal with increasing mass loading and decreasing Crowe number. The expansion simulation polytropic indices do not approach as close to the thermal equilibrium limit as the compression cases, particularly for mass loadings less than unity and for high pressure ratios, which may be due in part to the timing of the mass loading. For the same process conditions, expansion cases have equal or lower total mass loading than compression cases, and equal or higher polytropic indices than compression cases.

Combining results from matched compression and expansion simulations excluding spray work with the same pressure ratio, drop size, and piston parameters, the highest isothermal roundtrip efficiency cases are those with the highest mass loading cases, with slow compression speed and high spray flow rates. A spray-based system can reach a roundtrip efficiency greater than 95% with a pressure ratio of 10 with $ML_{\text{RT}} > 6$ for $Cr < 0.02$.

A second smaller set of compression and expansion simulations were run including spray work, using a relationship fitted to experimental spray data. For validation, compression work and spray work from simulations were compared to experimental data, and predicted work with less than 8% error.

When accounting for spray work, the highest roundtrip efficiency cases are those with moderate mass loadings and piston speed and long cylinder length. Isothermal roundtrip efficiencies tend to peak around a mass loading of $5 < ML_{RT} < 15$, and then decline as the additional spray work outweighs the additional temperature benefits of the spray. The highest isothermal roundtrip efficiency for a pressure ratio of 10 is 94.2% with the largest droplets ($80 \mu\text{m}$) and $ML_{RT} = 14$.

Some important design trade-offs for a high efficiency compression system can be informed from this study. For a given spray configuration, increasing process time via a longer cylinder and slower piston motion increases the efficiency. For a given piston and compression configuration, reduced droplet size and increased flow rate increases roundtrip efficiency when $ML < 1$, and reduced droplet size and increased flow rate must be balanced with increasing spray work to find the ideal roundtrip efficiency when $ML > 1$. For any given system, Crowe number is a driving factor for increasing efficiency for $ML < 1$, but Crowe number is no longer the sole factor at higher mass loadings and instead the Crowe number effect must be weighed against the impact of high spray work.

Given the large effect of spray work on the optimal high-efficiency design, spray work should be included for significant mass loadings (e.g. greater than unity) due to the potential adverse effect on efficiency and future work is recommended to implement a universal spray work equation to capture the effect of spray work in a larger variety of conditions. Additionally, efficiency may be increased by considering pre-mixed injection of droplets for expansion to increase the mass loading at the beginning of the expansion process, when the most work is extracted. The work herein using relatively small cylinders may be expanded in the future to design high-power systems with larger cylinder lengths on the scale of 1-5 m (for liquid pistons). Further investigation is recommended to consider effects of polydisperse droplet size distributions, multi-dimensionality, turbulence, wall-interactions, and droplet dynamics, and to investigate high-efficiency cases with experiments.

Chapter

8. Pre-mixed droplet injection for efficient air compression and expansion: 1-D and 2-D simulations

Abstract

One option for increasing the efficiency of compressed air energy storage (CAES) is to use water sprays to increase heat transfer during the compression and expansion processes and direct injection is the typical spray format. However, numerical simulations indicate that expansion has generally lower energy efficiency than compression for the same amount of direct injection droplet mass and same droplet size. Without spray injection expansion experiments, there remains uncertainty about the best method to achieve isothermal expansion. Herein, pre-mixed droplet injection is considered as a potential alternative to direct injection to improve efficiency for a given injected spray mass loading, especially for expansion. A parametric analysis is completed for pre-mixed compression and expansion simulations in 1-D, and the results indicate that the polytropic index trends with total mass loading and Crowe number are similar to those for direct injection. In addition, the pre-mixed simulations achieved higher roundtrip isothermal efficiencies than comparable direct injection simulations, for cases with moderate total mass loading. Additionally, three of the 1-D cases were investigated with unsteady 2-D axisymmetric simulations using ANSYS Fluent. Large air and droplet temperature variations throughout the chamber were seen in the 2-D simulations, violating some of the 1-D model assumptions, and the 1-D simulations consistently predicted higher mass loadings throughout the processes than the 2-D simulations. Despite these differences, the percent differences between the fast 1-D model and the more time-consuming 2-D model were less than 7% for pressure ratios of 10, indicating that the 1-D model may provide sufficient accuracy for identifying high-efficiency designs early in the design process. Future work is suggested to consider an extension to 3-D effects and study the ideal timing of sprays as a combination of pre-mixed and direct injection to achieve isothermal CAES.

Nomenclature

ρ	density ($\frac{\text{kg}}{\text{m}^3}$)
γ	ratio of specific heats of air
η	efficiency
τ	time constant (s)
c_s	water specific heat capacity at constant pressure ($\frac{\text{J}}{\text{kg-K}}$)
Cr	Crowe number
d	droplet diameter (m)
D	cylinder diameter (m)
g	Gravity (m^2/s)
k	air thermal conductivity ($\frac{\text{W}}{\text{m-K}}$)
L	vertical length from cylinder head (m)
m	mass (kg)
ML	mass loading
n	polytropic index
Nu	Nusselt number
P	pressure (Pa)
ΔP	overspray pressure (Pa)
PR	pressure ratio
q_{spray}	spray flow rate ($\frac{\text{L}}{\text{s}}$)
t	time
U_{piston}	piston speed ($\frac{\text{m}}{\text{s}}$)
V	volume (m^3)
w_{term}	droplet terminal relative velocity ($\frac{\text{m}}{\text{s}}$)
z	position (m)

Subscripts

1	beginning of process
2	end of process
a	air
adi	adiabatic
atm	atmospheric

avg	average
C	compression
CR	critical
cyl	cylinder
d	droplet
D	domain
E	expansion
fall	fall
init	initial
iso	isothermal
P	momentum
RT	roundtrip
spray	spray
T	thermal
tot	total

8.1. Introduction

A. Motivation

As discussed in Chapters 6 and 7, compressed air energy storage (CAES) is a low-cost, long-duration energy storage option which may be important for a fully renewable electrical grid. One option for increasing the efficiency of CAES is near-isothermal compression, where increased heat transfer allows the compressed air to maintain a near-constant temperature. Spray injection during the compression process was investigated in Chapters 6 and 7 and showed good improvements in efficiency at high mass loadings. However, spray nozzles in the compression chamber increase complexity, and since spray work has been found to contribute significantly to the total work, the timing and amount of spray should be critically considered.

In Chapter 7, the efficiency of the expansion process with droplet spray injection was investigated. When comparing compression and expansion processes with the same set-up and design parameters, it was found that the expansion processes had lower efficiency, particularly in the mid-range mass loadings around unity. In that range of total mass loadings, expansion simulations were not able to approach the thermal equilibrium limit for small Crowe numbers (while compression simulations did achieve this limit). This is attributed in part to a reduced mass of droplets injected at the beginning of the expansion for a direct injection process, when most of the useful work is extracted (as discussed in Chapter 7). Based on this result, it is hypothesized that the important parameter for high efficiency processes is not total mass loading, but rather the instantaneous mass loading during the highest work phase of the process.

B. Previous work

Previous researchers have explored spray injection during the compression or expansion process via numerical methods or physics-based approximations [188,190,192,202], generally with a focus on direct injection during the compression process. Qin & Loth [190] compared direct injection and pre-mixed injection cases and found that direct injection performed better for compression with sinusoidal piston motion, maintaining lower air temperature for the same mass loading, but did not consider expansion with spray injection. A recent study explored the timing of spray during the compression process, seeking to optimize the spray flow rate by balancing spray work against heat reduction, and found that the optimal system sprayed more droplets at the beginning of the process and less towards the end of the compression process, allowing those droplets to spend longer in the chamber and provide more heat exchange [210]. However, this work only considers small droplets ($\sim 30 \mu\text{m}$) and a low pressure ratio of 2.

Some studies have investigated near-isothermal CAES using higher-dimensional computational fluid dynamics, with a focus on the compression process. Qin & Loth [189] used 2-D modeling in ANSYS

Fluent to investigate spray-cooled compression for the first two stages of CAES and found that the 2-D model was able to give similar results to the 1-D simulations. Gouda *et al.* [211] modeled a slow moving liquid piston for isothermal compression and found that moving to faster speeds ($U_{piston} > 0.1$ m/s) would require heat removal measures (such as spray injection) to maintain a near-constant temperature. However, no CFD studies have been published investigating the expansion process for near-isothermal CAES.

Some experimental results are available for spray-cooled compression, such as those reported by Patil *et al.* [186], but no similar results have been published for expansion. The near-isothermal expansion process has been shown to have different fluid dynamics and heat transfer trends than the compression process (Chapter 7, Refs. [184,212]), but without experiments on spray injection expansion there remains uncertainty about the best method to achieve isothermal expansion.

Based on the work in Chapter 7, it is hypothesized that pre-mixed injection may be one way to simplify the system design (avoiding more complex in-cylinder spray systems) while also increasing the mass loading at the beginning of the expansion process when the extracted work is highest. Note, that spray work for pre-mixed injection will still be proportional to the total droplet mass injected, but that spray work may be better utilized.

C. Objectives

The purpose of this study is to investigate pre-mixed injection for near-isothermal compression and expansion via a parametric analysis with a 1-D numerical method and then investigate a few of these cases with a 2-D method. The 2-D simulations can provide a comparison to 1-D simulations to see how different assumptions between 1-D and 2-D give different results. This is the first study to the author's knowledge to investigate the thermodynamics of both compression and expansion with pre-mixed sprays, the first to determine the roundtrip efficiency of the combined compression/expansion process, and the first to investigate droplet spray and airflow properties for near-isothermal expansion in 2-D.

8.2. Methodology

A. 1-D numerical model

First, pre-mixed compression and expansion processes were modeled using the 1-D numerical model validated in Chapter 6 and used for the parametric analysis in Chapters 6 and 7. The 1-D model for compression is described in detail in Chapters 6 and 7 and builds upon work by Qin & Loth [190]. First-stage compression was simulated in a piston with an adiabatic boundary condition. The air in the cylinder is assumed to have uniform pressure, temperature, and density, obeying the ideal gas law. The starting air temperature and droplet temperature for all simulations is room temperature (300 K). The model assumes

1-D air flow along the z -axis, with a velocity varying linearly from the top center of the cylinder to that at the piston face (which moves at a constant speed).

A notional schematic of the compression and expansion processes is shown in Figure 8-1. For all simulations, the piston speed (U_{piston}), total cylinder length (L_{cyl}), total mass loading (ML_{tot}), droplet diameter (d), and maximum pressure ratio (PR) are set. Note that total mass loading is also equal to the initial mass loading for pre-mixed case since there is no spray injection after compression or expansion starts.

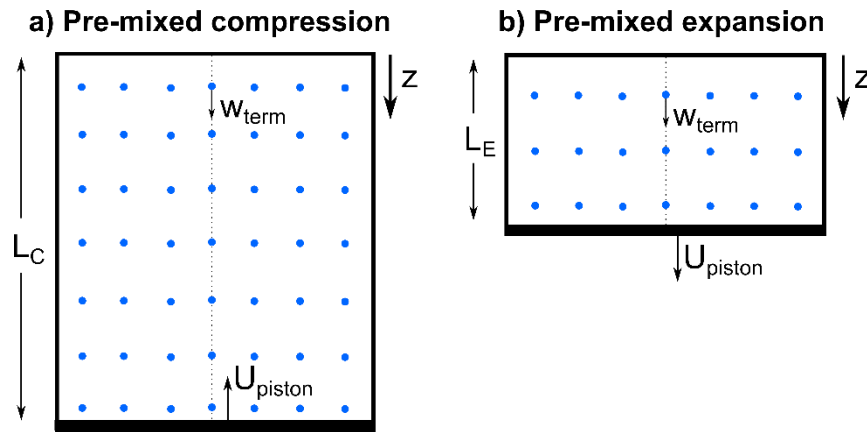


Figure 8-1: Pre-mixed spray notional schematic at the beginning of the process for a) compression, and b) expansion.

For compression, the cylinder is compressed from starting length ($L_1 = L_C = L_{\text{cyl}}$) and atmospheric pressure (P_{atm}) until the critical pressure (P_{CR}) is reached. For expansion, the cylinder is expanded from starting length ($L_1 = L_E = L_{\text{cyl}}/PR$) and critical pressure (P_{CR}) until atmospheric pressure (P_{atm}) is reached. The compression and expansion processes are further described in Chapter 7.

For pre-mixed droplet injection, the water droplets are mixed with the air before being drawn into the chamber for compression or expansion. Thus, the water droplets are evenly distributed throughout the chamber at the start of each process, and no additional droplets are added during the process. Once the process starts, the droplets move based on a linear combination of their terminal velocity and the local air velocity, and thus the droplet velocities are one-dimensional. Note that while spray work will still be required to inject the droplets into the inlet air and pre-mix the air stream, spray work is not included in the calculations herein. Heat transfer from the air to the droplets is assumed to be the dominant form of heat transfer during compression, and thus the piston and walls are considered adiabatic and heat transfer is only allowed to the droplets.

The numerical method employs a two-step process, where first the air is compressed or expanded adiabatically, and then heat transfer is allowed between the air and the droplets. Readers are referred to Chapter 6 and Chapter 6 Appendix for details on the numerical method.

A simulation result was removed from the dataset if any of the following occurred:

- Droplet momentum response time (τ_p) was greater than 10% of the total stroke time (terminal velocity assumption may not be valid),
- There were less than 100 steps in the simulation (potentially inadequate temporal discretization),
- Piston speed exceeded $\frac{U_{\text{piston}}}{t_{\text{iso}}} < 0.1g$ (ensuring that if this system was implemented with a real piston, the speed and acceleration would be physically realistic), or
- More than 10% of the initial cylinder volume was droplets (the pre-mixed spray significantly changed the cylinder volume).

B. 2-D model

The first-stage compression and expansion processes were also modeled in 2-D using ANSYS Fluent software with pre-mixed droplet injection. A notional schematic of the 2-D set-up is shown in Figure 8-2.

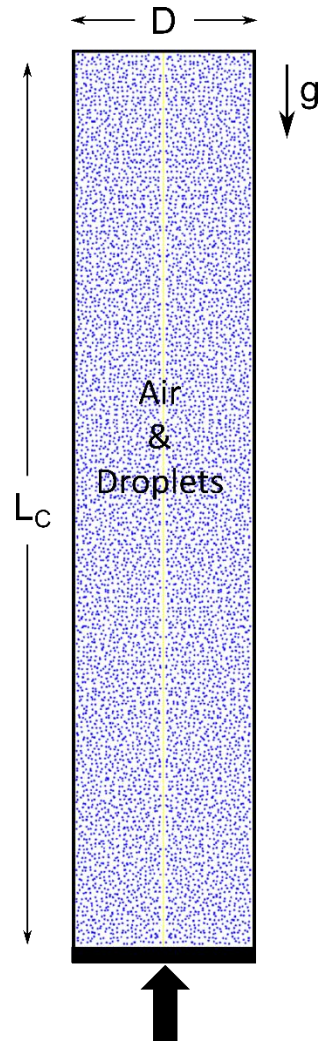


Figure 8-2. 2-D pre-mixed compression schematic at the beginning of compression, where each dot is a parcel, representing many droplets.

The 2-D computational multiphase fluid dynamics simulations employed the following settings:

- Axisymmetric about the cylinder centerline
- Transient with timestep given by $dt = 1 \times 10^{-5}$ s
- Adiabatic boundary conditions
- Continuous phase fluid
 - Air as ideal gas
 - k-omega SST turbulence model
- Discrete phase model for droplets
 - Inert particles, spherical liquid water
 - Discrete random walk for turbulent diffusion
 - Unsteady Lagrangian particle tracking
 - Two-way momentum, thermal energy and turbulence coupling
 - Droplets escape (are removed from simulation) via impact with walls and piston surface

Like the 1-D simulations described in Section 8.2A, the 2-D simulations start with air mixed with droplets at 300 K with no initial velocity and compress or expand with constant piston motion until the final pressure is reached. The droplets are considered to be inert, meaning they do not evaporate, freeze, coalesce, or breakup. The droplet parcels, droplet number, and initial conditions are all set before the simulation starts using an injection input file.

The major assumptions for each method are summarized and compared in Table 8-1.

Table 8-1. Assumptions for 1-D numerical method and 2-D Fluent model

1-D	2-D
Air as ideal gas and two-way coupling with drops for thermal energy (temperature)	SAME
Chamber walls and piston are adiabatic	SAME
Droplets evenly dispersed in chamber at start of process	SAME
Droplets as inert particles (do not evaporate, freeze, break-up, or coalesce)	SAME
Droplets move in 1-D along z-axis	Droplets move in 2-D
Droplets fall based on combination of terminal velocity and air velocity	Droplets have finite inertia and dynamics so that relative velocity can vary
Air velocity varies linearly in 1-D (wall boundary condition's allow slip velocity)	Air velocity based on turbulent flow (k- ω SST) and no-slip wall boundary conditions
Droplet velocity varies linearly in 1-D	Discrete random walk for droplet diffusion due to turbulence
One-way coupling for air flow	Two-way coupling for air momentum and turbulence based on drops

C. Outputs and nondimensional parameters

Mass loading (ML) is the ratio of droplet mass (m_d) currently aloft in the chamber to air mass (m_a) in the chamber at any given time, written as

$$ML = \frac{m_d}{m_a} \quad (8-1)$$

Other forms of mass loading are useful to define since the instantaneous mass loading defined above can vary over the course of a process. The average mass loading (ML_{avg}) is the time-averaged instantaneous mass loading over the compression or expansion process (from $t = 0$ to $t = t_2$).

$$ML_{avg} = \frac{\int_0^{t_2} ML dt}{t_2} \quad (8-2)$$

The total mass loading (ML_{tot}) is defined herein as the total mass of droplets in contact with air during the process, divided by the air mass, defined as

$$ML_{tot} = \frac{m_{d,1}}{m_a} \quad (8-3)$$

where for a pre-mixed process only the droplets in the chamber before the start of the process ($m_{d,1}$) are considered. The initial droplet mass is pre-mixed with the air and the drops are evenly dispersed throughout the chamber. The total mass loading proportional to the total spray work, for a fixed air mass.

When considering a combined compression and expansion process, the roundtrip mass loading (ML_{RT}) is defined as

$$ML_{RT} = \frac{ML_{tot,C} + ML_{tot,E}}{2} \quad (8-4)$$

which is the average of the compression total mass loading and the expansion total mass loading.

The Crowe number (Cr) was defined in Chapter 6 as the ratio of the droplet thermal response time (τ_T) to the fluid domain time scale (τ_D) and can be calculated before simulations as follows, where the isothermal process time (t_{iso}) is calculated the same for either compression or expansion. For pre-mixed processes, droplet fall time (t_{fall}) is estimated as half the maximum cylinder length. Thus, the droplet fall time estimate for pre-mixed injection (Eq. 8-5c) gives a shorter fall time than the direct injection estimate (Eq. 6-13a), since direct injection droplets are all injected at the top of the cylinder while pre-mixed droplets are evenly dispersed.

$$Cr = \frac{\text{thermal response time}}{\text{domain time scale}} = \frac{\tau_T}{\tau_D} \quad (8-5a)$$

$$Cr = \frac{\rho_d d^2 c_s}{6Nuk_a} \left(\frac{1}{t_{fall}} + \frac{1}{t_{iso}} \right) \quad (8-5b)$$

$$t_{fall} = \frac{\frac{L_{cyl}}{2}}{w_{term}} \quad (8-5c)$$

$$t_{iso} = \frac{|L_1 - L_{2,iso}|}{U_{piston}} = \frac{(1 - \frac{1}{PR})L_{cyl}}{U_{piston}} \quad (8-5d)$$

For all compression processes, $L_1 = L_C = L_{cyl}$, and for an isothermal process, $L_{2,iso} = \frac{L_{cyl}}{PR}$, for all expansion processes, $L_1 = L_E = \frac{L_{cyl}}{PR}$, and for an isothermal expansion process, $L_{2,iso} = L_{cyl}$. Thus $|L_1 - L_{2,iso}|$ is the stroke length for an isothermal process.

As outlined in Chapter 7, the compression and expansion processes each have specific equations for calculating their work, isothermal efficiency, and polytropic index. These are used to assess how close each process is to isothermal and how much energy is recoverable. When evaluating how well the droplets are able to improve the compression or expansion processes, the thermal equilibrium limit (defined in Chapter 5, based on Ref. [194]) can be used as a lower limit on polytropic indices for a given mass loading.

8.3. Parametric analysis with 1-D model

A. Test conditions

A matching set of compression and expansion simulations was run based on the parameters given in Table 8-2. The range of parameters was chosen to match the input parameters and output total mass loading from the direct injection simulations without spray work in Chapter 7. The cylinder diameter was fixed at $D = 0.1$.

Table 8-2. Parametric sweep parameters for compression and expansion with pre-mixed spray injection.

Parameter	Units	Values	Count
d	μm	200, 150, 100, 50, 25	5
L_{cyl}	m	0.1, 0.3, 0.5	3
U_{piston}	m/s	[0.03, 0.6] linear spacing	4
ML_{tot}	-	[0.04, 27] log spacing	6
PR	-	2, 6, 10	3
Total			1080

B. Results

The results of the pre-mixed 1-D simulations are shown in the figures below. The average polytropic indices of compression are shown in Figure 8-3 for compression and expansion parametric sweeps. Each point represents the average polytropic index of one simulation. When plotted against total mass loading, Figure 8-3(a-b) shows the simulation polytropic indices decreasing with increasing mass loading and approaching the isothermal limit of $n = 1$. The simulations are colored by Crowe number in Figure 8-3, and small Crowe numbers can be seen to approach the thermal equilibrium limit (defined as infinitely fast heat transfer with infinitely small droplets) in Figure 8-3a.

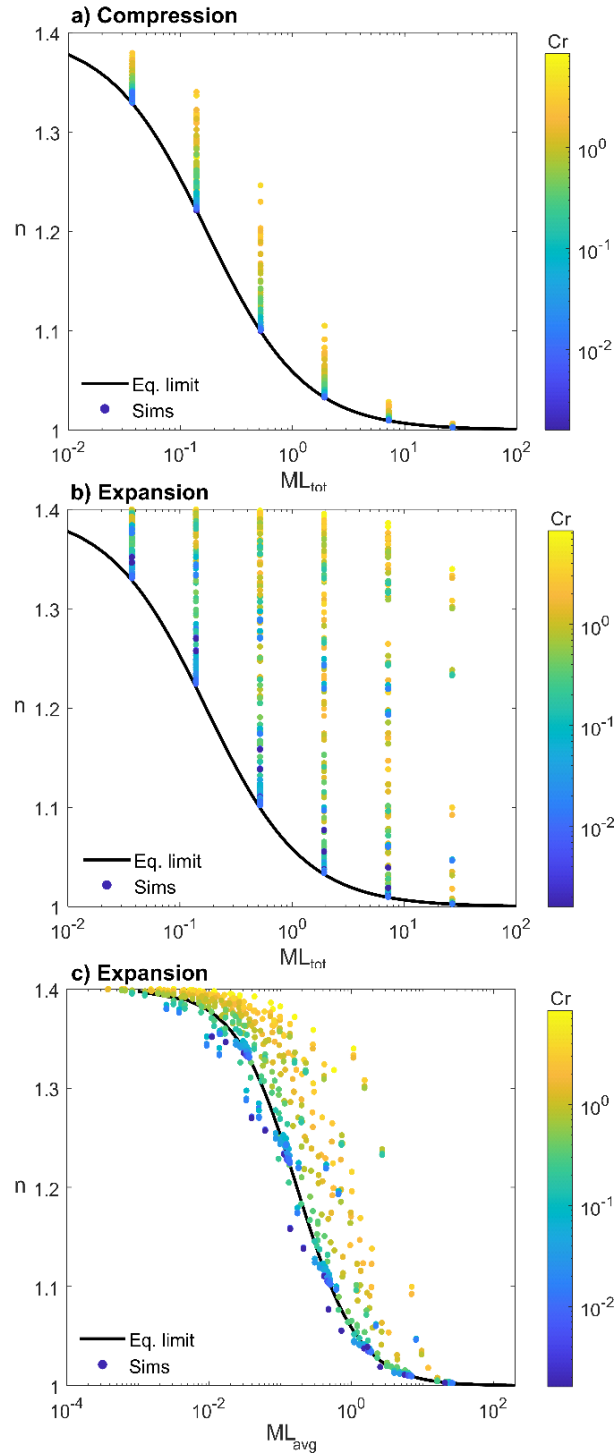


Figure 8-3(a-c): Pre-mixed spray simulation polytropic index (n) as a function of mass loading (ML), colored by Crowe number with thermal equilibrium limit shown with black line: a) compression with total mass loading, b) expansion with total mass loading, c) expansion with average aloft droplet mass loading.

In Figure 8-3b, there is not a clear pattern observed in the Crowe numbers. The total mass loading may not reflect the instantaneous mass loading in the chamber for the highest work times in the process (as discussed further in Chapter 7). Additionally, the relative magnitude of the droplet terminal velocity and the piston velocity has a large effect on the amount of time the droplets stay aloft. Changes in droplet mass loading and time aloft can thus affect the air temperature during the process and the resultant process time, which can lead to a lack of Crowe number trend, inconsistent with previous theory. The Crowe number relation is slightly inconsistent for both the compression and expansion cases, but the effect is much more noticeable in the expansion cases.

For comparison, Figure 8-3c plots the expansion cases against the *average* mass loading for each simulation. The average mass loading is better able to capture how much mass is available to transfer heat with the air and affect the polytropic index. The Crowe number trends are more consistent and clear in Figure 8-3c with smaller Crowe numbers tending to correlate with reduced polytropic index for a given average mass loading. However, plotting polytropic index by the average mass loading may result in simulations that appear to fall below the thermal equilibrium limit because the average mass loading does not represent the total mass of droplets which undergoes heat transfer within the chamber.

The matched compression and expansion simulations are combined to find the roundtrip isothermal efficiency and roundtrip total mass loading, plotted in Figure 8-4 by pressure ratio. Again, the Crowe number relations are less clear, but the efficiency does increase with increasing mass loading and some simulations are able to approach the thermal equilibrium limit. The range of simulation roundtrip efficiencies for a pressure ratio of 10 are marked with bars in Figure 8-4, which are then transferred to Figure 8-5 for further comparison.

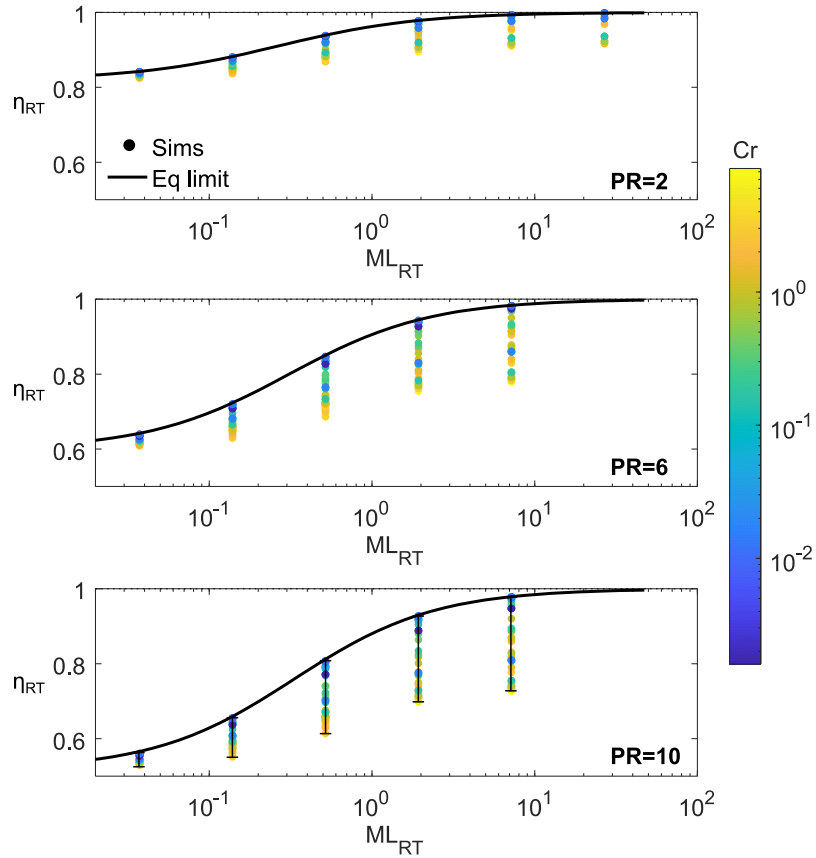


Figure 8-4. Pre-mixed spray combined compression and expansion simulations to find roundtrip efficiency as a function of roundtrip mass loading, divided by pressure ratio, with bars showing the efficiency ranges for PR=10.

In Figure 8-5, roundtrip isothermal efficiency is plotted against roundtrip total mass loading for a pressure ratio of 10 for direct injection (from Chapter 7 results) and pre-mixed injection simulations. The direct injection simulations were not able to reach high efficiencies in the moderate mass loading range of $0.1 < ML < 10$, even at low Crowe numbers. By comparison, the range of pre-mixed results indicated by the bars show that pre-mixed compression is able to achieve high roundtrip efficiency, up to the thermal equilibrium limit in that range.

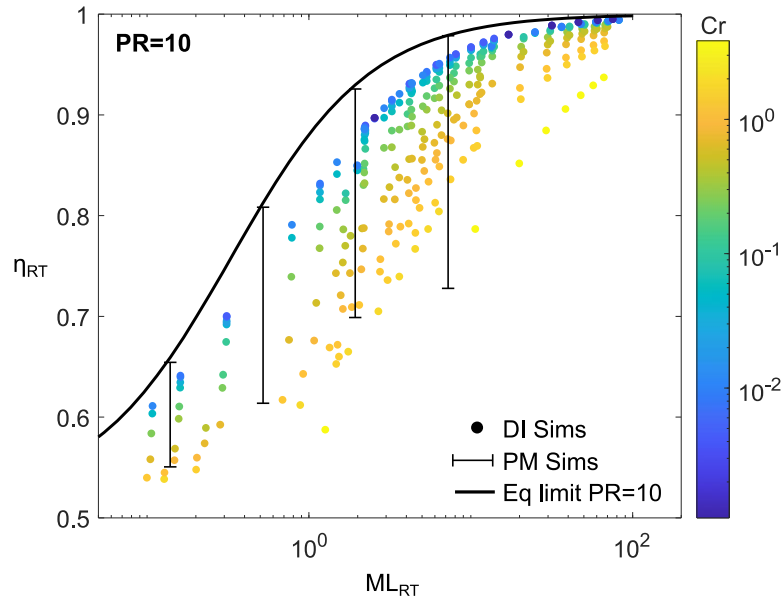


Figure 8-5. Roundtrip efficiency as a function of roundtrip mass loading between compression and expansion simulations, comparing direct injection (DI) simulations to the ranges found with pre-mixed (PM) simulations for a pressure ratio of 10.

Based on Figure 8-5, it can be seen that in some cases pre-mixed compression and expansion may be advantageous for achieving high efficiency compressed air energy storage with moderate mass loadings. However, at very high mass loadings (e.g. greater than 20), either option is able to achieve high efficiency with small Crowe numbers. The defining aspect for when pre-mixed droplet injection is preferable may be the ratio of droplet terminal velocity to piston speed, thus capturing the likelihood of droplets to remain aloft throughout the process. The distinction of when direct injection vs pre-mixed injection is preferred should be further studied.

8.4. 1-D vs 2-D simulation comparisons

A. Test conditions

A small number of cases were simulated in 2-D to assess the 1-D assumptions for the expansion model and to understand 2-D and turbulent flow effects, with the details listed in Table 8-3. As discussed in the Methodology, both methods used pre-mixed droplets that were evenly distributed throughout the chamber before the compression or expansion process started. The following parameters were held constant for all three cases: $L_{\text{cyl}} = 0.5$ m, $D = 0.1$ m, $PR = 10$, and $U_{\text{piston}} = 0.6$ m/s.

Table 8-3. Parameters for comparison cases between 1-D and 2-D

	d (μm)	ML_{tot}
Case 1	75	0.5
Case 2	50	0.15
Case 3	50	0.15

The case parameters were initially chosen to seek high-efficiency cases based on results from Chapters 6 and 7 with a realistic design that also prioritizes high power density (fast compression, large pressure ratio). With a droplet diameter of 50 μm , the Crowe number for this set up is 0.05, while a droplet diameter of 75 μm gives a Crowe number of 0.13. The numerical method used herein was suitable for mass loadings as high as 0.5 based on droplet volume limits.

B. Results

In the following, instantaneous visualizations of the 2-D results are shown at two times in the expansion process. These are followed by a more general analysis of each case in terms of pressure-volume relations and mass loading dynamics, concluding with overall thermodynamics and efficiencies of these cases compared to 1-D results.

The 2-D simulation temperature results are shown at $t = 0.2$ s (40% of expansion process) in Figure 8-6 and at $t = 0.5$ s (100% of expansion process) in Figure 8-7. Note that the simulations are axisymmetric, so only one side of the chamber is simulated and the results are mirrored over the center axis. Each dot is a parcel representing a cloud of many droplets ($\sim 3,000$ droplets/parcel for Case 1).

The first snapshot at $t = 0.2$ s already shows variation in temperatures in the axial and radial direction which are not captured by the 1-D model. The air temperature varies significantly throughout the domain, with the coldest temperatures at the top of the chamber where there are no droplets and thus no opportunities for heat transfer to keep the air from cooling down during expansion. The particle temperatures also vary radially through the cylinder, which is not captured by the 1-D model as it only allows for axial temperature variation. The warmer air and droplet temperatures along the centerline of the piston is attributed to a higher concentration of droplets near the center of the piston (as investigated with particle density plots). The lower droplet concentration towards the sidewalls is due to sidewall impacts which remove these drops from the simulation, which provides fewer droplets to exchange heat with the air in those areas.

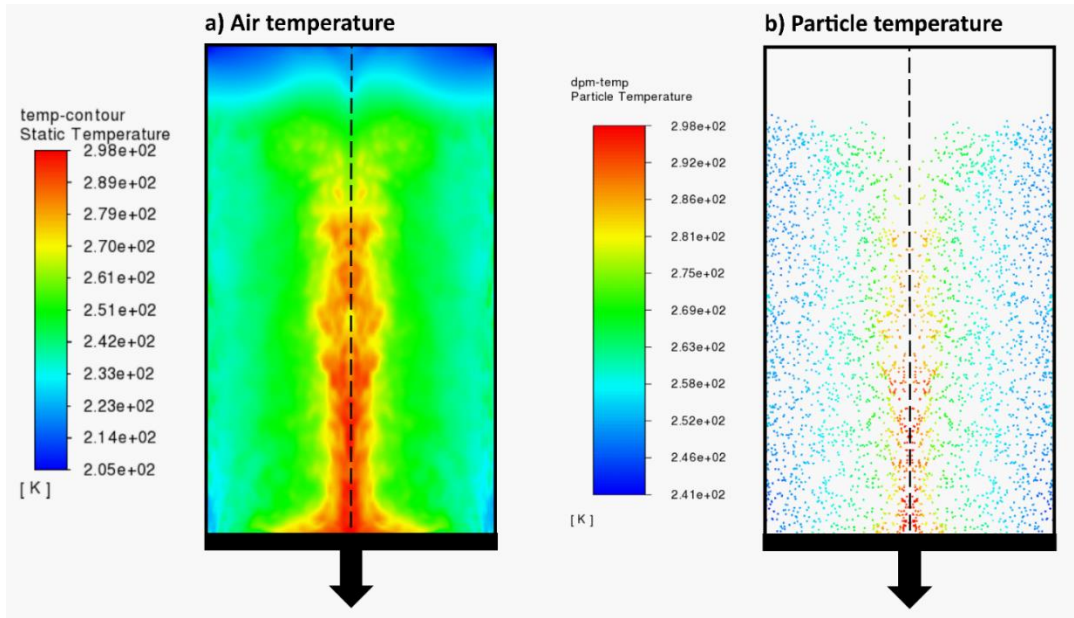


Figure 8-6. Case 1 pre-mixed expansion example 2-D simulation results at $t = 0.2$ s (40% of expansion) for a) air temperature and b) particle temperature.

Figure 8-7 shows the temperatures in the chamber at the end of the expansion process at $t = 0.5$ s. Again, the air and particle temperatures both vary significantly spatially. Most of the particle temperatures are below freezing, indicating that the droplets would need to be composed of a compound with a lower freezing point than water or else the droplets would freeze. Notably, a significant portion of the chamber has no droplets, as the droplets have shifted down over time due to gravity and the moving piston.

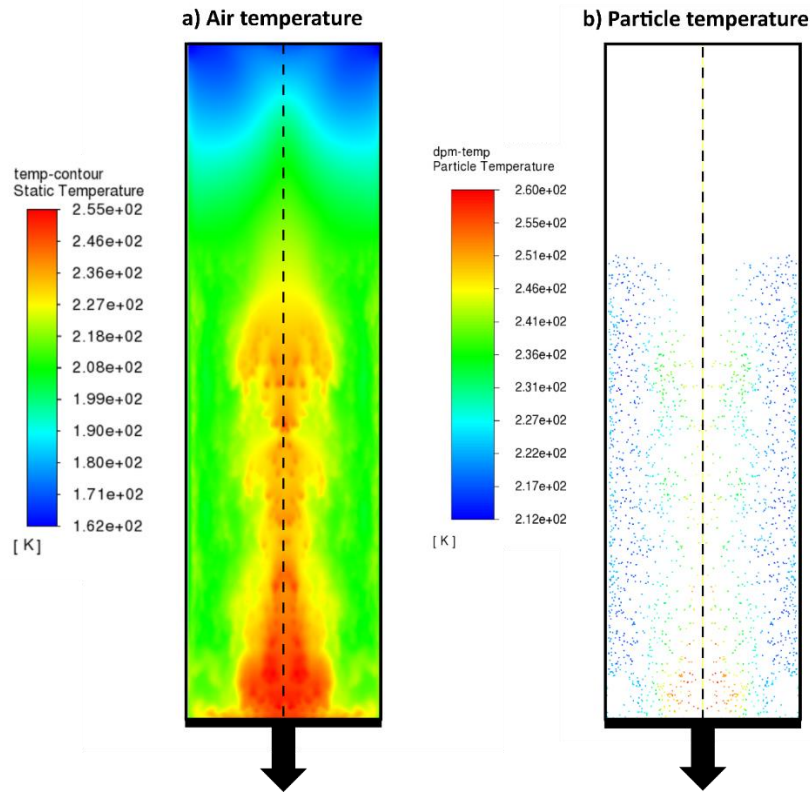


Figure 8-7. Case 1 pre-mixed expansion example 2-D simulation results at end of expansion process ($t = 0.5$ s) for a) air temperature and b) particle temperature.

The 2-D simulation for Case 1 (shown in Figure 8-6 and Figure 8-7) is then compared to a 1-D numerical method simulation for the same case in Figure 8-8. The 1-D and 2-D simulations start with similar curves on the pressure-volume plot but diverge towards the end of the simulation. Figure 8-8b shows the instantaneous mass loading over time for both simulations, which diverge significantly and end at different times based on the time at which the atmospheric pressure is reached. The 1-D simulation maintains a higher mass loading than the 2-D simulation and lies closer to the isothermal curve, resulting in a longer compression time.

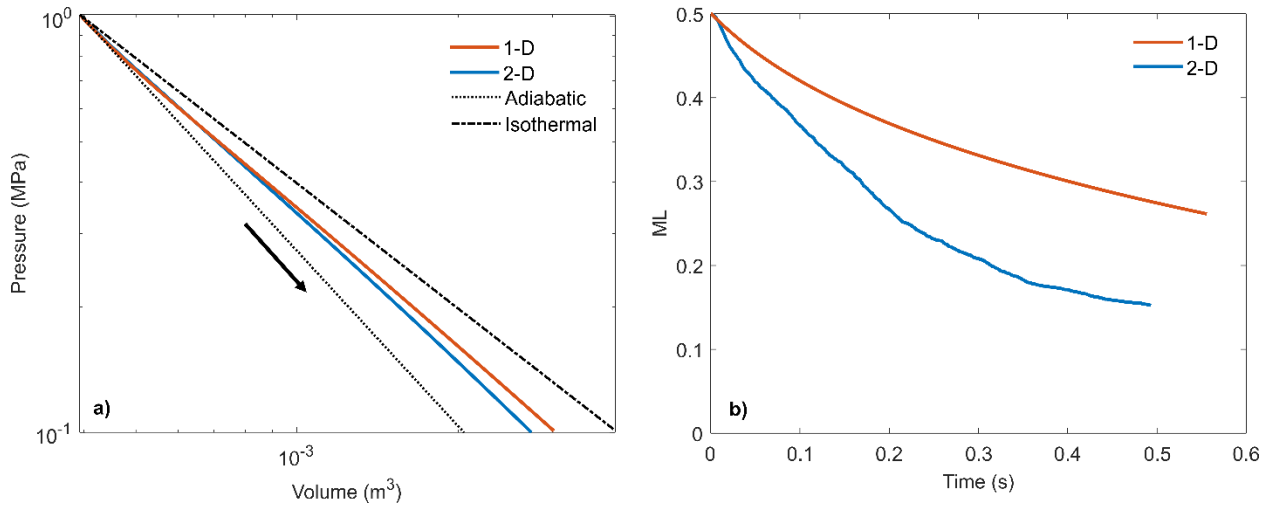


Figure 8-8. Case 1 expansion results for 75 μm droplets and $ML_{tot} = 0.5$ comparing between 1-D and 2-D simulations: a) pressure-volume, and b) instantaneous mass loading.

Cases 2 and 3 represent a matched pair of compression and expansion cases for the same droplet size and pre-mixed mass loading. The expansion case is plotted in Figure 8-9 with 1-D and 2-D simulations. Again, the 1-D simulation predicts higher mass loading throughout the expansion process than the 2-D simulation, and the 1-D simulation is consistently closer to the isothermal process.

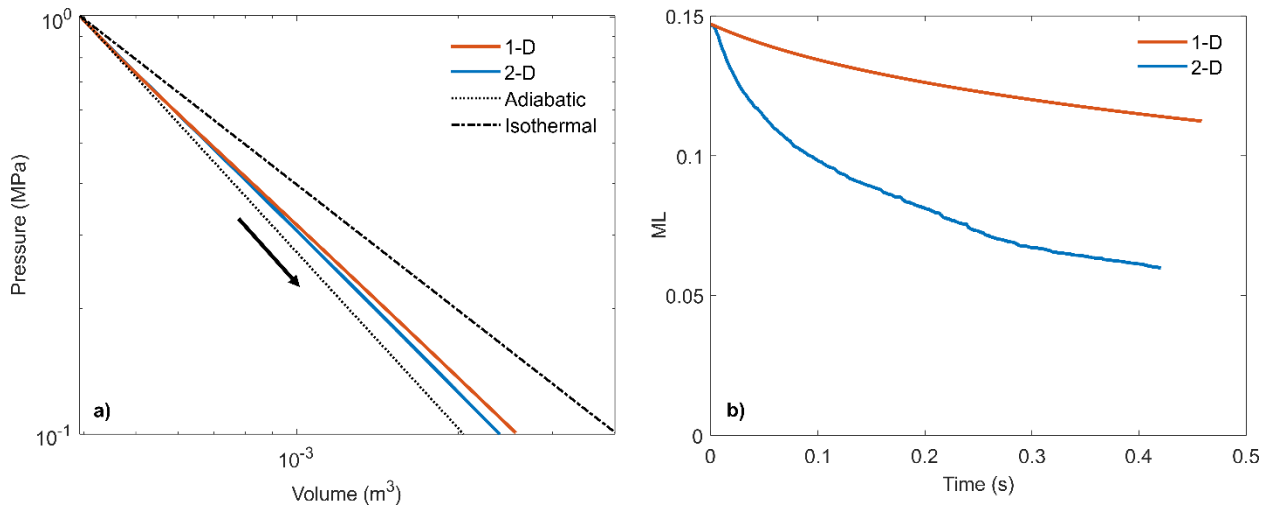


Figure 8-9. Case 2 expansion results for 50 μm droplets and $ML_{tot} = 0.147$ comparing between 1-D and 2-D simulations: a) pressure-volume, and b) instantaneous mass loading.

Case 3 is plotted in Figure 8-10 with 1-D and 2-D simulation results. As with expansion, the 1-D simulation predicts better performance than the 2-D simulation. However, in this compression case the mass loading of the 2-D simulation drops off significantly and does not level out as was seen in Cases 1 and 2.

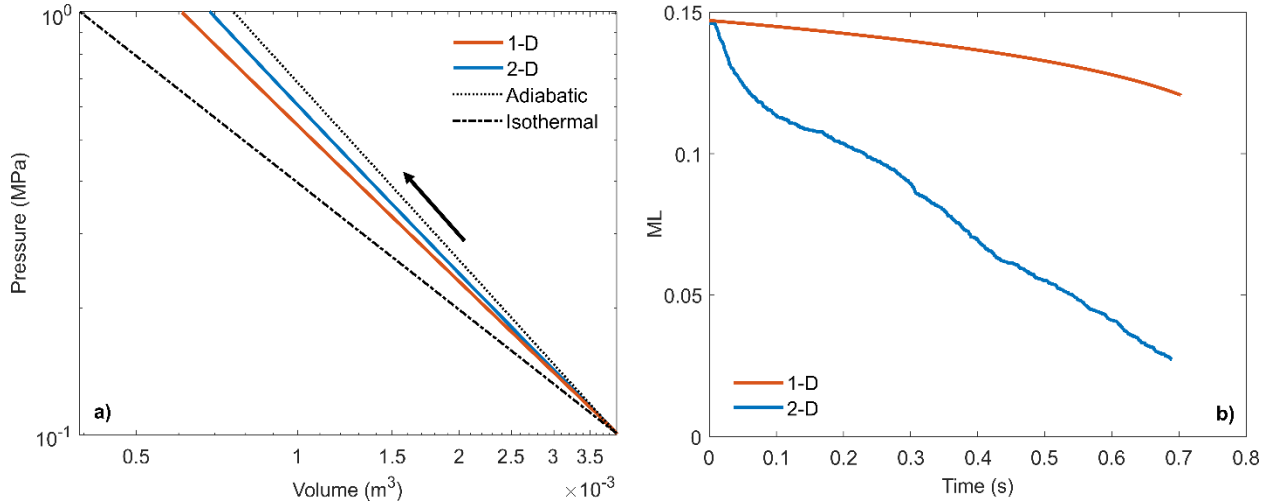


Figure 8-10. Case 3 compression results for 50 μm droplets and $ML_{tot} = 0.147$ comparing between 1-D and 2-D simulations: a) pressure-volume, and b) instantaneous mass loading.

The results from Cases 1-3 are summarized in Table 8-4, including the pre-defined parameters of droplet diameter and initial total mass loading. The average and final mass loadings are given in terms of percent of the initial (total) mass loading. All of the 1-D simulations herein have longer process times than their 2-D counterparts because the 1-D simulations predict the processes are more nearly isothermal than the 2-D simulations. The 1-D simulations consistently have lower polytropic indices (closer to isothermal) than the 2-D simulations. For the matched cases, Case 2 (expansion) has similar polytropic indices to Case 3 (compression), for the 1-D and 2-D simulations, respectively. The difference between the 1-D and 2-D polytropic indices is small for expansion cases, but the difference is larger for the compression case, likely caused by the larger difference in mass loading during the compression process.

The 1-D simulations only account for droplet loss through contact with the piston surface, while the 2-D simulations allow for droplets to exit the simulation via the piston or sidewalls (including the top of the chamber). In the 2-D cases examined herein, droplet loss via the sidewalls accounts for 15% and 43% of the total droplet mass loss for Case 1 and Case 2, respectively, which explains some of the discrepancy between the final mass loading in the 1-D and 2-D simulations. The droplet loss locations could not be recovered for Case 3.

Table 8-4. Comparing 1-D and 2-D simulations for 3 example cases. Droplet size and initial mass loading were set, while average and final mass loading, final air temperature, time to compression/expansion, and polytropic index depended on the process.

	Case 1 (Expan)		Case 2 (Expan)		Case 3 (Comp)	
	1-D	2-D	1-D	2-D	1-D	2-D
d (μm)	75	75	50	50	50	50
ML_{tot}	0.50	0.50	0.15	0.15	0.15	0.15
ML_{avg} %	70%	53%	86%	58%	93%	55%
ML_{final} %	52%	31%	76%	41%	82%	19%
Final air temp (K)	230	208	195	182	466	522
Process Time (s)	0.56	0.50	0.46	0.42	0.70	0.69
Polytropic index	1.14	1.19	1.24	1.28	1.23	1.31

The isothermal efficiencies for each case are compared in Table 8-5 for the 1-D and 2-D simulation results. The highest efficiency is achieved by Case 1, which has the highest total mass loading. The 1-D simulation consistently predicts a higher isothermal efficiency for each case than the 2-D simulation. The percent differences between the fast 1-D model and the more time-consuming 2-D model are less than 7%, indicating that the 1-D model may provide sufficient accuracy for identifying high-efficiency designs early in the design process.

Table 8-5. Comparing isothermal efficiencies for 1-D and 2-D simulations for 3 example cases.

	η_{iso} for 1-D	η_{iso} for 2-D	% Difference
Case 1 (Expan)	86.8%	84.0%	3%
Case 2 (Expan)	80.6%	78.7%	2%
Case 3 (Comp)	79.8%	75.4%	6%

8.5. Conclusions

A parametric analysis of the pre-mixed compression and expansion design space was completed using a 1-D numerical method to investigate roundtrip efficiency (excluding spray work effects). The polytropic indices for the pre-mixed 1-D simulations decrease with increasing mass loading and approach the isothermal limit. The expansion cases do not show a clear Crowe number trend when plotted against total mass loading, contrary to previous theory; however, when plotted against average mass loading, the expansion cases showed expected trends where smaller Crowe numbers tended to correlate with reduced

polytropic index for a given mass loading. When the compression and expansion results were combined for cases with the same spray design, pressure ratio, and piston design, the roundtrip isothermal efficiency was found to increase with increasing mass loading and approach the thermal equilibrium limit. The pre-mixed roundtrip simulations were able to achieve higher roundtrip efficiency than the direct injection simulations previously studied, using the same input parameters, in some scenarios in the moderate mass loading range of $0.1 < ML < 10$.

Three pre-mixed example cases were investigated in depth by comparing the 1-D numerical method to unsteady 2-D axisymmetric simulations. When looking at instantaneous results from the 2-D simulations, the air temperature and particle temperature are seen to vary significantly throughout the cylinder. Comparing the two simulation results on the pressure-volume plot, the 1-D and 2-D simulations start with similar curves but diverge towards the end of each simulation. The 1-D simulations consistently maintain a higher mass loading, lower polytropic index, and higher isothermal efficiency than the 2-D simulations, for all cases. The final temperatures at the end of the compression and expansion cases, for both 1-D and 2-D simulations, show that the droplets did not provide sufficient heat transfer to maintain a relatively constant air temperature during the processes.

The comparison of 1-D and 2-D simulation results illustrates that there are many effects captured in the 2-D simulations and neglected in the 1-D simulations which have a significant effect on the thermodynamic process. The assumption of uniform air temperature and radially uniform droplet temperature does not show good agreement with the instantaneous 2-D simulation results. Additionally, the 1-D simulations consistently over-predicted the mass loading over time compared to the 2-D simulations, in part due to neglecting any droplet interactions with the walls and the lack of turbulence under-predicting droplet loss at the piston surface. This may lead to the 1-D model preferring a long cylinder length because it does not consider the potential for droplet impacts on the sidewalls. Finally, the turbulence in the 2-D simulation causes more general variation in the particle velocities and locations that is not captured in the 1-D simulation.

However, despite these assumptions in the 1-D model, the 1-D and 2-D simulation isothermal efficiencies were less than 7% different for all 3 cases studied. Thus, the 1-D model may still be useful for rapidly identifying an upper-level of efficiency for a wide range of spray-based CAES designs.

Future work is suggested to extend the model into 3-D and consider the impact of effects such as injection swirl and nozzle configurations. Additionally, the ideal timing of sprays should be studied further, as the ideal system may be a combination of pre-mixed and direct injection sprays to achieve ICAES.

Chapter

9. Conclusions

9.1. Key results

The tower shadow effect on downwind turbine rotors was investigated in Chapters 2-3. A method for simulating the turbulent wind field conditions using meteorological tower data was developed and applied to the turbine in operational conditions. The tower shadow effect was simulated using the conventional Powles model and a new Eames model (developed herein), which includes the influence of upstream turbulence. Based on field test results, the more complex Eames model may not be necessary as the tower shadow effect can be reasonably modeled with the conventional Powles model. The tower shadow effect was found to increase the short-term Damage Equivalent Loads (DEL) by less than 10%, and the effect was small compared to the effect of turbulence.

When designing wind turbines or other renewable energy systems, a new design metric was proposed in Chapter 4, the Cost of Valued Energy (COVE), to better account for the time-varying value of energy generation. A simplified model for price based on a linear relationship with energy demand data was able to predict solar and wind energy value factor with less than 3% error. A case study showed the importance of COVE for renewable system design by relating it to Return on Investment and Value Factor.

Combining wind energy with an energy storage system in Chapter 5, a techno-economic analysis of Liquid Metal Battery storage located within the substructure of an offshore wind turbine indicated that adding storage can increase the relative value of the combined system. Dispatch simulations varying electrical line size and storage capacity found that line size can be reduced by 20% with 4 hours of storage or by 40% with 12 hours of storage, with negligible capacity factor losses. As storage prices continue to fall, the benefits found herein for LMB are predicted to improve and integrated Li-ion storage is predicted to become cost-effective as well.

Focusing on compressed air energy storage as a low-cost, long-duration energy storage options, compressed air energy storage was modeled in Chapters 6-8 using spray injection to reach near-isothermal compression and expansion processes. In Chapter 6, a theory-based equation for polytropic index was derived using the Crowe number. A 1-D numerical method for simulating spray-cooled compression was validated against published experimental results. A parametric analysis of the compression design space with the 1-D numerical method found that a high isothermal compression efficiency can be achieved with

droplet mass loadings of three or more coupled with a Crowe number of 0.1 or less. In Chapter 7, roundtrip efficiency was investigated via a parametric analysis of matched compression and expansion simulations. Additionally, spray work was found to have a significant effect on roundtrip efficiency for mass loadings greater than unity.

Pre-mixed droplet injection was investigated for compression and expansion in Chapter 8 via the 1-D numerical method and 2-D ANSYS Fluent simulations. The pre-mixed simulations were able to achieve higher roundtrip isothermal efficiencies than direct injection simulations, for some cases with moderate mass loading. Comparing the 1-D and 2-D simulation results, some of the 1-D assumptions were not validated by the 2-D results, but the percent differences between the 1-D and 2-D simulations were less than 7%.

9.2. Contributions to the field

This dissertation contributed to the fields of wind turbine modeling, techno-economic analysis of hybrid systems, and compression modeling with spray injection.

A new method was developed for replicating the field test conditions for computational simulation comparison and applied to the first field test data with a downwind flexible rotor. Additionally, a new tower shadow model was developed that considers the influence of wind field turbulence.

COVE was proposed as a new metric for renewable system design that values energy based on the time of generation, in a simple and easy-to-use manner. A techno-economic analysis of Liquid Metal Battery storage co-located within a wind turbine investigated energy storage capacity factors and economics for integrated long-duration storage for the first time and showed the benefits of long-duration storage for wind energy integration.

The theoretical behavior and the key nondimensional parameters of spray injection compression and expansion were characterized using theory and a 1-D numerical method. A new nondimensional number, the Crowe number, was proposed for the ratio of the droplet thermal response time to the domain time scale. Parametric analysis identified high efficiency designs for compression, roundtrip without spray work, roundtrip with spray work, and pre-mixed roundtrip without spray work. Additionally, near-isothermal expansion using spray droplets was investigated in 2-D for the first time and compared to 1-D model assumptions.

9.3. Future studies and recommendations

The Cost of Valued Energy (COVE) metric is still being refined and applied in new ways. It is suggested that this metric be used as the optimization object for designing a renewable energy system with energy storage and compared against other metric options to see which gives a preferred design.

The 1-D numerical method used in Chapters 6-8 was expanded and improved upon in this dissertation. Other researchers have modeled liquid piston heat transfer, which could be added to the 1-D model to allow for additional heat transfer in excess of that to the droplet spray. The 2-D Fluent simulations highlighted that some of the assumptions in the 1-D model may not be accurate, but additions to the 1-D code to remedy these differences may not be able to improve the accuracy significantly, since the 1-D and 2-D simulation results already predict similar isothermal efficiencies. Instead, simulations in 3-D could be implemented to study additional effects such as swirl and nozzle placement.

Super-rated operation of a wind turbine with energy storage was investigated and submitted as a patent but not included herein [213]. It proposed an alternative method for wind turbine control based on utilizing a mechanical energy storage system and decoupling the wind turbine rotor from the electrical generator. While systems-level simulations have been completed, further simulations on a component-level are suggested to further study this idea.

References

- [1] Stephen Nalley, Angelina LaRose. Annual Energy Outlook 2022 (AEO2022). Washington, DC: US Energy Information Administration; n.d.
- [2] Wiser R, Bolinger M. 2017 Wind Technologies Market Report. 2017.
- [3] Ananda GK, Bansal S, Selig MS. Aerodynamic Design of the 13.2 MW SUMR-13i Wind Turbine Rotor. 2018 Wind Energy Symposium 2018. <https://doi.org/10.2514/6.2018-0994>.
- [4] Zalkind DS, Pao LY, Martin DP, Johnson KE. Models used for the simulation and control of a segmented ultralight morphing rotor. *IFAC-PapersOnLine* 2017;50:4478–83. <https://doi.org/10.1016/j.ifacol.2017.08.377>.
- [5] Loth E, Fingersh L, Griffith D, Kaminski M, Qin C. Gravo-Aeroelastically Scaling for Extreme-Scale Wind Turbines. 35th AIAA Applied Aerodynamics Conference 2017:1–11. <https://doi.org/10.2514/6.2017-4215>.
- [6] Qin C (Chris), Loth E, Zalkind DS, Pao LY, Yao S, Griffith DT, et al. Downwind coning concept rotor for a 25 MW offshore wind turbine. *Renewable Energy* 2020;156:314–27. <https://doi.org/10.1016/j.renene.2020.04.039>.
- [7] Zalkind DS, Ananda GK, Chetan M, Martin DP, Bay CJ, Johnson KE, et al. System-level design studies for large rotors. *Wind Energy Science* 2019;4:595–618. <https://doi.org/10.5194/wes-4-595-2019>.
- [8] Matsunobu T, Hasegawa T, Isogawa M, Sato K, Futami M, Kato H. Development of 2-mw downwind turbine tailored to Japanese conditions. *Hitachi Review* 2009;58:213–8.
- [9] Kiyoki S, Sakamoto K, Kakuya H, Saeki M. 5-MW Downwind Wind Turbine Demonstration and Work Toward Smart Operation Control. *Hitachi Review* 2017;66.
- [10] Myhr A, Bjerkseter C, Ågotnes A, Nygaard TA. Levelised cost of energy for offshore floating wind turbines in a lifecycle perspective. *Renewable Energy* 2014;66:714–28. <https://doi.org/10.1016/j.renene.2014.01.017>.
- [11] Pawel I. The cost of storage - How to calculate the levelized cost of stored energy (LCOE) and applications to renewable energy generation. *Energy Procedia* 2014;46:68–77. <https://doi.org/10.1016/j.egypro.2014.01.159>.
- [12] Stehly T, Beiter P, Heimiller D, Scott G, Heimiller D, Scott G. 2017 Cost of Wind Energy Review. 2018.
- [13] Dufo-López R, Bernal-Agustín JL, Yusta-Loyo JM, Domínguez-Navarro JA, Ramírez-Rosado JJ, Lujano J, et al. Multi-objective optimization minimizing cost and life cycle emissions of stand-alone PV-wind-diesel systems with batteries storage. *Applied Energy* 2011;88:4033–41. <https://doi.org/10.1016/j.apenergy.2011.04.019>.
- [14] Mattar C, Guzmán-Ibarra MC. A techno-economic assessment of offshore wind energy in Chile. *Energy* 2017;133:191–205. <https://doi.org/10.1016/j.energy.2017.05.099>.
- [15] Becker S, Frew BA, Andresen GB, Zeyer T, Schramm S, Greiner M, et al. Features of a fully renewable US electricity system: Optimized mixes of wind and solar PV and transmission grid extensions. *Energy* 2014;72:443–58. <https://doi.org/10.1016/j.energy.2014.05.067>.
- [16] O’Leary K, Pakrashi V, Kelliher D. Optimization of composite material tower for offshore wind turbine structures. *Renewable Energy* 2019;140:928–42. <https://doi.org/10.1016/j.renene.2019.03.101>.
- [17] Chang G, Jones CA, Roberts JD, Neary VS. A comprehensive evaluation of factors affecting the levelized cost of wave energy conversion projects. *Renewable Energy* 2018;127:344–54. <https://doi.org/10.1016/j.renene.2018.04.071>.
- [18] Hirth L. The market value of variable renewables. The effect of solar wind power variability on their relative price. *Energy Economics* 2013;38:218–36. <https://doi.org/10.1016/j.eneco.2013.02.004>.

- [19] Dykes K, Veers P, Lantz E, Holttinen H, Carlson O, Tuohy A, et al. Results of IEA Wind TCP Workshop on a Grand Vision *iea wind*. 2019.
- [20] Kyriakopoulos GL, Arabatzis G. Electrical energy storage systems in electricity generation: Energy policies, innovative technologies, and regulatory regimes. *Renewable and Sustainable Energy Reviews* 2016;56:1044–67. <https://doi.org/10.1016/j.rser.2015.12.046>.
- [21] Jafari M, Botterud A, Sakti A. Decarbonizing power systems: A critical review of the role of energy storage. *Renewable and Sustainable Energy Reviews* 2022;158:112077. <https://doi.org/10.1016/j.rser.2022.112077>.
- [22] Wisner R, Bolinger M, Hoen B, Millstein D, Rand J, Barbose G, et al. Land-Based Wind Market Report: 2021 Edition. US Department of Energy Office of Energy Efficiency & Renewable Energy; 2021.
- [23] Iaconangelo D. Longer Turbine Blades have Slashed Wind Energy Costs. *E&E News* 2020.
- [24] NREL. Next generation wind rotors: because “supersizing” is reaching its limit. *Energy Post* 2019.
- [25] Eric Loth, Adam Steele, Chao Qin, Brian Ichter, Michael S. Selig PM. Downwind pre-aligned rotors for extreme-scale wind turbines. *Wind Energy* 2017;20:1241–59.
- [26] Johnson N, Bortolotti P, Dykes K, Barter G, Moriarty P, Carron S, et al. Investigation of Innovative Rotor Concepts for the Big Adaptive Rotor Project Investigation of Innovative Rotor Concepts for the Big Adaptive Rotor Project. 2019.
- [27] Sabale AK, Gopal NKV. Nonlinear Aeroelastic Analysis of Large Wind Turbines Under Turbulent Wind Conditions. *AIAA Journal* 2019;57:4416–32. <https://doi.org/10.2514/1.J057404>.
- [28] Noyes C, Qin C, Loth E. Tower shadow induced blade loads for an extreme-scale downwind turbine. *Wind Energy* 2020;23:458–70. <https://doi.org/10.1002/we.2415>.
- [29] O’Connor K, Loth E, Selig MS. Experiments on Fairing Designs for a Wind Turbine Tower. *AIAA Journal* 2016;54:1124–30. <https://doi.org/10.2514/1.J054318>.
- [30] Hand MM, Simms DA, Fingersh LJ, Jager DW, Cotrell JR, Schreck S, et al. Unsteady Aerodynamics Experiment Phase VI: Wind Tunnel Test Configurations and Available Data Campaigns. 2001. <https://doi.org/10.2172/15000240>.
- [31] Kaminski M, Loth E, Zalkind D, Pao L, Selig M, Johnson K. Servo-aero-gravo-elastic (SAGE) scaling and its application to a 13-MW downwind turbine. *Journal of Renewable and Sustainable Energy* 2020. <https://doi.org/10.1063/5.0021171>.
- [32] Yao S, Griffith DT, Chetan M, Bay CJ, Damiani R, Kaminski M, et al. A gravo-aeroelastically scaled wind turbine rotor at field-prototype scale with strict structural requirements. *Renewable Energy* 2020;156:535–47. <https://doi.org/10.1016/j.renene.2020.03.157>.
- [33] Noyes C, Qin C, Loth E. Pre-aligned downwind rotor for a 13.2 MW wind turbine. *Renewable Energy* 2018;116:749–54. <https://doi.org/10.1016/j.renene.2017.10.019>.
- [34] Yao S, Griffith DT, Chetan M, Bay CJ, Damiani R, Kaminski M, et al. Structural design of a 1/5th scale gravo-aeroelastically scaled wind turbine demonstrator blade for field testing. *AIAA Scitech 2019 Forum* 2019:1–9. <https://doi.org/10.2514/6.2019-1067>.
- [35] Bay CJ, Damiani R, Fingersh LJ, Hughes S, Chetan M, Yao S, et al. Design and Testing of a Scaled Demonstrator Turbine at the National Wind Technology Center. *AIAA Scitech 2019 Forum*, 2019. <https://doi.org/10.2514/6.2019-1068>.
- [36] Kaminski M, Noyes C, Loth E, Damiani R, Hughes S, Bay C, et al. Gravo-aeroelastic scaling of a 13-MW downwind rotor for 20% scale blades. *Wind Energy* 2020:1–17. <https://doi.org/10.1002/we.2569>.
- [37] Kaminski M. Field Testing and Simulating Servo-Aero-Gravoelastically Scaled Rotors for Extreme-Scale Wind Turbines 2020.
- [38] Powles SJR. The effects of tower shadow on the dynamics of a horizontal-axis wind turbine. *Wind Engineering* 1983;7:26–42.
- [39] IEC 61400-1 Wind turbines - Part 1: Design requirements 2005.
- [40] Simpson JG, Kaminski M, Loth E. Influence of tower shadow on downwind flexible rotors: Field tests and simulations. *Wind Energy* 2021;we.2703. <https://doi.org/10.1002/we.2703>.

- [41] OpenFAST, Open-source wind turbine simulation tool 2021.
- [42] Jonkman JM, Hayman GJ, Jonkman BJ, Damiani RR. AeroDyn v15 User's Guide and Theory Manual. 2015.
- [43] Moriarty PJ, Hansen AC. AeroDyn Theory Manual. Golden, CO: 2005. <https://doi.org/10.1146/annurev.fl.15.010183.001255>.
- [44] Chetan M, Yao S, Griffith DT. Multi-fidelity digital twin structural model for a sub-scale downwind wind turbine rotor blade. *Wind Energy* 2021;1–20. <https://doi.org/10.1002/we.2636>.
- [45] Roshko A. Experiments on the flow past a circular cylinder at very high Reynolds number. *Journal of Fluid Mechanics* 1961;10:345–56. <https://doi.org/10.1017/S0022112061000950>.
- [46] Jonkman BJ. TurbSim user's guide v2.00.00. Golden, CO: 2016.
- [47] Jonkman JM, Buhl ML. FAST Users Guide NREL/EL-500-29798. 2005.
- [48] Musial W, Beiter P, Spitsen P, Nunemaker J, Gevorgian V. 2018 Offshore Wind Technologies Market Report 2019.
- [49] Loth E, Steele A, Qin C, Ichter B, Selig MS, Moriarty P. Downwind pre-aligned rotors for extreme-scale wind turbines: Downwind pre-aligned rotors for extreme-scale wind turbines. *Wind Energy* 2017. <https://doi.org/10.1002/we.2092>.
- [50] Noyes C, Qin C, Loth E. Pre-aligned downwind rotor for a 13.2 MW wind turbine. *Renewable Energy* 2018;116:749–54. <https://doi.org/10.1016/j.renene.2017.10.019>.
- [51] Johnson N, Bortolotti P, Dykes KL, Barter GE, Moriarty PJ, Carron WS, et al. Investigation of Innovative Rotor Concepts for the Big Adaptive Rotor Project. 2019. <https://doi.org/10.2172/1563139>.
- [52] Wanke G, Bergami L, Zahle F, Verelst DR. Redesign of an upwind rotor for a downwind configuration: design changes and cost evaluation. *Wind Energy Sci* 2021;6:203–20. <https://doi.org/10.5194/wes-6-203-2021>.
- [53] Zalkind DS, Ananda GK, Chetan M, Martin DP, Bay CJ, Johnson KE, et al. System-level design studies for large rotors. *Wind Energy Sci* 2019;4:595–618. <https://doi.org/10.5194/wes-4-595-2019>.
- [54] Madsen HA. Low Frequency Noise from Wind Turbines Mechanisms of Generation and its Modelling 2010;29:13.
- [55] Yoshida S, Kiyoki S. Load Equivalent Tower Shadow Modelling for Downwind Turbines. *Transactions of Japan Society of Mechanical Engineers* 2007;73:1273–9.
- [56] Matsunobu T, Hasegawa T, Isogawa M, Sato K, Futami M, Kato H. Development of 2-MW downwind turbine tailored to Japanese conditions. *Hitachi Review* 2009;58:213–8.
- [57] Wang Z, Tian W, Hu H. A Comparative study on the aeromechanic performances of upwind and downwind horizontal-axis wind turbines. *Energy Conversion and Management* 2018;163:100–10. <https://doi.org/10.1016/j.enconman.2018.02.038>.
- [58] Noyes C, Qin C, Loth E. Tower shadow induced blade loads for an extreme-scale downwind turbine. *Wind Energy* 2020;23:458–70. <https://doi.org/10.1002/we.2415>.
- [59] Reiso M, Muskulus M. The simultaneous effect of a fairing tower and increased blade flexibility on a downwind mounted rotor. *Journal of Renewable and Sustainable Energy* 2013;5. <https://doi.org/10.1063/1.4803749>.
- [60] Yao S, Griffith DT, Chetan M, Bay CJ, Damiani R, Kaminski M, et al. A gravo-aeroelastically scaled wind turbine rotor at field-prototype scale with strict structural requirements. *Renewable Energy* 2020;156:535–47. <https://doi.org/10.1016/j.renene.2020.03.157>.
- [61] Bay CJ, Damiani R, Fingersh LJ, Hughes S, Chetan M, Yao S, et al. Design and Testing of a Scaled Demonstrator Turbine at the National Wind Technology Center. AIAA Scitech 2019 Forum, San Diego, California: American Institute of Aeronautics and Astronautics; 2019. <https://doi.org/10.2514/6.2019-1068>.
- [62] Kaminski M, Noyes C, Loth E, Damiani R, Hughes S, Bay C, et al. Gravo-aeroelastic scaling of a 13-MW downwind rotor for 20% scale blades. *Wind Energy* 2020;we.2569. <https://doi.org/10.1002/we.2569>.

- [63] Ananda GK, Bansal S, Selig MS. Aerodynamic Design of the 13.2 MW SUMR-13i Wind Turbine Rotor. 2018 Wind Energy Symposium, Kissimmee, Florida: American Institute of Aeronautics and Astronautics; 2018. <https://doi.org/10.2514/6.2018-0994>.
- [64] OpenFAST n.d.
- [65] Powles SRJ. The Effects of Tower Shadow on the Dynamics of a Horizontal Axis Wind Turbine.pdf. *Wind Engineering* 1983;7:26–42.
- [66] Jonkman JM, Hayman GJ, Jonkman BJ, Damiani RR. *AeroDyn v15 User’s Guide and Theory Manual*. National Renewable Energy Laboratory; 2015.
- [67] Reiso M, Hagen TR, Muskulus M. A calibration method for downwind wake models accounting for the unsteady behaviour of the wind turbine tower shadow behind monopile and truss towers. *Journal of Wind Engineering and Industrial Aerodynamics* 2013;121:29–38. <https://doi.org/10.1016/j.jweia.2013.07.016>.
- [68] Yoshida S. Combined Blade-Element Momentum—Lifting Line Model for Variable Loads on Downwind Turbine Towers. *Energies* 2018;11:2521. <https://doi.org/10.3390/en11102521>.
- [69] Yoshida S. Dynamic Stall Model for Tower Shadow Effects on Downwind Turbines and Its Scale Effects. *Energies* 2020;13:5237. <https://doi.org/10.3390/en13195237>.
- [70] Hoerner SF. *Fluid-dynamic drag*. 1965.
- [71] Simpson JG, Loth E. Field Tests and Simulations of Tower Shadow Effect for a Downwind Turbine. *AIAA Scitech 2021 Forum*, 2021, p. 1–8. <https://doi.org/10.2514/6.2021-1718>.
- [72] Kaminski M, Loth E, Zalkind D, Pao L, Selig M, Johnson K. Servo-aero-gravo-elastic (SAGE) scaling and its application to a 13-MW downwind turbine. *Journal of Renewable and Sustainable Energy* 2020. <https://doi.org/10.1063/5.0021171>.
- [73] Yoshida S, Fujii K, Hamasaki M, Takada A. Effect of Rotor Thrust on the Average Tower Drag of Downwind Turbines. *Energies* 2019;12:227. <https://doi.org/10.3390/en12020227>.
- [74] White FM. *Viscous Fluid Flow*. 3rd ed. McGraw-Hill; 2006.
- [75] Eames I, Jonsson C, Johnson PB. The growth of a cylinder wake in turbulent flow. *Journal of Turbulence* 2011;12:1–16. <https://doi.org/10.1080/14685248.2011.619985>.
- [76] Bell WH. The influence of turbulence on drag. *Ocean Engineering* 1979;6:329–40. [https://doi.org/10.1016/0029-8018\(79\)90021-0](https://doi.org/10.1016/0029-8018(79)90021-0).
- [77] National Renewable Energy Laboratory. Using the NewTower Feature of AeroDyn 14. 2005.
- [78] Roshko A. Experiments on the flow past a circular cylinder at very high Reynolds number. *Journal of Fluid Mechanics* 1961;10:345–56. <https://doi.org/10.1017/S0022112061000950>.
- [79] Sadeh WZ, Saharon DB. Turbulence effect on crossflow around a circular cylinder at subcritical Reynolds numbers. NASA; 1982.
- [80] Batham JP. Pressure distributions on circular cylinders at critical Reynolds numbers. *J Fluid Mech* 1973;57:209. <https://doi.org/10.1017/S0022112073001114>.
- [81] Heddleson CF, Brown DL, Cliffe RT. *Summary of Drag Coefficients of Various Shaped Cylinders*. GE Aircraft Nuclear Propulsion Department; 1957.
- [82] Cheung CK, Melbourne WH. *Wind Tunnel blockage effects on a circular cylinder in turbulent flows*, 1980.
- [83] Dryden HL, Hill GC. Wind pressure on circular cylinders and chimneys. *BUR STAN J RES* 1930;5:653. <https://doi.org/10.6028/jres.005.039>.
- [84] Hayman GJ, Jr MB. *Mlife User’s Guide for Version 1.00*. National Renewable Energy Laboratory; 2012.
- [85] Noyes C, Qin C, Loth E, Schreck S. Measurements and predictions of wind turbine tower shadow and fairing effects. *Journal of Wind Engineering and Industrial Aerodynamics* 2018;179:297–307. <https://doi.org/10.1016/j.jweia.2018.06.012>.
- [86] US Energy Information Administration. *Electric Power Annual 2017*. 2018.
- [87] Margolis R, Feldman D. *Solar Industry Update Q1 2019*. 2019. <https://doi.org/NREL/PR-6A20-68425>.
- [88] Lantz E, Wisser R, Hand M. *IEA Wind Task 26: The Past and Future Cost of Wind Energy*. 2012.

- [89] Wisser AR, Jenni K, Seel J, Baker E, Hand M. Forecasting Wind Energy Costs and Cost Drivers: The Views of the World ' s Leading Experts. 2016.
- [90] Haegel BNM, Margolis R, Buonassisi T, Feldman D, Garabedian R, Green M, et al. Terawatt-scale photovoltaics: Trajectories and challenges. *Science* 2017;141–4.
- [91] Ahlstrom M, Ela E, Riesz J, O'Sullivan J, Hobbs BF, O'Malley M, et al. The Evolution of the Market. *IEEE Power & Energy Magazine* 2015;6:60–6.
- [92] Denholm P, Sun Y, Mai T. *An Introduction to Grid Services: Concepts, Technical Requirements, and Provision from Wind* 2019.
- [93] Mai T, Mowers M, Eurek K. *Competitiveness Metrics for Electricity System Technologies (Forthcoming)*. Golden, CO: 2019.
- [94] Foster E, Contestabile M, Blazquez J, Manzano B, Workman M, Shah N. The unstudied barriers to widespread renewable energy deployment: Fossil fuel price responses. *Energy Policy* 2017;103:258–64. <https://doi.org/10.1016/j.enpol.2016.12.050>.
- [95] Djørup S, Thellufsen JZ, Sorknæs P. The electricity market in a renewable energy system. *Energy* 2018;162:148–57. <https://doi.org/10.1016/j.energy.2018.07.100>.
- [96] Wisser R, Mills A, Seel J, Levin T, Botterud A. *Impacts of Variable Renewable Energy on Bulk Power System Assets , Pricing , and Costs*. 2017.
- [97] Joskow PL. Comparing the cost of intermittent and dispatchable electricity generating technologies. *American Economic Review* 2011;100.
- [98] Ueckerdt F, Hirth L, Luderer G, Edenhofer O. System LCOE: What are the costs of variable renewables? *Energy* 2013;63:61–75. <https://doi.org/10.1016/j.energy.2013.10.072>.
- [99] EIA. *Levelized Cost of Electricity and Levelized Avoided Cost of Electricity Methodology Supplement*. 2013.
- [100] Borenstein S. The Private and Public Economics of Renewable Electricity Generation. *Journal of Economic Perspectives* 2012;26:67–92. <https://doi.org/10.3386/w17695>.
- [101] Hirth L, Ueckerdt F, Edenhofer O. Integration costs revisited - An economic framework for wind and solar variability. *Renewable Energy* 2015;74:925–39. <https://doi.org/10.1016/j.renene.2014.08.065>.
- [102] Namovicz C. *Assessing the economic value of new utility-scale renewable generation projects*. 2013.
- [103] EIA. *Levelized Cost and Levelized Avoided Cost of New Generation Resources in the Annual Energy Outlook 2018*. 2018.
- [104] Mills A, Wisser R. *Changes in the Economic Value of Variable Generation with Increasing Penetration Levels : A Pilot Study of California*. 2012.
- [105] Ueckerdt F, Brecha R, Luderer G. Analyzing major challenges of wind and solar variability in power systems. *Renewable Energy* 2015;81:1–10. <https://doi.org/10.1016/j.renene.2015.03.002>.
- [106] Byers C, Levin T, Botterud A. Capacity market design and renewable energy: Performance incentives, qualifying capacity, and demand curves. *Electricity Journal* 2018;31:65–74. <https://doi.org/10.1016/j.tej.2018.01.006>.
- [107] von Roon S, Huber M. *Modeling Spot Market Pricing with the Residual Load*. Enerday - 5th Conference on Energy Economics and Technology, 16.04.2010, Dresden, 2010.
- [108] Smolen J, Dudic B. The Role of Residual Demand in Electricity Price Analysis and Forecasting : Case of Czech Electricity Market. *International Journal of Energy Economics and Policy* 2017;7:152–8.
- [109] Motamedi A, Geidel C, Zareipour H, Rosehart WD. Electricity price forecasting considering residual demand. *IEEE PES Innovative Smart Grid Technologies Conference Europe* 2012:1–8. <https://doi.org/10.1109/ISGTEurope.2012.6465677>.
- [110] Wagner A. Residual Demand Modeling and Application to Electricity Pricing. *The Energy Journal* 2014;35. <https://doi.org/10.5547/01956574.35.2.3>.
- [111] Denholm P, Mai T. Timescales of energy storage needed for reducing renewable energy curtailment. *Renewable Energy* 2019;130:388–99. <https://doi.org/10.1016/j.renene.2018.06.079>.
- [112] Weron R. Electricity price forecasting: A review of the state-of-the-art with a look into the future. *International Journal of Forecasting* 2014;30:1030–81. <https://doi.org/10.1016/j.ijforecast.2014.08.008>.

- [113] Woo CK, Horowitz I, Moore J, Pacheco A. The impact of wind generation on the electricity spot-market price level and variance: The Texas experience. *Energy Policy* 2011;39:3939–44. <https://doi.org/10.1016/j.enpol.2011.03.084>.
- [114] Brancucci Martinez-Anido C, Brinkman G, Hodge BM. The impact of wind power on electricity prices. *Renewable Energy* 2016;94:474–87. <https://doi.org/10.1016/j.renene.2016.03.053>.
- [115] Jonkman J, Butterfield S, Musial W, Scott G. Definition of a 5-MW Reference Wind Turbine for Offshore System Development. 2009. <https://doi.org/10.2172/947422>.
- [116] Seel J, Mills A, Wiser R, Deb S, Asokkumar A, Hassanzadeh M, et al. Impacts of High Variable Renewable Energy Futures on Wholesale Electricity Prices, and on Electric-Sector Decision Making. 2018.
- [117] Kempton W, Pimenta FM, Veron DE, Colle BA. Electric power from offshore wind via synoptic-scale interconnection. *Proceedings of the National Academy of Sciences of the United States of America* 2010;107:7240–5. <https://doi.org/10.1073/pnas.0909075107>.
- [118] Grams CM, Beerli R, Pfenninger S, Staffell I, Wernli H. Balancing Europe’s wind-power output through spatial deployment informed by weather regimes. *Nature Climate Change* 2017;7:557–62. <https://doi.org/10.1038/NCLIMATE3338>.
- [119] Olauson J, Bergström H, Bergkvist M. Scenarios and Time Series of Future Wind Power. 2015.
- [120] Woo CK, Moore J, Schneiderman B, Ho T, Olson A, Alagappan L, et al. Merit-order effects of renewable energy and price divergence in California’s day-ahead and real-time electricity markets. *Energy Policy* 2016;92:299–312. <https://doi.org/10.1016/j.enpol.2016.02.023>.
- [121] Ashuri T, Zaaier MB, Martins JRR, van Bussel GJW, van Kuik GAM. Multidisciplinary design optimization of offshore wind turbines for minimum levelized cost of energy. *Renewable Energy* 2014;68:893–905. <https://doi.org/10.1016/j.renene.2014.02.045>.
- [122] Esteban MD, Diez JJ, López JS, Negro V. Why offshore wind energy? *Renewable Energy* 2011;36:444–50. <https://doi.org/10.1016/j.renene.2010.07.009>.
- [123] Zhao H, Wu Q, Hu S, Xu H, Rasmussen CN. Review of energy storage system for wind power integration support. *Applied Energy* 2015;137:545–53. <https://doi.org/10.1016/j.apenergy.2014.04.103>.
- [124] Notton G, Nivet ML, Voyant C, Paoli C, Darras C, Motte F, et al. Intermittent and stochastic character of renewable energy sources: Consequences, cost of intermittence and benefit of forecasting. *Renewable and Sustainable Energy Reviews* 2018;87:96–105. <https://doi.org/10.1016/j.rser.2018.02.007>.
- [125] Bludszweit H, Domínguez-Navarro JA. A probabilistic method for energy storage sizing based on wind power forecast uncertainty. *IEEE Transactions on Power Systems* 2011;26:1651–8. <https://doi.org/10.1109/TPWRS.2010.2089541>.
- [126] Teleke S, Baran ME, Bhattacharya S, Huang A. Validation of battery energy storage control for wind farm dispatching. *IEEE PES General Meeting, PES 2010* 2010;24:725–32. <https://doi.org/10.1109/PES.2010.5589640>.
- [127] Ding Y, Shao C, Yan J, Song Y, Zhang C, Guo C. Economical flexibility options for integrating fluctuating wind energy in power systems: The case of China. *Applied Energy* 2018;228:426–36. <https://doi.org/10.1016/j.apenergy.2018.06.066>.
- [128] Haggi E, Fowler M, Raahemifar K. Co-benefit analysis of incentives for energy generation and storage systems; a multi-stakeholder perspective. *International Journal of Hydrogen Energy* 2019;44:9643–71. <https://doi.org/10.1016/j.ijhydene.2018.08.150>.
- [129] Shaner MR, Davis SJ, Lewis NS, Caldeira K. Geophysical constraints on the reliability of solar and wind power in the United States. *Energy & Environmental Science* 2018;11:914–25. <https://doi.org/10.1039/C7EE03029K>.
- [130] Bassett K, Carriveau R, Ting DSK. Energy arbitrage and market opportunities for energy storage facilities in Ontario. *Journal of Energy Storage* 2018;20:478–84. <https://doi.org/10.1016/j.est.2018.10.015>.

- [131] Salles MBC, Huang J, Aziz MJ, Hogan WW. Potential arbitrage revenue of energy storage systems in PJM. *Energies* 2017;10. <https://doi.org/10.3390/en10081100>.
- [132] Salles MBC, Gadotti TN, Aziz MJ, Hogan WW. Breakeven analysis of energy storage systems in PJM energy markets. 2017 6th International Conference on Renewable Energy Research and Applications, ICRERA 2017, 2017, p. 395–400. <https://doi.org/10.1109/DISTRA.2017.8191092>.
- [133] Jafari M, Botterud A, Sakti A. Evaluation of Energy- and Capacity-Market Revenues from Lithium-ion Battery Systems for Offshore Wind Using Advanced Battery Models. *Applied Energy* 2020. <https://doi.org/10.1016/j.apenergy.2020.115417>.
- [134] US Energy Information Administration. U.S. Battery Storage Market Trends. 2018.
- [135] Cole W, Frazier AW. Cost Projections for Utility-Scale Battery Storage. Golden, CO: 2019.
- [136] Coffey B. Shades of Green: Wind-Battery Hybrid System Debuts in Ireland. GE Reports 2018.
- [137] St. John J. Tesla Batteries may be used for winter backup on Deepwater’s 90MW offshore wind farm. Green Tech Media 2017.
- [138] Wahlquist C. South Australia’s Tesla battery on track to make back a third of cost in a year. The Guardian 2018.
- [139] Yao DL, Choi SS, Tseng KJ, Lie TT. Determination of short-term power dispatch schedule for a wind farm incorporated with dual-battery energy storage scheme. *IEEE Transactions on Sustainable Energy* 2012;3:74–84. <https://doi.org/10.1109/TSSTE.2011.2163092>.
- [140] Qin C, Innes-Wimsatt E, Loth E. Hydraulic-electric hybrid wind turbines: Tower mass saving and energy storage capacity. *Renewable Energy* 2016;99:69–79. <https://doi.org/10.1016/j.renene.2016.06.037>.
- [141] ARPA-E. Duration Addition to electricity Storage (DAYS) Overview. 2018.
- [142] Hemmati R, Saboori H. Emergence of hybrid energy storage systems in renewable energy and transport applications – A review. *Renewable and Sustainable Energy Reviews* 2016;65:11–23. <https://doi.org/10.1016/j.rser.2016.06.029>.
- [143] Goldie-Scot L. A Behind the Scenes Take on Lithium-ion Battery Prices. BloombergNEF 2019.
- [144] Colthorpe A. BloombergNEF: Bullish on cost reductions, in line with others on global battery market forecast. *Energy Storage News* 2019.
- [145] Kong L, Li C, Jiang J, Pecht MG. Li-ion battery fire hazards and safety strategies. *Energies* 2018;11:1–11. <https://doi.org/10.3390/en11092191>.
- [146] Lu L, Han X, Li J, Hua J, Ouyang M. A review on the key issues for lithium-ion battery management in electric vehicles. *Journal of Power Sources* 2013;226:272–88. <https://doi.org/10.1016/j.jpowsour.2012.10.060>.
- [147] Mongird K, Fotedar V, Viswanathan V, Koritarov V, Balducci P, Hadjerioua B, et al. Energy Storage Technology and Cost Characterization Report. 2019.
- [148] Yin H, Chung B, Chen F, Ouchi T, Zhao J, Tanaka N, et al. Faradaically selective membrane for liquid metal displacement batteries. *Nature Energy* 2018;3:127–31. <https://doi.org/10.1038/s41560-017-0072-1>.
- [149] Ning X, Phadke S, Chung B, Yin H, Burke P, Sadoway DR. Self-healing Li-Bi liquid metal battery for grid-scale energy storage. *Journal of Power Sources* 2015;275:370–6. <https://doi.org/10.1016/j.jpowsour.2014.10.173>.
- [150] Li H, Yin H, Wang K, Cheng S, Jiang K, Sadoway DR. Liquid Metal Electrodes for Energy Storage Batteries. *Advanced Energy Materials* 2016;6:1–19. <https://doi.org/10.1002/aenm.201600483>.
- [151] Wang K, Jiang K, Chung B, Ouchi T, Burke PJ, Boysen DA, et al. Lithium-antimony-lead liquid metal battery for grid-level energy storage. *Nature* 2014;514:348–50. <https://doi.org/10.1038/nature13700>.
- [152] Ouchi T, Kim H, Sadoway DR. Multi-element liquid metal battery. US 2019/0089013 A1, 2019.
- [153] Ambri n.d. <https://ambri.com/> (accessed October 29, 2019).
- [154] Qu L, Qiao W. Constant power control of DFIG wind turbines with supercapacitor energy storage. *IEEE Transactions on Industry Applications* 2011;47:359–67. <https://doi.org/10.1109/TIA.2010.2090932>.

- [155] Fingersh LJ. Wind-Battery-Hydrogen Integration Study Wind-Battery-Hydrogen Integration Study. Golden, CO: 2004.
- [156] US Department of Energy. A2e: BUOY Lidar Project n.d. <https://a2e.energy.gov/projects/buoy> (accessed August 31, 2018).
- [157] Jonkman J, Butterfield S, Camp T, Nichols J, Azcona J, Martinez a. Offshore Code Comparison Collaboration within IEA Wind Annex XXIII: Phase II Results Regarding Monopile Foundation Modeling. IEA European Offshore Wind Conference 2008;15. <https://doi.org/NREL/CP-500-42471>.
- [158] May GJ, Davidson A, Monahov B. Lead batteries for utility energy storage: A review. *Journal of Energy Storage* 2018;15:145–57. <https://doi.org/10.1016/j.est.2017.11.008>.
- [159] Zhang C, Wei YL, Cao PF, Lin MC. Energy storage system: Current studies on batteries and power condition system. *Renewable and Sustainable Energy Reviews* 2018;82:3091–106. <https://doi.org/10.1016/j.rser.2017.10.030>.
- [160] National Oceanic and Atmospheric Administration. National Data Buoy Center, Station 44014 n.d. https://www.ndbc.noaa.gov/station_page.php?station=44014.
- [161] Bergman TL, Lavine AS, Incropera FP, Dewitt DP. *Fundamentals of Heat and Mass Transfer*. 7th ed. Wiley; 2011.
- [162] Li Q, Choi SS, Yuan Y, Yao DL. On the determination of battery energy storage capacity and short-term power dispatch of a wind farm. *IEEE Transactions on Sustainable Energy* 2011;2:148–58. <https://doi.org/10.1109/TSTE.2010.2095434>.
- [163] Korpaas M, Holen AT, Hildrum R. Operation and sizing of energy storage for wind power plants in a market system. *International Journal of Electrical Power and Energy System* 2003;25:599–606. [https://doi.org/10.1016/S0142-0615\(03\)00016-4](https://doi.org/10.1016/S0142-0615(03)00016-4).
- [164] Beiter P, Spitsen P, Nunemaker J, Tian T, Musial W, Lantz E, et al. 2017 Offshore Wind Technologies Market Update. 2018.
- [165] Simpson J, Loth E, Dykes K. Cost of Valued Energy for design of renewable energy systems. *Renewable Energy* 2020;153:290–300. <https://doi.org/10.1016/j.renene.2020.01.131>.
- [166] Nelson P, Gallagher K, Bloom I, Dees D, Ahmed S. BatPaC: Battery Manufacturing Cost Estimation 2017.
- [167] Nelson PA, Bloom KG, I Dees DW. Modeling the performance and cost of lithium-ion batteries for electric-drive vehicles, Chemical Sciences and Engineering division, Argonne National Laboratory, ANL 11/32. Argonne, IL: 2011. <https://doi.org/10.2172/1027714>.
- [168] Qin C, Saunders G, Loth E. Offshore wind energy storage concept for cost-of-rated-power savings. *Applied Energy* 2017;201:148–57. <https://doi.org/10.1016/j.apenergy.2017.04.077>.
- [169] PJM Interconnection. Data Miner 2. Real-Time Hourly LMPs. Historical pricing data 2018, Mid-Atlantic Region n.d.
- [170] Byers C, Levin T, Botterud A. Capacity market design and renewable energy: Performance incentives, qualifying capacity, and demand curves. *Electricity Journal* 2018;31:65–74. <https://doi.org/10.1016/j.tej.2018.01.006>.
- [171] Sukunta M. Personal Communication 2019.
- [172] PJM Interconnection Inc. 2021/2022 RPM Base Residual Auction Results. 2018.
- [173] Sioshansi R, Madaeni SH, Denholm P. A dynamic programming approach to estimate the capacity value of energy storage. *IEEE Transactions on Power Systems* 2014;29:395–403. <https://doi.org/10.1109/TPWRS.2013.2279839>.
- [174] Eroglu D, Zavadil KR, Gallagher KG. Critical link between materials chemistry and cell-level design for high energy density and low cost lithium-sulfur transportation battery. *Journal of the Electrochemical Society* 2015;162:A982–90. <https://doi.org/10.1149/2.0611506jes>.
- [175] Singerling SA. Bismuth. 2019. <https://doi.org/10.1017/CBO9781107415324.004>.
- [176] Dowling JA, Rinaldi KZ, Ruggles TH, Davis SJ, Yuan M, Tong F, et al. Role of Long-Duration Energy Storage in Variable Renewable Electricity Systems. *Joule* 2020;4:1907–28. <https://doi.org/10.1016/j.joule.2020.07.007>.

- [177] Guerra OJ. Beyond short-duration energy storage. *Nat Energy* 2021. <https://doi.org/10.1038/s41560-021-00837-2>.
- [178] Bennett JA, Simpson JG, Qin C, Fittro R, Koenig GM, Clarens AF, et al. Techno-economic analysis of offshore isothermal compressed air energy storage in saline aquifers co-located with wind power. *Applied Energy* 2021;303:117587. <https://doi.org/10.1016/j.apenergy.2021.117587>.
- [179] Li B, DeCarolis JF. A techno-economic assessment of offshore wind coupled to offshore compressed air energy storage. *Applied Energy* 2015;155:315–22. <https://doi.org/10.1016/j.apenergy.2015.05.111>.
- [180] Bazdar E, Sameti M, Nasiri F, Haghghat F. Compressed air energy storage in integrated energy systems: A review. *Renewable and Sustainable Energy Reviews* 2022;167:112701. <https://doi.org/10.1016/j.rser.2022.112701>.
- [181] Van de Ven JD, Li PY. Liquid piston gas compression. *Applied Energy* 2009;86:2183–91. <https://doi.org/10.1016/j.apenergy.2008.12.001>.
- [182] Zhang C, Li PY, Van de Ven JD, Simon TW. Design analysis of a liquid-piston compression chamber with application to compressed air energy storage. *Applied Thermal Engineering* 2016;101:704–9. <https://doi.org/10.1016/j.applthermaleng.2016.01.082>.
- [183] Neu T, Sollicc C, dos Santos Piccoli B. Experimental study of convective heat transfer during liquid piston compressions applied to near isothermal underwater compressed-air energy storage. *Journal of Energy Storage* 2020;32:101827. <https://doi.org/10.1016/j.est.2020.101827>.
- [184] Wieberdink J, Li PY, Simon TW, Ven JDV de. Effects of porous media insert on the efficiency and power density of a high pressure (210 bar) liquid piston air compressor/expander – An experimental study. *Applied Energy* 2018;212:1025–37. <https://doi.org/10.1016/j.apenergy.2017.12.093>.
- [185] Yan B, Wieberdink J, Shirazi F, Li PY, Simon TW, Van de Ven JD. Experimental study of heat transfer enhancement in a liquid piston compressor/expander using porous media inserts. *Applied Energy* 2015;154:40–50. <https://doi.org/10.1016/j.apenergy.2015.04.106>.
- [186] Patil VC, Acharya P, Ro PI. Experimental investigation of water spray injection in liquid piston for near-isothermal compression. *Applied Energy* 2020;259:114182. <https://doi.org/10.1016/j.apenergy.2019.114182>.
- [187] Khaljani M, Vennard A, Harrison J, Surplus D, Murphy A, Mahmoudi Y. Experimental and modelling analysis of efficiency enhancement in a liquid piston gas compressor using metal plate inserts for compressed air energy storage application. *Journal of Energy Storage* 2021;43:103240. <https://doi.org/10.1016/j.est.2021.103240>.
- [188] Guanwei J, Weiqing X, Maolin C, Yan S. Micron-sized water spray-cooled quasi-isothermal compression for compressed air energy storage. *Experimental Thermal and Fluid Science* 2018;96:470–81. <https://doi.org/10.1016/j.expthermflusci.2018.03.032>.
- [189] Qin C, Loth E. Simulation of spray direct injection for compressed air energy storage. *Applied Thermal Engineering* 2016;95:24–34. <https://doi.org/10.1016/j.applthermaleng.2015.11.008>.
- [190] Qin C, Loth E. Liquid piston compression efficiency with droplet heat transfer. *Applied Energy* 2014;114:539–50. <https://doi.org/10.1016/j.apenergy.2013.10.005>.
- [191] Ahn B, Patil VC, Ro PI. Effect of Integrating Metal Wire Mesh with Spray Injection for Liquid Piston Gas Compression. *Energies* 2021;14:3723. <https://doi.org/10.3390/en14133723>.
- [192] Yu Q, Wang Q, Tan X, Li X. Water spray heat transfer gas compression for compressed air energy system. *Renewable Energy* 2021;179:1106–21. <https://doi.org/10.1016/j.renene.2021.07.128>.
- [193] Dib G, Haberschill P, Rullière R, Revellin R. Thermodynamic investigation of quasi-isothermal air compression/expansion for energy storage. *Energy Conversion and Management* 2021;235:114027. <https://doi.org/10.1016/j.enconman.2021.114027>.
- [194] Kersey J, Loth E, Lankford D. Effect of Evaporating Droplets on Shock Waves. *AIAA Journal* 2010;48:1975–86. <https://doi.org/10.2514/1.J050162>.
- [195] Crowe C, Sommerfeld M, Tsuji Y. Multiphase flows with droplets and particles. CRC Press LLC; 1998.

- [196] Qin C, Loth E. Numerical description of a pressure-swirl nozzle spray. *Chemical Engineering and Processing - Process Intensification* 2016;107:68–79. <https://doi.org/10.1016/j.cep.2016.06.009>.
- [197] Loth E. *Fluid dynamics of particles, drops and bubbles*. Cambridge University Press; 2023.
- [198] Ranz WE, Marshall WR. Evaporation from drops - Part 1. *Chemical Engineering Progress* 1952;48:141–8.
- [199] Zhang X, Xu Y, Zhou X, Zhang Y, Li W, Zuo Z, et al. A near-isothermal expander for isothermal compressed air energy storage system. *Applied Energy* 2018;225:955–64. <https://doi.org/10.1016/j.apenergy.2018.04.055>.
- [200] Michael J. Moran, Howard N. Shapiro, Daisie D. Boettner, Maraget B. Bailey. *Fundamental of Engineering Thermodynamics*. 8th ed. Wiley; n.d.
- [201] Bell IH, Wronski J, Quoilin S, Lemort V. Pure and Pseudo-pure Fluid Thermophysical Property Evaluation and the Open-Source Thermophysical Property Library CoolProp. *Ind Eng Chem Res* 2014;53:2498–508. <https://doi.org/10.1021/ie4033999>.
- [202] Sapin P, Simpson M, Kirmse C, Markides CN. Dynamic modelling of water-droplet spray injection in reciprocating-piston compressors. *Proceedings of ECOS 2018 - The 31st International Conference On Efficiency, Cost, Optimization, Simulation And Environmental Impact Of Energy Systems*, Guimaraes, Portugal: 2018, p. 12.
- [203] Yu Q, Li X, Geng Y, Tan X. Study on quasi-isothermal expansion process of compressed air based on spray heat transfer. *Energy Reports* 2022;8:1995–2007. <https://doi.org/10.1016/j.egyr.2022.01.019>.
- [204] Hu S, Xu W, Cai M, Jia G. Energy efficiency and power density analysis of a tube array liquid piston air compressor/expander for compressed air energy storage. *Journal of Energy Storage* 2022;55:105674. <https://doi.org/10.1016/j.est.2022.105674>.
- [205] Odukomaiya A, Abu-Heiba A, Gluesenkamp KR, Abdelaziz O, Jackson RK, Daniel C, et al. Thermal analysis of near-isothermal compressed gas energy storage system. *Applied Energy* 2016;179:948–60. <https://doi.org/10.1016/j.apenergy.2016.07.059>.
- [206] Chen H. Thermodynamic analysis of an open type isothermal compressed air energy storage system based on hydraulic pump/turbine and spray cooling. *Energy Conversion and Management* 2020;13.
- [207] Lefebvre AH, McDonell VG. *Atomization and Sprays*. 2nd ed. CRC Press; 2017.
- [208] Qin C, Loth E, Li P, Simon T, Van de Ven J. Spray-cooling concept for wind-based compressed air energy storage. *Journal of Renewable and Sustainable Energy* 2014;6:043125. <https://doi.org/10.1063/1.4893434>.
- [209] Wang XF, Lefebvre AH. Mean drop sizes from pressure-swirl nozzles. *Journal of Propulsion and Power* 1987;3:11–8. <https://doi.org/10.2514/3.22946>.
- [210] Jia G, Nian X, Xu W, Shi Y, Cai M. Water-Spray-Cooled Quasi-Isothermal Compression Method: Water-Spray Flow Improvement. *Entropy* 2021;23:724. <https://doi.org/10.3390/e23060724>.
- [211] Gouda EM, Benaouicha M, Neu T, Fan Y, Luo L. Flow and heat transfer characteristics of air compression in a liquid piston for compressed air energy storage. *Energy* 2022;254:124305. <https://doi.org/10.1016/j.energy.2022.124305>.
- [212] Yan B. Experimental study of heat transfer enhancement in a liquid piston compressor/expander using porous media inserts. *Applied Energy* 2015;11.
- [213] Simpson JG, Loth E. Super-rated operational concept for increased wind turbine power with energy storage. *Energy Conversion and Management: X* 2022;14:100194. <https://doi.org/10.1016/j.ecmx.2022.100194>.